

Magazine of Civil Engineering

101(1), 2021

ISSN
2712-8172





ПОЛИТЕХ
Санкт-Петербургский
политехнический университет
Петра Великого

Инженерно-строительный институт
Центр дополнительных профессиональных программ
195251, г. Санкт-Петербург, Политехническая ул., 29,
тел/факс: 552-94-60, www.stroikursi.spbstu.ru,
stroikursi@mail.ru

**Приглашает специалистов организаций, вступающих в СРО,
на курсы повышения квалификации (72 часа)**

Код	Наименование программы	Виды работ*
Курсы по строительству		
БС-01-04	«Безопасность и качество выполнения общестроительных работ»	п.1,2, 3, 5, 6, 7, 9, 10, 11, 12, 13, 14
БС-01	«Безопасность и качество выполнения геодезических, подготовительных и земляных работ, устройства оснований и фундаментов»	1,2,3,5
БС-02	«Безопасность и качество возведения бетонных и железобетонных конструкций»	6,7
БС-03	«Безопасность и качество возведения металлических, каменных и деревянных конструкций»	9,10,11
БС-04	«Безопасность и качество выполнения фасадных работ, устройства кровель, защиты строительных конструкций, трубопроводов и оборудования»	12,13,14
БС-05	«Безопасность и качество устройства инженерных сетей и систем»	15,16,17,18,19
БС-06	«Безопасность и качество устройства электрических сетей и линий связи»	20,21
БС-08	«Безопасность и качество выполнения монтажных и пусконаладочных работ»	23,24
БС-12	«Безопасность и качество устройства мостов, эстакад и путепроводов»	29
БС-13	«Безопасность и качество выполнения гидротехнических, водолазных работ»	30
БС-14	«Безопасность и качество устройства промышленных печей и дымовых труб»	31
БС-15	«Осуществление строительного контроля»	32
БС-16	«Организация строительства, реконструкции и капитального ремонта. Выполнение функций технического заказчика и генерального подрядчика»	33
Курсы по проектированию		
БП-01	«Разработка схемы планировочной организации земельного участка, архитектурных решений, мероприятий по обеспечению доступа маломобильных групп населения»	1,2,11
БП-02	«Разработка конструктивных и объемно-планировочных решений зданий и сооружений»	3
БП-03	«Проектирование внутренних сетей инженерно-технического обеспечения»	4
БП-04	«Проектирование наружных сетей инженерно-технического обеспечения»	5
БП-05	«Разработка технологических решений при проектировании зданий и сооружений»	6
БП-06	«Разработка специальных разделов проектной документации»	7
БП-07	«Разработка проектов организации строительства»	8
БП-08	«Проектные решения по охране окружающей среды»	9
БП-09	«Проектные решения по обеспечению пожарной безопасности»	10
БП-10	«Обследование строительных конструкций и грунтов основания зданий и сооружений»	12
БП-11	«Организация проектных работ. Выполнение функций генерального проектировщика»	13
Э-01	«Проведение энергетических обследований с целью повышения энергетической эффективности и энергосбережения»	
Курсы по инженерным изысканиям		
И-01	«Инженерно-геодезические изыскания в строительстве»	1
И-02	«Инженерно-геологические изыскания в строительстве»	2,5
И-03	«Инженерно-гидрометеорологические изыскания в строительстве»	3
И-04	«Инженерно-экологические изыскания в строительстве»	4
И-05	«Организация работ по инженерным изысканиям»	7

*(согласно приказам Минрегионразвития РФ N 624 от 30 декабря 2009 г.)

**По окончании курса слушателю выдается удостоверение о краткосрочном повышении
квалификации установленного образца (72 ак. часа)**

Для регистрации на курс необходимо выслать заявку на участие, и копию диплома об образовании по телефону/факсу: 8(812) 552-94-60, 535-79-92, , e-mail: stroikursi@mail.ru.

Magazine of Civil Engineering

SCHOLAR JOURNAL

ISSN 2712-8172

Свидетельство о государственной регистрации:
Эл № ФС77-77906 от 19.02.2020,
выдано Роскомнадзором

Специализированный научный журнал.

Выходит с 09.2008.

Включен в Перечень ВАК РФ

Индексируется в БД Scopus

Периодичность: 8 раз в год

Учредитель и издатель:

Санкт-Петербургский политехнический университет
Петра Великого

Адрес редакции:

195251, СПб, ул. Политехническая, д. 29

Главный редактор:

Екатерина Александровна Линник

Научный редактор:

Виталий Владимирович Сергеев

Заместитель главного научного редактора:

Галина Леонидовна Козинец

Редакционная коллегия:

PhD, проф. Т. Аввад;
д.т.н., проф. М.И. Бальзанников
д.т.н., проф. А.И. Белостоцкий;
к.т.н., проф. А.И. Боровков;
д.т.н., проф. А. Бородинец;
PhD, проф. М. Велькович;
PhD, проф. Р.Д. Гарг;
PhD, М.Р. Гарифуллин;
Dr.-Ing, проф. Т. Грис;
д.т.н., проф. Т.А. Дацюк;
д.т.н., проф. В.В. Елистратов;
Dr.-Ing., проф. Т. Кэрки;
д.т.н., проф. Д.В. Козлов;
д.т.н., доцент С.В. Корниенко;
д.т.н., проф. Ю.Г. Лазарев;
д.т.н., проф. М.М. Мухаммадиев;
Dr.-Ing. Habil., проф. Х. Пастернак;
Dr.-Ing., проф. Ф. Рёгинер;
д.т.н., проф. Т.З. Султанов;
д.т.н., проф. М.Г. Тягунов;
акад. РАН, д.т.н., проф. М.П. Федоров;
Dr.-Ing., проф. Д. Хеэцк;
д.г.-м.н. А.Г. Шашкин;
д.т.н. В.Б. Штильман

Дата выхода: 19.02.2021

© ФГАОУ ВО СПбПУ, 2021
© Иллюстрация на обложке: Илья Смагин

Magazine of Civil Engineering

SCHOLAR JOURNAL

ISSN 2712-8172

Peer-reviewed scientific journal

Start date: 2008/09

8 issues per year

Publisher:

Peter the Great St. Petersburg Polytechnic University

Indexing:

Scopus, Russian Science Citation Index (WoS),
Compendex, EBSCO, Google Academia, Index
Copernicus, ProQuest, Ulrich's Serials Analysis System,
CNKI

Corresponding address:

29 Polytechnicheskaya st., Saint-Petersburg, 195251,
Russia

Editor-in-chief:

Ekaterina A. Linnik

Science editor:

Vitaly V. Sergeev

Deputy chief science editor:

Galina L. Kozinetc

Editorial board:

T. Awwad, PhD, professor
M.I. Balzannikov, D.Sc., professor
A.I. Belostotsky, D.Sc., professor
A.I. Borovkov, PhD, professor
A. Borodinets, Dr.Sc.Ing., professor
M. Veljkovic, PhD, professor
R.D. Garg, PhD, professor
M. Garifullin, PhD, postdoctorant
T. Gries, Dr.-Ing., professor
T.A. Datsyuk, D.Sc., professor
V.V. Elistratov, D.Sc., professor
T. Kärki, Dr.-Ing., professor
D.V. Kozlov, D.Sc., professor
S.V. Korniyenko, D.Sc., professor
Yu.G. Lazarev, D.Sc., professor
M.M. Muhammadiev, D.Sc., professor
H. Pasternak, Dr.-Ing.habil., professor
F. Rögener, Dr.-Ing., professor
T.Z. Sultanov, D.Sc., professor
M.G. Tyagunov, D.Sc., professor
M.P. Fedorov, D.Sc., professor
D. Heck, Dr.-Ing., professor
A.G. Shashkin, D.Sc.
V.B. Shtilman, D.Sc.

Date of issue: 19.02.2021

© Peter the Great St. Petersburg Polytechnic University.
All rights reserved.
© Coverpicture – Ilya Smagin

Contacts:

E-mail: mce@spbstu.ru

Web: <http://www.engstroy.spbstu.ru>

Contents

Selyantsev, I.M., Tusnin, A. Cold-formed steel joints with partial warping restraint	10101
El-Nimri, R., Abdel-Jaber, M.S., Hunaiti, Y.M., Abdel-Jaber, M. Behavior of light-gauge steel beams filled with recycled concrete	10102
Zaichenko, N.M., Nefedov, V.V. Poly(ethylene terephthalate) composite material with modified fly ash filler	10103
Inozemtcev, S.S., Korolev, E.V. Sodium alginate emulsions for asphalt concrete modifiers encapsulating: structural rheological properties	10104
Zerfu, K., Ekaputri, J.J. Bond strength in PVA fibre reinforced fly ash-based geopolymer concrete s	10105
Saoudi, B.S., Haddadi, S.H. Predicting creep deformation of asphalts modified with polymer using artificial neural networks	10106
Galishnikova, V.V., Kharun, M., Koroteev, D.D, Chiadighikaobi, P.C. Basalt fiber reinforced expanded clay concrete for building structures	10107
Duy, N.P., Anh, V.N., Hiep, D.V., Anh, N.M.T. Strength of concrete columns reinforced with Glass fiber reinforced polymer	10108
Jose, A., Kasthurba, A. Stabilization of lateritic soil for masonry applications	10109
Nikonorov, A., Badenko, V.L. Flood events dynamics estimation methodology in a GIS environment	10110
Matskina, M.M., Petrochenko, M.V., Radaev, A.E. Stochastic model of the construction process implemented with application of sliding formwork	10111
Safari Tarbozagh, A., Rezaifar, O, Gholhaki, M. Silica concrete compressive behavior under alternating magnetic field	10112
Sainov, M.P. Strength of ultra-high rockfill dam concrete face	10113
Badenko, V.L., Bolshakov, N.S., Tishchenko, E.B., Fedotov, A.A., Celani, A.C., Yadykin, V.K. Integration of Digital Twin and BIM Technologies within Factories of the future	10114



DOI: 10.34910/MCE.101.1

Cold-formed steel joints with partial warping restraint

I.M. Selyantsev^{a*}, A. Tusnin^b

^a Ltd "Non-state expertise of the Pskov region", Pskov, Russia

^b Moscow State University of Civil Engineering, Moscow, Russia

* E-mail: iselyantsev@gmail.com

Keywords: cold-formed structures, warping tests, semi-rigid joints, partial restraints, warping factor, warping restraint

Abstract. The article investigates the influence of joints on the warping torsion of cold-formed steel bars. The modern warping torsion theory suggests cold-formed steel bars to be simply supported or fixed at the ends. Simple support provides zero warping restraint. Fixed support provides full warping restraint at the joint of the bar. In real constructions cold-formed steel joints are partial warping restrained. Not considering the partial restraint of deformations by real joints leads to an incorrect assessment of the twist angles and the stress state of thin-walled steel bars in warping torsion. This article deals with an experimental and analytical investigation of warping torsion of cold-formed steel bars with bolted joints. Considered 142C16, 142C20, 262C23 and 262C29 sections. Five types of joints considered: a wall and both flanges of the bar end sections are fixed; the upper and lower flanges are fixed; the wall is fixed; the wall and the lower flange are fixed; the lower flange is fixed. First, analytical expressions for twist angles and bimoments for warping torsion for bars with partial warping restraints obtained. Analytical results are compared with the results of the warping torsion experiment conducted at Moscow State University of Civil Engineering. The cold-formed steel specification is shown to be a poor predictor for the twist angle and bimoment value of twisting members. The warping factor coefficient is recommended for the estimation of the degree of the joint warping constraint. Experimental values of warping factors for different joint types are obtained. The influence of partial warping restraints and cross-section deformation on the work of the tested cold-formed steel bars are evaluated.

1. Introduction

The technical theory of torsion of thin-walled rods of an open profile was created in the 30s of the 20th century in [1]. One of the main assumptions used in its development is the hypothesis of a rigid contour. It is assumed that the cross-section contour maintains its shape when the bar is twisted. Torsion leads not only to cross-section rotation about the center of twist but at the same time the points of the section undergo different displacements along the longitudinal axis. These displacements, called deformations, lead to warping of cross-sections of a thin-walled bar in the torsion. Because of warping restraint, additional sectorial normal stresses arise in the bar. The basic theory of thin-walled members with open cross-sections was developed by Vlasov [1]. To determine the twist angles and bimoments in the rod, Vlasov proposed the differential equation:

$$\theta^{IV} - k^2 \theta'' = \frac{m(z) - b'(z)}{EJ_\omega}, \quad (1)$$

where θ is the angle of twist of the rod; $m(z)$ is the intensity of external distributed twisting moments; $b'(z)$ is the derivative with respect to z of the intensity of external distributed bimoments; J_ω is the warping constant of the cross-section; J_d is the torsion constant of the cross-section; E is the modulus of elasticity;

G is the shear modulus; $k = \sqrt{\frac{GJ_d}{EJ_\omega}}$ is the elastic flexural-torsional characteristic of the thin-walled rod.

Selyantsev, I.M., Tusnin, A. Cold-formed steel joints with partial warping restraint. Magazine of Civil Engineering. 2021. 101(1). Article No. 10101. DOI: 10.34910/MCE.101.1



This work is licensed under a CC BY-NC 4.0

Equations of the elastic line of twist angles and bimoments for different types of load arrangements are presented in tabular form by Bychkov [2]. Solutions presented in [1] and [2] are valid for rods subjected to zero or completely warping restraints in the absence of a rod twisting in the supported sections.

A number of research studies have been carried out over the past decades to determine the influence of restraints on the work of cold-formed steel bars. A significant part of the studies is devoted to the study of the carrying capacity of cold-formed thin-walled steel bars, working in bending, compression, and torsion. In the studies reviewed issues of strength, overall and local stability. In [3–8], the results of theoretical and numerical studies of the strength and stability of cold-formed bars are presented. Solved problems of determining forces and displacements using rod and shell finite elements, propose theoretical solutions for determining bimoments taking into account bending moments, consider the problem of distortional buckling. The stress-strain state of cold-formed steel bars under torsion was studied experimentally [9] and theoretically [10]. In [9], considering the experimental data obtained, an expression for the bearing capacity of an eccentrically loaded C-profile bar was obtained. In [10], three methods are compared, the theory of calculating thin-walled constructions [1], the method of representing constrained torsion by bending with torsion, and the method of representing torsion by bending the shelves of a thin-walled rod by a pair of forces. The performed work confirmed the effectiveness of the theoretical and numerical methods used in the calculation of thin-walled structures experiencing bending, compression, and torsion.

Extensive experience has been gained in experimental studies of thin-walled systems [11–25]. The articles show the results of tests for bending and compression of C and Z shaped profiles, solid, perforated, with simple and complex edge stiffeners. The obtained data on strength and stability were compared with theoretical and numerical solutions. Based on the tests carried out in [12], an expression was given to evaluate the carrying capacity of thin-walled Z-profiles in biaxial bending. In [15] the method of selecting the effective width of the section elements for calculating the effective section properties was justified. In [16] the method for determining the effective width of the elements sections and method of determining the bearing capacity of the rod. The experience of experimental studies can be successfully adapted to solve the problems of the operation of cold-formed steel bars with various joints.

The Consideration of Saint-Venant's principle of using the Vlasov theory [1] is the work of [26]. It shows the influence of boundary conditions on the operation of thin-walled rods. In [27], the effect of conjunction flexibility on the critical load of cold-formed C-shaped profiles was studied. In addition to analytical data, tests of the considered structures are given.

Experimental and theoretical studies of the behavior of trusses made of thin-walled members were carried out in [28]. Taking into account the research carried out, a technique for strengthening the upper chord of the truss has been proposed, and an eaves joint has been developed.

The results of numerical and experimental studies of frame structures made of cold-formed steel members are presented in [29–31]. In [32], the results of experimental studies of bolted joints of cold-formed steel trusses are given. Bolted joints are considered semi-rigid to bend. The authors proposed a technique for numerical modeling of bolted joints, which is based on previous studies [33] and [34]. In [35, 36], experimental and numerical studies of structures made of thin-walled rods were carried out, and the rotation stiffness of semi-rigid nodal joints was determined. In [36], recommendations were given on numerical modeling, taking into account the initial imperfections and features of bolted joints.

The results of cyclic tests of the cold-formed frame joints and the method for determining the bearing capacity of bolted joints are presented in [37]. The refined method for calculating the bolted connections of thin-walled elements [38] is based on the results of experimental studies. Authors give recommendations on the determining the carrying capacity of bolted joints. Experimental studies of bolted connections for cold-formed frames were carried out in [39].

The common feature for these studies is that the joints supporting the rods are “idealized”, considered to be zero or completely warping restraint. The degree of restriction of deplanations with real joints is not considered. The effect of the degree of deplanation restriction is not taken into account. Also, in addition to [1] and [2], little attention is paid to the separately constrained torsion of the rod. Thus, despite extensive studies of the operation of thin-walled structures, the issues of accurately determining the forces and deformations in such structures, taking into account their actual joints, are of definite practical and scientific interest.

This article discusses the warping torsion of cold-formed steel bars with different bolted joint types. The Authors carried out a series of warping torsion tests of cold-formed C-shaped profiles of different lengths and sizes under different joint conditions. The Experimental results were compared with analytical solutions. The main goal of the study is to provide a method for bolted joints warping stiffness calculation. This method will be used to specify the influence of partial warping restraints on the twist angles and bimoments value of cold-formed steel bars. According to the warping torsion experimental results, a part of the torsion angles of the cold-formed bar, obtained by deforming the contour of the cross-section, will be estimated. The range

of the flexural-torsional characteristic kl will be determined beyond which the cross-section contour deformation can be neglected.

2. Methods

Practically used joints of cold-formed steel bars impose partial warping restraint in accordance with complete twist restraint. They do not provide zero or complete deplanations restriction at supported sections. Considering the joints to be zero or completely warping restraint leads to significant errors in determining the twist angles and the bimoments. Experimental and theoretical studies have been carried out at Moscow State University of Civil Engineering aimed at identifying the features of the behavior of cold-formed steel bars under various boundary conditions.

A series of warping torsion tests were conducted. A total of 40 cold-formed C-shaped bars of four sections 142C16, 142C20, 262C23, and 262C20 under different joint conditions were tested. Steel grade of cold-formed steel sections is S450GD EN 1036:2015. The elastic modulus is $E = 210000 \text{ N/mm}^2$, the shear modulus is $G \approx 81000 \text{ N/mm}^2$, the yield stress is $f_y = 450 \text{ N/mm}^2$. The lengths, dimensions of the cross-sections and the values of the flexural-torsional characteristics kl of the tested bars are given in Table 1. Warping torsion test arrangements are given in Fig. 1 and Fig. 2. the Bars were fixed at the ends. Torque was applied to the middle of the span of the bar. At the distance of 260 mm from the central section of the bar four LVDTs were located (see Fig. 1). Two on the upper flange and two on the lower flange. Torque moment values are listed in Table 2. The bars ends were bolted to a rigid fixed support structure. Five types of joints were considered

1. fixed wall and both flanges;
2. fixed upper and lower flange;
3. fixed wall;
4. fixed wall and a bottom flange;
5. fixed bottom flange.

Table 1. Section geometrical characteristics.

Profile	h (mm)	b (mm)	c (mm)	t (mm)
142C16	142	60	13	1.6
142C20	142	60	13	2.0
262C23	262	65	13	2.3
262C29	262	65	13	2.9

where: h is the wall height. b is the flange width. c is the flange stiffeners height. t is the wall thickness.

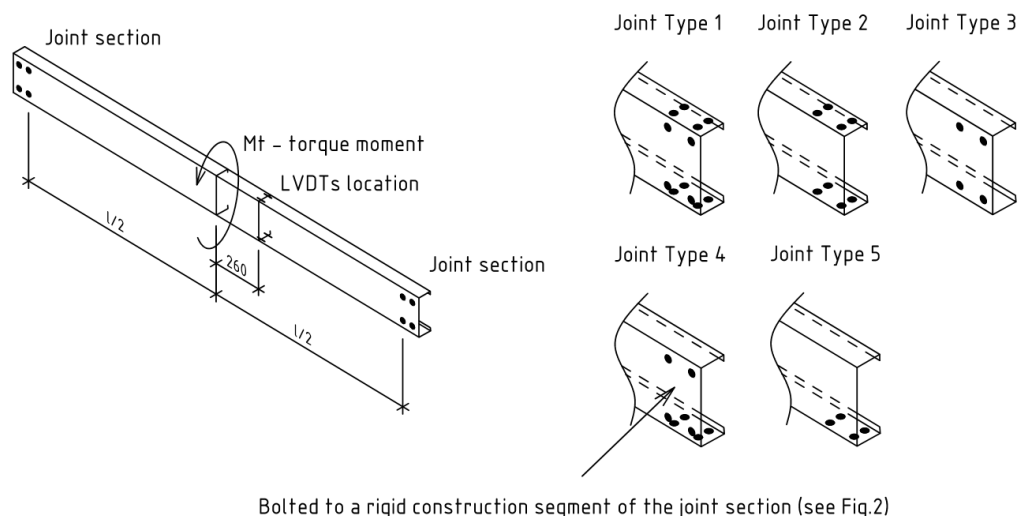


Figure 1. Warping torsion test arrangement. types of joints.

Table 2. Torque moment values.

Profile	l (mm)	kl	M_t (kN mm)				
			Type1	Type2	Type3	Type4	Type5
142C16	1955	0.864	146.6	146.8	859.6	703.0	20.0
142C20	1955	1.094	156.7	146.7	933.0	104.2	31.1
262C23	1955	0.698	229.1	229.1	205.9	229.2	49.2
262C29	1955	0.895	377.1	377.1	357.3	377.2	54.1
142C16	3940	1.706	380.9	337.9	298.7	360.0	17.8
142C20	3940	2.160	419.4	419.5	250.9	419.4	21.7
262C23	3940	1.379	133.8	133.8	113.8	133.9	54.5
262C29	3940	1.767	145.8	145.8	146.1	145.8	62.2

where: l is the length of the bar, kl is the dimensionless flexural-torsional characteristic of the bar,

$$kl = l \sqrt{\frac{GJ_t}{EJ_\omega}}$$

J_t is the St. Venan torsion constant of the bar cross section. J_ω is the warping constant of

the bar cross section. Torque moment M_t value is calculated as product of numbers of a load applied at the end of a loading device console to a distance from load application point to an axis of rotation of the loading device (see Fig. 2). Type 1, 2, 3, 4, 5 indicates joint types (see Fig. 1).

**Figure 2. Warping torsion of cold-formed C-shaped steel bar. Joint type 3.****Table 3. Experimental angles of twist θ_{exp} . The ratios of experimental and theoretical values of angles of twist.**

Profile	l (mm)	kl	θ_{exp} (grad)					$\theta_{exp}/\theta_{complete}$				
			Type 1	Type 2	Type 3	Type 4	Type 5	Type 1	Type 2	Type 3	Type 4	Type 5
142C16	1955	0.864	3.44	3.17	2.69	2.02	1.15	1.72	1.58	2.29	2.11	4.22
142C20	1955	1.094	2.74	2.95	2.05	2.11	1.27	1.45	1.66	1.81	1.68	3.38
262C23	1955	0.698	1.06	1.07	1.85	1.26	2.22	2.06	2.08	4.01	2.45	20.9
262C29	1955	0.895	1.43	1.45	1.87	1.57	1.47	2.07	2.10	2.86	2.27	14.9
142C16	3940	1.706	4.39	4.48	4.50	4.37	4.49	1.09	1.26	1.43	1.15	2.38
142C20	3940	2.160	3.55	3.55	3.05	3.55	4.27	0.98	0.98	1.41	0.98	2.29
262C23	3940	1.379	2.77	2.80	3.65	3.11	4.03	1.24	1.26	1.93	1.39	4.44
262C29	3940	1.767	2.38	2.43	3.33	2.56	3.25	1.22	1.25	1.71	1.32	3.92

Table 3 employs the following notations: θ_{exp} is experimental angles of twist at the central section of the bar. $\theta_{complete}$ is theoretical angles of twist calculated for bars at the central section of the bar with joints providing complete warping restriction (23).

Table 4. Experimental bimoment values $B_{\omega,exp}$. The ratios of experimental and theoretical values of bimoments.

Profile	l (mm)	kl	$B_{\omega,exp} / 10^4$ (kN mm ²)					$B_{\omega,exp} / B_{\omega,complete}$				
			Type 1	Type 2	Type 3	Type 4	Type 5	Type 1	Type 2	Type 3	Type 4	Type 5
142C16	1955	0.864	1.39	1.53	1.34	0.86	0.19	0.85	0.93	1.40	1.10	0.84
142C20	1955	1.094	1.79	1.85	1.71	1.55	0.46	0.99	1.09	1.58	1.28	1.28
262C23	1955	0.698	2.93	3.02	4.36	3.64	1.19	1.09	1.12	1.80	1.35	2.05
262C29	1955	0.895	4.88	4.98	7.02	5.52	1.22	1.11	1.13	1.68	1.25	1.93
142C16	3940	1.706	1.17	1.03	1.07	1.16	0.78	0.92	0.91	1.07	0.96	1.31
142C20	3940	2.160	1.37	1.39	1.32	1.47	0.97	1.01	1.02	1.62	1.08	1.38
262C23	3940	1.379	4.99	5.01	5.42	5.31	3.11	1.08	1.08	1.38	1.15	1.65
262C29	3940	1.767	5.13	5.22	6.18	5.34	3.43	1.05	1.07	1.26	1.09	1.64

where: $B_{\omega,exp}$ is experimental bimoment value. $B_{\omega,complete}$ is theoretical bimoment value calculated for bars with joints providing complete warping restriction (24).

As a result, the angles of twist θ_{exp} in the central section of the bar, Table 3, and bimoments $B_{\omega,exp}$ in the LVDTs location section, Table 4, were determined. A significant difference between the experimental and theoretical results calculated for joints with zero and complete warping restriction was found, Table 3, Table 4. To identify the causes of this mismatch, the effects of contour and form of cross-section deformation on the supports and in the place where the load was applied were studied. As a result, theoretical expressions were obtained for twisting angles and bimoments for bars with partial torsional and warping restraints. Theoretical expressions for the twisting angles and the bimoments described below. The level of joint warping restraint was determined on the reference bimoment perceived by the joint.

The theoretical solution to the effect of the influence of partial torsional and warping restraints on the behavior of cold-formed steel bars is based on Vlasov theory [1]. Consider the case when, on the supports (due to the flexibility of the joint), the twist angle and the deplanation are not equal to zero. In this case, on the supports, the twist angle θ is proportional to the level of torque moment on the joint section M_θ , and the degree of deplanation δ is proportional to the level of bimoment on the joint section $B_{\omega\theta}$. In this case, the relationship between internal forces and deformations for twist angles and deplanations on the supports can be written in the form:

$$\begin{cases} \theta_{01} = k_{\theta 1} M_{\theta 1}; \\ \theta_{02} = k_{\theta 2} M_{\theta 2}; \\ \delta_{01} = k_{\delta 1} B_{\omega\theta 1}; \\ \delta_{02} = k_{\delta 2} B_{\omega\theta 2}, \end{cases} \quad (2)$$

where k_θ and k_δ are the twist and deplanation flexibility of the joint, respectively. Index 0 represents the cross-section of the bar, and indices 1 and 2 represent the beginning and the end of the bar.

The solution of Eq. (1) can be written as:

$$\theta = A \cdot sh \, kz + B \cdot ch \, kz + C \cdot z + D + f(z) \quad (3)$$

where $f(z)$ is the particular solution of Eq (3). Instead of $ch \, kz$, $sh \, kz$, z and 1 in Eq. (3), we introduce the partial integrals $\psi_1(z)$, $\psi_2(z)$, $\psi_3(z)$, $\psi_4(z)$ which are linear combinations of the first:

$$\begin{cases} \psi_1 = a_1 sh \, kz + a_2 ch \, kz + a_3 z + a_4; \\ \psi_2 = b_1 sh \, kz + b_2 ch \, kz + b_3 z + b_4; \\ \psi_3 = c_1 sh \, kz + c_2 ch \, kz + c_3 z + c_4; \\ \psi_4 = d_1 sh \, kz + d_2 ch \, kz + d_3 z + d_4, \end{cases} \quad (4)$$

Then the solution of Eq. (1) can be written as:

$$\theta = A \cdot \psi_1 + B \cdot \psi_2 + C \cdot \psi_3 + D \cdot \psi_4 + f(z), \quad (5)$$

The constants A , B , C , and D are evaluated from the boundary conditions for the bar with partial torsional and warping restraints:

at $z = 0$:

$$\theta = k_{\theta 1} M_{01} \text{ and } \theta' = -\frac{B_{\omega 01}}{EJ_{\omega}},$$

at $z = l$:

$$\theta = k_{\theta 2} M_{02} \text{ and } \theta' = -\frac{B_{\omega 02}}{EJ_{\omega}} \quad (6)$$

To simplify further calculations, we take the partial integrals of the Eq. (5) so that they satisfy the following conditions:

$$\begin{cases} \psi_1(0) = 1; \psi_1'(0) = 0; \psi_1(l) = 0; \psi_1'(l) = 0; \\ \psi_2(0) = 0; \psi_2'(0) = 1; \psi_2(l) = 0; \psi_2'(l) = 0; \\ \psi_3(0) = 0; \psi_3'(0) = 0; \psi_3(l) = 1; \psi_3'(l) = 0; \\ \psi_4(0) = 0; \psi_4'(0) = 0; \psi_4(l) = 0; \psi_4'(l) = 1 \end{cases} \quad (7)$$

From these conditions we find:

$$\begin{cases} \psi_1 = 1 - \frac{z}{l}; \\ \psi_2 = \frac{1}{k^2} \left(\frac{z}{l} - 1 + \frac{sh kl \cdot ch kz - ch kl \cdot sh kz}{sh kl} \right); \\ \psi_3 = \frac{z}{l}; \\ \psi_4 = \frac{1}{k^2} \frac{sh kz}{sh kl} - \frac{z}{k^2 l}, \end{cases} \quad (8)$$

Consequently,

$$\theta = A \left(1 - \frac{z}{l} \right) + \frac{B}{k^2} \left(\frac{z}{l} - 1 + \frac{sh kl \cdot ch kz - ch kl \cdot sh kz}{sh kl} \right) + C \frac{z}{l} + \frac{D}{k^2} \left(\frac{sh kz}{sh kl} - \frac{z}{l} \right) + f(z). \quad (9)$$

Choose the particular solution of Eq. (3) $f(z)$ such that:

$$f(0) = 0; f'(0) = 0; f''(0) = 0; f'''(0) = 0. \quad (10)$$

Using the boundary conditions Eq. (6) for Eq. (9), using Eq. (10), we find four non-zero constants A , B , C and D :

$$A = k_{\theta 1} M_{01}; B = -\frac{B_{\omega 01}}{EJ_{\omega}}; C = k_{\theta 2} M_{02} - f(l); D = -\frac{B_{\omega 02}}{EJ_{\omega}} - f'(l). \quad (11)$$

Substituting Eq. (11) into Eq. (9), we obtain the equation of the elastic line of the twist angles for a bar with partial torsional and warping restraints:

$$\begin{aligned} \theta(z) = & -f(l) \frac{z}{l} + \frac{f'''(l)}{k^2} \left(\frac{z}{l} - \frac{sh kz}{sh kl} \right) + f(z) + k_{\theta 1} M_{01} \left(1 - \frac{z}{l} \right) \\ & + k_{\theta 2} M_{02} \frac{z}{l} - \frac{B_{\omega 01}}{EJ_{\omega} k^2} \left(\frac{z}{l} - 1 + \frac{ch kz - \frac{ch kl}{sh kl} sh kz}{sh kl} \right) - \frac{B_{\omega 02}}{EJ_{\omega} k^2} \left(\frac{sh kz}{sh kl} - \frac{z}{l} \right). \end{aligned} \quad (12)$$

Upon double differentiating the Eq. (12) with the respect to the z and multiplying it by $-EJ_{\omega}$, we obtain the equation of bimoments for a bar with partial torsional and warping restraints:

$$B_{\omega} = EJ_{\omega} \frac{f'''(l)}{sh kl} sh kz - EJ_{\omega} f''(z) + B_{\omega 01} \left(ch kz - \frac{ch kl}{sh kl} sh kz \right) + B_{\omega 02} \frac{sh kz}{sh kl}. \quad (13)$$

It can be seen that when $k_{\theta 1} = k_{\theta 2} = 0$ and $B_{\omega 01} = B_{\omega 02} = 0$, Eq. (12) will be transferred to the equation of the elastic line of the twist angles for the bar, with a complete twisting and zero warping restraints.

$$\theta(z) = -f(l) \frac{z}{l} + \frac{f'(l)}{k^2} \left(\frac{z}{l} - \frac{sh kz}{sh kl} \right) + f(z). \quad (14)$$

From the same boundary conditions, Eq. (13) will be transferred to the equation of the bimoments for the bar, with a complete twisting and zero warping restraints.

$$B_{\omega}(z) = EJ_{\omega} \frac{f'(l)}{sh kl} sh kz - EJ_{\omega} f'(z). \quad (15)$$

Similarly, taking the twist angles on the supports equal to zero $k_{\theta 1} = k_{\theta 2} = 0$ and assuming that the warping deformations are completely restrained, that is, $B_{\omega 01}$ and $B_{\omega 02}$ are equal to the support bimoments for a bar with a complete warping restraints, the Eq. (12) will be transformed into an equation of the elastic line of the twist angles for a bar with a complete warping and torsion restraints.

$$\theta(z) = -f(l) \frac{ch k(l-z) - ch kz + kz \cdot sh kl - ch kl + 1}{kl \cdot sh kl - 2ch kl + 2} - f'(l) \frac{kl \cdot ch kz - kz \cdot ch kl + sh kl - sh kz - sh k(l-z) - k(l-z)}{k(kl \cdot sh kl - 2ch kl + 2)} + f(z). \quad (16)$$

Eq. (13), becomes the equation of bimoments for a bar with similar boundary conditions.

$$B_{\omega}(z) = EJ_{\omega} k^2 f(l) \frac{ch k(l-z) - ch kz}{kl \cdot sh kl - 2ch kl + 2} + EJ_{\omega} k f'(l) \frac{kl \cdot ch kz - sh kz - sh k(l-z)}{kl \cdot sh kl - 2ch kl + 2} - EJ_{\omega} f'(z). \quad (17)$$

Substituting into Eq. (12) and Eq. (13) the expressions for the particular solution $f(z)$, one can obtain the values of the twist angles and the bimoments for different load arrangement.

3. Results and Discussion

Using the proposed theoretical solutions, the influence of distortion on the behavior of the tested cold-formed steel bars was evaluated. Particular solution $f(z)$ tested bars with torque applied to the center section of the bar can be written as:

$$f(z) = \frac{M}{k^3 EJ_{\omega}} \left[sh k \left(z - \frac{l}{2} \right) - k \left(z - \frac{l}{2} \right) \right], \quad (18)$$

where M is the applied torque moment. The values of particular solutions $f(z)$ for different load arrangement are listed in [2]. Substituting Eq. (18) into Eq. (12) and Eq. (13), taking into account that the right and left ends of the bar are fixed equally, $k_{\theta 1} = k_{\theta 2}$ and $k_{\delta 1} = k_{\delta 2}$, we obtain the expressions for the twist angles and the bending-twisting bimoment for tested partially torsion and warping restrained bars with a torque applied in the central section:

$$\theta(z) = \frac{M}{2k^3 EJ_{\omega}} \left(kz - \frac{sh kz}{ch \frac{kl}{2}} \right) - \frac{B_{\omega 0}}{k^2 EJ_{\omega}} \left[\frac{sh kz}{sh kl} (1 - ch kl) - 1 + ch kz \right] + k_{\theta} M_0, \quad (19)$$

$$B_{\omega}(z) = \frac{M}{2k} \frac{sh kz}{ch \frac{kl}{2}} + B_{\omega 0} \left[ch kz + \frac{sh kz}{sh kl} (1 - ch kl) \right], \quad (20)$$

where $B_{\omega 0}$ is the bimoment on the joint section; M_0 is the torque moment on the joint section.

When $B_{\omega 0} = 0$ and, $k_{\theta} = 0$ Eq. (19) and Eq. (20) will be transferred to the equations for the bar, with a complete twisting and zero warping restraints.

$$\theta(z) = \frac{M}{2k^3 EJ_\omega} \left(kz - \frac{sh \frac{kl}{2}}{ch \frac{kl}{2}} \right), \quad (21)$$

$$B_\omega(z) = \frac{M}{2k} \frac{sh \frac{kl}{2}}{ch \frac{kl}{2}}. \quad (22)$$

If $B_{\omega 0} = \frac{M}{2k} \frac{1 - ch \frac{kl}{2}}{sh \frac{kl}{2}}$ and $k_\theta = 0$, Eq. (19) and Eq. (20) will be transferred to the equations for the

bar, with a complete twisting and complete warping restraints.

$$\theta(z) = \frac{M}{k^3 EJ_\omega} \frac{\frac{kz}{2} sh \frac{kl}{2} - sh^2 \frac{kz}{2} - sh \frac{kz}{2} sh \frac{k(l-z)}{2}}{sh \frac{kl}{2}}, \quad (23)$$

$$B_\omega(z) = \frac{M}{2k} \frac{ch \frac{kz}{2} - ch k \left(\frac{l}{2} - z \right)}{sh \frac{kl}{2}}. \quad (24)$$

Let us compare the experimental values of the twist angles and bimoments with the theoretical values obtained for the bar with complete twisting and warping restraints. Calculations of the theoretical values of the twist angles and bimoments for bars with complete twisting and warping restraints are carried out using Eq (23) and Eq. (24). To obtain the values of the twist angles θ and the bimoments B_ω for bars with partial restraints, using Eq. (19) and Eq. (20), it is required to know the value of the bimoment on the joint section $B_{\omega 0}$ corresponding to the type joint.

Let us agree that the cross-section of the bar during the torque can be deformed in two ways – the cross-section contour can be deformed out of a plane, which leads to warping displacements. Cross-section in this case does not remain planar after deformation. And the cross-section form can be deformed in-plane without violating the flat section hypothesis. Warping deformations are considered when calculating the twist angles and bimoments according to the Eq. (19) and Eq. (20). In-plane cross-section deformations can be estimated from the results of the experiment.

During the experiment, stresses were measured at four points of the cross-section, located at 260 mm from the center of the bar. Placing the strain gauges at some distance from the point of application of the load minimizes the effect of cross-section in-plane deformation on the value of the measured bimoment. The value of the bimoment $B_{\omega 0}$ on the joint section is obtained from the processing of experimental data. $B_{\omega 0}$ was calculated using the experimental value of the bimoment B_ω on the strain gauges section, using Eq. (20).

The degree of constraint by the joint of the warping deformations, so-called deplanations, can be described by the warping factor coefficient:

$$K_\delta = \frac{B_{\omega 0, partial}}{B_{\omega 0, complete}}, \quad (25)$$

where K_δ is the warping factor; $B_{\omega 0, partial}$ is the bimoment on the joint section for the bar with partial warping restraint; $B_{\omega 0, complete}$ is the bimoment on the joint section for the bar with complete warping restraint.

A decrease in the joint bimoment is proportional to the warping factor coefficient K_δ , which leads to an increase in the value of the bimoment in the span of the bar. The values of the warping factor K_δ , for examined joint types, are given in Table 5.

Table 5. Mean values of the warping factors.

Warping factor	Joint type				
					
	type 1	type 2	type 3	type 4	type 5
K_δ	0.98	0.96	0.7	0.83	0.55
$B_{\omega 0, partial} / B_{\omega 0, complete}$	1.03	1.04	1.24	1.11	1.35

From Table 5, only two of the examined joint types, type 1 and 2, can be considered as complete warping restraint. And none of the examined joints can be considered as zero warping restraint. So, when only one flange is fixed, the bimoment on the joint is about half of the bimoment for the joint with complete warping restraint.

Using Eq. (25) for the warping factor K_δ , Eq. (19) and Eq. (20) for bimoment and twist angles can be written as:

$$\theta(z) = \frac{M}{2k^3 EJ_\omega} \left(kz - \frac{sh\ kz}{ch\ \frac{kl}{2}} \right) - \frac{K_\delta B_{\omega 0, complete}}{k^2 EJ_\omega} \left[\frac{sh\ kz}{sh\ kl} (1 - chkl) - 1 + ch\ kz \right] + k_\theta M_0, \quad (26)$$

$$B_\omega(z) = \frac{M}{2k} \frac{sh\ kz}{ch\ \frac{kl}{2}} + K_\delta B_{\omega 0, complete} \left[ch\ kz + \frac{sh\ kz}{sh\ kl} (1 - ch\ kl) \right]. \quad (27)$$

Considering the real joint conditions with the help of the proposed method leads to a more accurate, in comparison with the traditional method [1, 2], the assessment of the stress-strain state with warping torsion of cold-formed steel bars.

It should be noted that the question of determining the warping factor K_δ requires additional studies. When processing the experiment, the values of K_δ determined from the experimental results were used, which leads to the complete coincidence of the experimental values of the bimoment B_ω with the values obtained from Eq. (27). In the absence of a sufficient amount of experimental data, the K_δ values for different joint types can be preliminarily taken from Table 5.

Considering the experimental and theoretical studies carried out, the influence of the cross-section in-plane deformation on the behavior of the tested cold-formed bars was evaluated. The experimental angle of twist was estimated by the rotation of the loading device Fig. 2. The total twist angle is found as the sum of three values, the theoretical value taking into account the additional warping deformation of the bar on the joints Eq. (26), the additional angle of rotation of the loading device due to the in-plane deformation of the bar cross-section at the point of application of the load and the additional angle of twist due to in-plane bar cross-section deformation on the joints.

Comparing the value of the obtained angle of twist of the bar according to Eq. (26) with the experimental value θ_{exp} , it is possible to calculate the part of the angle of twist θ_χ obtained by in-plane cross-section deformation of the cold-formed bar at the joints and in the place of load application. The obtained values of the θ_χ/θ_{exp} relations for the tested bars with different types of joints are listed in Table 6.

Table 6. θ_χ/θ_{exp} .

Profile	l , mm	kl	θ_χ/θ_{exp}				
			type 1	type 2	type 3	type 4	type 5
262C23	1955	0.684	0.43	0.42	0.41	0.37	0.88
142C16	1955	0.876	0.43	0.35	0.27	0.37	0.73
262C29	1955	0.895	0.43	0.41	0.32	0.39	0.85
142C20	1955	1.072	0.26	0.27	0.13	0.14	0.54
262C23	3940	1.379	0.10	0.10	0.06	0.09	0.46
142C16	3940	1.766	0.17	0.19	0.10	0.18	0.26
262C29	3940	1.933	0.16	0.15	0.13	0.13	0.40
142C20	3940	2.161	0.00	0.03	0.11	0.05	0.20

Where θ_{exp} is the experimental value of the bar twist angle; $\theta_\chi = \theta_{exp} - \theta$ is the twist angle due to in-plane cross-section deformation; θ is the twist angle of the bar with partial warping restraints.

From Table 6 it can be seen that for joint types 1, 2, 3, and 4, depending on the flexural-torsional characteristic kl , up to 43 % of the angle of twist of a cold-formed bar, occurs due to in-plane cross-section deformation at the load application point and on the joint sections. For joint type 5, the contribution of the in-plane cross-section deformation to the twist angle of the cold-formed bar can be up to 88 %.

For joint types 1, 2, 3, and 4, with $kl > 2$, the magnitude of the twist angles of the cold-formed bar can be determined by the Eq. (26) with sufficient accuracy for practical use. The joint number 5 requires additional research, but it can be said that taking into account the partial warping restraint of the joint allows using Eq. (26) with a value of $kl > 3$. When joint types are 1, 2, 3, 4 and $kl < 2$, as well as when joint type 5 and $kl < 3$, the cross-section in-plane deformation cannot be neglected.

4. Conclusions

Based on the research conducted, it was established:

1. The degree of warping restriction with real joint types can be described by the value of the bimoment on the joint section $B_{\omega 0}$. When $B_{\omega 0}=0$, the joint is zero warping restrained. When $B_{\omega 0}=M/2k(1-ch kl/2)sh kl/2$ the joint is complete warping restrained.

2. Not considering the partial warping restriction by the joint leads to a significant error in the determination of the twist angles of the bar and bimoments. generally, the magnitudes of the twist angles θ and the bimoments B_ω with warping torsion of a thin-walled cold-formed steel bar can be determined by Eq. (12) and Eq. (13). In the case of a load in the form of a torque applied to the central section of the bar according to Eq. (26) and Eq. (27). To consider the type of joint, it is possible to use experimentally obtained values of the warping factor K_δ according to Table 5.

3. According to Eq. (13), additional twisting angles on the bar joints due to deformation of the bar ends or insufficient rigidity of the joint assembly design do not affect the values of bimoments along the bar length.

4. An indicator of the deformability of the cross-sectional contour is the value of the flexural-torsional characteristic of the bar, kl . The smaller it is, the greater the influence of the contour deformations on the operation of the bar during torsion.

5. For cases of fastening a cold-formed bar along two flanges and a wall, along a flange and a wall, along two flanges, as well as for fastening along a wall, the in-plane cross-section deformation can be neglected for $kl > 2$. The case of fastening a cold-formed bar along one flange requires additional study. Previously, we can say that in this case, the in-plane cross-section deformations can be neglected when $kl > 3$.

References

1. Vlasov, V.Z. Tonkostennyye uprugiyе sterzhni [Thin-walled elastic rods]. Moscow: Fizmatgiz, 1959. 574 p. (rus)
2. Bychkov, D.V. Stroitel'naya mekhanika sterzhnevyykh tonkostennykh konstruksiy [Structural mechanics of thin-walled bar structures]. Moscow: Gosstroyizdat, 1962. 475 p. (rus)
3. Erkmеn, R.E. Bridging multi-scale approach to consider the effects of local deformations in the analysis of thin-walled members. *Computational Mechanics*. 2013. No. 52. Pp. 65–79.
4. Keerthan, P., Mahendran, M. Numerical modeling of litemeel beams subject to shear. *Journal of Structural Engineering*. 2011. No. 137(12). Pp. 1428–1439.
5. Chen, J.K., Li, L.Y. Distortional buckling of cold-formed steel sections subjected to uniformly distributed transverse loading. *International Journal of Structural Stability and Dynamics*. 2010. No. 10(5). Pp. 1017–1030.
6. Schafer, B.W., Sarawit, A., Peköz, T. Complex edge stiffeners for thin-walled members. *Journal of Structural Engineering*. 2006. No. 2. Pp. 212–226.
7. Nazmeeva, T.V., Vatin, N.I. Numerical investigations of notched C-profile compressed members with initial imperfections. *Magazine of Civil Engineering*. 2016. No. 62(2). Pp. 92–101.
8. Pavlenko, A.D., Rybakov, V.A., Pikht, A.V., Mikhailov, E.S. Non-uniform torsion of thin-walled open-section multi-span beams. *Magazine of Civil Engineering*. 2016. No. 67(7). Pp. 55–69.
9. Put, B.M., Pi, Y.L., Trahair, N.S. Bending and torsion of cold-formed channel beams. *Journal of Structural Engineering*. 2002. No. 5. Pp. 540–546.
10. Melcher, J., Karmazínová, M. On problems of torsion analysis of steel members with open cross section. *Procedia Engineering*. 2012. Pp. 262–267.
11. Ghosn, A.A. Deflection of nested cold-formed steel Z-section beams. *Journal of Structural Engineering*. 2002. No. 11. Pp. 1423–1428.
12. Put, B.M., Pi, Y.L., Trahair, N.S. Biaxial bending of cold-formed Z-beams. *Journal of Structural Engineering*. 1999. No. 11. Pp. 1284–1290.
13. Garifullin, M., Bronzova, M., Sinelnikov, A., Vatin, N. Buckling analysis of cold-formed c-shaped columns with new type of perforation. *Proceedings of the International Conference on Engineering Sciences and Technologies. ESaT*. 2015. Pp. 63–68.
14. Vatin, N.I., Nazmeeva, T., Guslinsky, R. Problems of cold-bent notched C-shaped profile members. *Advanced Materials Research*. 2014. 941-944. Pp. 1871–1875.
15. Yu, C., Schafer, B.W. Local buckling tests on cold-formed steel beams. *Proceedings of the International Specialty Conference on Cold-Formed Steel Structures: Recent Research and Developments in Cold-Formed Steel Design and Construction*. 2002. No. 1. Pp. 1596–1606.
16. Zhou, X.H., Shi, Y. Flexural strength evaluation for cold-formed steel lip-reinforced built-up I-beams. *Advances in Structural Engineering*. 2011. No. 14(4). Pp. 597–611.
17. Šimić, D. Modelling of load transfer to laterally restrained thin-walled beams with open cross-section. *Transactions of Famena*. 2010. Pp. 47–56.
18. Pham, C.H., Hancock, G.J. Experimental investigation of high strength cold-formed C -sections in combined bending and shear. *Journal of Structural Engineering*. 2010. No. 10. Pp. 866–878.
19. Young, B., Hancock, G.J. Cold-formed steel channels subjected to concentrated bearing load. *Journal of Structural Engineering*. 2003. No. 8. Pp. 1003–1010.
20. Ghosn, A.A., Sinno, R.R. Load capacity of nested, laterally braced, cold-formed steel Z-section beams. *Journal of Structural Engineering*. 1996. No. 8. Pp. 968–971.
21. Pham, C.H., Hancock G.J. Direct strength design of cold-formed purlins. *Journal of Structural Engineering*. 2009. No. 3. Pp. 229–238.
22. Penava, D.Š., Radić, A., Ilijaš, T. Elastic stability analysis of thin-walled C- And Z-section beams without lateral restraints. *Transactions of Famena*. 2014. Pp. 41–52.
23. Yakovleva, Ye.L., Atavin, I.V., Kazakova, Yu.D., Maksudov, I.Kh. Strength characteristics of thin-walled elements. *Construction of Unique Buildings and Structures*. 2017. No. 12(63). DOI: 10.18720/CUBS.63.7 (rus)
24. Vatin, N., Sinelnikov, A., Garifullin, M., Trubina, D. Simulation of cold-formed steel beams in global and distortional buckling. *Applied Mechanics and Materials*. 2014. 633–634. Rr. 1037–1041.
25. Vatin, N.I., Havula, J., Martikainen, L., Sinelnikov, A.S., Orlova, A.V., Salamakhin, S.V. Thin-walled cross-sections and their joints: Tests and FEM-Modelling. *Advanced Materials Research*. 2014. 945–949. Pp. 1211–1215.
26. Goldshteyn, Yu.B. Printsip Sen-Venana i stesnennoye kruchenije tonkostennykh sterzhney otkrytogo profilya [Saint-Venant principle and constrained torsion of thin-walled open profile rods]. *Izvestiya vuzov. Investitsii. Stroitelstvo. Nedvizhimost*. 2016. No. 4(19) S. 75–83. (rus)
27. Rybakov, V., Molchanova, N., Laptev, V., Suslova, A., Sivokhin, A. The effect of conjunction flexibility on the local stability of steel thin-walled slab beams. *Proceedings of MATEC Web of Conferences*. 2016.
28. Wood, J.V., Dawe, J.L. Full-scale test behavior of cold-formed steel roof trusses. *Journal of Structural Engineering*. 2006. No. 4. Pp. 616–623.
29. Chung, K.F., Ho, H.C., Wang, A.J., Yu, W.K. Advances in analysis and design of cold-formed steel structures. *Advances in Structural Engineering*. 2009. No. 11(6) Pp. 615–632.
30. Wrzesien, A., Lim, J.B.P., Nethercot, D.A. Optimum joint detail for a general cold-formed steel portal frame. *Advances in Structural Engineering*. 2012. No. 15(9). Pp. 1623–1639.
31. Lim, J.B.P., Nethercot, D.A. Finite element idealization of a cold-formed steel portal frame. *Journal of Structural Engineering*. 2004. No. 1. Pp. 78–94.
32. Zaharia, R., Dubina, D. Stiffness of joints in bolted connected cold-formed steel trusses. *Journal of Constructional Steel Research*. 2006. No. 62. Pp. 240–249.

33. Toma, A.W., Stark, Jan W.B. Connections in cold-formed sections and steel sheets. Proceedings of International Specialty Conference on Cold-Formed Steel Structures. 1978. No. 5. Pp. 951–987.
34. Zadanfarokh, F., Bryan, E.R. Testing and design of bolted connections in cold formed steel sections. Proceedings of Eleventh International Specialty Conference on Cold-Formed Steel Structures. 1992. No. 3. Pp. 625–662.
35. Sngle, K.K., Bajoria, K.M., Talicotti, R.S. Stability and dynamic analysis of cold-formed storage rack structures with semirigid connections. International Journal of Structural Stability and Dynamics. 2011. No. 11(6). Pp. 1059–1088.
36. Dunai, L., Jakab, G. Stability behavior and design of nonconventional cold-formed steel structures – research review. International Journal of Structural Stability and Dynamics. 2011. No. 11(5). Pp. 903–927.
37. Uang, C.M., Sato, A., Hong, J.K., Wood, K. Cyclic testing and modeling of cold-formed steel special bolted moment frame connections. Journal of Structural Engineering. 2010. No. 8. Pp. 953–960.
38. Bolandim, E.A., Beck, A.T., Malite, M. Bolted connections in cold-formed steel: reliability analysis for rupture in net section. Journal of Structural Engineering. 2013. No. 5. Pp. 748–756.
39. Kwon, Y.B., Chung, H.S., Kim, G.D. Development of cold-formed steel portal frames with PRY sections. Advances in Structural Engineering. 2008. No. 11(6). Pp. 633–649.

Contacts:

Ilya Selyantsev, iselyantsev@gmail.com

Alexandr Tusnin, valeksol@mail.ru

© Selyantsev, I.M., Tusnin, A., 2021



DOI: 10.34910/MCE.101.2

Behavior of light-gauge steel beams filled with recycled concrete

R. El-Nimri^{a*}, M.S. Abdel-Jaber^a, Y.M. Hunaiti^a, M. Abdel-Jaber^b

^a The University of Jordan, Amman, Jordan

^b AlHussein Technical University, Amman, Jordan

* E-mail: rola.elnimri@gmail.com

Keywords: concretes, recycling, concrete aggregates, asphalt, composite materials, finite element method.

Abstract. This paper presents an experimental and a numerical investigation of light-gauge steel box sections filled with concrete made with a combination of natural aggregate (NA), recycled concrete aggregate (RCA), and recycled asphalt pavement (RAP). A total of 47 specimens, including 30 composite beams, 15 plain concrete beams, and 2 bare steel beams were tested. The main variables in the tests were the steel thickness (2 and 2.4 mm), the coarse aggregate type and replacement ratios. NA was replaced by RCA and RAP with replacement levels of 20 %, 40 %, 60 %, 80 %, and 100 % by the total weight of NA. In addition, RCA and RAP were incorporated in the same mixes with four replacement levels of (20 % RCA and 80 % RAP); (40 % RCA and 60 % RAP); (60 % RCA and 40 % RAP); and finally, with (80 % RCA and 20 % RAP). The experimental capacities were compared to the theoretical prediction of EC4, AISC-LRFD, AIJ, and the Rigid Plastic Theory (RPT). Moreover, a finite element analysis (FEA) was performed using ABAQUS software. The experimental results showed that the ultimate capacity of composite beams decreased with the increase of RCA and RAP percentage. However, both RCA and RAP enhanced the capacity of plain concrete beams. Current code provisions predicted lower capacities than the experimental values, and the FEA results showed reasonable agreement with the test results.

1. Introduction

Introducing recycled aggregate (RA) in construction is a sustainable move in the construction industry. It prevents the consumption of current natural resources and reduces the continuous storage of waste in landfills. Recycled Concrete Aggregate (RCA) and Recycled Asphalt Pavement (RAP) are potential materials to replace natural aggregate (NA) in concrete mixes. RCA is obtained by crushing, washing, and grading concrete elements obtained from the demolition of old concrete structures while RAP is the aggregate from the base course layer obtained from roadways demolition or to gain access to buried utilities. RAP is usually reused in excavations or base layers. However, new insights are developed to use RAP in concrete mixes. When RAP is crushed and sieved, a good-quality well-graded aggregate coated with an asphalt binder layer is obtained. Several researches studied the mechanical and physical properties of concrete made with RCA [1–4]. The major conclusions are that RCA was found to compare favorably with NA but with lower strength, larger absorption, and weaker durability, nevertheless, the trend in their development was the same. Recently, other studies were conducted to investigate the effect of using RCA on the compressive, flexural and shear behavior of reinforced concrete beams [5–8]. Results proved that RCA had a small effect on the flexural and shear strength of the beams, while the progression of nonlinear behavior until failure is similar to beams with NA. It was also noted that whenever the amount of RCA increases, the initial stiffness decreases while the ultimate flexural deflections increase. Other research projects were conducted to study the effect of using RAP in concrete mixes [4], [9–11]. The major conclusions are that for low to middle strength concrete, RAP was also found to compare favorably with NA, however, the mechanical and elastic characteristics of concrete mix decrease with the increase of RAP content. This reduction in the properties of recycled aggregate concrete (RAC) needs to be minimized when it is deployed in new construction.

The composite action in concrete filled into steel tubes and the confinement of concrete infill, enhances the performance and capacity of hollow structural steel (HSS) by all sorts of applications. This could be verified due to the section transformation to be more rigid and resists more buckling [12–15]. In addition, filling hollow

El-Nimri, R., Abdel-Jaber, M.S., Hunaiti, Y.M., Abdel-Jaber, M. Behavior of light-gauge steel beams filled with recycled concrete. Magazine of Civil Engineering. 2021. 101(1). Article No. 10102. DOI: 10.34910/MCE.101.2



This work is licensed under a CC BY-NC 4.0

steel beams provides several advantages, such as high ultimate moment of resistance, high construction speed without the need to any formwork or skilled workers, and small cross sections are needed to sustain a given load when compared to conventional reinforced beams. The major advantage of the composite action is to force the concrete infill and the steel tube to act as one unit, this interaction shifts the neutral axis upward leaving the concrete and steel above the neutral axis under compression and forces almost all the steel under the neutral axis to carry the tension force. Several research projects were conducted on composite beams made from HSS filled with mortar [13], normal concrete [14], foam, and lightweight concrete [12]. Results of previous studies showed that the bending capacity and ductility of filled and half-filled girders were higher than empty steel girders and the concrete filling enhanced the moment carrying capacity of steel hollow sections.

Because of the confinement provided by the steel tube, concrete infill is not exposed to prevailing conditions, this will enhance both the properties and behavior of the filled concrete. This characteristic if used with RAC will help to compensate the reduction of its mechanical properties. Yang and Han [16] studied the compressive and flexural behavior of recycled aggregate concrete filled steel tubes (RACFST) under short-term loadings. They stated that the behavior of RACFST is similar to the corresponding HSS columns and beams filled with normal concrete but with small reduction in capacity. It is thus expected that the RAC can be used in concrete-filled steel structures in future constructions as a replacement for hot-rolled steel or reinforced concrete structures in small to medium sized buildings. However, there is a lack of information on the behavior of light-gauge steel sections filled with RAC which indicates the need for further investigations.

Based on this literature review, this paper will investigate the flexural behavior of light-gauge steel filled with normal and recycled concrete. 15 concrete mixes divided into three groups will be considered. The first group will include five mixes with RCA at replacement levels of 20 %, 40 %, 60 %, 80 %, and 100 %. The second group will include five mixes with RAP at replacement levels of 20 %, 40 %, 60 %, 80 %, and 100 %. The third group will combine RCA and RAP together with the following percentages (1) 20 % RCA and 80 % RAP; (2) 40 % RCA and 60 % RAP; (3) 60 % RCA and 40 % RAP, and (4) 80 % RCA and 20 % RAP. One composite beam from each steel thickness and one plain concrete beam will be cast from each concrete batch, in addition, two bare steel beams will be tested as well. All beams will be tested under two-point loading. Ultimate capacities and deflections will be recorded and compared to a control specimen made with NA only. Experimental results will be compared to the theoretical prediction of EC4, AISC-LRFD, AIJ, and the Rigid Plastic Theory (RPT). Moreover, a simulation model using ABAQUS software will be made, and a finite element analysis (FEA) will be conducted.

2. Methods

2.1. Materials

2.1.1. Cement

Portland – Pozzolana Cement was used in all concrete mixes.

2.1.2. Aggregates

Fine aggregates used in this research are silica sand. While the coarse aggregates used are mainly three types: NA, RCA, and RAP. The RCA was obtained by hand crushing concrete cubes from different locations without knowing their compressive strength. The RAP was obtained from a roadway demolition site. Fig. 1 shows the coarse aggregates used in this study. All coarse aggregates used in this investigation has a maximum size of 20 mm and were sieved to get aggregates to size gradation between sieve number 20 and sieve number 4. Sieve analysis was made according to ACI committee E-701 code [17, 18] and results are illustrated in Fig. 2.



a) NA

b) RCA

c) RAP

Figure 1. Photos of coarse aggregate used (a) NA; (b) RCA; (c) RAP.

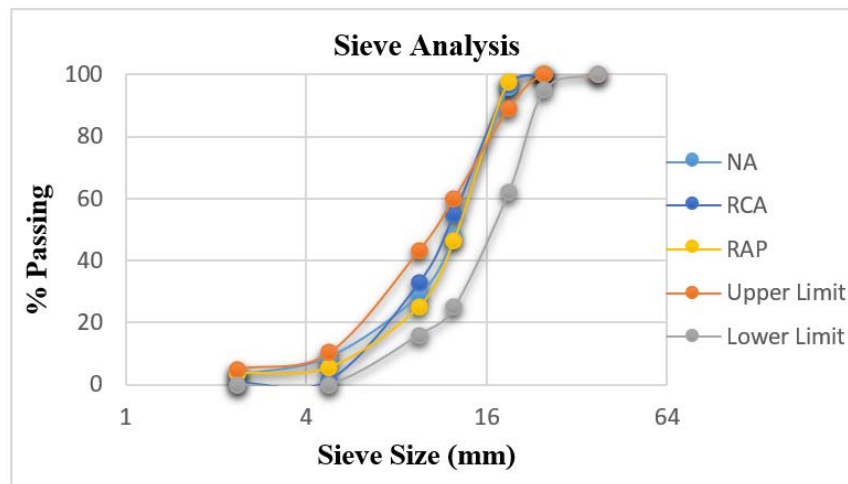


Figure 2. Coarse aggregates sieve analysis.

2.1.3. Light-gauge steel

Light – gauge steel or what is known as cold formed steel was used in this study with two different thicknesses (2 and 2.4 mm). This type of steel is formed or shaped at room temperature without any exposure to heat. Steel sheets are coated with zinc, which is known as galvanized steel, the main objective of this layer is to protect the steel from corrosion.

2.2. Experimental Program

2.2.1. Aggregates properties

Specific gravity and absorption tests were performed according to ASTM C 127 [19]. Results are shown in Table 1. It is observed that RCA has higher absorption value than NA, this might be attributed to the presence of cement paste in the aggregates which increases the absorption and lowers the specific gravity. Also, RAP have a lower specific gravity and a higher absorption, not as high as RCA, this is because the asphalt binder that coats RAP prevents the aggregates from absorbing too much water.

Table 1. Properties of coarse aggregates.

Property	NA	RCA	RAP
Specific Gravity (Apparent)	2.71	2.65	2.32
Specific Gravity (Bulk Dry)	2.63	2.24	2.00
Specific Gravity (Bulk SSD)	2.66	2.40	2.25
Water Absorption %	1.23	6.92	2.42
Bulk Density (Unit Weight kg/m ³)	1669	1371	1316

2.2.2. Tensile test results

Yield strength, tensile strength and elongation tests were made according to ASTM A370 [20] standards for two steel samples from each thickness and the results are shown in Table 2.

Table 2. Properties of steel

Sample	Yield Strength (MPa)	Tensile Strength (MPa)	Elongation (%)
$t = 2 \text{ mm}$	1	285	350
	2	275	350
$t = 2.4 \text{ mm}$	3	270	357.2
	4	290	353.4

2.2.3. Concrete mix proportions

Fifteen concrete mixes were made with effective water-to-cement (w/c) ratio of 0.48 to achieve a target compressive strength of 30 MPa at 28 days. NA was replaced by RCA and RAP. Table 3 shows the mix proportions and concrete properties.

2.2.4. Concrete compressive strength

The compressive strength was determined by testing 6 cubes of 150 mm side length. Cubes were filled in three layers; each layer was stroke 35 times. Two cubes from each concrete batch were tested at 7 days, and all remaining cubes were tested at 28 days. It can be noticed that RAP-NA cubes gained more compressive strength at 7 days than RCA-NA cubes. The highest compressive strength was recorded for the 100 % NA mix followed by the combination of RCA-NA then the combination of RAP-NA, where the compressive strength decreased with the increase of RA levels. RCA-RAP compressive strength was noticed to be in between RCA-NA and RAP-NA combinations, where the compressive strength increased with the increase of RCA level except for 40 %RCA+60 %RAP and 60 %RCA+40 %RAP. This could be due to the water absorption amount.

The maximum compressive strength of 100 %NA at 28 days was 37.6 MPa. For RCA-NA combinations, the highest compressive strength was recorded for 20 %RCA+80 %NA with a value of 32.4 MPa while the lowest was recorded for 100 %RCA with a value of 20.8 MPa. For RAP-NA combinations, the highest compressive strength was recorded for 20 %RAP+80 %NA with a value of 28.0 MPa while the lowest was recorded for 100 %RAP with a value of 23.0 MPa. For RCA-RAP combinations, the highest compressive strength was recorded for 80 %RCA+20 %RAP with a value of 27.7 MPa while the lowest was recorded for 20 %RCA+80 %RAP with a value of 23.2 MPa.

Table 3. Mix proportions and concrete properties.

Mix Number	Cement (kg/m ³)	Water (kg/m ³)	Coarse Aggregate (kg/m ³)			Fine Aggregate (kg/m ³)	f_{cu} at 7 days (MPa)	f_{cu} at 28 days (MPa)
			NA	RCA	RAP			
Control Mix	375	180	1145	0	0	638	23.4	37.6
20% RCA + 80% NA	375	180	916	229	0	638	19.8	32.4
40% RCA + 60% NA	375	180	687	458	0	638	16.1	29.0
60% RCA + 40% NA	375	180	458	687	0	638	17.0	30.1
80% RCA + 20% NA	375	180	229	916	0	638	17.8	27.9
100% RCA	375	180	0	1145	0	638	13.4	20.8
20% RAP + 80% NA	375	180	916	0	229	638	20.5	28.0
40% RAP + 60% NA	375	180	687	0	458	638	16.9	26.9
60% RAP + 40% NA	375	180	458	0	687	638	19.7	27.0
80% RAP + 20% NA	375	180	229	0	916	638	16.4	25.1
100% RAP	375	180	0	0	1145	638	18.0	23.0
20% RCA + 80% RAP	375	180	0	229	916	638	17.8	23.2
40% RCA + 60% RAP	375	180	0	458	687	638	15.3	21.8
60% RCA + 40% RAP	375	180	0	687	458	638	17.7	21.9
80% RCA + 20% RAP	375	180	0	916	229	638	18.1	27.7

2.2.5. Specimens details

The flexural behavior was investigated by casting one composite beam from each steel thickness in addition to one plain concrete beam from each concrete mix. Moreover, two bare steel beams were tested as well. All beams have a square cross-section of 100×100 mm and 1200 mm length (Fig. 3b). The steel tube was made by welding two steel sheets (Fig. 3a) using an Exx70 weld type with 3 mm weld thickness. In order to avoid any slipping between concrete and steel, rivets were used on both the top and bottom surfaces of composite beams spaced at 100 mm (Fig. 3c).

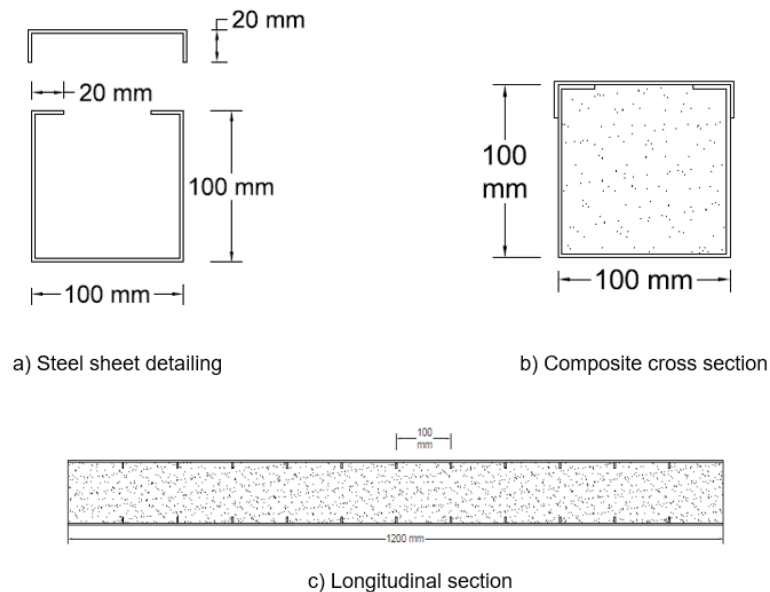


Figure 3. Composite beams sections.

For composite beams all specimens' labels start with B followed by the steel thickness then the aggregates used (R designated for RCA, P for RAP, and N for NA). For example, specimen B2.4–R20–N80 means it is a composite beam with 2.4 mm steel thickness filled with concrete containing 20 % RCA and 80 % NA. For plain concrete beams, the same labels are used without the steel thickness. Bare steel labels are B2 and B2.4 correspond to hollow steel beams with 2- and 2.4-mm thickness, respectively.

2.2.6. Test setup

Two-point loading test was conducted using a 700 kN capacity MFL Prüf-systeme Universal Testing Machine. Specimens were treated as simply supported beams lying on two concrete supports that contains two steel rods located at 100 mm from each end of the beam. Three LVDT devices with 0.01 mm accuracy were placed under the mid-span and applying load locations to measure the deflections during the test. Fig. 4 shows the test setup.

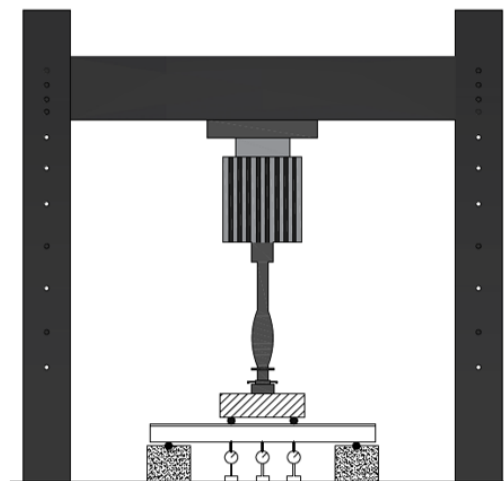


Figure 4. Test setup.

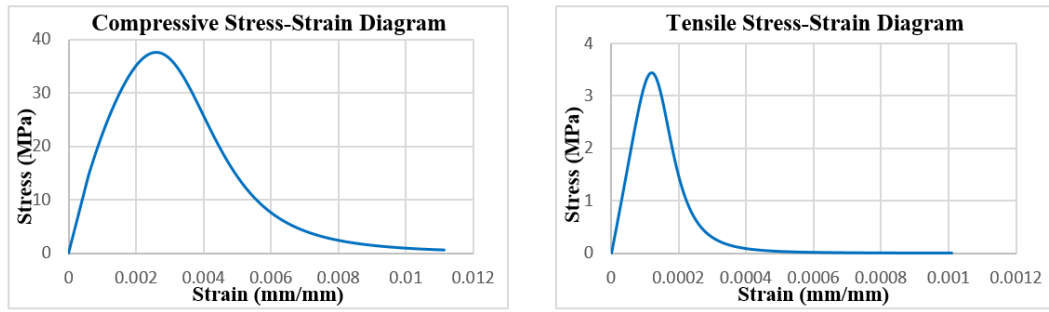
2.3. Finite Element Model

2.3.1. Parts

Composite beam is constructed from two main parts, the steel sheet cover and the concrete filling. To simulate the actual test setup, discrete rigid rods were created.

2.3.2. Materials definition

Steel was defined as an elastic plastic material with 0.3 Poisson's ratio. While concrete was defined as an elastic material, but the plasticity of concrete was defined using concrete damage plasticity. Tsai's equations were used to obtain the compressive and tensile stress-strain diagrams [21]. Fig. 5 shows the stress-strain diagrams for 100 %NA mix.



a) Compressive stress-strain diagram for 100%NA b) Tensile stress-strain diagram for 100%NA
Figure 5. Compressive and tensile stress-strain diagrams for 100%NA.

2.3.3. Sections

Sections were defined as solid homogeneous type, with each section assigned to one of the pre-defined materials. Then all parts were assigned to their corresponding sections. However, test setup parts were not assigned to any section because they were defined as a discrete rigid type.

2.3.4. Meshing

Steel plate and concrete filling parts were meshed with approximate global seeds size of 30 mm and assigned to 3D stress family, while the rods were meshed with approximate global seeds size of 4.2 mm with discrete rigid element family. All parts were assigned to hexahedral element shape and meshed before the assembly of the model. Fig. 6 shows the meshed model in ABAQUS.

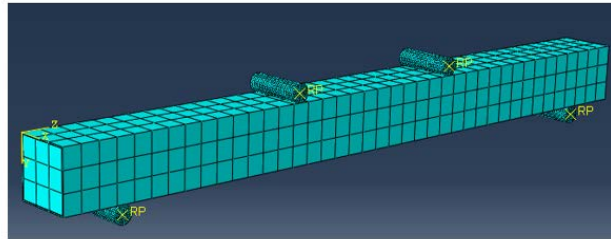


Figure 6. Model mesh.

2.3.5. Interactions

In order to ensure that all parts behave as one unit during the run, interactions must be created. General contact interaction was defined with 0.3 friction coefficient and hard contact property to ensure the hard contact between the rods and the beam, while a cohesive interface was defined between the concrete outer surface and steel inner surface.

2.3.6. Boundary conditions

Supports are defined as two rods located at 100 mm from each end of the beam, the two supports were assigned as pin supports to simulate the actual test setup. Because the rods were defined as discrete rigid elements, boundary conditions need to be assigned to their reference points. In order to be consistent with the supports, both rods were prohibited from moving in any direction. The remaining two rods were used to induce the displacement to the beam; thus, the two rods were allowed to move in the Y – direction (U2) only. A dynamic explicit step was defined to induce the displacement to the beam. This test is applicable as long as the kinetic energy is maintained to a very small quantity, and this is achieved by increasing the step time. The experimentally conducted deflection was applied to the rods using the boundary conditions (Fig. 7) with a smooth step amplitude.

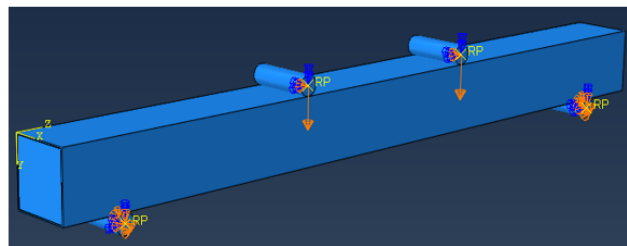


Figure 7. Boundary conditions.

2.3.7. History output request

The reaction forces and the mid-span deflection were requested as output data. After analysis, the load-deflection behavior obtained from ABAQUS was compared to the experimental results.

2.4. Analytical Considerations

2.4.1. Ultimate moment of resistance according to EC4 ($M_{pl,Rd}$)

The ultimate moment of resistance according to EC4 [22] is calculated based on a full plastic stress distribution on the composite cross section assuming compatibility between concrete and steel (Fig. 8).

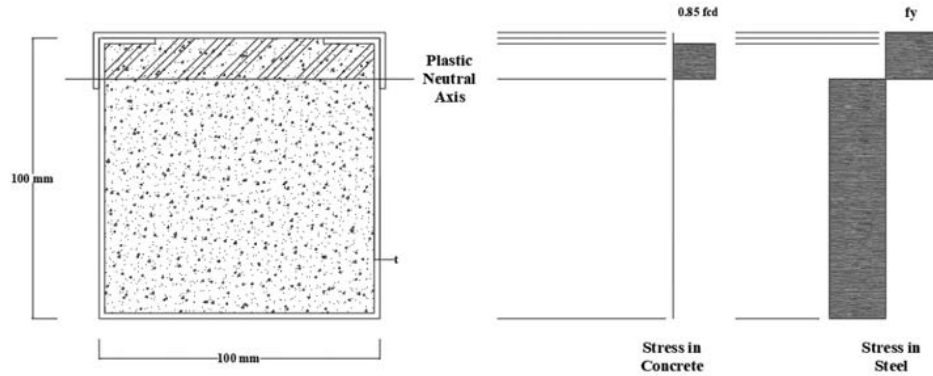


Figure 8. Stress distribution in concrete-filled steel section based on EC4.

The concrete at the tension zone is ignored, while the concrete at the compression zone is under a uniform compression stress equals to $0.85f_{cd}$, where f_{cd} is the compressive cylinder strength of concrete at 28 days. Structural steel is stressed to its design yield strength f_{yd} in tension and compression zones.

2.4.2. Ultimate moment of resistance according to AISC-LRFD and AIJ provisions

The AISC-LRFD [23] and the AIJ [24] provisions assume that the moment capacity of HSS beams filled with concrete depends only on the steel section alone (M_{p-AISC}). Thus, the ultimate moment of resistance is assumed to be calculated based on a full plastic stress distribution on the steel section without any contribution from concrete (Fig. 9).

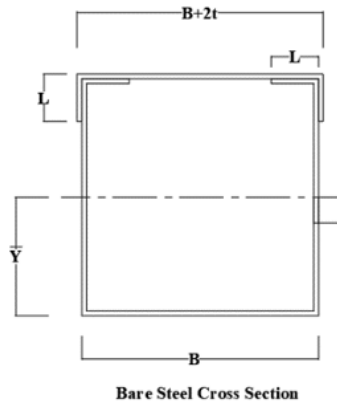


Figure 9. Bare steel cross section.

The centroid of the steel section from the bottom face of the beam (Fig. 9) is calculated using the following equation:

$$\bar{Y} = \frac{\sum A \times \bar{y}}{\sum A} \dots \dots \dots (1)$$

The plastic moment (M_p) is determined according to the following equation:

$$M_p = f_y \times Z \dots \dots \dots (2)$$

where: f_y is the steel yield stress.

Z is the section modulus (first moment of area around the centroid)

2.4.3. Ultimate moment of resistance according to RPT

Rigid plastic analysis theory is used to develop the equations of moment capacity for composite HSS beams filled with concrete [25, 26]. The flexural capacity is determined by considering the distribution of forces on both steel and concrete sections individually and introducing a bond force that represents the interaction

of concrete and steel together. The distribution of strains for full interaction and partial interaction and forces in concrete and steel across the section is shown in Fig. 10.

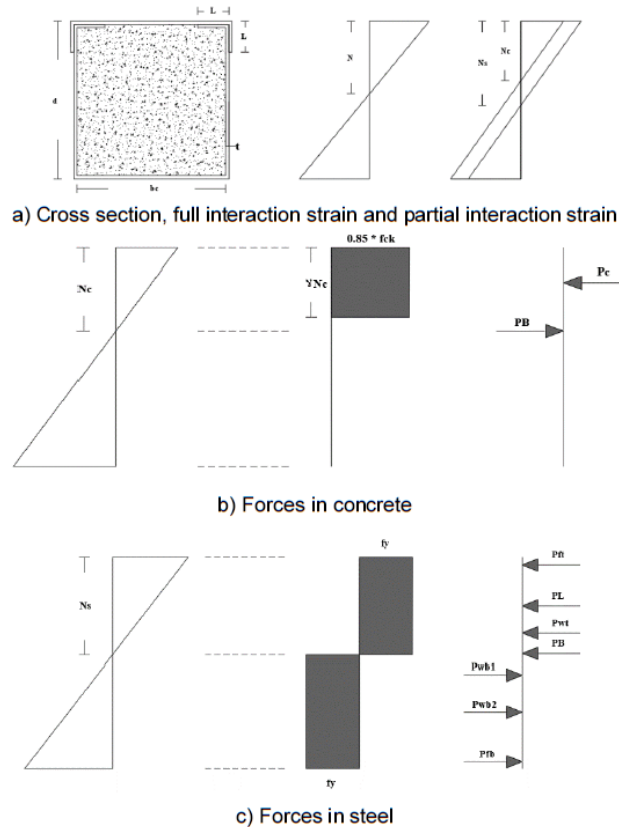


Figure 10. Rigid plastic analysis theory charts.

For the case where the neutral axis is at the overlap between the upper cap and the vertical web of the steel:

Let P_c is the force in concrete, P_B is the bond force, P_{ft} is the force in the top flange, P_L is the force in the horizontal lip, P_{wt} is the force in the vertical lip due to compression, P_{wb1} is the force in the vertical lip due to tension, P_{wb2} is the force in the web due to tension, P_{fb} is the force in the bottom flange, L is the lip length, d is the section depth, t is the steel sheets thickness, b_c is the width of concrete, f_{ck} is the characteristics compressive strength of concrete, N_c and N_s are the depth of concrete and steel neutral axes from the beam's top fiber and N is the depth of the neutral axis of the composite section from the beam's top fiber when full interaction takes place.

Considering the equilibrium of forces in concrete, the depth of the neutral axis will be given by the equation:

$$N_c = \frac{P_B + 1.7\gamma \times f_{ck} \times t \times (L - t)}{0.85\gamma \times f_{ck} \times b_c} \dots\dots\dots (3)$$

where γ is a reduction factor:

$$\gamma = 0.85 - 0.007(f_{ck} - 28) \dots\dots\dots (4)$$

Considering the equilibrium of forces in steel, the depth of the neutral axis will be given by the equation:

$$N_s = \frac{2t^2 \times f_y + 2d \times t \times f_y - P_B}{8t \times f_y} \dots\dots\dots (5)$$

Taking the moment of all forces around the top fiber of the beam, the ultimate moment capacity can be determined from the expression (6):

$$M_u = t \times f_y \left(d^2 + d \times b_c + L^2 - 4N_s^2 \right) - t^2 \times f_y \times (b_c - 3L) + 3t^3 \times f_y - 0.425f_{ck} \times (b_c \times t^2 + 2t^3 - 2L \times t^2 + b_c (\gamma \times N_c - t)^2) \dots\dots\dots (6)$$

For full interaction between steel and concrete $N_s = N_c = N$, thus, the bonding force will be calculated from the expression:

$$P_B = \frac{1.7\gamma \times f_{ck} \times t \times f_y (b_c \times t + b_c \times d - 8L \times t + 8t^2)}{8t \times f_y + 0.85\gamma \times f_{ck} \times b_c} \dots\dots\dots (7)$$

For the case where the neutral axis is under the overlap between the upper cap and the vertical web of the steel:

Considering the equilibrium of forces in concrete and steel, the depth of the neutral axes will be given by the equations:

$$N_c = \frac{P_B + 1.7\gamma \times f_{ck} \times t \times (L - t)}{0.85\gamma \times f_{ck} \times b_c} \dots\dots\dots (8)$$

$$N_s = \frac{2t^2 \times f_y + 2d \times t \times f_y - 4L \times t \times f_y - P_B}{4t \times f_y} \dots\dots\dots (9)$$

Taking the moment of all forces around the top fiber of the beam, the ultimate moment capacity can be determined from the expression (10):

$$M_u = t \times f_y (d^2 + d \times b_c - L^2 - 2N_s^2) + t^2 \times f_y \times (L - b_c) - 5t^3 \times f_y - 0.425f_{ck} \times (b_c \times t^2 + 2t^3 - 2L \times t^2 + b_c (\gamma \times N_c - t)^2) \dots\dots\dots (10)$$

For full interaction between steel and concrete $N_s = N_c = N$, thus, the bonding force will be calculated from the expression:

$$P_B = \frac{1.7\gamma \times f_{ck} \times t \times f_y (b_c \times t + b_c \times d - 2b_c \times L + 4t^2)}{4t \times f_y + 0.85\gamma \times f_{ck} \times b_c} \dots\dots\dots (11)$$

3. Results and Discussion

3.1. General Behavior and Failure Modes

All composite beams failed in a ductile manner and have a flexural behavior similar to beams made with 100 % NA. Failure of the steel tube involved several local buckles that were symmetric and distributed equally at the compression zone without any tensile fracture observed at the tension zone. Beams were cut longitudinally to visualize the concrete core failure. Concrete was crushed at the compression region where local buckles took place, in addition to tensile cracks that were found at the tension zone. All the experimental observations of this study match the results obtained by Yang and Han [16]. For bare steel beams, local buckles occurred in a wider range at the compression zone, in addition to buckling of steel at the tension zone near the support region. Plain concrete beams failed in a pure flexural way, where a flexural crack initiated near the extreme tensile fiber of the beam and propagated vertically until it reached the extreme compressive fiber. Fig. 11 and 12 show the failure modes of all beams.





Figure 11. Composite beams failure modes.



Figure 12. Plain concrete beams failure modes.

3.2. Flexural Capacity

Flexural capacity of all beams is shown in Table 4. All composite beams made with 2.4 mm steel thickness had higher load capacities compared with the 2 mm steel thickness beams made from the same concrete mixes. In addition, beams within the same group developed a similar capacity pattern for both steel thicknesses (Fig. 13).

Table 4. Beams flexural capacity.

Group	Mix Number	2 mm		2.4 mm		Plain Concrete Beams (kN.m)	f_{cu} at 28 days (MPa)
		Capacity (kN)	Moment (kN.m)	Capacity (kN)	Moment (kN.m)		
Control	Control Mix	86.89	14.48	102.60	17.10	0.48	37.6
Group 1	20% RCA + 80% NA	73.08	12.18	97.32	16.22	0.71	32.4
	40% RCA + 60% NA	70.47	11.75	96.48	16.08	0.50	29.0
	60% RCA + 40% NA	69.47	11.58	90.31	15.05	0.60	30.1
	80% RCA + 20% NA	70.48	11.75	87.58	14.60	0.61	27.9
	100% RCA	65.87	10.98	87.98	14.66	0.58	20.8
Group 2	20% RAP + 80% NA	67.78	11.30	91.29	15.21	0.50	28.0
	40% RAP + 60% NA	65.47	10.91	88.58	14.76	0.57	26.9
	60% RAP + 40% NA	65.57	10.93	88.08	14.68	0.63	27.0
	80% RAP + 20% NA			84.28	14.05	0.58	25.1
	100% RAP			81.57	13.60	0.53	23.0
Group 3	20% RCA + 80% RAP	70.17	11.69	84.97	14.16	0.61	23.2
	40% RCA + 60% RAP	73.67	12.28	86.78	14.46	0.60	21.8
	60% RCA + 40% RAP	73.67	12.28	85.58	14.26	0.56	21.9
	80% RCA + 20% RAP	75.57	12.60	87.48	14.58	0.55	27.7
	Bare Steel	45.56	7.59	67.07	11.18		

Comparing the results of RACFST to the control specimens, it was observed that beams made with 100 % NA had the highest capacity among all specimens. This is attributed to the compressive strength of the concrete mixes which decreases with the use of RA. Although the compressive strength of some mixes was

lower than expected because of the water absorption amount (100 % RCA, 40% RCA+60 % RAP and 60 % RCA+40 % RAP), the behavior and capacity of RACFST were not affected. In addition, the results of B2-P80-N20 and B2-P100 did not match the capacity pattern so the results were eliminated.

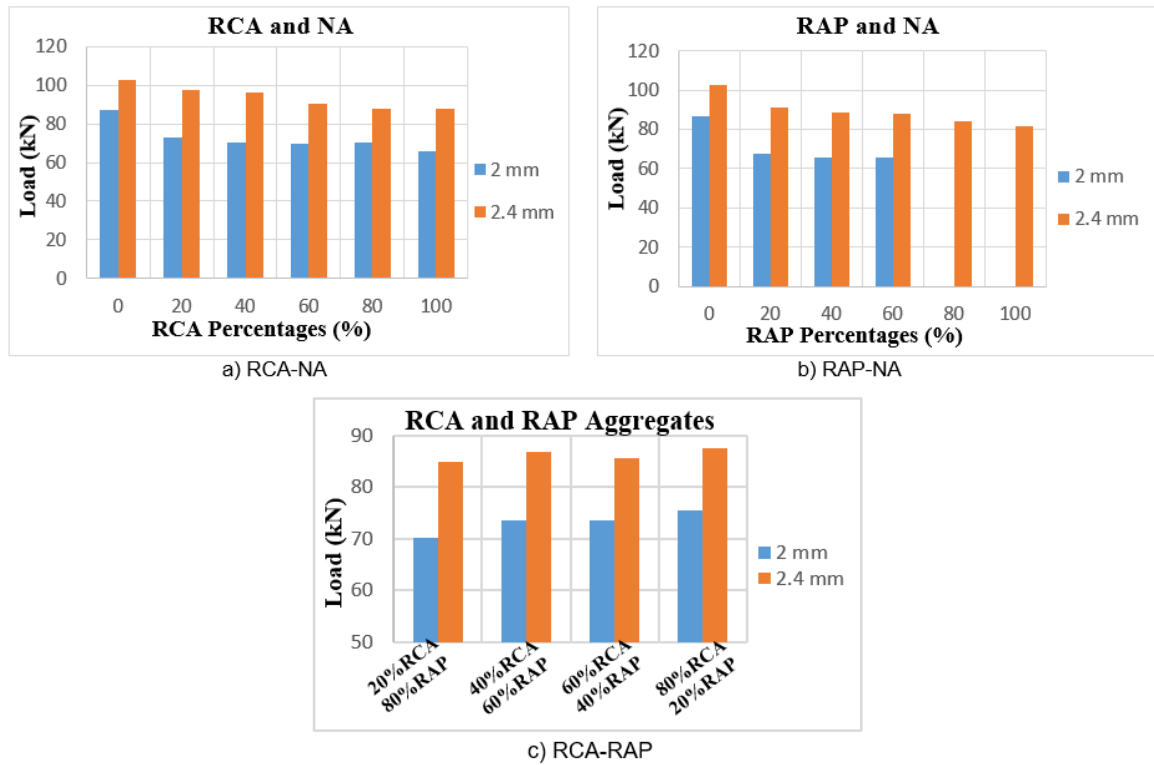


Figure 13. Beams capacity for different steel thicknesses.

The combination of RCA and NA (Group 1) gave higher load values than the combination of RAP and NA (Group 2) at the same replacement percentages, thus, RCA had the ability to sustain more loads than RAP. This is reflected on the results of the beams made with a combination of RCA and RAP (Group 3) as the capacity of beams increased with the increase of RCA percentage in the concrete mix. As opposed to their use in mixtures containing any RA (RCA and RAP) with NA where the capacity decreased with the increase of RA percentage.

Concrete filling of both NA concrete and RAC enhanced the behavior and the capacity of bare steel beams of both thicknesses. Fig. 14 shows the capacity of composite and bare steel beams.

RA had a significant influence on the flexural behavior of plain concrete beams. All beams made with RA of both RCA and RAP in all their combinations gave higher results than the plain concrete beam made with 100 %NA. The capacity of plain concrete beams containing RCA decreased with the increase of RCA percentages in the mix, while the capacity of the plain concrete beams made with RAP increased with the increase of RAP percentages except for B-P80-N20 and B-P100, this could be due to some errors in the test. For samples containing RCA and RAP, the capacity decreased with the increase of RCA percentages. Fig. 15 shows the results of the plain concrete beams.

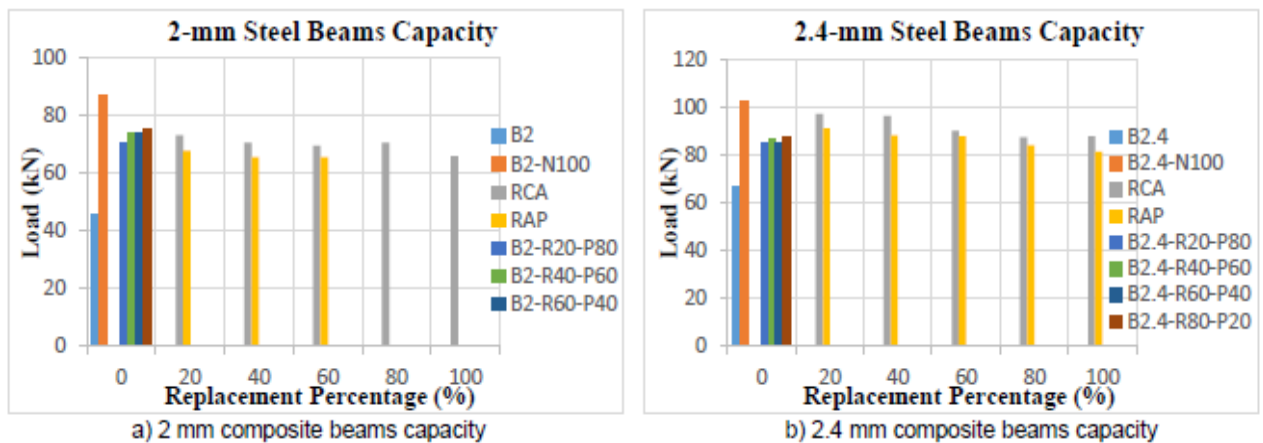


Figure 14. Capacity of composite and bare steel beams.

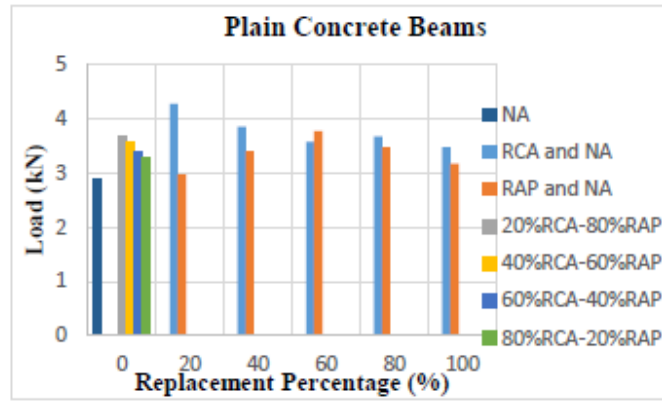


Figure 15. Capacity of the plain concrete beams.

3.3. Moment Deflection Behavior

All specimens showed an identical moment-deflection behavior, this behavior is divided into two phases. Phase one starts from the zero moments up to about 60 % of the ultimate moment capacity where the beams had a linear behavior which indicates the elastic performance of the specimens.

After this point, higher deflection values were measured with a slight increase in load, this represents phase two that indicates the ductile response of the beam specimens with gradually decreasing stiffness. Fig. 16 shows the moment deflection behavior of composite and bare steel beams.

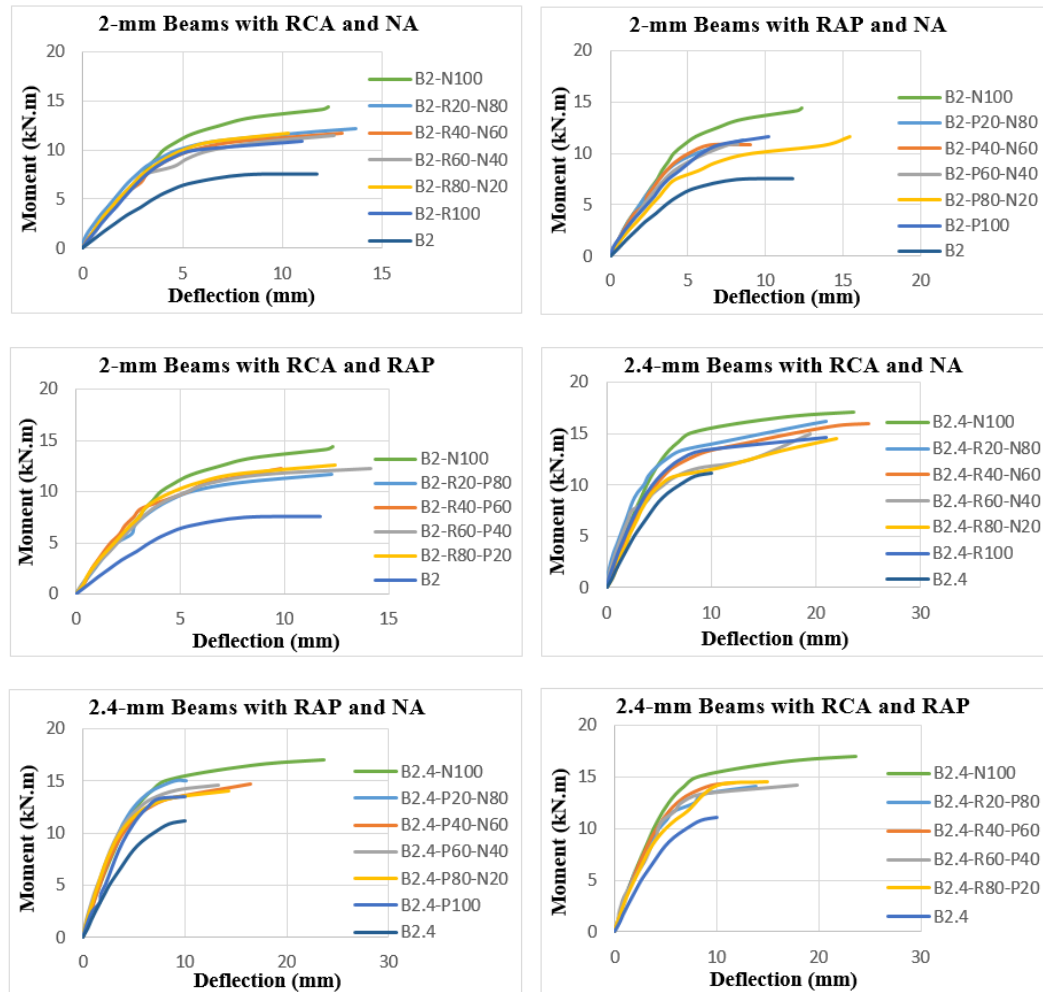


Figure 16. Moment deflection behavior.

The deflected shape of all beams was the same and had the shape of approximately a half sine wave. Yang and Han [16] reported similar observation. Specimens B2-R40-N60 and B2.4-R80-P20 were selected to illustrate the development of the deflected shape of the composite beams (Fig. 17), where the deflection values were plotted at different moment levels for each sample.

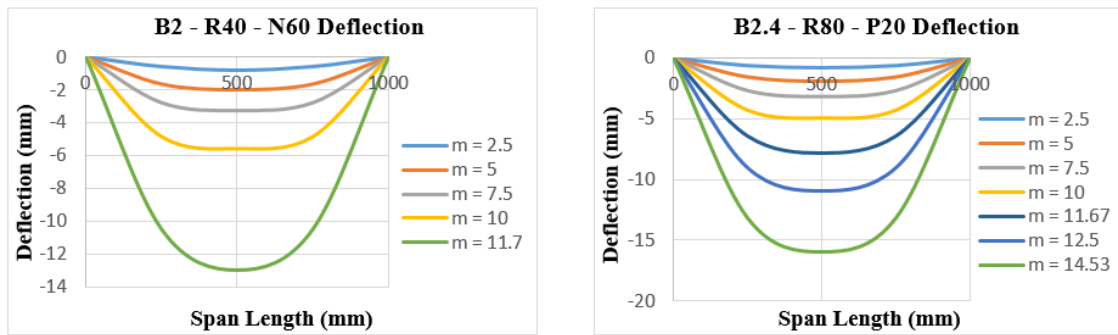


Figure 17. Deflection development at different moment levels.

3.4. Theoretical Ultimate Moment of Resistance

In order to investigate the validity of codes' equations, the ultimate moment capacities were calculated according to EC4, AISC-LRFD, AIJ, and the RPT. Tables 5 and 6 show the theoretical predicted values compared to the experimental results. Mean, Coefficient of Variation (COV), and the reduction percent (%) were also calculated. All codes gave a safe prediction of the ultimate moment capacities of composite beams as the RPT gave the closest moment value of all codes with a COV and a reduction percent of 0.0682 and about 12 % for samples with 2 mm steel and a COV and a reduction percent of 0.0526 and almost 18 % for samples with 2.4 mm steel.

Table 5. Theoretical capacity of composite beams with 2 mm steel thickness.

Mix	M_{ue}	EC4		AISC-LRFD		AIJ		RPT	
		$M_{pl,Rd}$	$\frac{M_{pl,Rd}}{M_{ue}}$	M_{u-AISC}	$\frac{M_{u-AISC}}{M_{ue}}$	M_{u-AIJ}	$\frac{M_{u-AIJ}}{M_{ue}}$	M_{u-RPT}	$\frac{M_{u-RPT}}{M_{ue}}$
B2 – N100	14.48	10.28	0.710	9.66	0.667	9.66	0.667	10.49	0.725
B2 – R20 – N80	12.18	10.24	0.841	9.66	0.793	9.66	0.793	10.45	0.858
B2 – R40 – N60	11.75	10.21	0.869	9.66	0.822	9.66	0.822	10.41	0.886
B2 – R60 – N40	11.58	10.22	0.883	9.66	0.834	9.66	0.834	10.42	0.900
B2 – R80 – N20	11.75	10.20	0.868	9.66	0.822	9.66	0.822	10.40	0.885
B2 – R100	10.98	10.13	0.923	9.66	0.880	9.66	0.880	10.25	0.934
B2 – P20 – N80	11.30	10.20	0.903	9.66	0.855	9.66	0.855	10.40	0.921
B2 – P40 – N60	10.91	10.19	0.934	9.66	0.885	9.66	0.885	10.39	0.952
B2 – P60 – N40	10.93	10.19	0.932	9.66	0.884	9.66	0.884	10.39	0.951
B2 – P80 – N20									
B2 – P100									
B2 – R20 – P80	11.69	10.16	0.869	9.66	0.826	9.66	0.826	10.28	0.879
B2 – R40 – P60	12.28	10.14	0.826	9.66	0.787	9.66	0.787	10.27	0.836
B2 – R60 – P40	12.28	10.15	0.827	9.66	0.787	9.66	0.787	10.27	0.836
B2 – R80 – P20	12.60	10.20	0.810	9.66	0.767	9.66	0.767	10.40	0.826
Mean		0.861		0.816		0.816		0.876	
Coefficient of variation		0.0683		0.0699		0.0699		0.0682	
Reduction Percent (%)		13.9		18.4		18.4		12.4	

Table 6. Theoretical capacity of composite beams with 2.4 mm steel thickness.

Mix	M_{ue}	EC4		AISC-LRFD		AIJ		RPT	
		$M_{pl,Rd}$	$\frac{M_{pl,Rd}}{M_{ue}}$	M_{u-AISC}	$\frac{M_{u-AISC}}{M_{ue}}$	M_{u-AIJ}	$\frac{M_{u-AIJ}}{M_{ue}}$	M_{u-RPT}	$\frac{M_{u-RPT}}{M_{ue}}$
B2.4 – N100	17.10	12.22	0.715	11.58	0.677	11.58	0.677	12.45	0.728
B2.4 – R20 – N80	16.22	12.18	0.751	11.58	0.714	11.58	0.714	12.30	0.759
B2.4 – R40 – N60	16.08	12.15	0.756	11.58	0.720	11.58	0.720	12.27	0.763
B2.4 – R60 – N40	15.05	12.16	0.808	11.58	0.769	11.58	0.769	12.28	0.816
B2.4 – R80 – N20	14.60	12.14	0.832	11.58	0.793	11.58	0.793	12.25	0.839
B2.4 – R100	14.66	12.06	0.823	11.58	0.790	11.58	0.790	12.16	0.829
B2.4 – P20 – N80	15.21	12.14	0.798	11.58	0.761	11.58	0.761	12.25	0.805
B2.4 – P40 – N60	14.76	12.13	0.822	11.58	0.784	11.58	0.784	12.24	0.829
B2.4 – P60 – N40	14.68	12.13	0.826	11.58	0.789	11.58	0.789	12.24	0.834
B2.4 – P80 – N20	14.05	12.11	0.862	11.58	0.824	11.58	0.824	12.22	0.870
B2.4 – P100	13.60	12.09	0.889	11.58	0.852	11.58	0.852	12.19	0.897
B2.4 – R20 – P80	14.16	12.09	0.854	11.58	0.818	11.58	0.818	12.19	0.861
B2.4 – R40 – P60	14.46	12.07	0.835	11.58	0.801	11.58	0.801	12.17	0.842
B2.4 – R60 – P40	14.26	12.07	0.846	11.58	0.812	11.58	0.812	12.17	0.854
B2.4 – R80 – P20	14.58	12.40	0.851	11.58	0.794	11.58	0.794	12.25	0.840
Mean		0.818		0.780		0.780		0.824	
Coefficient of variation		0.0550		0.0569		0.0569		0.0526	
Reduction Percent (%)		18.2		22.0		22.0		17.6	

3.5. FEA Results

In order to ensure a static analysis using a dynamic explicit step, the kinetic energy throughout the analysis must be a very small quantity. Fig. 18 shows the kinetic energy of Sample B2 – P60 – N40.

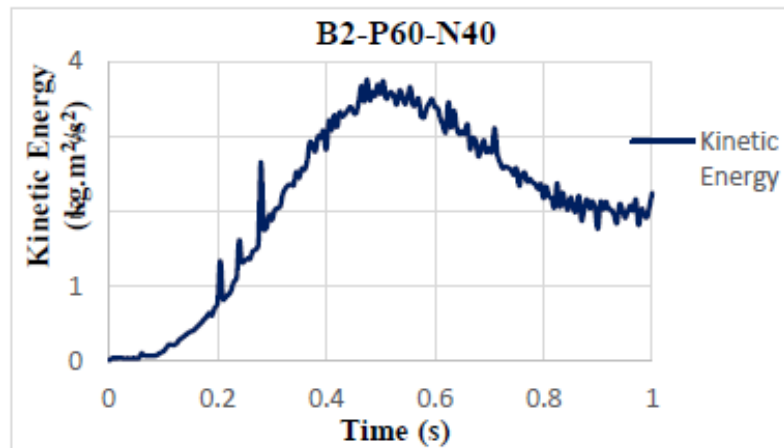


Figure 18. Kinetic energy of beam B2 – P60 – N40.

All beams analyzed in ABAQUS showed nearly the same deflected shape as the experimental one. Fig. 19 shows the deflected shape obtained from ABAQUS for the sample B2-R20-N80.

The maximum principal plastic strain results of FE simulation for the sample B2.4-N100 is presented in Fig. 20. It illustrates the cracking of concrete based on the stress–strain relationship. The results agreed well with the experimental concrete cracks that were found after cutting the composite beams.

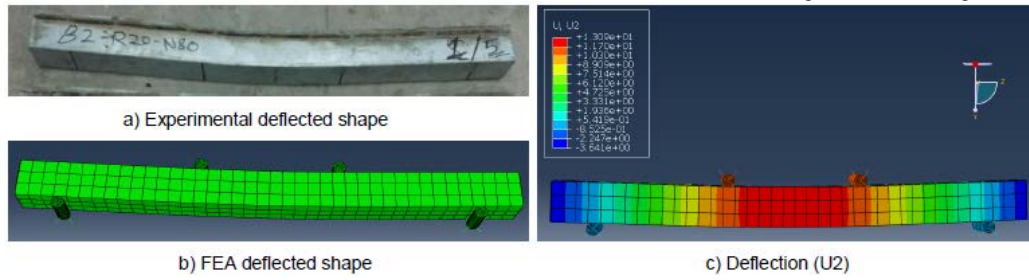


Figure 19. Experimental and FEA deflected shape for beam B2-R20-N80.

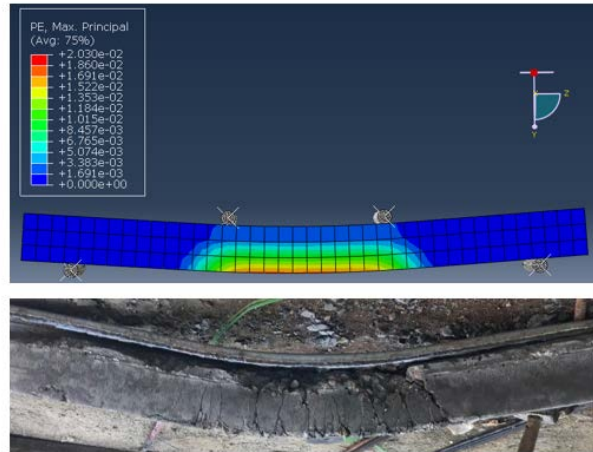
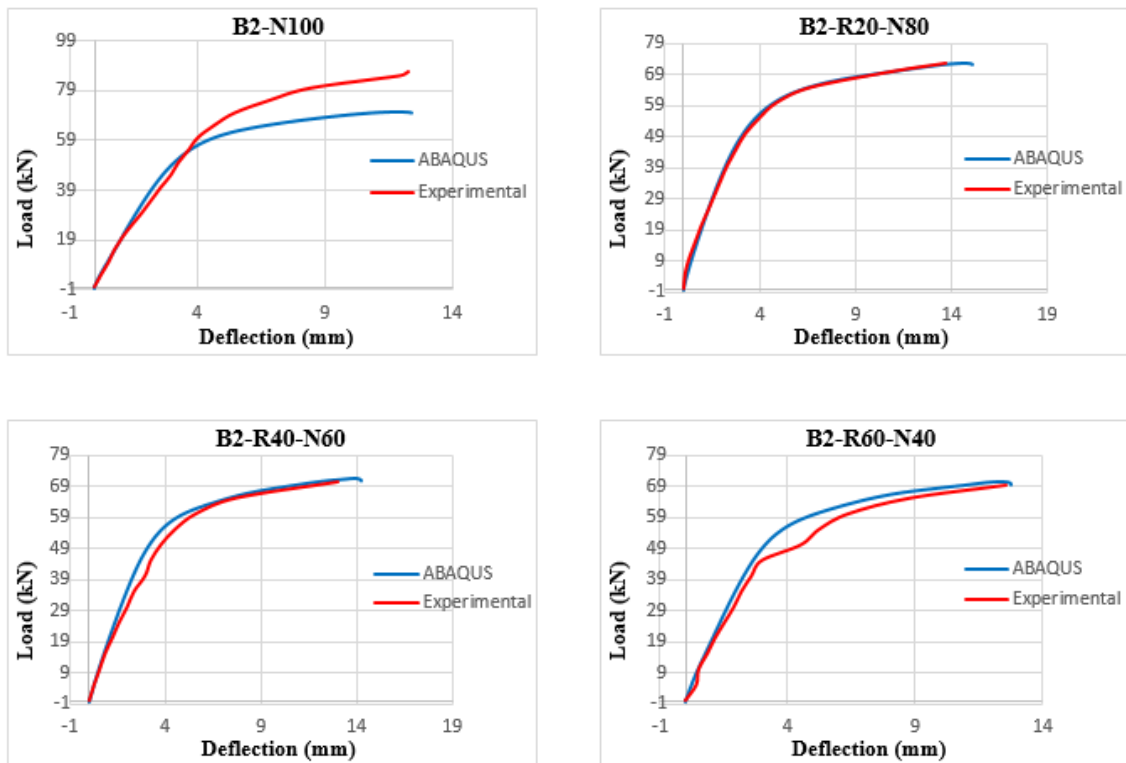


Figure 20. Maximum principal plastic strain for B2.4-N100.

Reaction forces and mid-span deflections were the history output requests for the analysis. All beams analyzed in ABAQUS showed nearly the same Load-Deflection behavior as the experimental behavior. Fig. 21 and 22 show a comparison between the experimental load deflection behavior and the one obtained from ABAQUS.



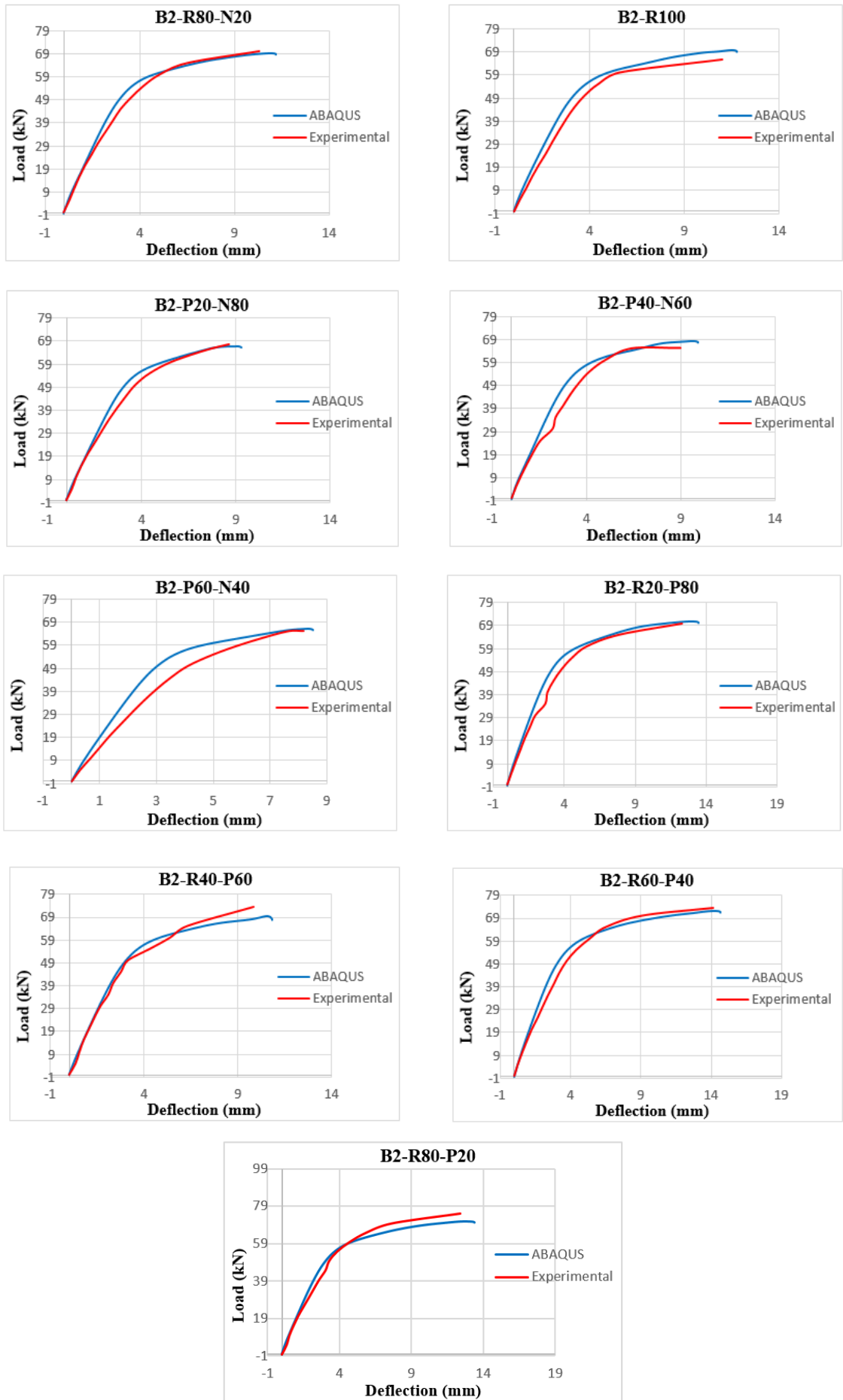
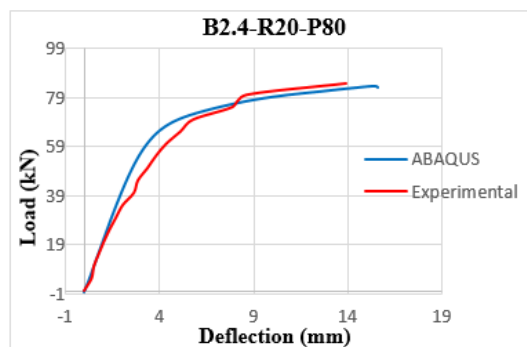
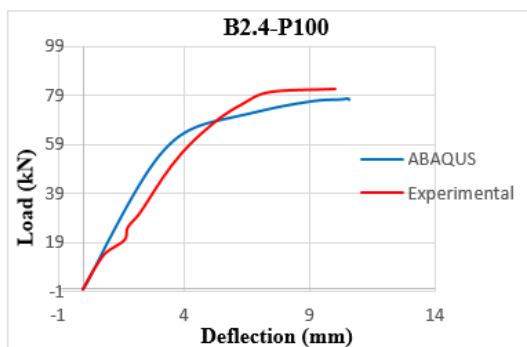
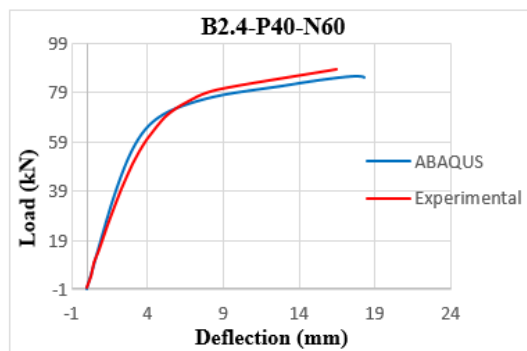
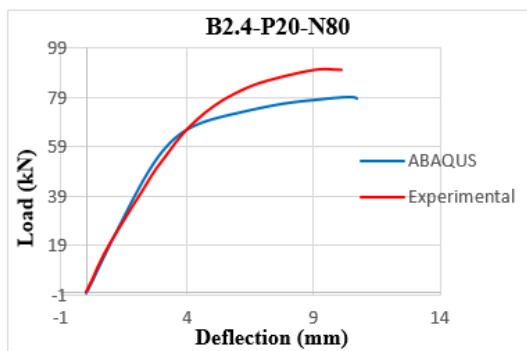
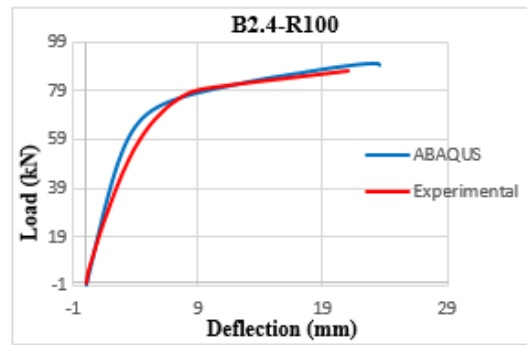
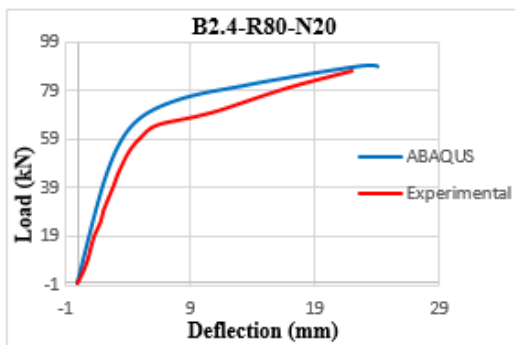
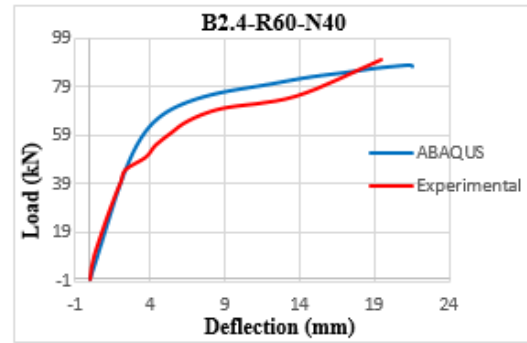
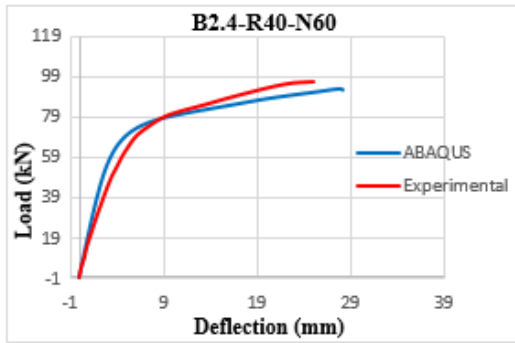
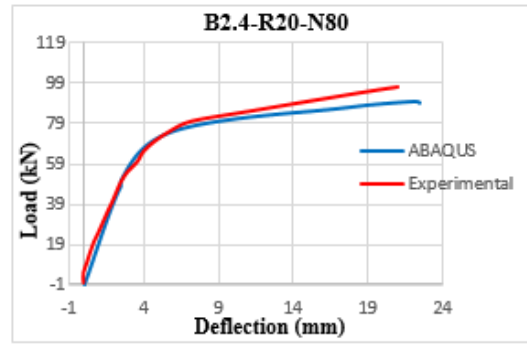
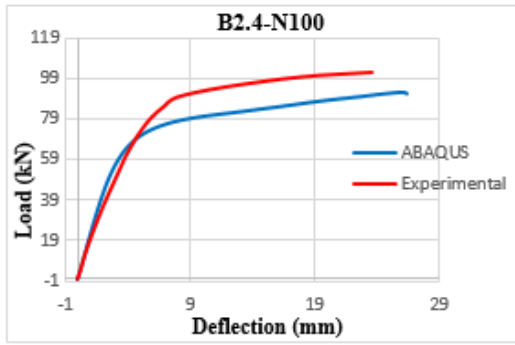


Figure 21. Comparison between experimental and ABAQUS load deflection behavior for 2 mm steel.



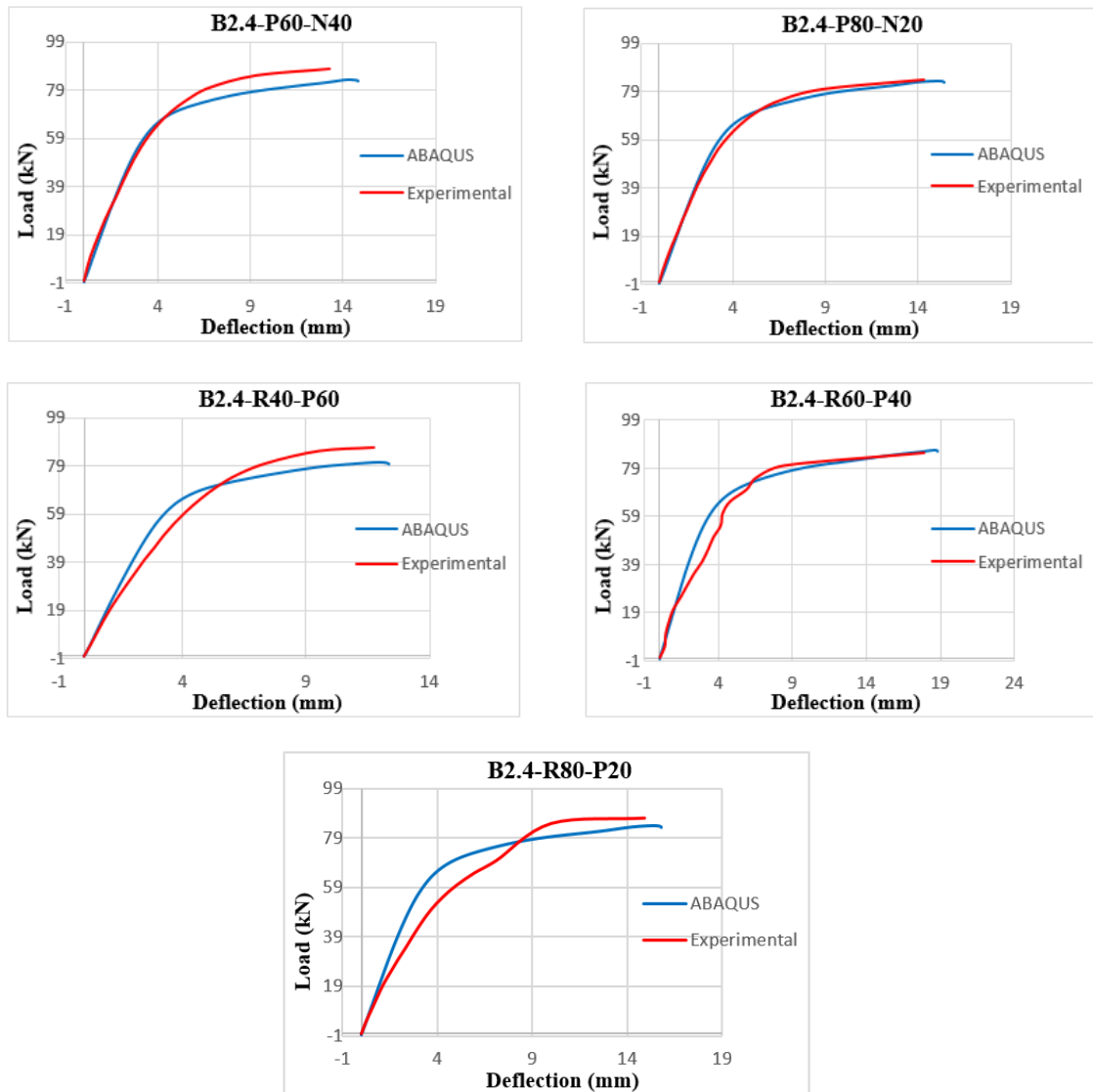


Figure 22. Comparison between experimental and ABAQUS load deflection behavior for 2.4 mm steel.

3.6. Discussion

In general, all composite columns filled with recycled concrete showed a reduction in capacity. For samples with 2 mm steel thickness, the moment capacities of the RACFST for RCA-NA, RAP-NA, and RCA-RAP were about (16 % to 24 %), (22 % to 25 %), and (13 % to 19 %) lower than the control specimen B2-N100, respectively. While for samples with 2.4 mm steel thickness, the moment capacities for RCA-NA, RAP-NA, and RCA-RAP were about (5 % to 15 %), (11 % to 21 %), and (15 % to 17 %) lower than the control specimen B2.4-N100, respectively. This reduction for RCA-NA could be attributed to the presence of old cement paste that requires higher water absorption. While for RAP-NA can be attributed to the presence of asphalt binder coating which weakens the bond between the aggregate and the concrete matrix. For RCA-RAP combination, the moment capacities were ranging between RCA-NA and RAP-NA combinations. This could be an indication that RCA-RAP could be a promising technique in replacing NA for future constructions.

Concrete filling enhanced the behavior and capacity of bare steel beams. For samples with 2 mm steel thickness, the moment capacity B2 was enhanced by about (45 % to 60 %), (44 % to 49 %), (54 % to 66 %), and 91 % for RCA-NA, RAP-NA, RCA-RAP, and the control beam B2-N100, respectively. While for samples with 2.4 mm steel thickness, the moment capacity of B2.4 was enhanced by about (31 % to 45 %), (22 % to 36 %), (27 % to 30 %), and 53 % for RCA-NA, RAP-NA, RCA-RAP, and the control beam B2.4-N100, respectively. It can be noticed that the enhancement of the moment capacity caused by the concrete filling decreases with the increase of the steel thickness used.

RA had a positive influence on the flexural behavior of all plain concrete beams. The capacity increased with the increase of RAP and decreased with the increase of RCA.

RA did not have a significant effect on the deflection behavior. RACFST developed similar moment deflection behavior as the control beams.

4. Conclusions

The flexural behavior of light-gauge steel filled with normal and recycled concrete was investigated in this study. Different coarse aggregate combinations were used: RCA-NA, RAP-NA, and RCA-RAP with different replacement levels. The following conclusions can be drawn from this study:

1. It is feasible to use RA of both types (RCA and RAP) in cold formed steel filled sections with low to medium compressive strength, as they gave promising results.
2. The flexural behavior of HSS beams filled with RAC is similar to the corresponding control samples that were filled with NA concrete at all loading stages.
3. All beams failed in a ductile manner and developed moments in excess of the theoretically predicted values. Buckling of steel sheets, cracking and separation of concrete from steel governed the failure of composite beams.
4. The ultimate capacity of RACFST decreased with the increase of the RA percentages. The optimum mixes were (20 %RCA+80 %NA), (20 %RAP+80 %NA), and (80 %RCA+20 %RAP) for RCA-NA, RAP-NA, and RCA-RAP combinations, respectively.
5. Concrete infill enhanced the capacity of HSS beams. Moreover, concrete filling provides more rigidity to hollow steel beams and enhances their ability to resist buckling as well.
6. All beams developed similar moment-deflection behavior until they reached the code predicted ultimate moments, then, exhibited a slight change in the moment-deflection behavior up to failure.
7. The RA of both types had a good influence on the flexural behavior of plain concrete beams, the capacity decreases with the increase of RCA percentages and increases with the increase of RAP percentages. The optimum mixes were reported to be (20 %RCA+80 %NA), (60 %RAP+40 %NA), and (20 %RCA+80 %RAP) for RCA-NA, RAP-NA, and RCA-RAP combinations, respectively.
8. The loading capacities of RACFST can be conservatively predicted by the current code provisions of EC4, AISC-LRFD, AIJ, and the RPT recommendations, as the AISC-LRFD and AIJ codes significantly underestimated the moment capacity of RACFST while the RPT gives the best prediction of the test results than other methods with a COV value of 0.0682 and 0.0526 for composite beams made with 2- and 2.4-mm steel sheets, respectively.
9. Based on AISC-LRFD and AIJ code provisions, when a composite member is subjected to a pure flexural load, the predicted moment capacity depends only on the steel section, and thus it will be conservative no matter what type of aggregates is used.
10. FEA results showed reasonable agreement and high degree of similarity with the experimental results, however, there were several differences between FEA and experimental results. Numerical results proved that ABAQUS software is effective and predicts the ultimate capacity of concrete filled tubes with acceptable accuracy.

5. Acknowledgements

The authors would like to thank Deanship of Academic Research at The University of Jordan for their financial support to perform this research.

References

1. Corinaldesi, V. Mechanical and elastic behaviour of concretes made of recycled-concrete coarse aggregates. *Constr. Build. Mater.* 2010. Vol. 24. No. 9. Pp. 1616–1620.
2. Etxeberria, M., Vázquez, E., Marí, A., Barra, M. Influence of amount of recycled coarse aggregates and production process on properties of recycled aggregate concrete. *Cem. Concr. Res.* 2007. Vol. 37. No. 5. Pp. 735–742.
3. Rahal, K. Mechanical properties of concrete with recycled coarse aggregate. *Mechanical properties of concrete with recycled coarse aggregate.* 2007. Vol. 42. No. January. Pp. 407–415.
4. Shatarat, N.K., Katkhuda, H.N., Hyari, K.H., Asi, I. Effect of using recycled coarse aggregate and recycled asphalt pavement on the properties of pervious concrete. *Struct. Eng. Mech.* 2018. Vol. 67. No. 3. Pp. 283–290.
5. Al-Tarawneh, K.L. Flexural Performance of Reinforced Concrete Beams Made with Two Types of Coarse Recycled Aggregates. RCA AND RAP. Unpublished Master's Thesis, The University of Jordan, Amman, Jordan, 2018.

6. Katkhuda, H.I., Shatarat, N. Shear behavior of reinforced concrete beams using treated recycled concrete aggregate. *Constr. Build. Mater.* 2016. Vol. 125. Pp. 63–71.
7. Knaack, A.M., Kurama, Y.C. Behavior of reinforced concrete beams with recycled concrete coarse aggregates. *J. Struct. Eng. (United States)*. 2015. Vol. 141. No. 3.
8. Shatarat, N., Alhaq, A.A., Katkhuda, H., Jaber, M.A. Investigation of axial compressive behavior of reinforced concrete columns using Recycled Coarse Aggregate and Recycled Asphalt Pavement aggregate. *Constr. Build. Mater.* 2019. Vol. 217. No. May. Pp. 384–393.
9. Huang, B., Shu, X., Burdette, E.G. Mechanical properties of concrete containing recycled asphalt pavements. *Magazine of Concrete Research*. 2006. Vol. 58. No. 5. Pp. 313–320
10. Larbi, R., Morsli, M., Bali, A., Benyoussef, E.-H. Mechanical and elastic properties of concretes made with recycled asphalt. *International Journal of Advances in Mechanical and Civil Engineering*. 2017. Vol. 4. No. 3.
11. Okafor, F.O. Performance of recycled asphalt pavement as coarse aggregate in concrete. *Leonardo Electron. J. Pract. Technol.* 2010. Vol. 9. No. 17. Pp. 47–58.
12. Hunaiti, Y.M. Strength of composite sections with foamed and lightweight aggregate concrete *J. Mater. Civ. Eng.* 1997. Vol. 9. No. 2. Pp. 58–61.
13. Nakamura, S.-i., Morishita, H. Bending strength of concrete-filled narrow-width steel box girder. *J. Constr. Steel Res.* 2008. Vol. 64. No. 1. Pp. 128–133.
14. Soundararajan, A., Shanmugasundaram, K. Flexural behaviour of concrete-filled steel hollow sections beams. *J. Civ. Eng. Manag.* 2008. Vol. 14. No. 2. Pp. 107–114.
15. Varma, A.H., Ricles, J.M., Sause, R., Lu, L.W. Experimental behavior of high strength square concrete-filled steel tube beam-columns. *J. Struct. Eng.* 2002. Vol. 128. No. 3. Pp. 309–318.
16. Yang, Y.F., Man, L.H. Compressive and flexural behaviour of recycled aggregate concrete filled steel tubes (RACFST) under short-term loadings. *Steel Compos. Struct.* 2006. Vol. 6. No. 3. Pp. 257–284.
17. Building Code Requirements for Structural Concrete (ACI 318-14) Commentary on Building Code Requirements for Structural Concrete (ACI 318R-14) An ACI Standard and Report from HIS. 2014.
18. Bulletin, A.C.I.E. Aggregates for Concrete ACI Education Bulletin E1-07. *Concr. Constr.* 2007. P. 29.
19. ASTM. ASTM C 127-08: Standard Test Method for Density, Relative Density (Specific Gravity), and Absorption of Fine Aggregate. 2008. Pp. 1–7.
20. ASTM. A370: Standard Test Methods and Definitions for Mechanical Testing of Steel Products. ASTM Int. 2014. Pp. 1–50.
21. Allouzi, R., Alkloub, A., Naghawi, H., Al-Ajarmeh, R. Fracture Modeling of Concrete in Plain and Reinforced Concrete Members. *Int. J. Civ. Eng.* 2019. Vol. 17. No. 7. Pp. 1029–1042.
22. Europeenne, N. EUROPEAN STANDARD Eurocode 4: Design of composite steel and concrete structures-Part 1-1: General rules and rules for buildings. 2004.
23. Load and resistance factor design specification for structural steel buildings. 1999.
24. AIJ (1997). Recommendations for design and construction of concrete filled steel tubular structures. Architectural Institute of Japan, Tokyo, Japan.
25. Valsa Ipe, T., Sharada Bai, H., Manjula Vani, K., Iqbal, M.M.Z. Flexural behavior of cold-formed steel concrete composite beams. *Steel Compos. Struct.* 2013. Vol. 14. No. 2. Pp. 105–120.
26. Jyothi, K.N., Valsa Ipe, T. Performance of Infilled Cold Formed Steel Channel Section Beams. *Int. J. Eng. Res.* 2015. Vol. V4. No. 12. Pp. 446–451.

Contacts:

Rola El-Nimri, rola.elnimri@gmail.com

Mu'tasim Abdel-Jaber, m.abduljaber@ju.edu.jo

Yasser Hunaiti, hunaiti@ju.edu.jo

Ma'en Abdel-Jaber, maen.abdel-jaber@htu.edu.jo

© El-Nimri, R., Abdel-Jaber, M.S., Hunaiti, Y.M., Abdel-Jaber, M., 2021



DOI: 10.34910/MCE.101.3

Poly(ethylene terephthalate) composite material with modified fly ash filler

N.M. Zaichenko*, **V.V. Nefedov**

Donbas National Academy of Civil Engineering and Architecture, Donetsk region, Ukraine

* E-mail: zaichenko_nikola@mail.ru

Keywords: poly(ethylene terephthalate) composite material, fly ash filler, crystallinity, modification, sulphuric acid, mechanical and physical properties.

Abstract. The effect of the fly ash (FA) filler modified by sulphuric acid on the mechanical and physical properties of poly(ethylene terephthalate) composite material (PCM) has been investigated. The results of the presented study can be formulated as follow. The element and oxide composition of original (as received) fly ash is affected by the modification of sulphuric acid of 5 % concentration. At the same time, the variations in the particle size distribution of filler can be observed. In particular, the modified FA filler has an increased content of fine particles. The XRD pattern of as received fly ash indicates the presence of both crystalline (25 %) and amorphous phases (75 %) while XRD pattern of FA after chemical modification points to the fact that the content of crystalline phase has been increased up to 40 % but the content of amorphous phase has been decreased up to 60 %. The results of mechanical and physical properties of PCM with various content of unmodified fly ash filler (55, 60, 65, 70, and 75 %) indicate that compressive and flexural strength tends to rise with increasing concentration from 55 to 65 percent. In the certain case when the fly ash filler is modified by sulphuric acid of 5 % concentration, the values of compressive and flexural strength of PCM at 65 % FA loading is higher than compared with PCM on the base of unmodified filler. The strength gain may be attributed to the increasing crystallinity in the recycled poly(ethylene terephthalate) (rPET) matrix of the composite material as the fly ash content is increased. The XRD, DTA/TGA data of pure rPET and PCM are in conformity with the results of mechanical and physical properties of PCM.

1. Introduction

Plastics have outgrown most manufactured materials and have long been under environmental scrutiny. However, robust global information, particularly about their end-of-life fate, is lacking. By identifying and synthesizing dispersed data on production, use, and end-of-life management of polymer resins, synthetic fibers, and additives, the authors [1] estimate that 8300 million metric tons (Mt) as of virgin plastics have been produced until 2017. As of 2015, approximately 6300 Mt of plastic waste had been generated, around 9 % of which had been recycled, 12 % had been incinerated, and 79 % had been accumulated in landfills or the natural environment. If current production and waste management trends continue, roughly 12,000 Mt of plastic waste will be in landfills or in the natural environment by 2050 [1]. For instance, waste PET plastic is neither environmentally biodegradable nor compostable, which creates disposal problems. Recycling has emerged as the most practical method to deal with this problem, especially with products such as PET beverage bottles [2]. PET recycling is one of the most successful and common examples of polymer recycle processing. In Russian Federation of the total volume of recycled PET, about 63 % falls on fibers and non-woven materials, the second largest consumer (about 17 %) is the manufacture of preforms for PET bottles; the third is the production of strapping and packaging materials – about 16 %, and the production of polymer composites and other materials – less than 1 % [3].

The negative environmental impact of the steadily increasing use of plastic and composite materials requires the development of new combinations of materials, possibly with improved properties, but with reduced environmental harm [4]. Thus, the questions of application of polymer composite materials, made with the use of technological and operational waste, in building structures are topical today [5]. There is growing trend towards the development of composites with low environmental impact and good commercial

Zaichenko, N.M., Nefedov, V.V. Poly(ethylene terephthalate) composite material with modified fly ash filler. Magazine of Civil Engineering. 2021. 101(1). Article No. 10103. DOI: 10.18720/MCE.101.3



This work is licensed under a [CC BY-NC 4.0](https://creativecommons.org/licenses/by-nc/4.0/)

viability. To achieve this goal, researchers implemented cost-effective processing methods and developed novel material systems involving low-cost fillers. One such material system is the so-called polymer concrete, which is often prepared by loading polyester resin with high levels of fillers such as fine sand, limestone or micro-marble particles [6, 7].

The use of fly ash of thermal power plants as a filler in polymer composite materials has recently attracted increased attention, especially in terms of cost / large stock ratio. It provides a number of advantages: it is the best way to recycle FA and, since it is cheap and abundantly available, it reduces the total cost of composites [8–11]. Fly ash has been used in polymer matrix composites, saving the other commonly used mineral fillers in polymers, thereby reducing the greenhouse emissions. Its applicability is widely studied in various building materials, but the scope of application is limited. As a result, FA is accumulated over the years in surrounding areas of thermal power plants and creates a huge environmental burden. In the Donbas region of Ukraine, more than 5 million m³ of ash and slag wastes are stored in ash dumps of thermal power plants.

Fly ash, being generated as a waste material, needs to be benefitted before its use as a filler in plastic materials. The main drawbacks of fly ash in comparison with commercial mineral fillers are its larger particle size and smooth spherical inert surface. The surface modification of fly ash can be achieved through two methods; the first is a chemical activation and the second is a mechanical activation. It is well known that FA has a surface polarity due to the presence of silanol, aluminol and other types of –OH groups attached to the metal/non-metal atoms of the constituents of FA. On the other hand, many of the commercial polymers do not have substantial polarity that can match with that of the FA particles [6, 7]. Therefore, building up interfaces based on electrostatic attraction is highly unlikely. It has been determined that fly ash with the surface activated by alkali treatment of sodium hydroxide solution proved to develop uniform interfaces in polymer composite material, with significant effect on the compression resistance and on impact [12]. According to [13] treatment of fly ash by sulphuric acid can obviously change the surface area, microstructure and phase composition. Besides, it has been reported that the surface silanol groups responsible for generating Brönsted acidity are enhanced [14]. The results of our recent investigation pointed out that treatment of fly ash filler by 5 % concentration solution of sulphuric acid to improve adhesion to the rPET polymeric matrix increases the overall properties of PCM, especially compressive strength and apparent density. The highest value of compressive strength of samples with unmodified fly ash filler had PCM with 65 % filler concentration. On the other hand, PCM samples with modified fly ash filler had the compressive strength value that is higher on 11.2 % [15].

It is a matter of common knowledge, that PET is a crystallisable thermoplastic polymer because of its regularity in chemical and geometric structures. It is either in the semi-crystalline or in the amorphous state [16, 17]. The degree of PET crystallinity is about 65–85 % [13]. Nucleating agents affect the crystallization of PET. Some studies have investigated the effect of the additives on crystallization behaviour. Talc, kaolin, silicon oxide, and titanium oxide have been used as fillers; they act as effective nucleating agents for PET. The overall rate of crystallization depends on the volume concentration, the size distribution, and the nucleating ability of the additives [18]. In turn, the levels of crystallinity and morphology significantly affect the properties of the polymers [19].

In a presence of inorganic filler, the crystallization conditions of polymers and, consequently, the general degree of crystallinity and the nature of supramolecular formations are changed. The factors which affecting the properties of crystalline polymers in the absence of filler also determine the mechanical behaviour of filled crystalline polymers. It should be borne in mind that the filler is often incorporated into the polymer precisely with the aim of influencing the nature of crystallization and structure formation and, thus, its mechanical properties [20]. For instance, the crystalline morphology and the crystallization behaviour of PET in the PET/SiO₂ composites were affected significantly by the SiO₂ inorganic nanoparticles [21]. According to [12] the incorporation of fly ash (0.25 % by mass) into PET polymer matrix increases the crystallinity of the composite by 24 % compared to the original polymer sample. The results of the investigation [22] indicate that both nano-CaCO₃ and ultra-fine talc exhibited heterogeneous nucleation effect on the crystallization of poly(trimethylene terephthalate) (PTT) composite, and more significant nucleation effect was observed in PTT/nano-CaCO₃ composite due to the smaller size and better dispersion of nano-CaCO₃ in PTT matrix. Mechanical properties study suggested that the incorporation of nano-CaCO₃ and ultra-fine talc greatly improved the tensile and flexural properties of PTT composite.

In another study [21] the authors have reported that attributed to the formation of Si–O–Ti bonds in the PET matrix, the crystalline morphology and the crystallization behaviour of the PET in PET/SiO₂/TiO₂ composites were affected significantly by the SiO₂ and TiO₂ inorganic nanoparticles (content of filler 5.49, 10.07, and 13.05 wt. %). At the same time, no quantitative data regarding PCM with high level (more than 50 wt. %) of mineral filler, in particular fly ash chemically modified by sulphuric acid, have previously been reported. Therefore the aim of this study is to investigate the mechanical (compressive and flexural strength) and physical (apparent density, water absorption) properties of poly(ethylene terephthalate) composite material filled with high level content of fly ash (55–75 wt. %) in original (as received) and chemically modified state. Besides, it is necessary to take into account and to investigate the influence of fly ash filler on the polymer crystallization characteristics in accordance with XRD and DTA/TGA data of pure rPET and PCM.

2. Materials and methods

2.1. Materials and methods

Class F (according to ASTM C-618) fly ash used in this study was collected from the thermal power plant of Donetsk region (Ukraine). The particle size distribution of fly ash was determined by the ANALYSETTE 22 Compact laser diffraction particle size analyser. The particle size of as received fly ash lies mainly in the range of 5–10, 10–20, 20–30, and 30–40 μm . The material has the specific surface area of 320 m^2/kg and bulk density of 1156 kg/m^3 . The composition of elements and oxides was determined by wavelength dispersive X-ray fluorescence method (ARL OPTIM'X 200W spectrometer). The main constituents are silica, alumina and ferric oxides of 57.19, 25.05, and 8.94 %, respectively, while traces of other oxides (K_2O 3.09 %, CaO 1.79 %, MgO 1.45 %, TiO_2 1.05 %, Na_2O 0.68 %, P_2O_5 0.27 %, and SO_3 0.18 %) were also detected.

PET bottles were as the raw material for manufacturing the rPCM matrix. PET bottles were prepared for processing by washing in warm water, removing caps and shredding into approximately 3–5 mm-size flakes using a knife crusher.

Diffraction studies of fly ash samples were conducted with the help of 26 ARL X'TRA X-ray diffractometer (ARL, Switzerland) using $\text{CuK}\alpha$ radiation ($\lambda = 1.54056 \text{ \AA}$) at a voltage of 40 kV and a current of 20 mA. The scanning was carried in 4 to 70 degrees 2-theta range with a step of 0.02 degrees. X-ray phase studies of the rPET and PCM samples were performed on the X-ray diffractometer DRON-4-07 installation. The diffraction pattern was recorded at a wavelength of $\lambda = 1.54178 \text{ \AA}$ in a step-by-step mode ($2\theta = 10\text{--}80^\circ$ with a step of 0.1° and exposure time of 5 s) at 27 kV, 15 mA. PCM samples were prepared with different content of fly ash filler (55–75 wt. %).

Thermal analysis of the pure rPET and PCM samples using methods of thermogravimetric (TGA) and differential thermal analysis (DTA) (SETARAM Labsys DTA/TGA/DSC) in the temperature range 50–500 $^\circ\text{C}$ was carried out. Based on the analysis of the TGA-DTA curves, the temperatures of glass transition, melting and destruction of the rPET and PCM samples were determined and the influence of the filler addition on the thermal properties was analysed.

Compressive strength of the PCM samples was tested according to ASTM D 695 "Standard Test Method for Compressive Properties of Rigid Plastics" using servo-hydraulic system ADVANTEST 9. Compressive properties were checked at speed of 1.5 mm/min. Load cell of 5 kN was used to sense the load. Five specimens (12.7×12.7×25.4 mm prism) of each formulation were tested and their average value was calculated. Flexural strength of the PCM samples was tested according to ASTM D 790 "Standard Test Methods for Flexural Properties of Unreinforced and Reinforced Plastics and Electrical Insulating Materials" (procedure A, a strain rate of 0.01 mm/min, 127×12.7×3.2 mm molding bars of rectangular cross section). Apparent density and water absorption of the PCM samples were tested according to ASTM D 792 "Standard Test Methods for Density and Specific Gravity (Relative Density) of Plastics by Displacement" and D 570 "Standard Test Method for Water Absorption of Plastics", respectively.

2.2. Processing

Modifying the fly ash filler was achieved by acid-leaching method. Sulphuric acid (H_2SO_4) solution of 5, 10, and 15 % concentration was used for modification. A sample of fly ash filler was placed into the acid solution for about 1 hour then was dried to constant weight at a temperature of 105–110 $^\circ\text{C}$.

Melted recycled PET material and fly ash filler were mixed in a vessel to disperse fly ash particles in the polymer matrix. Samples of PCM were made by compression molding at a temperature of 255–285 $^\circ\text{C}$. After the molding process, the samples were cooled to solidify the melted rPET material to form a composite material having a matrix comprising rPET and dispersoids distributed in the matrix and comprising fly ash particles [2]. The PCM samples were prepared on the base of formulations with different content (55–75 wt. %) of unmodified (as received) and modified fly ash filler (Table 1).

Table 1. Formulations of PCM.

Formulation, %	FA		Concentration of sulphuric acid, %
	as received	modified	
1 – rPET : FA = 45 : 55	+	–	–
2 – rPET : FA = 40 : 60	+	–	–
3 – rPET : FA = 35 : 65	+	–	–
4 – rPET : FA = 30 : 70	+	–	–
5 – rPET : FA = 25 : 75	+	–	–
6 – rPET : FA = 35 : 65	–	+	5
7 – rPET : FA = 35 : 65	–	+	10
8 – rPET : FA = 35 : 65	–	+	15

3. Results and Discussion

3.1. Physical properties and oxide composition of modified fly ash

The characteristics (element and oxide composition) of original (as received) and modified FA samples are displayed in Table 2 that indicates decreasing content of the major oxides (silica, alumina, and ferric) after the treatment of fly ash by sulphuric acid of 5 % concentration. At the same time, one can see the presence of significant increment in SO₃ concentration. The authors of the investigation [14] had reported that chemical activation of fly ash by 5M concentration of various acids (HCl, HNO₃, H₂SO₄, and HClO₄) resulted in changing element and oxide composition as well as in increasing specific surface area of material. The highest effect had been reached when sulphuric acid was used as a modifying agent.

Related investigations of the effect of activation and modification on the microstructure and element composition of fly ash and related results have been performed by Qiu, M., Wang, Y., Niu, M. et al. [13]. They believed that a corresponding chemical reaction of free inorganic composition of FA with acid was occurred; consequently, fly ash particles acted out the inherent surface hole. Besides, acid damaged aluminosilicate vitreous structure of particles surface and led to the Si–O and Al–O bond tetrahedron structure flabby and fractured with soluble SiO₂ and Al₂O₃ increasing and forming new cavities, thereby the specific surface area of fly ash was increased [13].

In this investigation, we established that chemical modification of FA by sulphuric acid brought the variations in the particle size distribution of filler. It was determined with the help of laser diffraction particle size analyser (Fig. 1). It can be seen that modified FA has an increased content of fine particles. The fineness of tested FA samples is represented by the particles with maximum (d₉₈%) and median (d₅₀%) size of 139.15 and 27.66 μm (unmodified FA), 84.79 and 18.55 μm (modified FA), respectively. Besides, the content of the particles less than 2 μm is 8.71 % (modified FA) as compared with 5.86 % (as received FA).

Table 2. Element and oxide composition of the fly ash used.

Element	Content, %		Oxide	Content, %	
	as received FA	modified FA		as received FA	modified FA
Si	26.74	23.73	SiO ₂	57.19	50.76
Al	13.26	11.03	Al ₂ O ₃	25.05	20.85
Fe	6.25	5.88	Fe ₂ O ₃	8.94	8.41
K	2.57	2.47	K ₂ O	3.09	2.97
Ca	1.28	1.16	CaO	1.79	1.62
Mg	0.876	0.670	MgO	1.45	1.11
Ti	0.632	0.604	TiO ₂	1.05	1.01
Na	0.501	0.357	Na ₂ O	0.676	0.482
P	0.118	0.123	P ₂ O ₅	0.270	0.282
S	0.072	4.890	SO ₃	0.180	12.22

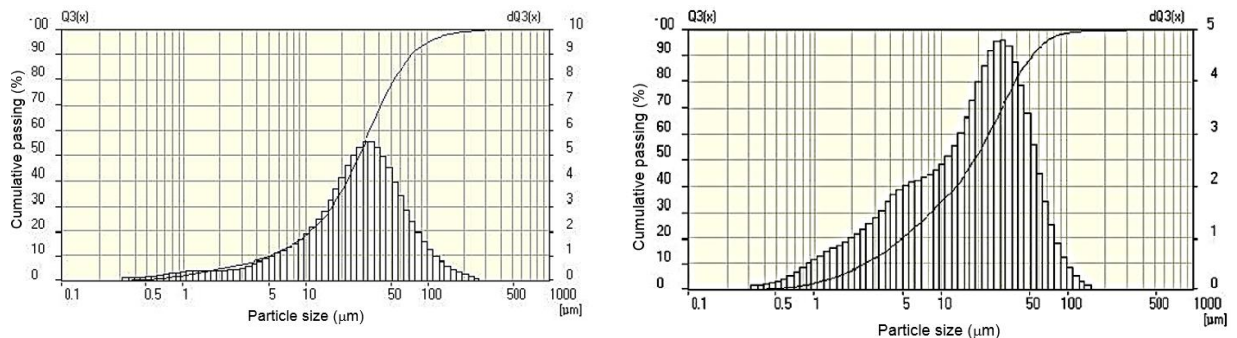
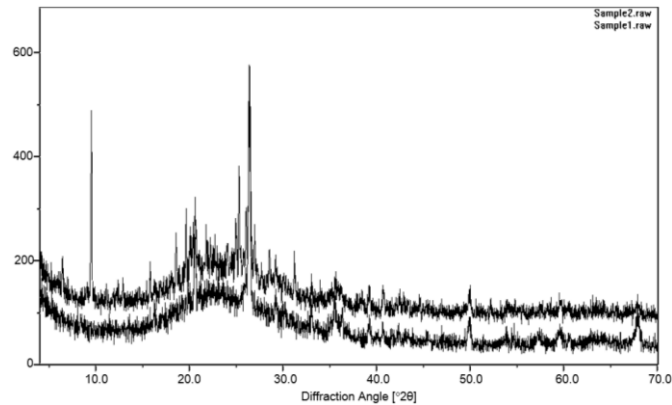


Figure 1. Integral and differential particle size distribution of as received fly ash (left) and modified fly ash (right).

The XRD patterns of as received fly ash shown in Fig. 2 indicate the presence of both crystalline (25 %) and amorphous phases (75 %). The main phases are quartz SiO₂ (19.6 %), hematite α-Fe₂O₃ (5.4 %), and amorphous substance (75.0 %). The diffraction peaks of 2θ°: 20.94° (*d*-spacing 0.424 nm), 26.67° (*d* = 0.334 nm), 36.65° (*d* = 0.245 nm), 50.29° (*d* = 0.181 nm), and 68.31° (*d* = 0.137 nm) all belong to the main characteristic peaks of quartz. Hematite is represented by diffraction reflections of 2θ°: 33.23°

($d = 0.269$ nm), 35.70° ($d = 0.251$ nm), 40.93° ($d = 0.220$ nm), and 54.16° ($d = 0.169$ nm). The broad halo over the range $15\text{--}35^\circ$ implies the presence of amorphous phase with crystalline inclusions of quartz.



**Figure 2. XRD patterns of fly ash filler:
sample 1 – FA as received; sample 2 – FA modified by sulphuric acid.**

XRD pattern of FA after chemical modification (Fig. 2) points to the fact that the content of crystalline phase has been increased up to 40 % while the content of amorphous phase has been decreased up to 60 %. In comparison with the unmodified sample the main crystalline phases are represented by the weaker diffraction peaks of quartz SiO_2 (11.8 % content) and hematite $\alpha\text{-Fe}_2\text{O}_3$ (3.3 %). On the other hand, some new substances in the crystalline state have been detected. They are: magnetite Fe_3O_4 (8.7 %) – diffraction peaks of 2θ : 18.24° ($d = 0.486$ nm), 30.06° ($d = 0.297$ nm), gypsum (calcium sulphate) $\text{CaSO}_4 \cdot 2\text{H}_2\text{O}$ (8.1 %) – 2θ : 9.9° ($d = 0.756$ nm), 29.17° ($d = 0.306$ nm), 31.9° ($d = 0.280$ nm), and alunogen $\text{Al}_2(\text{SO}_4)_3 \cdot 17\text{H}_2\text{O}$ (8.1 %) – 2θ : 6.1° ($d = 0.145$ nm), 19.6° ($d = 0.453$ nm), 24.7° ($d = 0.360$ nm).

3.2. Mechanical and physical properties of PCM

The polymeric composite materials based on recycled PET and fly ash filler are low-cost materials that can be used in various building products, for indoor and outdoor applications like pavement slabs, roof tile, insulating wall, etc. Their particular application depends mainly on the physical and mechanical properties [12]. The compressive strength results are shown in Fig. 3. It can be seen that compressive strength tends to increase from 57.7 to 73.3 MPa with increasing concentration of unmodified fly ash from 55 to 65 percent. For comparison, the compressive strength value of virgin rPET sample is 55.8 MPa. The strength gain may be attributed to the increasing crystallinity in the rPET matrix of the composite material as the fly ash content is increased. During molding the fly ash filler is believed to act as a thermal insulator. This reduces the cooling rate and increases the crystallinity of the rPET material by allowing the rPET molecules to arrange themselves in an ordered pattern. Besides, the fly ash particle causes the crack to propagate around the particle, which increases the stress (energy) required to produce an equivalent crack length in contrast to the stress (energy) required with no fly ash particles present in the matrix [2]. However, when the fly ash filler content is beyond 65 % (from 70 to 75 %) compressive strength is decreased. Probably, the reason has to do with poor dispersion and homogenization of filler in the polymeric matrix at higher concentration, as well as decreased interfacial bonding. Thereby an effective total surface area for responding the applied stress is reduced. Besides, it is necessary to take into account the fact that in case of sufficiently thin layers of polymer between filler particles, the crystallization process is inhibited, and crystallization may not occur [20].

In the certain case when the fly ash filler is modified by sulphuric acid of 5 % concentration, the value of compressive strength of PCM sample at 65 % FA loading is higher on 18.9 percent (87.2 MPa) as compared with PCM sample on the base of unmodified filler. This result may come from the fact that modifying the surface of FA filler by sulphuric acid tends to strengthen acid-basic adhesion interactions between PCM components. In support of this interpretation, one can argue determined in our previous study [15] that the thermodynamic work of adhesion between rPET polymer and fly ash surface modified by 5 and 10 % concentration H_2SO_4 was increased on 1.29 and 2.14 %, respectively. However, the values of compressive strength of PCM samples containing 65 % of fly ash filler treated by sulphuric acid of 10 and 15 % concentration are well below the values of compressive strength of PCM samples containing 65 % of fly ash filler treated by sulphuric acid of 5 % concentration despite the higher thermodynamic work of adhesion. It is presumably because of the increased weak sulphuric formations (SO_3) on the FA surface after acid treatment that impedes the adhesion contact of components.

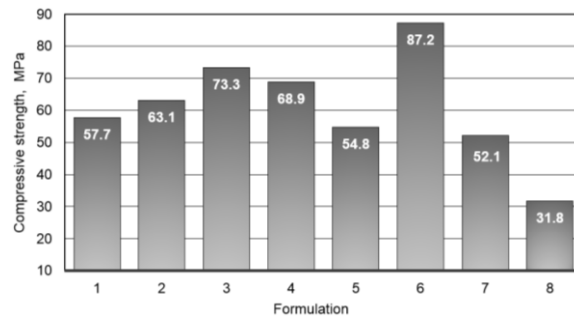


Figure 3. Compressive strength of PCM samples.

Flexural strength as well as compressive strength of PCM can be found to increase as the percent loading of fly ash is increased from 55 to 65 % (Fig. 4). For comparison, the flexural strength value of virgin rPET sample is 51.7 MPa. Thus, a relatively low content of FA 55–60 % does not provide the values of flexural strength compared to the virgin rPET sample. The optimal FA loading is 65 %, probably it is due to good dispersion of filler into polymer matrix and hence due to increasing the total area for deformation stress. However, beyond this value, the flexural strength decreases.

In the certain case when the fly ash filler is modified by sulphuric acid of 5 % concentration, the value of flexural strength of PCM sample at 65 % FA loading is higher on 5.1 percent (66.3 MPa) in comparison with PCM sample on the base of unmodified filler. It is also noteworthy, that flexural strength of PCM samples with FA modified by sulphuric acid of 10 and 15 % concentration is dramatically decreased.

It has been determined that the higher concentration of the fly ash in the PCM the higher the values of apparent density and the lower values of water absorption. This corresponds to the S. Anandhan's obtained data [23]. The values of apparent density and water absorption of the PCM samples with content of fly ash 65 % (treated by 5 % concentration H_2SO_4) are 1722 kg/m^3 and 0.19 %, respectively. For comparison, these values for the virgin rPET are 1410 kg/m^3 and 0.31 %, respectively.

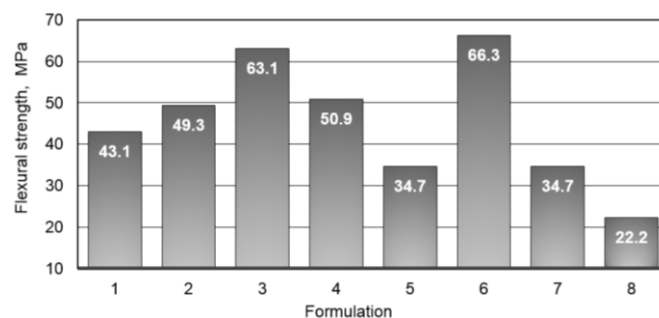


Figure 4. Flexural strength of PCM samples.

3.3. Phase analysis of pure rPET and PCM

Poly(ethylene terephthalate) is a semi-crystalline thermoplastic resin that in accordance with [21] is characterized by three intense Bragg diffraction peaks occurring at $2\theta = 17.5^\circ$, 23.1° , and 26.1° corresponded to (010), (110) and (100) lattice planes of triclinic crystal of PET. The broad peak $2\theta = 23.0^\circ$ points up the presence of an amorphous phase [24]. X-ray diffraction pattern of the pure rPET sample obtained is shown in Fig. 5. There are six characteristics intense peaks [25] on the diffractogram – 26.1° ($d = 0.341 \text{ nm}$, $IR = 100 \%$), 22.8° ($d = 0.389 \text{ nm}$, $IR = 81.8 \%$), 17.5° ($d = 0.506 \text{ nm}$, $IR = 79.9 \%$), 16.4° ($d = 0.540 \text{ nm}$, $IR = 79.8 \%$), 21.5° ($d = 0.413 \text{ nm}$, $IR = 78.4 \%$), 32.5° ($d = 0.275 \text{ nm}$, $IR = 48.4 \%$).

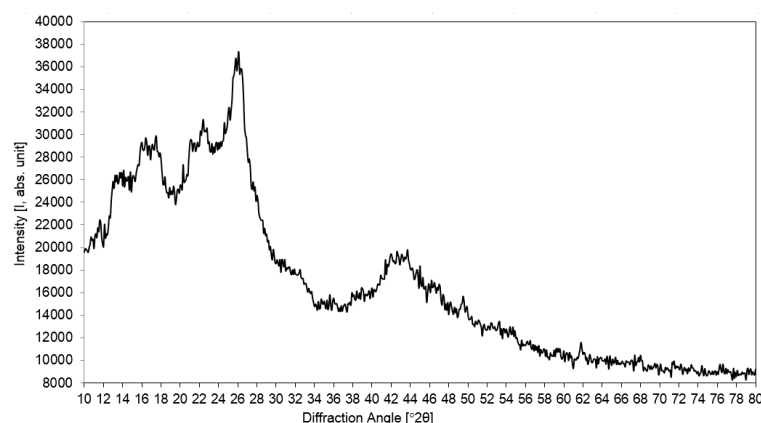


Figure 5. X-ray diffraction pattern of pure rPET.

Fig. 6 displays the XRD patterns of samples of PCM formulations 1, 3, 4, 6 (Table 2). By comparing the plots of the X-ray diffractograms of the fly ash (Fig. 2), pure rPET (Fig. 5) and the PCM samples (Fig. 6), it does not appear that the composite of the rPET matrix and the fly ash filler produced any new constituents. At the same time, it can be seen that the intensity of characteristic diffraction peaks of the rPET matrix is varied with the increment of the FA filler content. Setting the intensity of characteristic diffraction peaks of the PCM sample of formulation 1 (55 % FA content) at 100 %, the relative intensity of characteristic diffraction peaks of the PCM samples of formulations 3, 4 and 6 one can analyse in Table 3. It follows from these results that the intensity of characteristic diffraction peaks of the PCM sample of formulation 3 are higher in comparison with the sample of formulation 1. As mentioned above, fly ash filler is believed to act as a thermal insulator during molding. This reduces the cooling rate and increases the crystallinity of the rPET material by allowing the rPET molecules to arrange themselves in an ordered pattern. The highest values of relative intensity of diffraction peaks has the PCM sample of formulation 6 containing 65 % fly ash filler modified by sulphuric acid. On the other hand, when the content of FA filler is beyond 65 % the intensity of the diffraction peaks is the smallest among all the samples being investigated. Perhaps, in case of sufficiently thin layers of polymer between filler particles (high FA concentration) the crystallization process is inhibited. So, in our opinion it is clear that the XRD data are in conformity with the results of mechanical and physical properties of PCM.

3.4. Thermal analysis of the rPET and PCM samples

The thermal behaviour as well as the crystallization behaviour of the rPET and PCM samples has been characterized by the thermogravimetric (TGA) and differential thermal analysis (DTA). DTA/TG curves of thermal decomposition of pure rPET and PCM sample of formulation 6 (35 % rPET : 65 % the modified FA filler) are presented in Fig. 7 and Fig. 8, respectively. TG curves show that above 350 °C the mass is decreased by thermal decomposition.

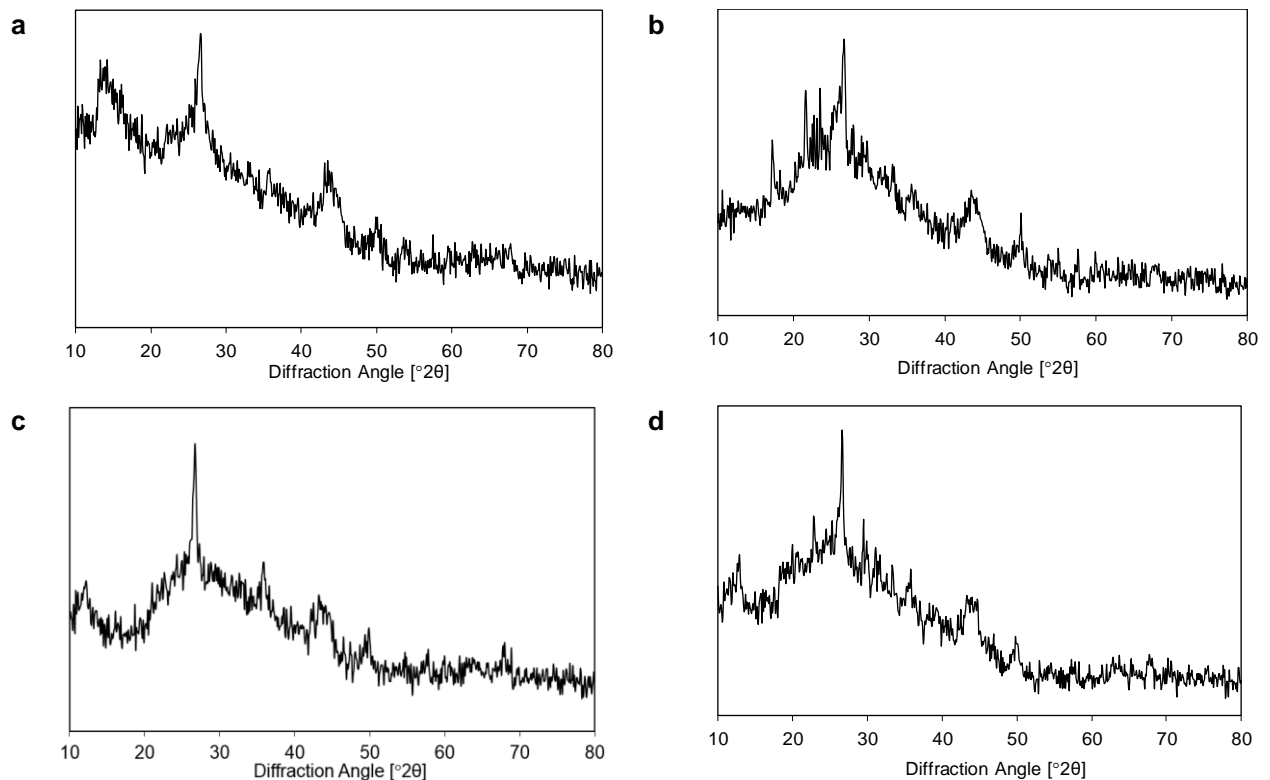


Figure 6. X-ray diffractograms of PCM:
a – 55 wt.% FA; b – 65 wt.% FA; c – 70 wt.% FA; d – 65 wt.% FA modified.

Table 3. The relative intensity of characteristic diffraction peaks of the PCM samples.

Formulation	Intensity of characteristic diffraction peaks, 2 theta, deg.											
	32.5		26.1		22.8		21.5		17.5		16.4	
	a.u.	%	a.u.	%	a.u.	%	a.u.	%	a.u.	%	a.u.	%
1 (Fig. 6 a)	13832	100	17136	100	15632	100	14912	100	16128	100	16376	100
3 (Fig. 6 b)	14440	104	17976	105	15864	101	16984	114	16184	100	16528	101
4 (Fig. 6 c)	14480	105	16656	97	14944	95.5	13989	94	12888	80	13228	81
6 (Fig. 6 d)	14960	108	18728	109	17352	111	17145	115	16376	101.5	14256	87

The value of mass loss comprises 35 and 33 % for pure rPET and PCM, respectively. In turn, DTA curves show a glass transition temperature T_g – 75 °C for pure rPET and 97 °C for PCM. In accordance with [18, 19] polymers with high crystallinity have a higher glass transition temperature T_g , higher modulus, toughness, stiffness, tensile strength, hardness and are more resistant to solvents, but have less impact strength. The rPET sample has an endotherm peak at 250 °C while the PCM one – at 251 °C.

It is well known that melting of pure PET happens in the range 225–260 °C with peak melting temperature at 255 °C [26, 27]. Broad exotherm with two peaks at 398 (rPET) and 417 °C (PCM) indicates a decomposition of polymer. Thus, the sample with fly ash filler has higher values of temperature of glass transition (97 > 75 °C), melting (251 > 250 °C) and decomposition (417 > 398 °C) in comparison with virgin rPET sample.

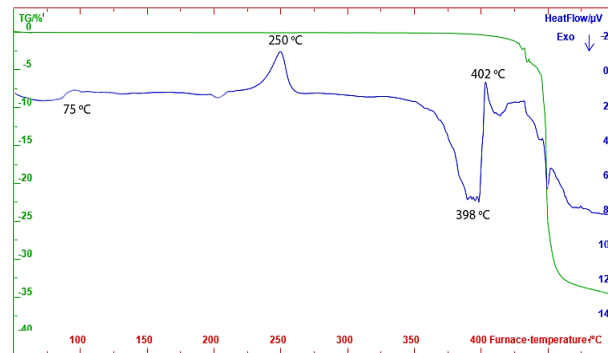


Figure 7. DTA/TG curves of rPET sample.

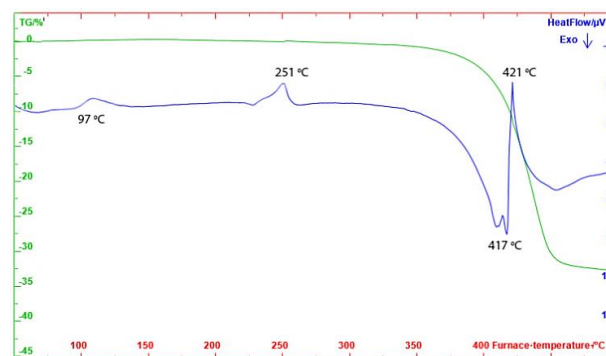


Figure 8. DTA/TG curves of PCM sample with 65 % fly ash concentration.

Effect of increasing temperature of glass transition and decomposition presumably stated because the filler particles drain thermal energy during PCM heating. A slight increase in the melting temperature of the PCM sample compared to the rPET sample indicates an increase in the degree of crystallinity due to the filler addition.

4. Conclusions

The properties of poly(ethylene terephthalate) composite material with the fly ash filler modified by sulphuric acid have been investigated. The results of the presented study can be formulated as follow:

1. The element and oxide composition of original (as received) fly ash is affected by the modification of sulphuric acid of 5 % concentration solution. It is displayed by decreasing content of the major oxides (silica, alumina, and ferric). At the same time, the presence of significant increment in SO_3 concentration can be seen. It is due to a corresponding chemical reaction of free inorganic composition of FA with acid, which damages aluminosilicate vitreous structure of particles surface and leads to the Si–O and Al–O bond tetrahedron structure flabby and fractured with soluble SiO_2 and Al_2O_3 increasing and forming new cavities. As a result, chemical modification of FA by sulphuric acid brings the variations in the particle size distribution of filler. In particular, the modified FA filler has an increased content of fine particles.

2. The XRD pattern of as received fly ash indicates the presence both of crystalline (25 %) and of amorphous phases (75 %). The main phases are quartz SiO_2 (19.6 %), hematite $\alpha\text{-Fe}_2\text{O}_3$ (5.4 %), and amorphous substance (75.0 %). On the other hand, XRD pattern of FA after chemical modification points to the fact that the content of crystalline phase has been increased up to 40 % while the content of amorphous phase has been decreased up to 60 %. In comparison with the unmodified sample the main crystalline phases are represented by the weaker diffraction peaks of quartz SiO_2 (11.8 %) and hematite $\alpha\text{-Fe}_2\text{O}_3$ (3.3 %).

Besides, some new substances in the crystalline state have been detected: magnetite Fe_3O_4 (8.7 %), gypsum (calcium sulphate) (8.1 %), and alunogen (8.1 %).

3. The results of mechanical and physical properties of PCM with various content of unmodified fly ash (55, 60, 65, 70, 75 %) filler indicate that compressive and flexural strength tends to increase from 57.7 to 73.3 MPa and from 43.1 to 63.1 MPa, respectively, with increasing concentration of FA from 55 to 65 percent. In the certain case when the fly ash filler is modified by sulphuric acid of 5 % concentration, the values of compressive and flexural strength of PCM sample at 65 % FA loading are higher on 18.9 percent (87.2 MPa) and on 5.1 % (66.3 MPa), respectively, as compared with PCM sample on the base of unmodified filler. The strength gain may be attributed to the increasing crystallinity in the rPET matrix of the composite material as the fly ash content is increased. Fly ash filler is believed to act as a thermal insulator during molding. This reduces the cooling rate and increases the crystallinity of the rPET material by allowing the rPET molecules to arrange themselves in an ordered pattern. The XRD, DTA/TGA data of pure rPET and PCM are in conformity with the results of mechanical and physical properties of PCM.

5. Acknowledgement

The authors appreciate the National Research Moscow State University of Civil Engineering (NRU MGSU) for providing the opportunity to carry out this research.

References

- Geyer, R., Jambeck, J.R., Law, K.L. Production, use, and fate of all plastics ever made. *Science Advances*. 2017. 3(7). e1700782. DOI: 10.1126/sciadv.1700782
- Li, Y., Peyton, R.L., White, D.J. Composite material composed of fly ash and waste polyethylene terephthalate. *Iowa State University Patents*. 2003. 66 p. URL: <http://lib.dr.iastate.edu/patents/66>
- Rzaev, K.V. Rossijskij ryok vtorichnoj pererabotki plastmass: sostoyanie, tendenczii, perspektivy [Russian market of plastic recycling: state, trends, prospects]. *Polimernye materialy. Izdeliya, oborudovanie, tekhnologii*. 2018. No. 8. Pp. 8–14. (rus)
- Chen, J.C., Wu, C.M., Pu, F.C., Chiu, C.H. Fabrication and mechanical properties of self-reinforced poly(ethylene terephthalate) composites. *eXPRESS Polym Letters*. 2011. 5(3). Pp. 228–237. DOI: 10.3144/expresspolymlett.2011.22
- Ogorodov, L.I., Lustina, O.V. Mechanical characteristics of polyethylene. *Magazine of Civil Engineering*. 2017. No. 6(74). Pp. 17–32. DOI: 10.18720/MCE.74.2
- Vakulenko, D.A., Turusov, R.A. Water resistance of polymer compounds. *Magazine of Civil Engineering*. 2017. No. 7(75). Pp. 106–113. DOI: 10.18720/MCE.75.10
- Ahmad, I., Mahanwar, P.A. Mechanical properties of fly ash filled high density polyethylene. *Journal of Minerals and Materials Characterization and Engineering*. 2010. 9(3). Pp. 183–198. DOI: 10.4236/jmmce.2010.93016
- Sahai, R.S.N., Mahanwar, P.A. Effect of particle size and concentration of fly ash on mechanical properties of polyphenylene oxide composites. *International Journal of Chemical, Environmental and Biological Sciences*. 2015. 3(2). Pp. 164–168.
- Sahai, R.S.N., Pawar, N. Studies on mechanical properties of fly ash filled PPO composite with coupling agent. *International Journal of Chemical, Environmental and Biological Sciences*. 2014. 2(4). Pp. 187–192.
- Kishore, Kulkarni, S., Sunil, D., Sharathchandra, S. Effect of surface treatment on the impact behaviour of fly-ash filled polymer composites. *Polymer International*. 2002. 51(12). Pp. 1378–1384. DOI: 10.1002/pi.1055
- Sreekanth, M.S., Bambole, V.A., Mhaske, S., Mahanwar, P. Effect of particle size and concentration of fly ash on properties of polyester thermoplastic elastomer composites. *Journal of Minerals and Materials Characterization and Engineering*. 2009. 8(3). Pp. 237–248. DOI: 10.4236/jmmce.2009.83021
- Duta, A., Cazan, C., Cosnita, M. Fly ash in optimized composites based on recycled plastics and rubber. *Proceedings of the World of Coal Ash (WOCA) Conference, Denver, CO, USA*. 2011.
- Qiu, M., Wang, Y., Niu, M., Han, Q., Zhang, M. Effects of activation and modification on the microstructure and composition of fly ash. *American Chemical Science Journal*. 2016. 14(4). Pp. 1–6. DOI: 10.9734/ACSJ/2016/26348
- Sharma, A., Srivastava, K., Devra, V., Rani, A. Modification in properties of fly ash through mechanical and chemical activation. *American Chemical Science*. 2012. 2(4). Pp. 177–187.
- Zaichenko, N., Nefedov, V. Composite material based on the polyethylene terephthalate polymer and modified fly ash filler. *MATEC Web of Conferences*. 2018. 245. 03007. DOI: 10.1051/mateconf/201824503007
- Baldenegro-Perez, L.A., Navarro-Rodriguez, D., Medellin-Rodriguez, F.J., et al. Molecular weight and crystallization temperature effects on poly(ethylene terephthalate) (PET) homopolymers, an isothermal crystallization analysis. *Polymers*. 2014. 6. Pp. 583–600. DOI: 10.3390/polym6020583
- Singh, D., Malik, H.K., Gupta, C.K., Singh, V. X-Ray diffraction studies for identification of polyethylene terephthalate fibres. *Indian Journal of Science and Technology*. 2017. 10(17). DOI: 10.17485/ijst/2017/v10i17/110232
- Demirel, B., Yaras, A., Elçiçek, H. Crystallization behavior of PET materials. *Balıkesir Üniversitesi Fen Bilimleri Enstitüsü Dergisi*. 2011. 13(1). Pp. 26–35.
- Groeninckx, G., Berghmans, H., Overbergh, N., Smets, G. Crystallization of poly(ethylene terephthalate) induced by inorganic compounds. I. Crystallization behavior from the glassy state in a low-temperature region. *Journal Polymer Science: Polymer Physics*. 1974. 12(2). Pp. 303–316. DOI: 10.1002/pol.1974.180120207
- Lipatov, Yu.S. *Fizicheskaya khimiya napolnennykh polimerov [Physical chemistry of filled polymers]*. M.: Khimiya, 1977. 304 p. (rus)
- Zhu, J., Xu, Q., Ren, Q., Liu, X. Study on the crystallization of poly(ethylene terephthalate)/ $\text{SiO}_2/\text{TiO}_2$ hybrid nanocomposites by sol-gel method. *Asian Journal of Chemistry*. 2013. 25(16). Pp. 9174–9178. DOI: 10.14233/ajchem.2013.15142
- Lin, Z., Mai, K. Effect of inorganic filler on the crystallization, mechanical properties and rheological behavior of poly(trimethylene terephthalate). *Polymer-Plastics Technology and Engineering*. 2007. 46(4). Pp. 417–420. DOI: 10.1080/03602550701244600

23. Anandhan, S. Recent trends in fly ash utilization in polymer composites. *International Journal of Waste Resources*. 2014. 4(3). 149. DOI: 10.4172/2252-5211.1000149
24. Bhat, N.V., Deshmukh, R.R. X-ray crystallographic studies of polymeric materials. *Indian Journal of Pure and Applied Physics*. 2002. 40(1). Pp. 361–366.
25. Mallick, B. X-ray diffraction analysis of polymeric solid using Bragg-Brentano geometry. *International Journal of Materials Chemistry and Physics*. 2015. 1(3). Pp. 265–270.
26. Wunderlich, B. *Thermal analysis of polymeric materials*. Springer-Verlag Berlin Heidelberg. 2005. 894 p. DOI: 10.1007/b137476
27. Mishra, D.D. Thermal analysis of polyethylene terephthalate (PET) – coke composites prepared by mechanical alloying technique. *Preprints*. 2016. 2016080099. DOI: 10.20944/preprints201608.0099.v1

Contacts:

Nikolai Zaichenko, zaichenko_nikola@mail.ru

Vladislav Nefedov, vlad.n1991@gmail.com

© Zaichenko, N.M., Nefedov, V.V., 2021



DOI: 10.34910/MCE.101.4

Sodium alginate emulsions for asphalt concrete modifiers encapsulating: structural rheological properties

S.S. Inozemtcev*, **E.V. Korolev**

National Research Moscow State Civil Engineering University, Moscow, Russia

* E-mail: inozemtsevss@mail.ru

Keywords: emulsion, sodium alginate, rheology, structure, encapsulation, self-healing, asphalt concrete, asphalt, pavement, durability.

Abstract. The ratio of components for the production of alginate emulsions are established, which can be used in the design of compositions for encapsulating various types of reducing agents. The high resistance of alginate emulsions to segregation corresponds to a structured system, the onset of the destruction of which is determined by the ratio O/A. The structure of stable alginate emulsions is characterized by an average particle size of the dispersed phase from 5 to 7 μm , the average distance between which is from 7 to 9 μm . The change in the particle size distribution of the dispersed phase occurs during the process of water evaporation from the alginate emulsion, which is explained by a decrease in the volume of the dispersion medium, the approach of the particles, their collision, compression, and pooling. An increase in particle diameter occurs on average by 28 % over 5 days, which is accompanied by an increase in viscosity by 4 times.

1. Introduction

The developing construction industry needs materials with unique properties that increase the functionality and reduce the resource consumption of structures during construction and operation. The creation of "smart" materials is a promising solution in the field of materials science, aimed at increasing the durability of structures [1–3]. The formation of their own internal impacts, which ensures the maintenance of structure parameters at the required level, is a key condition for classifying the material as "smart". "Reactions" of the material to a change in the structure parameters under the influence of operational factors of natural and/or artificial origin are provided at the material design stage. Materials, including asphalt concrete, with the ability to restore their own functionality in construction are a promising type of smart materials for pavement. This property of the material is usually called "self-healing" [3, 4].

The durability of asphalt concrete is inversely proportional to the speed and intensity of the course of destructive processes. Thus to increase the service life of the asphalt concrete pavement solutions are needed to ensure the duration of the state of the structure of asphalt concrete without defects due to giving it unique properties, independently restore the integrity of the composite and its ability to resist influencing factors.

Developments using encapsulated reducing agents are more common among technological solutions for the formation of this new operational property [5–12]. The encapsulated reducing agent is introduced into the asphalt mix in the form of capsules of various shapes made on the basis of polymer compounds formed during curing of the capsule [13–17].

The authors of [18] proposed a technologically simple method for producing capsules that can be used as part of an asphalt mix. An aqueous solution based on sodium alginate ($\text{C}_6\text{H}_7\text{O}_6\text{Na}$), which is the sodium salt of alginic acid extracted from brown algae, is used to encapsulate the reducing agent. The effectiveness of the use of calcium-alginate capsules is determined by the complex of physical-mechanical properties of the capsules and the technological properties of the emulsion for their production. The properties of alginate emulsions determine the capsule production rate, their size and the reducing agent content [19]. Therefore, the determination of the influences of prescription factors on the structure and properties of emulsions will make it possible to control the physical-mechanical properties of capsules. This will expand the list of reducing agents that can be encapsulated using alginate technology.

Inozemtcev, S.S., Korolev, E.V. Sodium alginate emulsions for asphalt concrete modifiers encapsulating: structural rheological properties. Magazine of Civil Engineering. 2021. 101(1). Article No. 10104. DOI: 10.18720/MCE.101.4



This work is licensed under a [CC BY-NC 4.0](https://creativecommons.org/licenses/by-nc/4.0/)

Sodium alginate is poorly wetted by water because the particles of alginate powder intensively stick together and form aggregates. Effective preparation of the emulsion using sodium alginate is achieved by high-speed mixing to destroy agglomerates [18]. During high-speed mixing sodium alginate interacts with water and forms a colloidal solution.

Capsules obtained by various methods have sizes from 10 μm to 3 mm. in which the encapsulated reducing agent is predominantly vegetable oils [20, 21, 24–27]. Industrial rejuvenator is an Alternative variant of the reducing agent, which is a mixture of low molecular weight compounds and oils [22–24, 27].

As a rule, the capsule shape is spherical or ellipsoidal, which facilitates their use in the process of mixing with other components of the asphalt mix [21, 22]. The technology has a significant drawback if the container for the reducing agent is fiber: premature destruction of the containers during mixing and during operation.

The highest content of the reducing agent in the capsules is achieved in the shells of calcium alginate, which is explained by the simplicity of the preparation technology and a wide range of variable dosages of the components.

It should be noted that bitumen has its own potential for self-healing, which depends on both physical and chemical properties. Self-healing of a binder in asphalt concrete occurs in the absence of a dynamic effect, which is aimed at restoring fatigue damage in the material. The degree of recovery is determined by the relaxation time [28].

Rejuvenators, organic oils with different molecular weights are used as a reducing agent by the authors of all the works reviewed. The mechanism of action of such a reducing agent in asphalt concrete is the dissolution of bitumen components aged during operation and local reduction of fragility. In bitumen self-healing occurs at the molecular level due to reversible hydrogen bonding with the formation of new cross-links and chains [28, 29] through ditopic and tritopic molecules [30]. In the case of oil-based oil rejuvenators these processes do not occur, therefore the effect of combining bitumen molecules is not observed. There is only a partial dilution of the components of bitumen in the rejuvenator, which contributes to reducing the potential for the development of a crack.

A search is needed for compounds that will provide a similar recovery mechanism to improve self-healing technology. However, it was established [31] that sunflower oil traditionally used as a reducing agent also has a structuring effect on the properties of the emulsion. Therefore, the reducing agent appears to be a mixture of a functional compound that provides a reduction mechanism and a structuring component (sunflower oil or similar) that provides stable emulsions for encapsulation. In this regard one of the important tasks of the technology of encapsulation of a reducing agent is to determine the maximum concentration of sunflower oil, which provides an emulsion with predetermined geometric characteristics and rheological properties.

2. Methods

An aqueous solution based on sodium alginate is used to prepare an alginate emulsion. Sodium alginate ($\text{C}_6\text{H}_7\text{O}_6\text{Na}$) is a sodium salt of alginic acid extracted from brown algae. A sunflower oil-based reducing agent has been used as an ordinary rejuvenator. The main properties of sunflower oil are presented in Table 1.

Table 1. The main properties of sunflower oil.

Parameter	Unit	Value	Method
Viscosity at 25 °C	Pa·s	0.05	–
Density at 25 °C	g/cm^3	0.918 ± 0.05	ISO 3675 ISO 3838
Acid value	mg KOH/g	0.025 ± 0.01	ISO 660
Fractional composition:			
palmitic acid	%	6.61	
stearic acid	%	3.61	
oleic acid	%	30.91	ISO 5508
linoleic acid	%	57.13	
other	%	1.74	

Samples of water emulsions with different contents of sodium alginate from 1.0 to 3.0 % and sunflower oil from 5 to 30 % were made to study the influence of prescription factors on the geometric parameters and rheological properties of alginate emulsions as well as to establish the intensity of the influence of sunflower oil on their structure formation.

Alginate emulsions were obtained by mixing sodium alginate and sunflower oil in water in various proportions and mixing for 2 minutes using an overhead stirrer with a drive rotation speed of at least 2000 rpm [32].

The dynamic viscosity and yield strength of the emulsion were determined using a MCR 101. Anton Paar rotational viscometer using a coaxial cylinder measuring system (Fig. 1). The outer cylinder was filled with an emulsion sample and the inner cylinder was lowered into the sample using an automatic drive. The sample was thermostated at 25 °C for 30 minutes before measurement. After that dynamic viscosity was determined at a constant shear rate of 50 s⁻¹. The viscosity value was calculated as the arithmetic average of 10 measurements under given conditions. At the next stage to determine the yield strength the shear stress was measured during the increase in the shear rate to 3500 s⁻¹. Yield strength was determined according to the scheme shown in Fig. 2. The arithmetic average of at least 3 measurements is the result of determining the viscosity and yield strength.

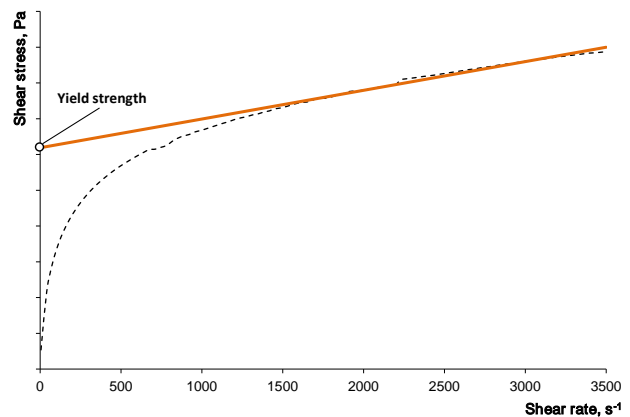
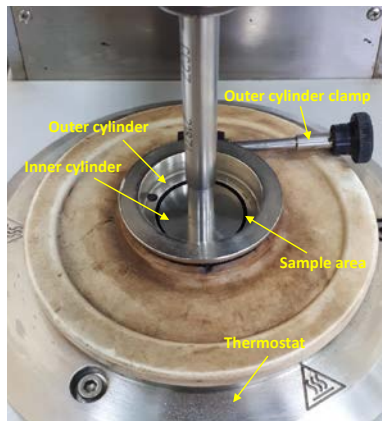


Figure 1. Coaxial cylinder measuring system. Figure 2. Yield strength determination scheme.

The structural parameters of alginate emulsions were studied using a Nikon Eclipse MA200 optical microscope using Thixomet software with calibrated electronic instruments and scales. The geometric parameters of the structure of alginate emulsions were measured at a zoom of 200 times.

Changes in the mass of alginate emulsion samples were measured every 24 hours for 18 days using electronic scales with an accuracy of 0.001 grams. Samples of alginate emulsions were stored in a beaker without a cover under natural conditions at a temperature of 24 ± 0.1 °C and air humidity of 50 %. The arithmetic average of at least 3 measurements is the result of determining the changes in the mass of alginate emulsion.

The selection of mathematical models of the dependence of changes in the properties of emulsions was carried out by the coefficient of determination coefficient, which is presented in Table 2.

Table 2. Coefficients of determination.

Parameter	Coefficient of determination R^2 for O/A ratio					Figure
	3.0	2.3	1.8	1.3	1.0	
Viscosity	0.98	0.96	0.95	0.94	0.93	3
Yield strength	1.00	1.00	1.00	0.97	0.94	5
Number of contacts	1.00	1.00	1.00	0.99	0.99	6
Changing O/A ratio			0.99			7
Start time of the destruction			0.99			9

The values recognized as an error in the measurement were not used in the calculation and the tests were repeated.

The results of statistical processing of viscosity data (standard deviation and coefficient of variation) are presented in Fig. 3.

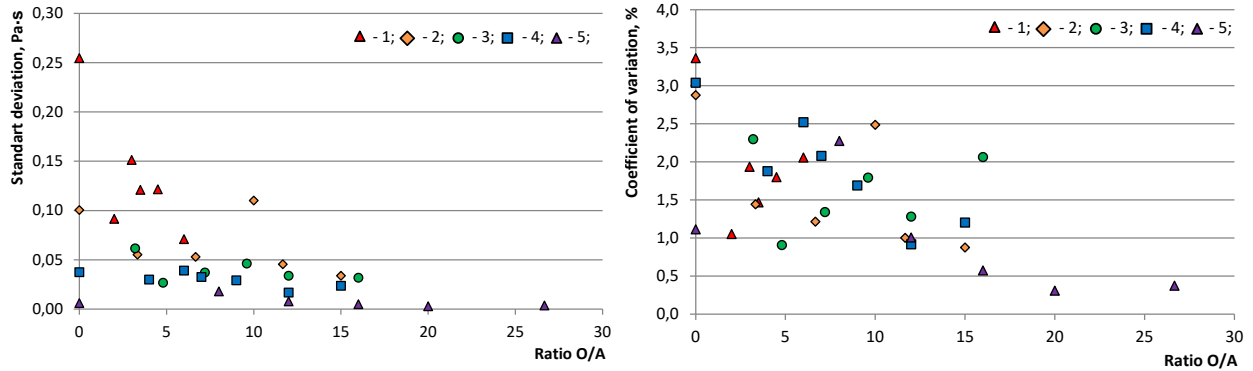


Figure 3. Results of statistical processing of viscosity data with the content of sodium alginate: 1 – 3.0 %; 2 – 2.3 %; 3 – 1.8 %; 4 – 1.3 %; 5 – 1.0 %.

It is obvious that standard deviation and coefficient of variation decrease slightly with a decrease in the content of sodium alginate and an increase in the content of reducing agent in the emulsion. This is due to the improvement of technological properties, which allows to obtain emulsions with greater uniformity. The results of statistical processing of yield stress data have a similar dependence of the change on the content of emulsion components.

The results of statistical processing of data on the particle diameter of the emulsion are presented in Table 3.

Table 3. Statistical analysis of data on the particle diameter of the emulsion.

Param.	Parameter value for O/A, μm														
	SA = 3.0 %			SA = 2.3 %			SA = 1.8 %			SA = 1.3 %			SA = 1.0 %		
	0.95	1.6	2.85	1.4	2.8	4.2	3.2	6.4	9.6	7.85	15.7	25.0	12.73	25.47	33.0
Min	2.1	2.0	2.0	1.8	0.9	1.7	2.0	2.1	1.8	2.1	1.9	2.1	2.1	2.1	2.8
Max	10.1	18.3	16.3	10.2	21.4	16.3	18.2	26.5	20.8	19.0	17.6	21.5	37.6	20.9	60.6
<i>R</i>	8.0	16.4	14.3	8.4	20.5	14.6	16.2	24.4	19.0	16.9	15.7	19.4	35.5	18.8	57.8
\bar{X}	4.8	5.4	7.0	5.0	5.6	6.5	5.9	6.6	7.6	7.4	6.9	8.5	14.0	8.6	12.4

Note: Param. is parameters; SA is sodium alginate content; Min is minimum sample value; Max is maximum sample value; *R* is sample range; \bar{X} is expected value.

The data sample size for measuring the particle diameter of the emulsion was at least 100 values.

3. Results and Discussion

The main technological property in accordance with the encapsulation technology, which ensures the formation of capsules with specified sizes and wall thickness, is the viscosity and yield strength of the emulsion. Determining the ability of alginate emulsions of different composition to resist the flow will allow establishing the presence of a structuring effect that sunflower oil has. The study of the effect of sunflower oil on viscosity was evaluated on the composition of emulsions with different contents of sodium alginate the results are shown in Fig. 4.

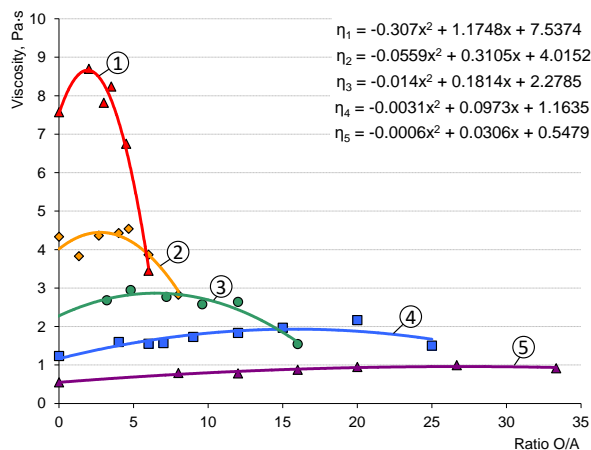


Figure 4. The dependence of the change in viscosity of emulsions on the ratio O/A (Oil content/Sodium alginate content) with the content of sodium alginate: 1 – 3.0 %; 2 – 2.3 %; 3 – 1.8 %; 4 – 1.3 %; 5 – 1.0 %.

It should be noted that the change in viscosity for emulsions with different contents of sodium alginate has extremum with the increase in the content of sunflower oil. It indicates the contribution of sunflower oil to the formation of the structure of the emulsion and its ability to resist flow. The concentration of sunflower oil the introduction of which ensures the maximum viscosity of the emulsion is equal to:

$$C_{oil} = C_{al} \frac{b}{2a}, \quad (1)$$

where C_{al} is the concentration of sodium alginate; a , b are the empirical coefficients of the equation $\eta(r) = -ar^2 + br + c$; r is the ratio of O/A.

According to the values of empirical coefficients $\eta(r) = f(r)$ presented in Fig. 3 the dependence

$$\frac{dC_{oil}}{dC_{al}} = \frac{40.5}{C_{al}^{2.5}}, \quad (2)$$

which clearly shows that the intensity of the sunflower oil structuring effect depends on the concentration of sodium alginate. From this dependence it follows that the decrease in the content of sodium alginate leads to the increase in the amount of sunflower oil necessary for maximum structural effect.

The extremum dependence of viscosity changes indicates the structural differences of emulsions with different component contents, which affect the ability to resist flow characterizing the manufacturability and efficiency of the process of obtaining capsules with a modifier.

The particle size distribution of emulsions with different contents of alginate and sunflower oil is shown in Fig. 5.

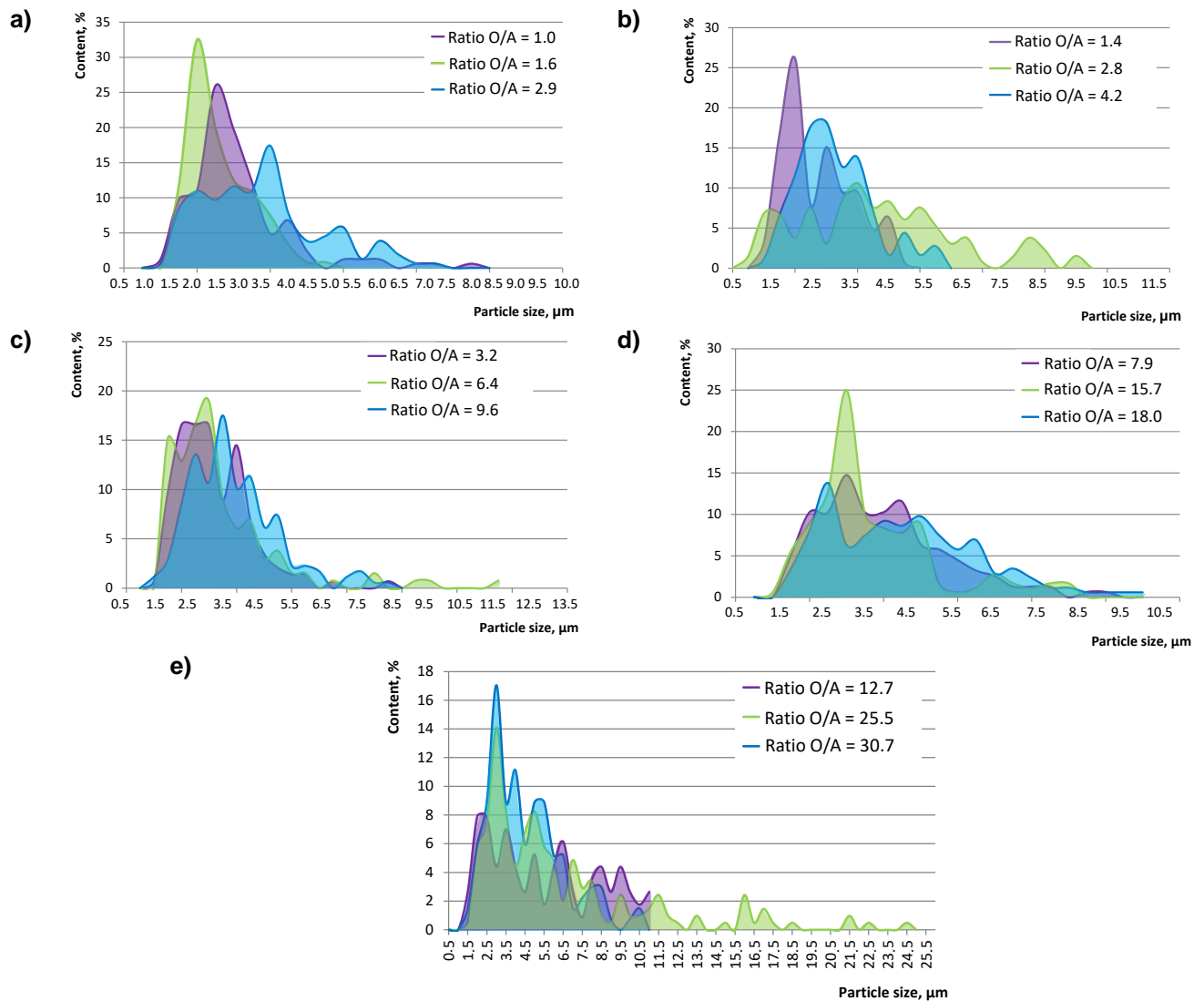


Figure 5. Particle size distribution of the dispersed phase in the emulsion with the content of sodium alginate: a) 3.0 %; b) 2.3 %; c) 1.8 %; d) 1.35 %; e) 1.0 %.

An analysis of particle size distribution of the dispersed phase in the emulsion shows that the average particle diameter increases with the increase in the O/A ratio and with the decrease in the total content of sodium alginate, which indicates a structuring effect. A detailed analysis of the particle size distribution of the ordinary emulsions and emulsions after aging is presented in Table 2. The number of contacts of the particles of the dispersed phase in the emulsion will be determined to take into account the obtained particle size distribution of its:

$$\chi = \sum_{i=1}^n \frac{C_i}{d_i^2}, \tag{3}$$

where d_i is the particle diameter of the i -th fraction, m; C_i is content of the i -th fraction; n is the number of fractions.

The results of calculating the number of contacts of dispersed phase particles in alginate emulsions are presented in Fig. 6.

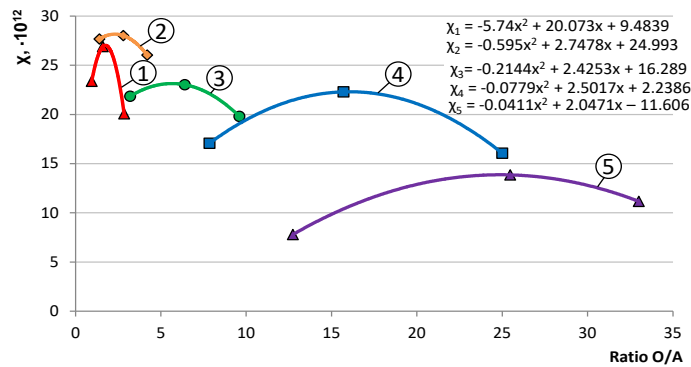


Figure 6. The dependence of the change in the number of contacts of the particles of the emulsion on the ratio O/A with the content of sodium alginate: 1 – 3.0 %; 2 – 2.3 %; 3 – 1.8 %; 4 – 1.3 %; 5 – 1.0 %.

Fig. 6 shows that the abscissas (ratios O/A) of the maxima for two groups of the indicated characteristics (viscosity and the number of contacts) are located quite close: as a rule, the maxima $\chi_i = f(O/A)$ are achieved at lower values of the ratio O/A. The general model of the interdependence of structural parameters and mechanical properties is the model of a homogeneous solid (solids with uniformly distributed bonds; for the emulsion at the first stage of analysis, this model is applicable) proposed by P.A. Rebinder [33, 34]. For the case under consideration (emulsion) the Rebinder model can be represented as:

$$\eta = k \cdot f_c \cdot \chi^n, \tag{4}$$

where f_c is the contact strength; k, n are constants (in the classical Rebinder formula $n = 2/3$).

The presented model demonstrates that the number of contacts, which in accordance with (3), nonlinearly depends on the particle diameter (particle size distribution of the dispersed phase of the emulsion) is a key factor affecting the rheological properties of the emulsion (viscosity, yield strength of the emulsion – Fig. 7).

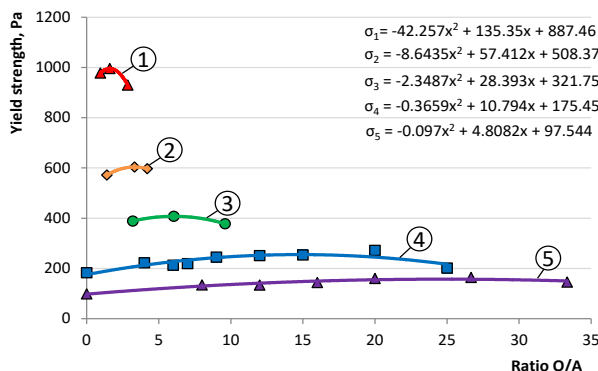


Figure 7. The dependence of the change in yield strength on the ratio O/A with the content of sodium alginate: 1 – 3.0 %; 2 – 2.3 %; 3 – 1.8 %; 4 – 1.3 %; 5 – 1.0 %.

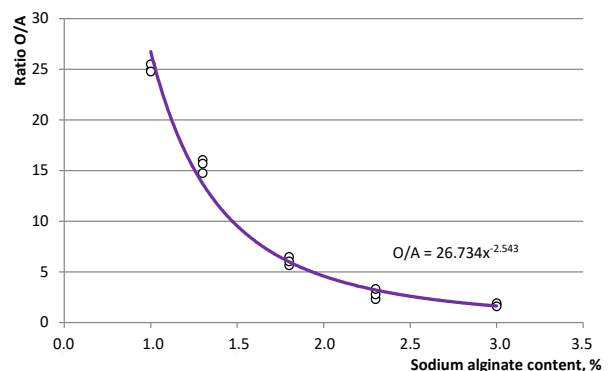


Figure 8. Dependence of changes in the ratio O/A on the content of sodium alginate for emulsions with maximum viscosity, yield strength, and the number of contacts.

An analysis of Fig. 4, Fig. 6 and Fig. 7 shows that the extremums in the graphs for the disperse systems under study with different contents of sodium alginate are observed at similar ratios O/A. It allows determining the dependence of the control parameter O/A on the content of sodium alginate for the development of encapsulation technology (Fig. 8), which is consistent with the following results [35]. From this figure the structuring function of sunflower oil is visible, which is a nonlinear dependence of its content on the amount of sodium alginate:

$$C_{oil} = \frac{26.734}{C_{al}^{1.543}} \quad (5)$$

The calculation of the curvature coefficient was carried out to analyze the obtained dependence (Fig. 9):

$$k = \frac{y'}{(1 + y'^2)^{3/2}}$$

where y' and y'' are the first and the second derivative, respectively.

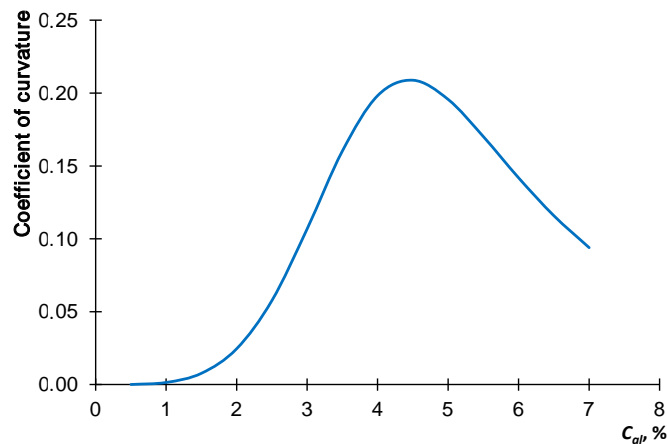


Figure 9. Curvature coefficient of the function (5).

Analysis (5) by standard methods shows that the coefficient of curvature of the function has a maximum at $C_{al} = 4.5\%$ indicating that the effect of the concentration of sodium alginate on the content of sunflower oil and its structuring effect is not significant. The resulting relationship indicates that the selected concentration of sodium alginate is correct.

The encapsulation process includes the step of dividing the alginate emulsion into individual particles and is a process with a fixed duration, which depends on the characteristics of the separatory funnels and the properties of the emulsions. Aqueous alginate emulsions and solutions obtained on their basis are unstable in time, since under natural conditions water evaporates (Fig. 10), which contributes to a change in the properties of the entire dispersed system.

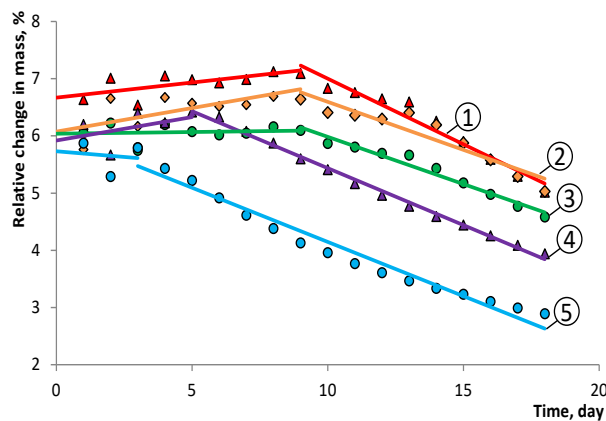


Figure 10. The dependence of the mass change of the samples of emulsions with the content of sodium alginate: 1 – 3.0 % (O/A=1.9); 2 – 2.3 % (O/A=2.8); 3 – 1.8 % (O/A=6.4); 4 – 1.5 % (O/A=9.4); 5 – 1.3 % (O/A=15.7).

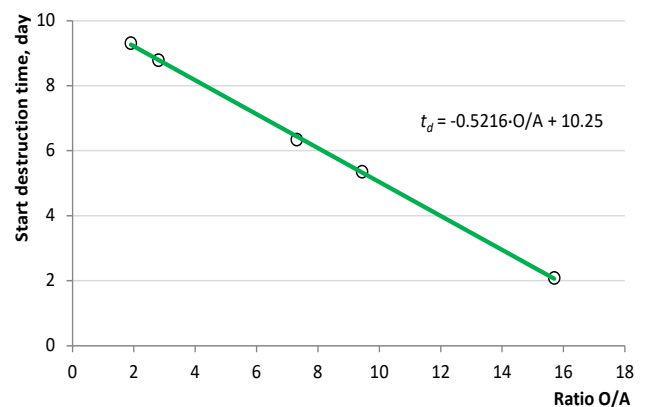


Figure 11. The dependence of the start time of the destruction of the emulsion on the ratio O/A.

The two main stages can be distinguished on the dependencies of the mass change of the emulsion samples over time, where at the initial stage a constant mass change is observed, which indicates the preservation of the dispersion system. The beginning of the next stage is the beginning of segregation and destruction of the emulsion, after which an oil film is formed on the surface of the sample and prevents further evaporation of moisture at the same rate. Water evaporation is slowed down more strongly in emulsions with lower sodium alginate content and a high O/A ratio, which indicates more intense destruction. The segregation stages in such emulsions begin earlier (Fig. 12).

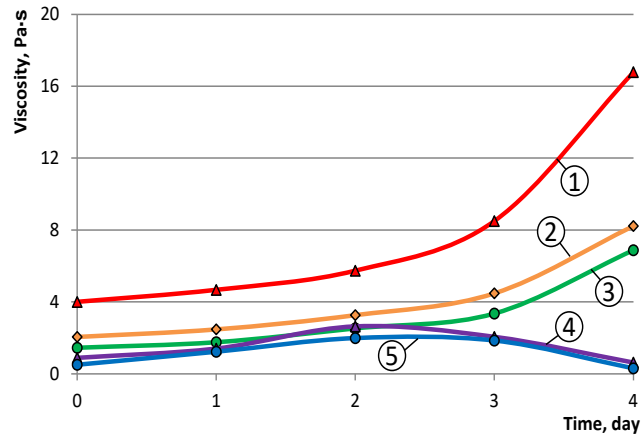


Figure 11. The dependence of the change in viscosity of emulsion samples with the content of sodium alginate: 1 – 3.0 % (O/A=1.9); 2 – 2.3 % (O/A=2.8); 3 – 1.8 % (O/A=6.4); 4 – 1.3 % (O/A=15.7); 5 – 1.0 % (O/A=19.1).

The change in the viscosity of the studied alginate emulsions confirms the time of onset of segregation in emulsions with a sodium alginate content of less than 1.3 % at a ratio $O/A > 15$, which happens two days after preparation. Maximum viscosity is observed on the second day for samples 4 and 5, after which the separation occurs. the alginate emulsion is destroyed and the viscosity is decreased. This is consistent with the results of the mass loss determination obtained previously. The increase in viscosity is observed more than 4 times for compositions 1...3 (Fig. 12) during the study period. no emulsion segregation was observed. which began not earlier than after 7 days (Fig. 11). Stability alginate emulsions increase up to 21-28 days when storing in an airtight screw-cap vessel [35, 36].

The change in the properties of alginate emulsions depends on the parameters of its structure, which are varied with a change in composition after the evaporation of water. The results of the study of changes in the structural parameters of alginate emulsions over time are presented in Table 4.

Table 4. Changes in the structural parameters of alginate emulsions.

#	Parameters	Ratio O/A	Sodium alginate content, %	The value of the parameter in a day, μm					
				0	1	2	3	4	5
1	Max diameter	1.9	3.0	18.21	18.54	18.87	19.20	19.53	19.86
2		2.8	2.3	19.26	19.50	19.74	19.98	20.22	20.46
3		6.4	1.8	29.50	28.70	27.90	27.10	26.30	25.50
4		15.7	1.3	18.97	28.14	37.31	46.48	55.65	64.82
5		27.2	1.0	22.78	25.21	27.64	30.07	32.50	34.93
6	Minimum diameter	1.9	3.0	1.90	1.96	2.02	2.09	2.15	2.21
7		2.8	2.3	1.10	1.39	1.68	1.97	2.26	2.56
8		6.4	1.8	2.47	2.10	1.73	1.37	1.00	0.63
9		15.7	1.3	1.99	2.23	2.47	2.71	2.95	3.19
10		27.2	1.0	2.40	2.20	2.00	1.81	1.61	1.41
11	Average diameter	1.9	3.0	5.44	5.66	5.89	6.12	6.34	6.57
12		2.8	2.3	5.64	5.85	6.06	6.27	6.48	6.69
13		6.4	1.8	6.68	7.05	7.41	7.77	8.13	8.49
14		15.7	1.3	7.03	7.99	8.96	9.92	10.89	11.86
15		27.2	1.0	8.95	9.04	9.12	9.21	9.30	9.38
16	The distance between the particles of the dispersed phase	1.9	3.0	8.65	6.93	5.22	3.51	1.79	0.08
17		2.8	2.3	8.96	6.82	4.68	2.54	0.41	–
18		6.4	1.8	7.62	5.96	4.29	2.62	0.96	–
19		15.7	1.3	2.85	2.33	1.81	1.29	0.76	0.24
20		27.2	1.0	2.12	1.63	1.14	0.64	0.15	–

Analysis of changes in the structural parameters of alginate emulsions shows that the particle size distribution changes during the evaporation of water the boundaries of the maximum and minimum particle sizes of the dispersed phase are increased. and the average diameter increases. The increase in particle diameter occurs on average by 28 % within 5 days. Alginate emulsions with clove oil with a particle diameter of 1 to 10 μm are also obtained in [35]. The change in the particle size distribution of the dispersed phase of the emulsion is caused by the decrease in the volume of the dispersion medium during the evaporation of water the approach of the particles together their collision, compression and pooling (Fig. 13).

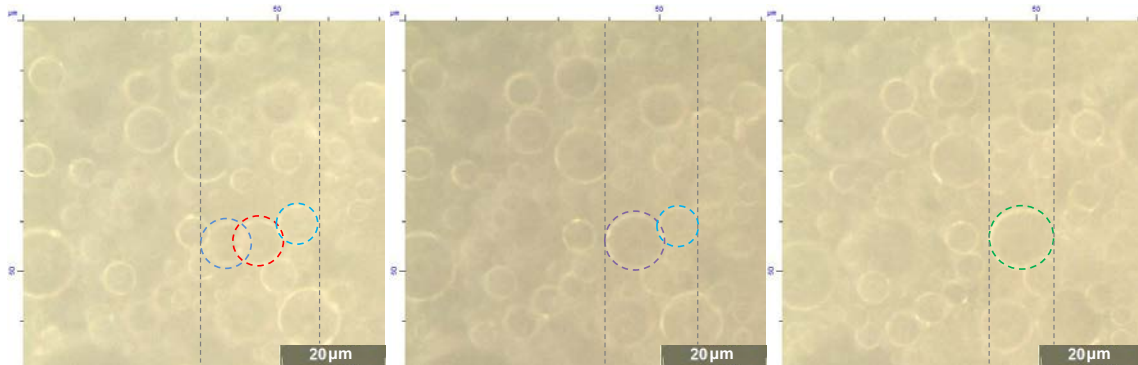


Figure 13. Micrograph of the process of pooling particles of the emulsion (from left to right).

The most part of the dispersed phase is in contact after 4 ... 5 days. which is accompanied by a sharp increase in their viscosity for stable emulsions (sodium alginate content of 1.8...3.0 %). A similar mechanism according to which there is a sequential increase in the particle size of the emulsion is observed during encapsulation, when individual drops of the emulsion are converted into capsules with an alginate shell during drying [37, 38]. Calcium is a component that prevents the premature destruction of emulsions in such technology during the formation of individual drops from emulsions [23, 25, 27, 38].

4. Conclusion

1. The ratio of components for the production of alginate emulsions are established, which can be used in the design of compositions for encapsulating various types of reducing agents. The range can be calculated by changing the O/A ratio depending on the content of sodium alginate, at which the maximum viscosity of the emulsions is achieved $C_{ai}: O/A = 26.734C_{al}^{-2.543}$.

2. The high resistance of alginate emulsions to segregation corresponds to a structured system the onset of the destruction of which is determined by the O/A ratio and can be described by the dependence $t_d = -0.5216 \cdot O/A + 10.25$.

3. The structure of stable alginate emulsions is characterized by an average particle size of the dispersed phase from 5 to 7 μm , the average distance between which is from 7 to 9 μm .

4. The change in the particle size distribution of the dispersed phase occurs during the process of water evaporation from the alginate emulsion, which is explained by the decrease in the volume of the dispersion medium, the approach of the particles, their collision, compression and pooling. The increase in particle diameter occurs on average by 28 % over 5 days. which is accompanied by the increase in viscosity by 4 times.

5. Acknowledgments

This work was financially supported by the Russian Science Foundation (project # 19-79-00262).

References

1. Bengisu, M., Ferrara, M. Materials that Move: Smart Materials, Intelligent Design. PoliMI SpringerBriefs. 2018. 139 p.
2. Shahinpoor, M., Schneider, H.-J. Intelligent Materials. 2007. 532 p.
3. Inozemtcev, S.S., Korolev, E.V. Review of Road Materials Self-healing: Problems and Perspective. IOP Conference Series: Materials Science and Engineering. 2020. 855(1). 012010. DOI: 10.1088/1757-899X/855/1/012010
4. Kumar, G.S. Self-healing materials: fundamentals, design Strategies, and applications (1st ed.). Weinheim: Wiley. 2009. VCH. 307 p.
5. Inozemtcev, S.S., Korolev, E.V. Interaction process on the phases interface "bitumen – dispersed phase from cement stone". Magazine of Civil Engineering. 2018. 82(6). Pp. 60–67. DOI: 10.18720/MCE.82.6
6. Jonkers, H.M. Self healing concrete: A biological approach. In Self healing materials – An alternative approach to 20 centuries of materials science. 2007. Pp. 195 –204.
7. Jonkers ,H.M., Schlangen, E. Development of a bacteria – based self healing concrete. In Tailor made concrete structures - new solutions for our society. Proc. Int. FIB symposium. 2008. Pp. 425–430. DOI: 10.1201/9781439828410.ch72
8. Jonkers, H.M., Schlangen, E. Bacteria-based self-healing concrete. International journal of restoration of buildings and monuments. 2009. 15(4). Pp. 255–265. DOI: 10.1016/j.proeng.2013.03.005

9. Jonkers, H.M., Thijssen, A., Muijzer, G., Copuroglu, O., Schlangen, E. Application of bacteria as self-healing agent for the development of sustainable concrete. *Ecological engineering*. 2010. 36(2). Pp. 230–235. DOI:10.1016/j.ecoleng.2008.12.036
10. Zemskov, S., Jonkers, H.M., Vermolen, F.J. An analytical model for the probability characteristics of a crack hitting an encapsulated self-healing agent in concrete. In V.P. Gerdt, W. Koepf, E.W. Mayr & E.V. Vorozhtsov (Eds.), *Computer Algebra in Scientific Computing*. 2010. 6244. Pp. 280–292.
11. Jonkers, H.M., Loosdrecht, M. Biogeocivil engineering. *Ecological engineering*. 2010. 36 (2). Pp. 97–98. DOI: 10.1016/j.ecoleng.2009.09.011
12. Teltayev, B., Porto, M., Caputo, P., Loise, V., Eskandarsefat, S., Rossi, C.O. Bitumen and bitumen modification: A review on latest advances. *Applied Sciences (Switzerland)*. 2019. 9(4). 742. DOI: 10.3390/app9040742
13. Shekhovtsova, S.Yu., Korolev, E.V., Inozemtcev, S.S., Yu, J., Yu, H. Method of forecasting the strength and thermal sensitive asphalt concrete. *Magazine of Civil Engineering*. 2019. 89 (5). Pp. 129–140. DOI: 10.18720/MCE.89.11
14. Feng, X. Self-healing mechanism of a novel cementitious composite using microcapsules. *Proc. Int. Conf. on Durability of Concrete Structures*. 2008. Pp. 195–204. DOI: 10.3390/ma6062182
15. Mihashi, H., Kaneko, Y., Nishiwaki, T., Otsuka, K. Fundamental Study on Development of Intelligent Concrete Characterized by Self-Healing Capability for Strength. *Trans. Japan Concrete. Inst.*.2000. 11 (2). Pp. 21–28. DOI: 10.3151/crt1990.11.2_21
16. Van Tittelboom, K., Wang, J., Araújo, M., Snoeck, D., Gruyaert, E., Debbaut, B., Derluyn, H., Cnudde, V., Tsangouri, E., Van Hemelrijck, D., De Belie, N. Comparison of different approaches for self-healing concrete in a large-scale lab test. *Constr. Build. Mater.* 2016. 107. Pp. 125–137. DOI: 10.1016/j.conbuildmat.2015.12.186
17. Thao, T.D.P., Johnson, T.J.S., Tong, Q.S., Dai, P.S. Implementation of self-healing in concrete-proof of concept. *IES J.Part A: Civ. Struct. Eng.* 2(2). Pp. 116–125. DOI: 10.1080/19373260902843506
18. Han, S., Choi, E.K., Park, W., Yi C., Chung, N. Effectiveness of expanded clay as a bacteria carrier for self-healing concrete. *Applied Biological Chemistry*. 2019. 62(1). Pp. 19–24. DOI: 10.1186/s13765-019-0426-4
19. Inozemtcev, S.S., Korolev, E.V. Technological features of production calcium-alginate microcapsules for self-healing asphalt. *MATEC Web of Conferences electronic collection*. 2018. P. 01008. DOI: 10.1051/mateconf/201825101008
20. Su J.F., Schlangen E., Qiu J. Design and construction of microcapsules containing rejuvenator for asphalt. *Powder technology*. 2004. Vol. 235. Pp. 563–571. DOI: 10.1016/j.powtec.2012.11.013
21. Su J.F., Wang Y.Y., Han N.X., Yang P., Han S. Experimental investigation and mechanism analysis of novel multi-self-healing behaviors of bitumen using microcapsules containing rejuvenator. *Construction Building Material*. 2016. Vol. 106. Pp. 3170–329. DOI: 10.1016/j.conbuildmat.2015.12.120
22. Raquel Casado Barrasaa, Víctor Blanco López, Carlos Martín-Portugués Montoliua, Verónica Contreras Ibáñezb, Josefina Pedrajasc, Julio Santarénd Addressing durability of asphalt concrete by self-healing mechanism. *Procedia – Social and Behavioral Sciences*. 2014. Vol. 162. Pp. 188–197. DOI: 10.1016/j.sbspro.2014.12.199
23. Su, J.F., Schlangen, E. Synthesis and physicochemical properties of novel high compact microcapsules containing rejuvenator applied in asphalt. *Chemical Engineering Journal*. 2012. Vol. 198–199. Pp. 289–300. DOI: 10.1016/j.cej.2012.05.094
24. Bin, Xue, Huifeng, Wang, Jianzhong, Pei, Rui, Li, Jiupeng, Zhang, Zepeng, Fan. Study on self-healing microcapsule containing rejuvenator for asphalt. *Construction and Building Materials*. 2007. Vol. 135. Pp. 641–649. DOI: 10.1016/j.conbuildmat.2016.12.165
25. Al-Mansooria, T., Micaloabc, R., Artamendid, I., Norambuena-Contrerasae, J., Garcia, A. Microcapsules for self-healing of asphalt mixture without compromising mechanical performance. *Construction and Building Materials*. 2017. Vol. 155. Pp. 1091–1100. DOI: 10.1016/j.conbuildmat.2017.08.137
26. Koryachkina, S.Ya., Prigarina, O.M. Nauchnyye osnovy proizvodstva produktov pitaniya: uchebnoye posobiye dlya vysshego professional'nogo obrazovaniya [The scientific basis of food production: a textbook for higher professional education] / Ore: FGBOU VPO «Gosuniversitet UNPK». 2011. 377 p.
27. Xua, S., Tabaković, A., Liua, X., Schlangena, E. Calcium alginate capsules encapsulating rejuvenator as healing system for asphalt mastic. *Construction and Building Materials*. 2018. Vol. 169. Pp. 379–387. DOI: 10.1016/j.conbuildmat.2018.01.046
28. Li, R., Zhou, T., Pei, J. Design, preparation and properties of microcapsules containing rejuvenator for asphalt, *Constr. Build. Mater.* 2015. Vol. 99. Pp. 143–149. DOI: 10.1016/j.conbuildmat.2015.09.017
29. Fisher, H. Self repairing materials – dream or reality? *Natural Science*. 2010. 2(8). Pp. 873–901. DOI: 10.4236/ns.2010.28110
30. Qiu, J., Van de Ven, M.F.C., Wu, S., Yu, J., Molenaar, A.A.A. Investigation of self healing capability of bituminous binders. *Road Materials Pavement Design*. 2009. 10. 1. Pp. 81–94. DOI: 10.1080/14680629.2009.9690237
31. Cordier, P., Tournilhac, F., Soulié-Ziakovic, C., Leibler, L. Self-healing and thermoreversible rubber from supramolecular assembly. *Nature*. 2008. 451. Pp. 977–980. DOI: 10.1038/nature06669
32. Kuhn, W. Deduction of particle shape and size from viscosity and flow double refraction. *Z. Phys. Chem.* 1932. 161. Pp. 1–32.
33. Schukin, E.D., Pertsov, A.V., Amelina, E.A. *Colloid chemistry*. 4th ed., Rev., M.: Higher. school, 2006. 444 p.
34. Malkin, A.Ya., Isaev, A.I. *Reologiya: ponyatiya, metody, primeneniya* [Rheology: concepts, methods, applications]. St. Petersburg. 2007. 560 p. (rus)
35. Doderio, A., Vicini, S., Alloisio, M., Castellano, M. Sodium alginate solutions: correlation between rheological properties and spinnability. *Journal of Materials Science*. 2019. 54 (10). Pp. 8034–8046. DOI:10.1007/s10853-019-03446-3
36. Najafi-Soulari, S., Shekarchizadeh, H., Kadivar, M. Encapsulation Optimization of Lemon Balm Antioxidants in Calcium Alginate Hydrogels. *Journal of Biomaterials Science, Polymer Edition* 2016. 27. Pp. 1631–1644. DOI: 10.1080/09205063.2016.1226042
37. Purwanti, N., Zehn, S.A., Pusfitasari, E.D., Khalid, N., Febrianto, E.Y., Mardjan, S.S., Andreas, Kobayashi I. Emulsion stability of clove oil in chitosan and sodium alginate matrix. *International Journal of Food Properties*. 2018. 21(1). Pp. 566–581. DOI: 10.1080/10942912.2018.1454946
38. Xu, S., Tabaković, A., Liu, X., Palin, D., Schlangen, E. Optimization of the calcium alginate capsules for self-healing asphalt. *Applied Sciences (Switzerland)*. 2019. 9 (3). 468. DOI: 10.3390/app9030468

Contacts:

Sergei Inozemtcev, inozemtsevss@mail.ru

Evgeniy Korolev, korolev@nocnt.ru

© Inozemtcev, S.S., Korolev, E.V., 2021



DOI: 10.34910/MCE.101.5

Bond strength in PVA fibre reinforced fly ash-based geopolymer concrete

K. Zerfu^{a*}, J.J. Ekaputri^b

^a Jimma University, Jimma, Ethiopia

^b Institut Teknologi Sepuluh Nopember, Surabaya, East Java, Indonesia

* E-mail: kefiyalewz@gmail.com

Keywords: PVA fibre, geopolymer concrete, bond strength, pull-out test, fly ash, alkali solution, mechanical properties.

Abstract. This paper presents the effect of polyvinyl alcohol (PVA) fibre on the bond strength in geopolymer concrete. The main focus of the study is to investigate how bond performance is affected by varying the amount of PVA fibre content. The PVA fibre content of 0 %, 0.2 %, 0.4 %, 0.6 % and 0.8 % by volume of concrete were utilized. Alkali activated class F fly ash was used to prepare the concrete specimens. Moreover, the Ordinary Portland cement (OPC) specimen was also prepared to conduct the comparative study. The results showed that the application of PVA fibre improves the bond resistance between the pull-out bar and concrete matrix. It has been investigated that the utilization of PVA fibre in geopolymer concrete improves up to 25.9 % bond strength as compared with the concrete without PVA fibre. The addition of PVA fibre provides a more ductile mode of failure in both geopolymer and OPC concrete than to the concrete without PVA fibre. For the different percentages of PVA fibre used, the specimen with 0.6 % PVA fibre shows maximum compressive strength, splitting and bond strength. The comparative study reveals that the specimen with and without PVA fibre blended geopolymer concrete shows higher bond strength than OPC concrete.

1. Introduction

As the most widely used binder in concrete, the main problem behind the ordinary Portland cement (OPC) is it requires large burning fossil fuels. The production of OPC is currently exceeding 2.6 billion tons per year worldwide, and growing at 5 % annually affecting the total cement production accounts for roughly 5–8 % of the global carbon-di-oxide (CO₂) [1–3]. Among the greenhouse gasses, carbon-di-oxide (CO₂) contributes about 65 % of the global warming caused mainly by economic growth and human population [4]. As a result, it is necessary to search environmentally friendly binding agents for concrete.

Currently geopolymer concrete (GPC) is becoming a novel construction material, which significantly reduces the above stated problem. According to the previous researches, utilization of geopolymer concrete generates up to 60 % less CO₂ than the OPC production [5–8]. In addition, the geopolymer concrete has better mechanical properties and higher resistance in aggressive environment, as compared to the conventional concrete [9–13]. The previous studies revealed that low calcium fly ash (class F) has been investigated as a suitable material for geopolymer concrete binder because of its wide availability, pertinent silica and alumina composition and less water demand. The low-calcium fly ash based GPC had shown excellent mechanical and durability properties at short and long term tests [14]. In addition, according to [15] fly ash-based geopolymer concrete provides an excellent sulfate resistance as compared to cement based concrete.

Several researches were conducted to understand the concrete-steel bond behavior in the OPC concrete by considering different parameters that affect the bond resistance. However, few studies were presented on the bond behavior of GPC. Some attempts were reported in the previous studies about the important property of the hardened GPC, which was its bond with reinforcing steel bars and concrete matrix [16–19]. To provide wide acceptance of the geopolymer concrete in the construction industry, different factors should be studied on the bond strength between the geopolymer concrete and the reinforcing bar.

Zerfu, K., Ekaputri, J.J. Bond strength in PVA fibre reinforced fly ash-based geopolymer concrete. Magazine of Civil Engineering. 2021. 101(1). Article No. 10105. DOI: 10.34910/MCE.101.5



This work is licensed under a CC BY-NC 4.0

The bond between the reinforcing bar and concrete is an important factor, which allows durability for the reinforced concrete structures. If there is a better bond, cracks will be minimized and the rebar will be also being better protected from corrosion [20]. The previous study indicates that even partial replacement of fly ash to OPC concrete increases the bond performance of the concrete [21]. Previous studies shows that to enhance the mechanical bond between the concrete matrix and its reinforcement, the addition of glass fibre, steel fibres, glass, carbon, aramid and hybrid fibres are recommended [22–26]. The recent study showed that the concrete with polyvinyl alcohol (PVA) fibre and fly ash stabilized soil with polypropylene fibre has a better mechanical strength and changed the brittle behavior into a ductile one [18], [27], [28]. Furthermore, studies showed that the fibrous geopolymer concrete generally provide better bond strength than the OPC concrete [29], [30].

Due to high brittle property of geopolymer concrete, an intensive study needed to improve the ductile behavior of geopolymer concrete. Therefore, this paper mainly shows the effect of PVA fibre on the bond strength in geopolymer concrete. Apparently, other physical, chemical and mechanical properties of the material and test specimens are also presented. As a main study parameter, the PVA fibre content of 0 %, 0.2 %, 0.4 %, 0.6 % and 0.8 % by volume of concrete were utilized.

2. Materials and Methods

2.1. Materials

The materials used to prepare the pull-out specimens were fly ash, an alkali solution, aggregates, steel pull-out bar and PVA fibre. The fly ash class F was used as a binder material from PT. Petrokimia Gresik, Indonesia, with reference to the quality standard [31]. The fly ash has a specific gravity of 2.67. Its chemical properties are depicted in section 3.1. The locally available coarse and fine aggregates were used in this research from PT. Surya Beton, Indonesia. The coarse aggregates from the crushed stone with maximum size less than 12 mm, and fine aggregates from fine sand, which passes through 4.75 mm sieve, in surface saturated dry condition, were used to make GPC specimens.

The alkali solution, which is a mixture of NaOH and Na₂SiO₃, was used. The sodium silicate solution has a composition of Na₂O, SiO₂ and water content of 15 %, 30 % and 55 % by mass, respectively. The concentration of NaOH solution is eight moles. The sodium silicate was supplied by PT. Kasmaji Inti Utama, Indonesia. The PVA fibre is the main variable, which was used to study its effect on the bond strength. Table 1 shows the mechanical properties of the PVA fibre, which is obtained from manufacturer manual.

Table 1. Properties of PVA fibre.

Fibre type	Tensile strength (MPa)	Flexural strength (GPa)	Diameter (µm)	Length (mm)	Density (gr/cc)	Melting temperature (°C)	Water absorption
RECS15	1600.00	40.00	38.00	8.00	1.30	225.00	< 1 %

The mix design was prepared for 35 MPa concrete strength, which can guarantee the satisfactory properties of concrete for a particular job. The mix proportions of materials were intended to obtain concrete specimen with the density of 2400 kg/m³, as provided in Table 2. The GPC paste with an aggregate ratio of 1:3 by the mass was used. The quantity of fine to coarse aggregate by the mass ratio of 2:3 was mixed together with GPC paste and alkali solution. The alkali solution, which is a mixture of sodium silicate to sodium hydroxide, having a mix ratio of 2.5 by mass, was used to prepare the test specimen. The PVA fibre of 0 %, 0.2 %, 0.4 %, 0.6 % and 0.8 % by volume of concrete was utilized as the main parameter. The maximum amount of fibre was limited to 0.8 %, because of the workability issue of the GPC paste.

Table 2. Mix Design for the preparation of concrete specimens.

Material	Mass (Kg/m ³)							
	GPC					OPC		
	GPC-1 0% PVA	GPC-2 0.2% PVA	GPC-3 0.4% PVA	GPC-4 0.6% PVA	GPC-5 0.8% PVA	OPC-1 0% PVA	OPC-2 0.4% PVA	
Coarse aggregate	1080	1080	1080	1080	1080	1012	1012	
Fine aggregate	720	720	720	720	720	620	620	
Fly ash	390	390	390	390	390	-	-	
Na ₂ SiO ₃	150	150	150	150	150	-	-	
NaOH	60	60	60	60	60	-	-	
PVA fibre	-	3	5	8	10	-	5	
Cement	-	-	-	-	-	533	533	
Water	-	-	-	-	-	237	237	

To conduct the comparative pullout test study between the geopolymer and conventional OPC concrete, primarily OPC concrete specimens having close compressive strength with geopolymer concrete were prepared. Accordingly, an analysis was conducted by keeping the other parameters, such as the diameter of the bar, bond length, cover and PVA fibre content constant. The specimens with 0 % and 0.4 % PVA fibre content were used for comparison. Ribbed bar with a diameter of 16 mm was used to perform the pullout test. The average yield and ultimate tensile stress of the pull-out bar are 492.9 MPa and 622.6 MPa, respectively.

As shown in Figure 1 the alkali solution is prepared prior to mixing process. During the preparation of the solution there is high generation of heat. Thus, the solution has to cool down before mixing with other ingredients. The PVA fiber was added after the fresh geopolymer concrete was well mixed. Addition of PVA fibre at the same with aggregate and fly ash leads to formation of balling.

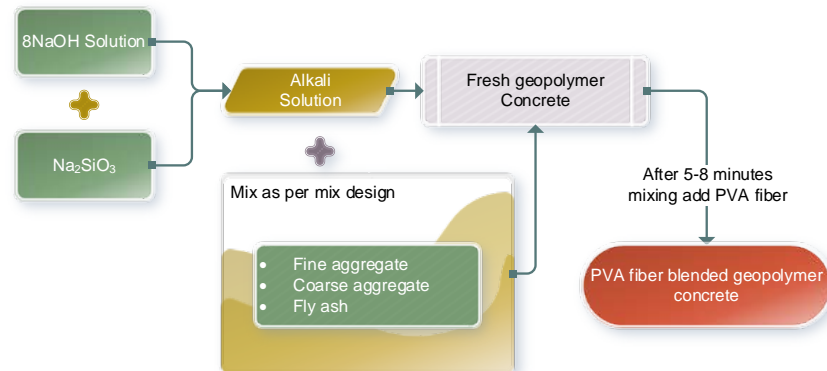
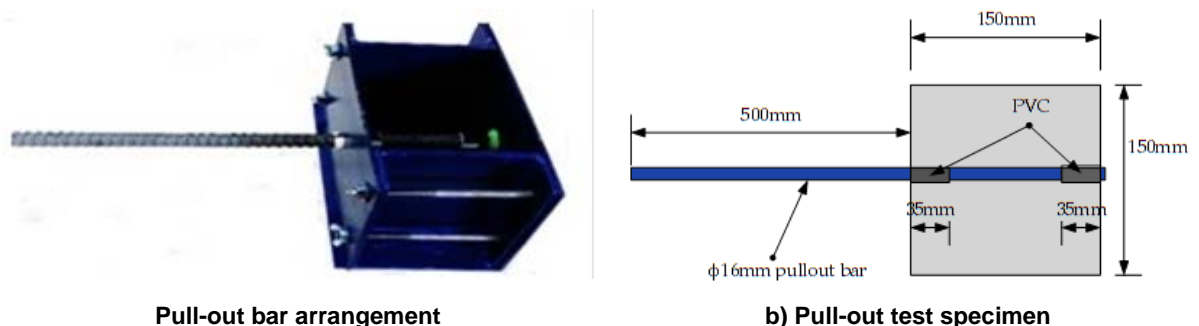


Figure 1. A schematic flow diagram for the preparation of PVA fibre blended GPC.

2.2. Test specimen preparation and curing

For each variation, three cubical lollipop specimens with the size of 150 mm were prepared. For the pullout load application, adequate length was provided based on the test machine. Accordingly, the steel cube mold with the interior dimension of 150 mm was used, as shown in Figure 2(a). To achieve the required bond length at the centre of the specimen, the PVC pipe was used. The PVC pipe was embedded such that, it neither restrains the slip of the bar nor affects the transfer of the bar forces to the concrete along the bond length. Figure 2(b) shows the arrangement for PVC pipe and the pullout bar in a concrete cube. The pullout deformed bar of diameter 16 mm, with 80 mm embedment length, was positioned horizontally at the middle of the specimens. One end of the pullout bar was projected out from the surface of concrete specimen about 500 mm, to grip the rebar to apply the pullout load. On the other free-load end, the rebar is projected at the surface of the specimen to set linear variable differential transformer (LVDT).



Pull-out bar arrangement

b) Pull-out test specimen

Figure 2. Mold setup and schematic for pull-out test specimen.

Before casting, molds were coated with the lubricant oil to make the demolding process easy. After that, fresh concrete was poured in three layers, and each layer was compacted by using a vibrator and compacting rod, with a special consideration of not disturbing the position of the pull-out. Even though all fresh concrete mixtures were poured in three layers, the compaction time varied. Especially for specimens containing 0.6 % and 0.8 % PVA fibre, the compaction time was longer as compared to the other mixes. This is related to the workability issue of the mixes. As the PVA fibre content increases, the workability of fresh concrete decreases drastically. After casting, specimens were kept at room temperature for one day. Then after one day, the concrete specimens were demolded and cured for 28 days in a moist condition. In addition to the pull-out specimens, the compressive and splitting test for the cylindrical specimens were prepared for each variation. For these specimens, the curing condition is the same as the pull-out specimens. After 28 days of curing, the compressive and splitting tests were conducted.

2.3. . Experimental setup for pullout test

To conduct the pull-out test, Universal Testing Machine having a model I/H-500KNI was used. A steel plate of size 200×200×13 mm, with a central opening of diameter 20 mm, was placed at the loaded surface of the concrete specimen. This plate was intended to make a smoother surface for the test specimen and to allow a free failure of concrete because of the pull-out load. The pull-out tests were conducted under controlled displacements according to [22]. Figure 3 shows pull-out setup for all specimens.

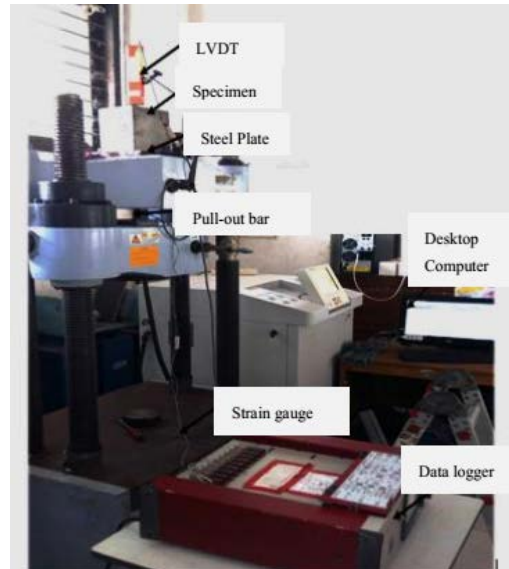


Figure 3. Experimental pull-out test setup.

During testing, at the unloaded end of the pull-out bar, one LVDT was mounted to measure the end displacement. The loading was recorded by using the mounted desktop computer with the test machine, which recorded the load and stroke at the same time. The load was applied to the pull-out bar at a rate of 1 mm/min.

3. Results and Discussions

3.1. Test results for Fly Ash

3.1.1. XRF and XRD Results

In order to determine the chemical composition of the fly ash, XRF test was conducted. The percentage composition of chemical and compound from this investigation are depicted in Table 3. such as silica, alumina, calcium and ferrite were determined with this testing. Additionally, the classification of fly ash as class F (low calcium) or C (high Calcium) referred to ASTM C618 [31] were evaluated. According to ASTM C618, if the percentage content sum of SiO₂, Al₂O₃, and Fe₂O₃ is greater or equal to 70 %, the fly ash is classified as class F. Hence, for the test result it was concluded that the class of fly ash used in the mixture is class F.

Table 3. Chemical composition of the fly ash based on X-ray diffraction (XRF) analysis result.

Oxides	SiO ₂	Al ₂ O ₃	Fe ₂ O ₃	CaO	MgO	K ₂ O	SO ₃	TiO ₂	Mn ₂ O ₃	Na ₂ O	Cr ₂ O ₃
Results (%)	48.47	26.05	12.54	5.18	2.77	1.66	1.05	0.92	0.19	0.47	0.02

Using composition of the alkali-fly ash mixture in the paste, the ratio of Si to Al by atom mass was fixed at 1.89 where from 48.47 % of silica content of fly ash, around 70 % is considered as a reactive silica. According to our previous results [14] this ratio was the most recommended for geopolymer concrete mixing.

Figure 4 shows the XRD pattern of fly ash-based geopolymer paste. The results show that the major peak of crystalline is quartz (SiO₂) and albite (Na-Al-Si complex). In addition, as a raw material, the fly ash also contained magnetite (Fe₃O₄), which influenced the reddish color of both fly ash and the concrete [32].

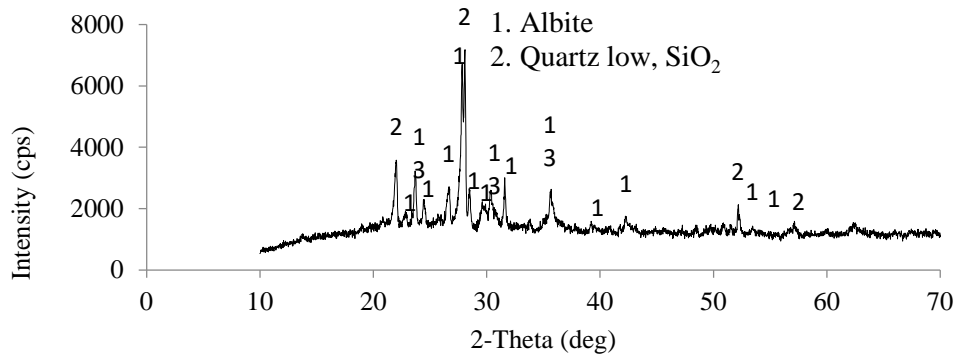


Figure 4. XRD result for geopolymer paste.

3.1.2. Scanning Electron Microscope (SEM)

The Scanning Electron Microscope (SEM) used in order to investigate the morphology of particles [32][33]. As stated in previous study, the morphology particle shape data can be also utilized to predict the mechanical and physical properties of material [34]. The SEM test result of fly ash is shown in Figure 5(a) and the concrete in Figure 5 (b). It is clearly shown that almost all fly ash particles dissolved in alkali-silica alumina system during geopolymerization process. This is also an indicator that the dense paste contributes to a high mechanical strength.

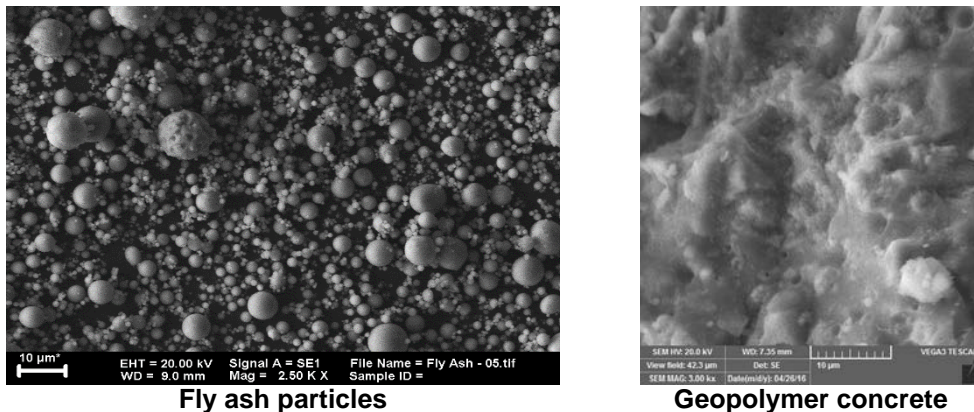


Figure 5. SEM results for fly ash and geopolymer concrete.

3.2. Concrete compressive and split tensile test

Three cylindrical concrete specimens with a diameter of 10 cm and height of 20 cm were prepared for each variation, according to ASTM C39 [35]. The compressive strength for GPC and OPC specimens without fibre content was calculated as 36.08 MPa and 37.19 MPa, respectively. Once more, for each variation of the PVA fibre, three specimens were tested. It has been investigated that the addition of PVA fibre improves the compressive strength. Studies also reported that the application of fibre in geopolymer mixtures enhances the compressive strength; conversely, the high addition of fibre restrains free flow and dropped the slump significantly [26].

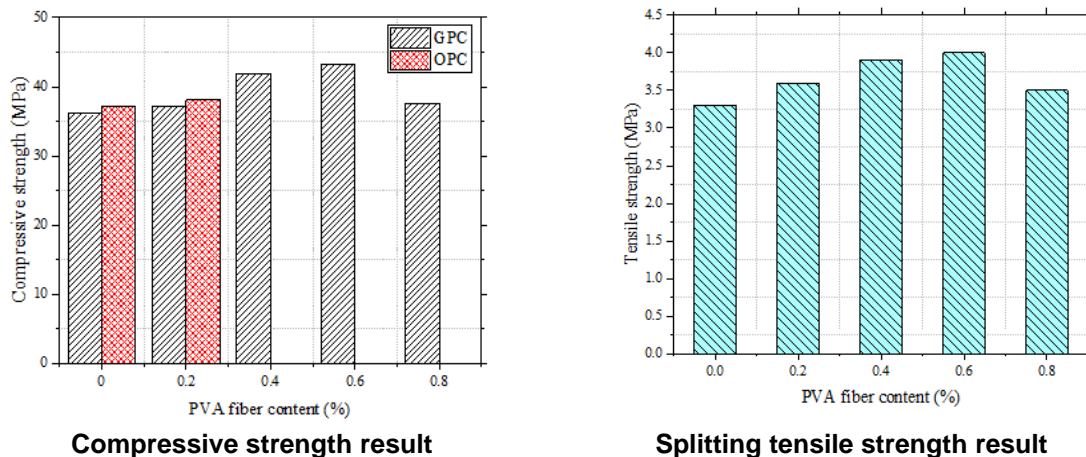


Figure 6. Experimental compressive and splitting tensile strength test results.

As depicted in Figure 6(a), the specimen with 0.6 % PVA fibre results in the maximum compressive strength, i.e. 43.16 MPa. For the specimen with 0.8 % PVA fibre, the compressive strength decreases, unlike the other specimens. This shows that the utilization of PVA fibre higher than 0.6 % has a tendency to decrease the strength of concrete significantly. It is an interesting fact to observe it experimentally, because it has a relation with the compacting problems during the casting. As shown in Figure 6(b), the split tensile test result also follows the same pattern as the compressive strength test. It proved that the fibre contributed lateral confinement to resist the uniaxial load. If the fibre mixes well with the geopolymer matrix, it also prevents the compressive load from opening more cracks during the splitting test. It is also an evidence that the crack opening is transferred from the matrix to the fibre before it gaps become wider and another crack starts to occur. When the fibres direction is perpendicular to the crack, they resist to the split of the matrix. This mechanism is recorded in Figure 7 by micro-camera with 750 x magnification. The fibres are very well bond with geopolymer matrix.

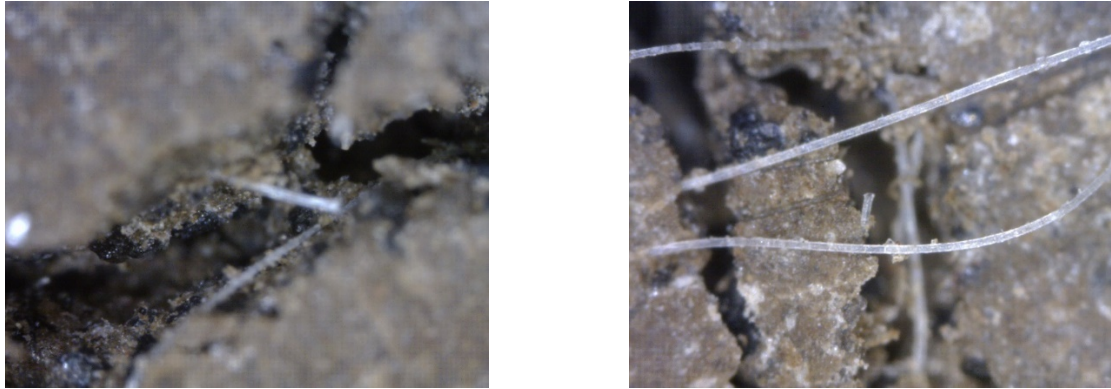


Figure 7. PVA fibre in the matrix and crack gap during splitting test.

The correlation of the experimental split tensile strength result, from the current study and the formerly predicted empirical relations between the compressive and splitting tensile strength by different sources, is depicted in Table 4. As shown in Table 4, the two empirical relations stated for GFRC and PFRC by [37] fairly estimated splitting tensile strength for PVA fibre reinforced concrete. Hence, the authors of this study also recommend these two equations for the prediction of splitting tensile strength from compressive strength of PVA fibre reinforced concrete.

Table 4. Study on the empirical relation between splitting tensile and compressive strength with current study.

Source	Relationship	Split tensile strength, f_{tsp} (MPa) for each PVA fibre variation				
		0%	0.2%	0.4%	0.6%	0.8%
Current study	Experimental results	3.30	3.60	3.90	4.00	3.50
[38]	$f_{tsp} = 0.56 f_c^{0.5}$ for $f_c \leq 83MPa$	3.36	3.41	3.62	3.68	3.43
[39]	$f_{tsp} = 0.38 f_c^{0.63}$ for $f_c \leq 120MPa$	3.64	3.71	3.99	4.07	3.73
[37]	$f_{tsp} = 0.60 f_c^{0.5}$ for GFRC*	3.60	3.66	3.88	3.94	3.68
[37]	$f_{tsp} = 0.55 f_c^{0.5}$ for PFRC**	3.30	3.35	3.56	3.61	3.37
[40]	$f_{tsp} = 0.12 f_c^{0.92}$ for HSFRC***	3.25	3.34	3.72	3.83	3.38

Note:

- GFRC* is glass fibre reinforced concrete
- PFRC** is polypropylene fibre reinforced concrete
- HSFRC*** is High-strength steel fibre reinforce concrete
- f_c is Compressive strength (MPa) for each PVA fibre variation

3.3. Tensile test results for pull-out bar

Before conducting the effect of PVA fibre on the bond strength, determination of the mechanical properties of the pullout bars are a compulsory task. The tensile tests were conducted for all batch of pull-

out bars to minimize possible errors during the pull-out test. In this regard, nine rebar samples—three samples from each three 12 m long ribbed bar—were used to check the consistency of the pull-out bars. This is conducted because the mechanical properties, such as the minimum upper yield strength and elongation values directly influence the pull-out test. The results obtained from the tensile test for nine samples are discussed in Table 5. Conventionally, steel bars are named by metric diameter. Therefore, diameter 16 mm was preferred for the designation. Hence, the metric diameter is used for the pull-out test result calculation. The test results in Table 5 shows that the steel bars used in this study are sufficient to achieve optimum performance for structural application.

Table 5. Tensile strength test result for pullout bar.

Batch No.	Length (mm)	Weight (Kg)	Nominal diameter (mm)	Metric diameter (mm)	Nominal area (mm ²)	Yield force (N)	Yield stress (N/mm ²)	Ultimate force (N)	Ultimate stress (N/mm ²)
1	500.00	0.76	15.70	16.00	193.76	99637.40	495.56	125138.00	622.39
	500.00	0.76	15.70	16.00	193.76	100498.00	499.84	125975.00	626.55
	500.00	0.76	15.70	16.00	193.76	96474.70	479.83	124955.00	621.48
	500.00	0.76	15.70	16.00	193.76	99589.60	495.32	126126.00	627.30
2	500.00	0.76	15.70	16.00	193.76	101414.00	504.39	125983.00	626.59
	500.00	0.76	15.70	16.00	193.76	99884.40	496.78	125871.00	626.03
	500.00	0.76	15.70	16.00	193.76	98745.20	491.12	125035.00	621.87
3	500.00	0.76	15.70	16.00	193.76	97335.10	484.11	123179.00	612.64
	500.00	0.76	15.70	16.00	193.76	98378.70	489.30	124381.00	618.62
	Average						99106.34	492.91	125182.56

3.4. Pull-out test results

The average bond strength was calculated by dividing the applied load to the surface area of the embedded length of the pullout bar, as shown in Eq. (1) [41], [42]. The bond stress is calculated by assuming that a uniform stress will occur along the bond length. The maximum bond stress values for the pullout specimens with 0 %, 0.2 %, 0.4 %, 0.6 % and 0.8 % PVA fibre are 15.74 MPa, 20.24 MPa, 21.22 MPa, 21.23 MPa and 15.05 MPa, respectively. Accordingly, the specimen with 0.6 % PVA fibre shows the highest bond strength, which is similar case with the compressive strength, and it is similar to the specimen containing 0.4 % PVA fibre. Significantly, the bond strength increases with the compressive strength of the concrete. However, for 0.8 % PVA fibre, the bond strength decreases as compared with the other specimens. As presented in previous study by [43] the random orientation of fibers leads to anisotropic behavior and increasing voids, which directly decreases interfacial bonding. Figure 8 depicts the experimental results for the pullout tests.

As shown in Figure 8, the failure mode for each PVA fibre variation is slightly different. The GPC without fibre shows a brittle failure, which cannot totally resist any load after the ultimate bond load. During the experimental test, all GPCs without fibre failed by splitting. However, specimens with PVA fibre show slight ductile failure. The pull-out specimens with 0.2 % and 0.4 % PVA content show a very close failure mode, in which both specimens show a ductile failure. It was also investigated that the crack openings were significantly reduced by the PVA fibre addition. This phenomenon is related to the results of the splitting test.

$$\tau = \frac{P}{\pi * \varphi_b * l_b}, \quad (1)$$

where τ is Bond strength, MPa;

P is Pull-out load, N;

φ_b is Pull-out bar diameter, mm;

l_b is Bond length, mm.

However, the specimens with 0.6 % and 0.8 % PVA fibre content failed in more a ductile mode, as compared to other specimens. Wherever a given concrete becomes stiffer and less workable, it needs more time to be compacted. Nevertheless, because of the short setting time of GPC paste, spending more time on compacting was worth the task. Furthermore, the extended vibration disturbs the position of

reinforcement bar and PVC pipe. The bond between the concrete matrix and the surface of reinforcement bar was also affected as a result of the high content fibre.

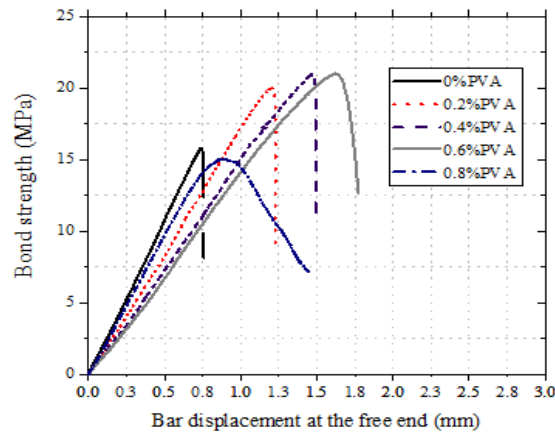


Figure 8. Pull-out test results for each PVA fibre variation.

3.5. Comparative Study

The comparative study was conducted for specimens without fibre and 0.4 % fibre contents. This study also depicted that higher potential in bond strength in GPC. However, the slump test result indicates that 0.4 % fibre addition shows better workability in OPC concrete, as compared to the GPC paste. The experimental results obtained for the comparative study for slump test is presented in Table 6.

Table 6. Results for slump test.

Paste type	PVA fibre content (%)	Slump test result (cm)
OPC	0.0	16.20
OPC	0.4	12.60
GPC	0.0	9.00
GPC	0.4	5.00

It can be clearly understood from Figure 9 that an addition of PVA fibre improves the bond strength in both the concrete types. Numerically, the specimen with 0.4 % PVA fibre content by volume in OPC concrete shows 12.4 % increase in bond strength from OPC concrete without fibre. As compared to the GPC, utilisation of fibre in OPC concrete shows less improvement in bond strength, which is almost the same as the GPC without fibre. Even though the compressive strength of OPC concrete, which is 37.19 MPa, is slightly higher than the GPC, the GPC matrix has better bond resistance.

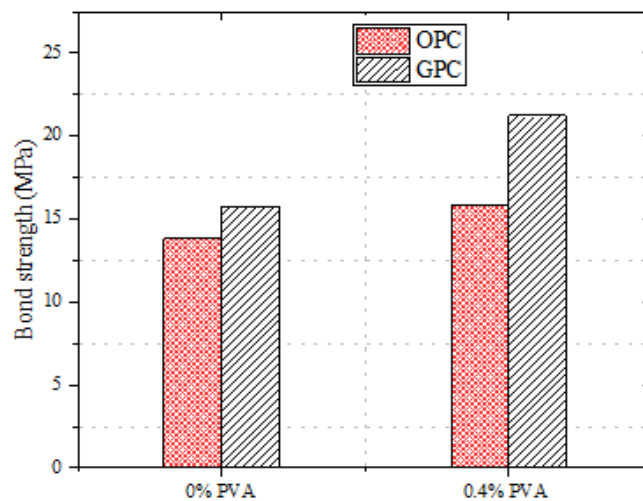


Figure 9. Comparative study between geopolymer and OPC concrete pull-out test.

As shown in Figure 10, the pull-out specimens fail by splitting; the same type of failure was stated in the previous studies by [22], [24]. However, the extent of cracking is different in both geopolymer and OPC concrete. The specimens without fibre fully separated by splitting crack. For the fibre reinforced concrete, the specimens show small cracks around the supported face of the concrete.



a. GPC specimen without PVA fibre



b. OPC specimen without PVA fibre



c. GPC specimen with 0.4% PVA fibre



d. OPC specimen with 0.4% PVA fibre

Figure 10. Comparative study for the splitting cracks failures.

It is clearly seen that the brittle failure in concrete specimens without PVA fibre is more substantial than the PVA fibre reinforced concrete in both cases. The patterns of cracks are also slightly similar, which occurs along the pull-out bar direction. The crack patterns in Figure 10(a) and Figure 10(b) shows that the GPC is more brittle than the OPC concrete. This phenomenon is insignificant in PVA fibre reinforced pullout specimens. As shown in Figure 10(c) and Figure 10(d), the crack opening is minimised by the addition of PVA fibre in both the specimens. Again, GPC shows a wider crack opening, as compared to OPC concrete, in 0.4 % PVA fibre reinforced specimens.

4. Conclusions

This paper focuses on the effect of PVA fibre on bond strength in geopolymer concrete, with the aim to contribute to the experimental database and provide comprehensive understanding on the role of PVA fibre. The PVA fibre variation of 0 %, 0.2 %, 0.4 %, 0.6 % and 0.8 % by volume of geopolymer concrete was used as the main study parameter. Hence, five mix designs that are one mix design without fibre and four mix designs with fibre were prepared for the experimental work. Prior to the pull-out test, a compressive test was conducted to investigate the effect of PVA fibre on the mechanical properties of geopolymer concrete. Afterwards, the direct pull-out test was conducted for each variation to analyse how the PVA fibre addition affects the bond resistance between the concrete matrix and pull-out bar. To this end, the ultimate bond load, crack patterns and failure mechanism was studied. In addition, the OPC concrete specimens, having close compressive strength with geopolymer concrete, were prepared to conduct the comparative study. Thus, the specimens with 0 % and 0.4 % PVA fibre content were used for a comparative study. The overall conclusions from this study are given as follows:

1. It has been investigated that the addition of PVA fibre improves both compressive and bond strength for the concrete mix. The experimental study reveals that the utilization of PVA fibre in geopolymer concrete shows about 19.62 % increase in the compressive strength.

2. The same trend as the compressive strength is also observed for the bond strength. The addition of PVA fibre improves the bond strength of concrete by about 25.9 % in geopolymer concrete.
3. The optimum amount of PVA fibre addition is 0.4 % by volume of the concrete. Even though the specimen with 0.6 % PVA fibre content has the highest bond strength, the workability of the mix is poor.
4. The utilization of PVA fibre for more than 0.6 % has shown a tendency to decrease the bond resistance. The specimen with 0.8 % PVA fibre content reveals this condition. As the PVA fibre content increases, the workability of the fresh concrete decreases.
5. A comparative study reveals that both the non-PVA and PVA fibre blended geopolymer concrete shows higher bond strength than the OPC concrete. The addition of PVA fibre provides a more ductile mode of failure in both geopolymer and OPC concrete, as compared to the concrete without PVA fibre.
6. The utilization of PVA fibre in OPC concrete results in the less increment in bond strength, as compared to the geopolymer concrete.

5. Acknowledgments

The authors would like to thank the Laboratorium Beton dan Bahan Bangunan, Kampus ITS, for providing all necessary equipment and machineries for the experimental work. The authors also would like to pass their deep gratitude to Kasmaji Inti Utama, PT. Petrokimia Gresik and SBI Surya Beton Indonesia companies for the material support. The experiment was fully supported by the Indonesian Ministry of Education and Culture under the 3rd year of PTUPT Grant. Ekaputri was also partially funded by the Indonesian Ministry of Research, Technology, and Higher Education under the WCU Program managed by Institut Teknologi Bandung.

References

1. Oliver, J., Jassens-Maehout, G., Peters, J. Trends in Global CO₂ Emissions: 2012 Report 2012.
2. Kirupa, A.D. Strength and stability characteristics of GGBS and red mud based geopolymer concrete incorporated with hybrid fibres. *The Indian Concrete Journal*. 2015.
3. Adewumi, A.A., Ismail, M., Yusuf, M.O., Maslehuiddin, M., Mohamed, H.D., Bahru, J., Al-batin, H., Arabia, S., Arabia, S. Strength and microstructure of alkali-activated natural pozzolan and limestone powder mortar. *Magazine of Civil Engineering*. 2019. 92(8). Pp. 36–47. DOI: 10.18720/MCE.92.3
4. Dong, K., Jiang, H., Sun, R., Dong, X. Driving forces and mitigation potential of global CO₂ emissions from 1980 through 2030: Evidence from countries with different income levels. *Science of the Total Environment*. 2019. 649. Pp. 335–343. DOI: 10.1016/j.scitotenv.2018.08.326
5. Carreño-gallardo, C., Tejeda-ochoa, A., Perez-ordonez, O.I., Ledezma-sillas, J.E. Journal of Environmental Chemical Engineering In the CO₂ emission remediation by means of alternative geopolymers as substitutes for cements. *Journal of Environmental Chemical Engineering*. 2018. 6(4). Pp. 4878–4884. DOI: 10.1016/j.jece.2018.07.033
6. Zhuang, X.Y., Chen, L., Komarneni, S., Zhou, C.H., Tong, D.S., Yang, H.M., Yu, W.H., Wang, H. Fly ash-based geopolymer: Clean production, properties and applications. *Journal of Cleaner Production*. 2016. 125. Pp. 253–267. DOI: 10.1016/j.jclepro.2016.03.019
7. Davidovits, J. Geopolymer ement. Review, Geopolymer Institute. 2013. Pp. 1–11.
8. Kefiyalew and Januarti. Review on Alkali-Activated Fly Ash Based Geopolymer Concrete. *Materials Science Forum*. 2016. 841. Pp. 162–169. URL: 10.4028/www.scientific.net/MSF.841.162.
9. Pilehvar, S., Szcotok, A.M., Rodríguez, J.F., Valentini, L., Lanzón, M., Pamies, R., Kjøniksen, A.L. Effect of freeze-thaw cycles on the mechanical behavior of geopolymer concrete and Portland cement concrete containing micro-encapsulated phase change materials. *Construction and Building Materials*. 2019. 200. Pp. 94–103. DOI: 10.1016/j.conbuildmat.2018.12.057
10. Pasupathy, K., Berndt, M., Sanjayan, J., Rajeev, P. Cement and Concrete Research Durability of low - calcium fly ash based geopolymer concrete culvert in a saline environment. *Cement and Concrete Research*. 2017. 100 (May). Pp. 297–310. DOI: 10.1016/j.cemconres.2017.07.010
11. Tennakoon, C., Shayan, A., Sanjayan, J.G., Xu, A. Chloride ingress and steel corrosion in geopolymer concrete based on long term tests. *Materials and Design*. 2017. 116. Pp. 287–299. DOI: 10.1016/j.matdes.2016.12.030
12. Tittarelli, F., Mobili, A., Giosuè, C., Belli, A., Bellezze, T. Corrosion behaviour of bare and galvanized steel in geopolymer and Ordinary Portland Cement based mortars with the same strength class exposed to chlorides. *Corrosion Science*. 2018. 134(December 2016). Pp. 64–77. DOI: 10.1016/j.corsci.2018.02.014
13. Erofeev, V.T., Rodin, A.I., Yakunin, V.V., Tuvin, M.N. Structure, composition and properties of geopolymers from mineral wool waste. *Magazine of Civil Engineering*. 2019. 90 (6). Pp. 3–14. DOI: 10.18720/MCE.90.1
14. Leonard Wijaya, A., Jaya Ekaputri, J., Triwulan. Factors influencing strength and setting time of fly ash based-geopolymer paste. *MATEC Web of Conferences*. 2017. 138. Pp. 01010. DOI: 10.1051/mateconf/201713801010
15. Jianhe Xie, J.Z., Junjie Wang, C.W., Peiyan Huang, A., Fang, C. Sulfate Resistance of Recycled Aggregate Concrete. *materials*, MDPI. 2019. 12. DOI: 10.3390/ma12081247
16. Cristina Zanotti, Paulo H.R. Borges, Aamer Bhutta, Yang Du, N.B. Bond Strength of PVA Fiber Reinforced Geopolymer repair to Portland Cement Concrete Substrate. 9th RILEM International Symposium on Fiber Reinforced Concrete – BEFIB 2016. 2016.
17. Sarker, P.K. Bond strength of reinforcing steel embedded in fly ash-based geopolymer concrete Bond strength of reinforcing steel embedded in fly ash-based geopolymer concrete. 2015. (June 2011). DOI: 10.1617/s11527-010-9683-8
18. Tekle, B.H., Khennane, A., Kayali, O. Bond behaviour of GFRP reinforced geopolymer cement concrete. 2017. 04002. Pp. 1–10.

19. Dahou, Z., Castel, A., Noushini, A. Prediction of the steel-concrete bond strength from the compressive strength of Portland cement and geopolymer concretes. *Construction and Building Materials*. 2016. 119. Pp. 329–342. DOI: 10.1016/j.conbuildmat.2016.05.002
20. Jiang, C., Wu, Y., Dai, M. Degradation of steel-to-concrete bond due to corrosion. *Construction and Building Materials*. 2017. (October). DOI: 10.1016/j.conbuildmat.2017.09.142. URL: <https://doi.org/10.1016/j.conbuildmat.2017.09.142>.
21. Arezoumandi, M. Effect of fly ash replacement level on the bond strength of reinforcing steel in concrete beams. *Journal of Cleaner Production*. 2015. 87. Pp. 745–751.
22. Maranan, G., Manalo, A., Karunasena, K., Benmokrane, B. Bond Stress-Slip Behavior: Case of GFRP Bars in Geopolymer Concrete. *Journal of Materials in Civil Engineering*. 2015. 27(1). Pp. 04014116.
23. Hossain, K.M.A., Ametrano, D., Lachemi, M. Bond Strength of Standard and High-Modulus GFRP Bars in High-Strength Concrete. *Journal of Materials in Civil Engineering*. 2014. 26(3). Pp. 449–456. DOI:10.1061/(ASCE)MT.1943-5533.0000758. URL: <http://ascelibrary.org/doi/10.1061/%2528ASCE%2529MT.1943-5533.0000758>.
24. Alves, J., El-Ragaby, A., El-Salakawy, E. Durability of GFRP Bars' Bond to Concrete under Different Loading and Environmental Conditions. *Journal of Composites for Construction*. 2011. 15(3). Pp. 249–262.
25. ARAÚJO, D.L. Influence of steel fibers on the reinforcement bond of straight steel bars. *IBRACON Structures and Materials Journal*. 2013. 6. Pp. 307–338.
26. Achillides, Z. Bond Behavior of FRP Bars Under Direct Pullout Conditions.pdf. *Journal of Composites for Construction*. 2004. 8. Pp. 173–181.
27. A.Şenol, C.G. Effect of Fly Ash and Polypropylene Fibers Content on the Soft Soils. *International Journal of Civil Engineering*. 2014. 12(2). Pp. 134–145.
28. Januarti Jaya Ekaputri. Effect of PVA fiber in increasing mechanical strength on paste containing glass powder. 2015.
29. Nematollahi, B., Sanjayan, J., Shaikh, F.U.A. Comparative deflection hardening behavior of short fiber reinforced geopolymer composites. *Construction and Building Materials*. 2014. 70. Pp. 54–64. DOI:10.1016/j.conbuildmat.2014.07.085. URL: <http://dx.doi.org/10.1016/j.conbuildmat.2014.07.085>.
30. Nematollahi, B., Sanjayan, J., Qiu, J., Yang, E.H. High ductile behavior of a polyethylene fiber-reinforced one-part geopolymer composite: A micromechanics-based investigation. *Archives of Civil and Mechanical Engineering*. 2017. 17(3). Pp. 555–563. DOI: 10.1016/j.acme.2016.12.005. URL: <http://dx.doi.org/10.1016/j.acme.2016.12.005>.
31. ASTM C 618 –03. Standard specification for coal fly ash and raw or calcined natural pozzolan for use in concrete.2003.
32. Risdanareni, P., Puspitasari, P., Jaya, E.J. Chemical and Physical Characterization of Fly Ash as Geopolymer Material. *MATEC Web of Conferences*. 2017. 01031. DOI: 10.1051/mateconf/20179701031
33. A. Fernandez-Jime´nez, A.P. Characterisation of fly ashes. Potential reactivity as alkaline cements q. 2003. 2361 (May 2019). DOI: 10.1016/S0016-2361(03)00194-7
34. Liu, H., Sun, Q., Wang, B., Wang, P., Zou, J. Morphology and Composition of Microspheres in Fly Ash from the Luohuang Power Plant, Chongqing,. *Minerals-MDPI*. 2016. DOI: 10.3390/min6020030
35. ASTM C 39. Compressive strength of cylindrical concrete specimens 2000.
36. Abdullah, M.M.A.B., Tahir, M.F.M., Tajudin, M.A.F.M.A., Ekaputri, J.J., Bayuaji, R., Khatim, N.A.M. Study on the geopolymer concrete properties reinforced with hooked steel fiber. *IOP Conference Series: Materials Science and Engineering*. 2017. 267(1). DOI: 10.1088/1757-899X/267/1/012014
37. Choi, Y., Yuan, R.L. Experimental relationship between splitting tensile strength and compressive strength of GFRC and PFRC. 2005. 35. Pp. 1587–1591. DOI: 10.1016/j.cemconres.2004.09.010
38. ACI Committee 318. Building Code Requirements for Structural Concrete (ACI 318-14) And Commentary (ACI 318R-14)2014.
39. Girgin, Z.C., Ar, E. Evaluation of Ratio between Splitting Tensile Strength and Compressive Strength for Concretes up to 120 MPa and its Application in Strength Criterion. 2006. (103).
40. Ramadoss Perumal. Correlation of compressive and other engineering properties of high-performance steel fiber-reinforced concrete. *Journal of Materials in Civil Engineering*. 2014. DOI: 10.1061/(ASCE)MT.1943-5533.0001050
41. Tastani, S.P., Pantazopoulou, S.J. Direct Tension Pullout Bond Test: Experimental Results. 136 (6) 2010.
42. Castel, A., Foster, S.J. Bond strength between blended slag and Class F fly ash geopolymer concrete with steel reinforcement. *Cement and Concrete Research*. 2015. 72. Pp. 48–53. DOI: 10.1016/j.cemconres.2015.02.016
43. Bhat, R., Mohan, N., Sharma, S., Pratap, A., Keni, A.P., Sodani, D. Mechanical testing and microstructure characterization of glass fiber reinforced isophthalic polyester composites. *Integrative Medicine Research*. 2019. 8(4). Pp. 3653–3661. DOI: 10.1016/j.jmrt.2019.06.003

Contacts:

Kefiyalew Zerfu, kefiyalewz@gmail.com

Januarti Jaya Ekaputri, januarti_je@yahoo.com



DOI: 10.34910/MCE.101.6

Predicting creep deformation of asphalts modified with polymer using artificial neural networks

B.S. Saoudi*, S.H. Haddadi

Faculté de Génie Civil / USTHB Laboratoire de recherche Environnement, Eau, Géomécanique et Ouvrages (LEEGO), Bab Ezzouar, Algérie

* E-mail: saoudibra@yahoo.fr

Keywords: Neural Networks, asphalt concrete, static creep test, creep rate, rubber contents

Abstract. This study presents an application of the Artificial Neural Networks (ANN) for creep rate prediction of asphalt concrete modified with different rubber contents. Acrylonitrile butadiene rubbers (NBR) under powder form are used in this study. The polymer is an industrial waste produced by the Algerian Elastomer Company. The most appropriate model is the multilayer back propagation network. It is produced to implement the complexity of the non-linear between the data network and the product result. It is established by the incorporation of an important experimental database and by an appropriate choice of the architecture and of the learning process. We will show that the developed ANN model received rubber contents, test temperature, compactness and the loading stress as the input and provided the creep rate as the output has better capability to predict the final creep rate in a short time with low error. The model is further applied to evaluate the effect with different contents of polymer on creep rate of bituminous concrete modified. Obtained results show that creep rate is reduced at 2 % of polymer adding. However, an increase in percentage of additives over 2 % does not help to reduce permanent deformation of asphalt mixtures. ANN model introduced provided a more accurate tool for the design of bituminous concretes modified.

1. Introduction

Road pavement structures are exposed to very complex damaged effects among traffic and climate have a dominant influence on the behavior of pavement materials. In many countries like Canada, United States, France, etc..., pavements are subjected to high thermal amplitudes and the phenomenon of the thermal cracking. In Algeria, the phenomenon of permanent deformations (rutting) is largely observed [1]. Rutting due to permanent deformations is considered one among of the major distress mechanisms found in asphalt pavements. Rutting can be an issue in almost any climate conditions, especially in high-temperature regions that results in decreased pavement service life. It may be caused either by a deformation of the support soil or by a thinning by creep of the bituminous [2]. To reducing the extent of these deformations, researchers tried to improve pavement properties by reinforcing them with additives like polymers and crumb rubber. Modified binders are often used to progress the durability and hot mix asphalt (HMA) performance when pure binders can not meet specifics demands under severe conditions [3–11]. Although, many research studies have been developed to reduce asphalt concrete rutting, the formation of rutting mechanism is very complicated task in to interpret it mathematically [12, 13].

Life span of road pavement is an important topic in national economy, for similar reasons, it is very important to predict rutting in asphalt concrete in order to maintain the legitimate function of pavement and its maintenance. In this aspect, many researchers have used Modern acknowledgment techniques such as neural networks, genetic algorithms to predict the performance of asphalt mixtures considering different effective parameters [14, 15]. An important interest was observed for the artificial neural network method due to its advantages. ANN able to learning directly from examples and finding a relation between input and output variables [16].

ANN applications. Very detailed information about the applications of ANN in geotechnical and pavement engineering can be found in the literature. In a study published by Ritchie, Kaseko and Bavarian [17], an artificial neural network system is developed for automated pavement evaluation. In another work



Kaseko and Ritchie [18], used neural networks in the detection of pavement cracks with image processing. Comparative analysis of two neural networks using pavement performance prediction as defined by the International Roughness Index, have been proposed by Roberts and al [19]. Kim and Kim [20], have been used the neural networks to predict layer modeling from falling weight deflect meter (FWD) and surface wave measurements. Mei et al [21], have developed a program with neural networks that allows real depths of cracks can be quickly assessed, surface cracks or fatigue cracks in bituminous pavements. Thodesen, Xiao, and Serji NA Mirkhanian [22], have been used the statistical regression and neural network (NN) approaches in predicting the viscosity values of crumb rubber modified binder at various temperatures. Tapkın, Çevik and Us [23], presents an application of ANN for the prediction of repeated creep test results for polypropylene modified asphalt mixtures. Terzi *et al.* [24], have be used the artificial neural networks for studying the asphalt concrete stability estimate from non-destructive test methods. Ghanizadeh and Ahadi [25], have published into their paper an application of Artificial Neural Networks for Analysis of Flexible Pavements under Static Loading of Standard Axle. Mirabdolazimi and Shafabakhsh [26], proposed ANN model for rutting depth of hot mix asphalts modified with forta fiber. Kamboozia, Ziari and Behbahani [27] have been used ANN approach to predicting rut depth of asphalt concrete by using of visco-elastic parameters. Alrashydah and Abo-Qudais [28] presents two predictive models, one with multiple regression analysis and the other with feed-forward ANN used to predict the HMA creep compliance behavior. Ziari et al [29] in his paper, presents multiple regression and artificial neural networks to modeling of creep compliance behavior in asphalt mixes.

The main objective of this study was to evaluate the using of ANN approach to predict creep rate of modified and unmodified asphalt concrete, we interested to the incorporation of an acrylonitrile butadiene rubber (NBR) elastomer under powder form. The polymer is an industrial waste produced by the Algerian Elastomer Company (SAEL in Algeria). In the primary concern to preserve the environment against these waste we thought of exploited these waste in the asphalt pavement roads. ANN model with two hidden layers is developed to predict the effectiveness introduction of the polymer on creep rate of bituminous concrete. Training, testing, and validation stages of the model are performed using an experimental well-organized database. We show that this approach is also very advantageous because it takes account of the essential factors (the rubber contents, the temperature, the compactness and the loading stress). The concept of creep rate, [1] evaluated in a static creep test is applied as a measure of the performance of modified asphalt concrete compared to unmodified asphalt concrete.

2. Methods

Aggregates. The following (Table 1), presents the intrinsic characteristics of the aggregates used in this study. The various tests on aggregates show that the materials chosen have good intrinsic characteristics.

Table 1. Characteristics of aggregates.

tests	Granular class		
	0/3	3/8	8/15
Cleanliness (%)	-	2.33	1.57
Sand equivalent (%)	39	-	-
Los Angeles (%)	-	16	14
Micro Deval (%)	-	9	16
Specific density	2.58	2.70	2.70

In experimental investigations, 35/50 penetration grade bitumen, which properties described in (Table 2), has been used to prepare the modified bitumen.

Table 2. Asphalt properties.

Bitumen grade	35/50	Specification
Penetration at 25 °C (1/10 mm)	42	35 to 50
Softening point, ring and ball (°C)	51.6	50 to 58
Relative density (g/cm ³)	1.029	-
Ductility at 25 °C (mm)	> 1000	> 1000
Penetration index _{LCPC}	0.545	-

Additive. The polymer used as additive in this work, is a blackish industrial waste produced from the elastomer application company (SEAL in Algeria). It is used in powder form (Fig. 1). The powder is composed of grains smaller than 0.8 mm of diameter. The density is 1.22 measured compared with the ethanol density (0.79).



Figure 1. Waste in the powders form.

The static uniaxial creep test is considered as the simplest test used for evaluating the deformation behavior of viscoelastic materials such as asphalt mixtures. It was developed by the Shell organization in Amsterdam for testing bituminous mixtures in the 1970's. The test can be conducted either by applying a constant stress (creep test) or constant strain rate in tension or compression. The sample used for this test is usually cylindrical in shape and a friction reduction system between the specimen and loading plates is used. (Fig. 2) shows a typical test result for loading and unloading phases; the figure shows the initial strain which comprises elastic and plastic behavior which is known as time independent strain and occurs when the load is applied. This stage is followed by the time dependent strain which is also known as delayed elastic and viscous strain. Although, the creep test is used to estimate the performance properties of asphalt mixtures.

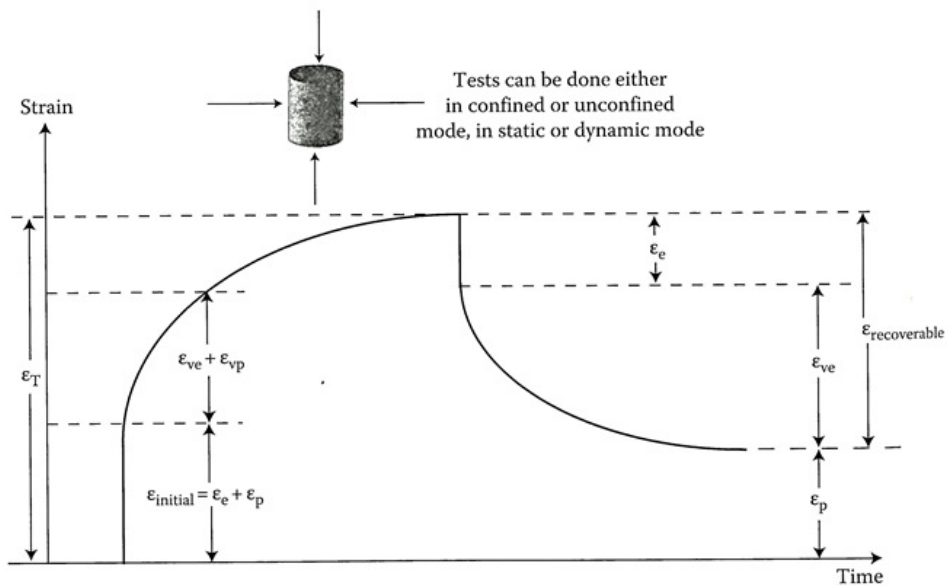


Figure 2. Typical Strain Results from Creep Testing:

where ϵ_T is total strain; ϵ_e is elastic strain; ϵ_p is plastic strain; ϵ_{ve} is viscoelastic strain; ϵ_{vp} is viscoplastic strain.

The static creep test was conducted according to the methodology and specifications listed by Haddadi, Ghorbel and Laradi [1]. Table 3 summarizes the properties of all tested specimens (data base).

Table 3. Properties of the test specimens.

Properties of the test specimens	Data
Percentage of polymer (%)	0 %, -2 %, 3 % and 4 %
Temperature (°C)	25 °C, 40 °C and 60 °C
Stress (Mpa)	Min 0.010 Max 0.825
Compactness (%)	Min 65.41 % Max 96.92 %
Experimental Creep rate %	Min 47.46 % Max 88.92 %

During the last decade, ANN were a primary center of interest for data-processing search and provide convenient solutions and often strongly precise to the problems of civil engineering. The artificial neural networks are considered among the biological metaphors used in our days for solving problems [30]. They are causing the attempts of a mathematical modeling of human brain functioning. The ANN (Fig. 2) is driven into him having a set of associated input-output databases on a learning rule. The learning process uses an algorithm, in which the ANN develops a function between inputs and outputs. Generally, in a learning process, neurons receive inputs ($E_1 \dots E_n$) and transmit them to the neurons in the hidden layer, which are responsible for simple mathematical calculations, involving connection weights ($W_{11}, \dots W_{1n}$), bias ($b_1, \dots b_n$) and the input value equation (1) [13]. The result of these neurons is passed by a transfer function (F) equation (2) to each neuron that limits the output with the minimum and maximum authorized limits. The choice of the type of this function is a very essential element of ANN and often of the nonlinear functions will be needed [31], Once applied function, the final results are produced. After that, these results become the inputs to all the neurons in the next layer, and the calculation process is repeated. Through the layers to the output layer, the output values are produced in the output neurons (Y_k) equation (3). At this stage, an error value of output is calculated between the produced output and the desired output (target). Generally, the learning and iterative process stops when an acceptable gap is reached. On completion of the learning process, the network should be able to give the output solution for any data set.

$$I_k = \sum_{i=1}^n W_{ik} E_i + b_i, \quad (1)$$

$$F(I_k) = \text{tansig}(I_k) = \frac{2}{1 + \exp^{-2I_k}} - 1, \quad (2)$$

$$Y_k = F(I_k) \quad (3)$$

Hyperbolic tangent transfer function equation (2) in the term of neural networks, is related to a bipolar *sigmoid*, which has an output in the range of -1 to +1. Mathematically equivalent to $\tanh(n)$. It differs in that it runs faster than \tanh , but the results can have very small numerical differences. This function is a good trade-off for neural networks, where speed is more important than the exact shape of the transfer function.

It may be noted that a back-propagation neural network with one (or more) sigmoid-type hidden layer(s) and a linear output layer can approximate any arbitrary (linear or nonlinear) function [30]. The number of hidden layers is normally chosen to be only one to reduce the network complexity and increase the computational efficiency [31]. In this way, a back-propagation neural network is selected for this prediction study, and it consists of four layers: one input layer (source nodes), two hidden layers with ten neurons in the first layer and five neurons in the second layer (with tangent hyperbolic sigmoid activation function), and one output layer with pure linear activation function (Fig. 3).

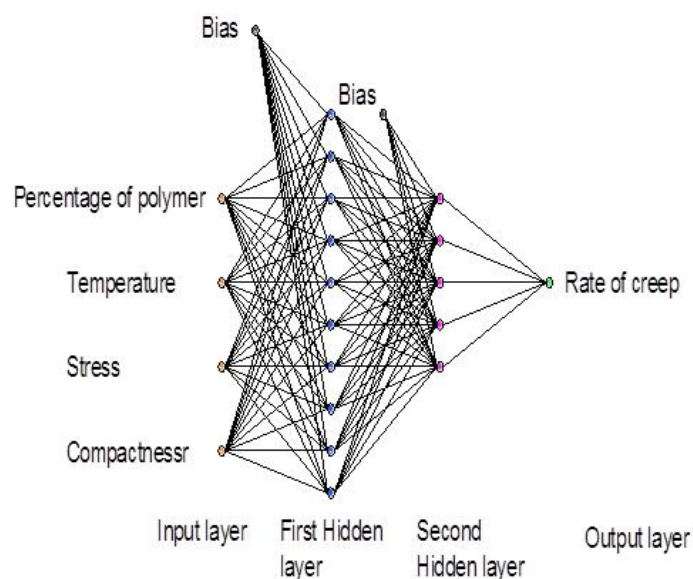


Figure 3. Neural network architecture.

The tangent hyperbolic sigmoid activation function "*tansig*" is more effective for nonlinear applications. In each of the two hidden layers, we use 10 and 5 neurons, respectively. Depending on to these neurons, we will adjust the matrix of the weights and will fix the weights of connections with bias to find results effective.

The Levenberg algorithm (*trainlm*) is used for the learning because it is more effective than other algorithms, as regards the use of time and memory in the execution [13]. The performance of the model is measured by the mean of square error function (*MSE*) equation (4), and "*R*" equation (5). Regression "*R*" values measured the correlation between predicted and measured values. *R* value equal 1; imply a precise relationship, 0 a random relationship. The superb performance of the model it has been ensured by the higher value of *R* and lower *MSE* value.

The input data have been divided randomly by the "dividerand" Matlab, in 70 %, 15 % and 15 % indicating the percentage of training or learning, the percentage of validation and the percentage of control or test, respectively.

$$MSE = \frac{1}{N} \sum_{k=1}^n \left(y_k - \bar{y}_k \right)^2 \quad (4)$$

$$R = \frac{\sum_{k=1}^n \left(y_k - \bar{y}_k \right) \left(y_k^* - \bar{y}_k^* \right)}{\sqrt{\sum_{k=1}^n \left(y_k - \bar{y}_k \right)^2 \sum_{k=1}^n \left(y_k^* - \bar{y}_k^* \right)^2}}, \quad (5)$$

where y_k is the desired value;

y_k^* is the estimated value;

N is the number of neurons in the output layer;

n is the number of vectors presented to the network;

$$\bar{y}_k = \frac{1}{n} \sum_{k=1}^n y_k; \quad \bar{y}_k^* = \frac{1}{n} \sum_{k=1}^n y_k^*$$

The database is divided into three parts: Learning (70 %), Testing (15 %) and validation (15 %). A set of training data was used to train the ANN model. The set of validation data was used to stop the learning process, and the set of test data was used to evaluate the ANN model performance. After completion of the learning process. Each set of data consists of vectors of the influencing parameters, and corresponding creep rate. After distributing the data will be normalized between -1 and +1. Before the submission to the ANN for them to be in agreement with the bounds of the Tangent sigmoid transfer function used in the hidden layers and the linear sigmoid function of the output layer.

The architecture of the developed ANN model is first described, followed by the determination of its learning parameters and performance. The model was trained and tested with a set of learning data, testing, and validation using the back-propagation algorithm. Implementation and simulation were performed using MATLAB software. Initially, the optimal number of neurons in the hidden layer was determined (Fig. 2).

3. Results and Discussion

ANN model analysis. The precision of the artificial neuron network depends principally on the chosen architecture of the neuron network. The number of hidden layers and neurons in each layer do not obey any rule of selection. The optimal network architecture was determined using the error correction approach.

The creep rate values predicted with ANN and the experimental values of the different mixtures studied are shown in (Fig. 4). It can be concluded that the proposed ANN could learn the relationship between the different input parameters (temperature, rubber contents, loading stress and compactness) and the output parameter (creep rate). We remark, that the values of the creep rate predicted with ANN are close to the measured experimental values. This means that ANN is able to generalize the input and output variables with a good precision. The error percentage between the predicted and measured creep rate is also shown in this (Fig. 4), easily we can see the error is very low between these two values.

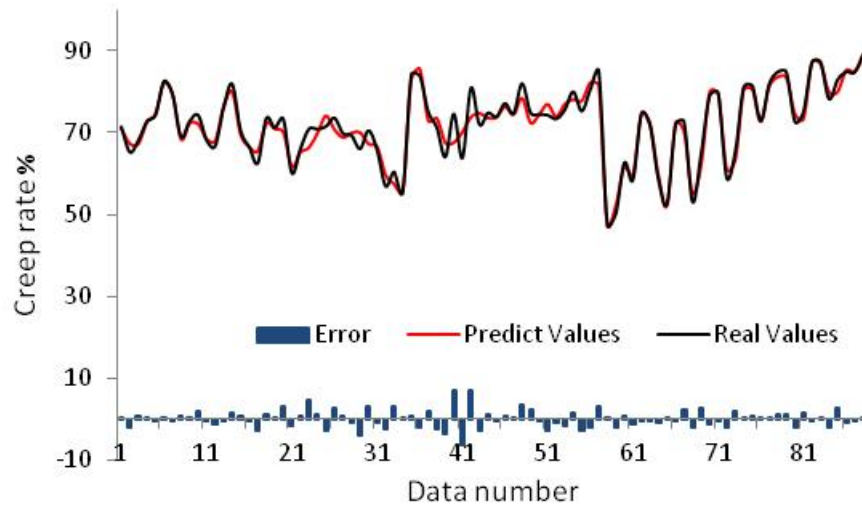


Figure 4. Comparison of real values and predicted values.

The relationship between the predicted creep rate and the experimentally measured creep rate is shown in the (Fig. 5). We can observe the creep rate predicted values are very close to experimental values creep rate. This demonstrates a good correlation between the input and output parameters of the ANN model developed. Also, in this (Fig. 5), the correlation coefficient R values in training, validation and testing the data set are 0.9839; 0.9838; 0.9922 and 0.9858, respectively. This result implies that; the developed model has considerable accuracy for predicting.

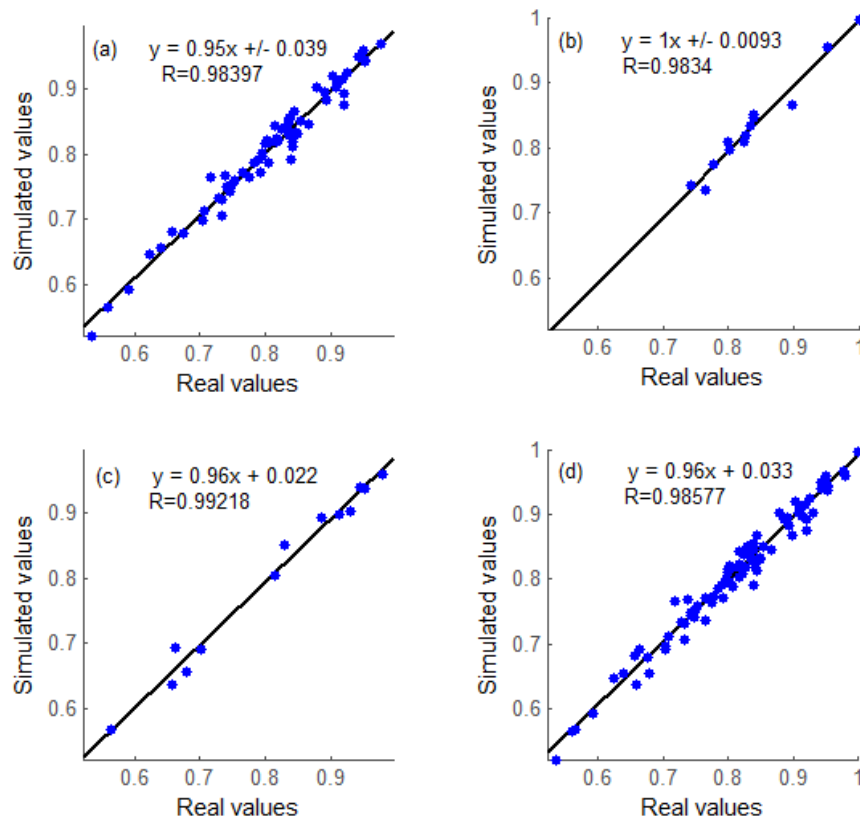


Figure 5. Relationship between the Real and ANN predicted values for (a) training data, (b) validation data, (c) testing data, and (d) all data.

Influence of polymer content on creep rate. The ANN model developed depending on four input constants, it is very precious to appreciate the influence of each constant on creep rate. For this purpose, the ANN model is applied to simulate the effect of additive content and temperature on creep rate.

Fig. 6 shows the variation of creep rate with polymer content (Temperature was kept constant at 25 °C, and 60 °C, the stress was kept at 0.14 MPa). It can be seen that at 2 % additive contents in both cases of temperature, the creep rate is reduced compared with others percent additive contents.

The critical observation is that the creep rate predicted values is very close to the experimental measured values on both cases. It can be concluded that the ANN developed model has important accuracy for predicting.

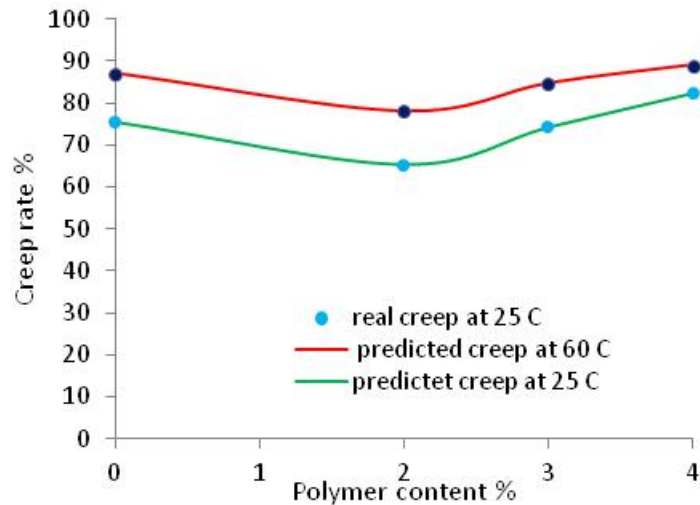


Figure 6. Effect of polymer content on final creep rate at 25 °C and 60 °C.

Fig. 7 hosts the variation of creep rate with temperature (Polymer content was kept constant at 2 % and the stress was kept at 0.14 MPa).

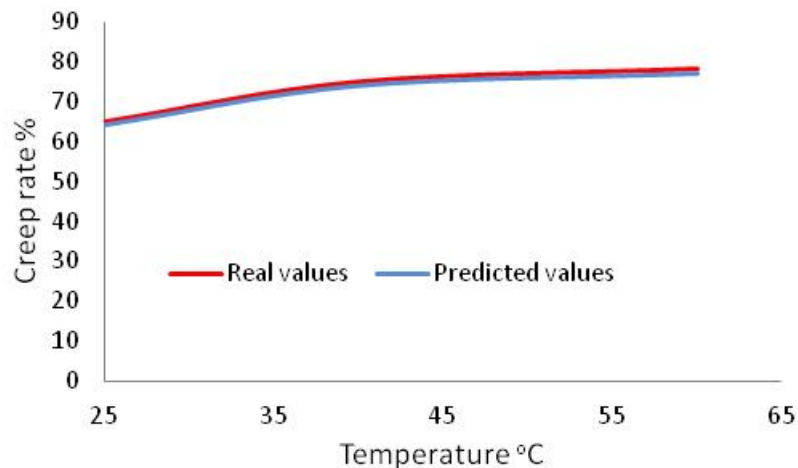


Figure 7. Effect of temperature on final creep rate.

It can be seen that the creep rate is influenced by temperature, the creep rate decreases at low temperature 25 °C and the increase in high temperature 60 °C. The critical observation is the two curves are superposed. It can be concluded that the ANN developed model can be used to predict the effect of temperature on creep deformation.

According to the results it should be noted that the use of polymers improves the creep behavior of bituminous concretes. As it was proved earlier [23], [28], artificial neural network proposed model found to be an effective tool to predict asphalt concrete creep deformation.

The reader must not forget that the obtained results at the end of this study is valid only for a specific type of aggregate, bitumen, polymer, modification technique, static creep test [1] and laboratory conditions

4. Conclusion

In this study, the ANN model was proposed to achieve a high degree of precision in the prediction of modified asphalt concrete creep rate. Based on the results of this study, the following outcomes were achieved:

1. Rubber contents, testing temperatures, compactness, and stress condition have a significant impact on creep rate. Back-propagation neural networks algorithms are used for the process.

2. The experimental creep rate values versus the predicted values by ANN compared using correlation coefficient R. The performance of the model is measured by the mean square error function (MSE). The correlation coefficient R is greater than 0.98 %. It is clearly shown that the ANN model proposed has better capability to predict the final creep rate in a short time with low error. It has indicated good agreement between ANN predicted values and experimental ones.

3. In addition, the ANN is applied to observe the effect of additive content and the temperature on creep rate. The results indicate that the creep rate of asphalt concrete can be improved through incorporating 2 % of the polymer in the powder form into the mixtures. That means the polymers reduce the creep rate. The increase in additive contents over 2 % (3 % and 4 %) does not reduce significantly the creep rate. So, the creep rate is also influenced by variation of temperature, the results indicate that the creep rate increases with temperature.

4. The ANN proposed in this work can be useful in the design of future studies on this topic for making a primary decision about the use of different variables in the modified or unmodified asphalt mixtures.

References

- Haddadi, S., Ghorbel, E., Laradi, N. Fluage des bétons bitumineux Influence de la classe du bitume. 2016. 8189 (May). DOI: 10.1080/19648189.2008.9693011
- Huang, Y.H. Pavement Analysis and Desig (Section edition). 2004. Pp. 775.
- Bahia, H.U., Hanson, D.I., Zeng, M., Zhai, H., Khatri, M.A., Anderson, R.M. Characterization of Modified Asphalt Binders in Superpave Mix Design 2001.
- Airey, G.D. Rheological evaluation of ethylene vinyl acetate polymer modified bitumens. 2002. 16. Pp. 473–487.
- Ag, E. Use of waste high density polyethylene as bitumen modifier in asphalt concrete mix. 2004. 58. Pp. 267–271. DOI: 10.1016/S0167-577X(03)00458-0
- Frantzis, P. Crumb Rubber-Bitumen Interactions : Diffusion of Bitumen into Rubber. 2004. (August). Pp. 387–390.
- Xiao, F., Amirkhanian, S., Asce, M., Juang, C.H., Asce, M. Rutting Resistance of Rubberized Asphalt Concrete Pavements Containing Reclaimed Asphalt. 2007. 1561 (June). DOI: 10.1061/(ASCE)0899-1561(2007)19
- Romero, M., Fernandes, S., Madalena, M., Forte, C., Figueiredo, L., Leite, M., Marumbi, R., Caxias, D. De, Brazil, R.J. Rheological Evaluation of Polymer-Modified Asphalt Binders 2. Materials and Methods. 2008. 11(3). Pp. 381–386.
- Ziari, H., Goli, A., Asce, A.M., Amini, A. Effect of Crumb Rubber Modifier on the Performance Properties of Rubberized Binders. 2016. Pp. 1–9. DOI: 10.1061/(ASCE)MT.1943-5533.0001661
- Venudharan, V., Biligiri, K.P. Conceptualization of permanent deformation characteristics of rubber modified asphalt binders: Energy-based algorithm and rheological modeling. Construction and Building Materials. 2016. 126. Pp. 388–397. DOI: 10.1016/j.conbuildmat.2016.09.065.
- Behnood, A., Modiri Gharehveran, M. Morphology, rheology, and physical properties of polymer-modified asphalt binders. European Polymer Journal. 2019. 112. Pp. 766–791. DOI: 10.1016/j.eurpolymj.2018.10.049.
- Tarefder, R.A., White, L., Zaman, M. Neural Network Model for Asphalt Concrete Permeability. 2005. (February). Pp. 19–27.
- Dhaka, V.S. Comprehensive Neural Network Techniques Application in Wheat Yield Prediction. 2015. 4(8). Pp. 2936–2944.
- Thodesen, C., Xiao, F., Amirkhanian, S.N. Modeling viscosity behavior of crumb rubber modified binders. Construction and Building Materials. 2009. 23 (9). Pp. 3053–3062. DOI: 10.1016/j.conbuildmat.2009.04.005.
- Venudharan, V., Biligiri, K.P. Heuristic principles to predict the effect of crumb rubber gradation on asphalt binder rutting performance. Journal of Materials in Civil Engineering. 2017. 29(8). Pp. 1–10. DOI: 10.1061/(ASCE)MT.1943-5533.0001880
- Zavrtanik, N., Prosen, J., Tušar, M., Turk, G. The use of artificial neural networks for modeling air void content in aggregate mixture. Automation in Construction. 2016. 63. Pp. 155–161. DOI: 10.1016/j.autcon.2015.12.009
- Ritchie, S.G., Kaseko, M., Bavarian, B. Development of an Intelligent System for Automated Pavement Evaluation. Transportation Research Record: Journal of the Transportation Research Board. 1991. (1311). Pp. 112–119. URL: <http://trid.trb.org/view.aspx?id=365537>.
- Kaseko, M.S., Ritchie, S.G. A neural network-based methodology for pavement crack detection and classification. Transportation Research Part C. 1993. 1(4). Pp. 275–291. DOI: 10.1016/0968-090X(93)90002-W
- Roberts, C.A., Attoh-Okine, N.O. A Comparative Analysis of Two Artificial Neural Networks Using Pavement Performance Prediction. Computer-Aided Civil and Infrastructure Engineering. 1998. 13(5). Pp. 339–348. DOI: 10.1111/0885-9507.00112
- Kim, Y., Kim, Y.R. Prediction of layer moduli from falling weight deflectometer and surface wave measurements using artificial neural network. Transportation Research Record. 1998. (1639). Pp. 53–61. DOI: 10.3141/1639-06
- Mei, X., Gunaratne, M., Lu, J.J., Dietrich, B. Neural network for rapid depth evaluation of shallow cracks in asphalt pavements. Computer-Aided Civil and Infrastructure Engineering. 2004. 19(3). Pp. 223–230. DOI: 10.1111/j.1467-8667.2004.00350.x
- Thodesen, C., Xiao, F., Amirkhanian, S.N. Modeling viscosity behavior of crumb rubber modified binders Modeling viscosity behavior of crumb rubber modified binders. Construction and Building Materials. 2009. 23(9). Pp. 3053–3062. DOI: 10.1016/j.conbuildmat.2009.04.005. URL: <http://dx.doi.org/10.1016/j.conbuildmat.2009.04.005>.
- Tapkın, S., Çevik, A., Us, Ü. Expert Systems with Applications Prediction of Marshall test results for polypropylene modified dense bituminous mixtures using neural networks. 2010. 37. Pp. 4660–4670. DOI: 10.1016/j.eswa.2009.12.042
- Terzi, S., Karaşahin, M., Gökova, S., Tahta, M., Morova, N., Uzun, I. Asphalt concrete stability estimation from non-destructive test methods with artificial neural networks. Neural Computing and Applications. 2013. 23(3–4). Pp. 989–997. DOI: 10.1007/s00521-012-1023-1

25. Ghanizadeh, A.R., Ahadi, M.R. Application of artificial neural networks for analysis of flexible pavements under static loading of standard axle. *International Journal of Transportation Engineering*. 2015. 3(1). Pp. 31–43.
26. Mirabdolazimi, S.M., Shafabakhsh, G. Rutting depth prediction of hot mix asphalts modified with forta fiber using artificial neural networks and genetic programming technique. *Construction and Building Materials*. 2017. 148. Pp. 666–674. DOI: 10.1016/j.conbuildmat.2017.05.088. URL: <http://dx.doi.org/10.1016/j.conbuildmat.2017.05.088>.
27. Kamboozia, N., Ziari, H., Behbahani, H. Artificial neural networks approach to predicting rut depth of asphalt concrete by using of visco-elastic parameters. *Construction and Building Materials*. 2018. 158. Pp. 873–882. DOI: 10.1016/j.conbuildmat.2017.10.088
28. Alrashydah, E.I., Abo-Qudais, S.A. Modeling of creep compliance behavior in asphalt mixes using multiple regression and artificial neural networks. *Construction and Building Materials*. 2018. 159. Pp. 635–641. DOI: 10.1016/j.conbuildmat.2017.10.132.
29. Ziari, H., Amini, A., Goli, A., Mirzaeiyan, D. Predicting rutting performance of carbon nano tube (CNT) asphalt binders using regression models and neural networks. *Construction and Building Materials*. 2018. 160. Pp. 415–426. DOI: 10.1016/j.con-buildmat.2017.11.071
30. Simon Haykin (McMaster University, Hamilton, Ontario, C. *Neural Networks – A Comprehensive Foundation – Simon Haykin.pdf*2005.
31. 배상현, 백형래이진섭. *Neural Network Toolbox Documentation*. 조선대학교 출판부. 1998. Pp. 846.

Contacts:

Brahim Saoudi, saoudibra@yahoo.fr

Smail Haddadi, smail_haddadi@yahoo.fr

© Saoudi, B.S.,Haddadi, S.H., 2021



DOI: 10.34910/MCE.101.7

Basalt fiber reinforced expanded clay concrete for building structures

V.V. Galishnikova, M. Kharun, D.D. Koroteev, P.C. Chiadighikaobi*

Peoples Friendship University of Russia (RUDN University), Moscow, Russian Federation

* E-mail: passydking2@mail.ru

Keywords: expanded clay concrete, basalt fiber, compressive strength, flexural strength, finite element analysis

Abstract. Expanded clay concrete is a perspective structural material because of its lightweight, heat and sound insulating properties. However, due to its brittleness and low strength to flexure and compression it cannot be used in load bearing structures. Adding basalt fiber in concrete increases mechanical properties. The research work presents an experimental study of the mechanical behavior of structural expanded clay basalt fiber concrete. The main purpose of this study was to test the effect of chopped basalt fiber in expanded clay concrete to improve its strength. An experimental characterization of mechanical behavior by compressive and flexural tests was achieved. Dispersed chopped basalt fiber was used as reinforcement of specimens with sizes of 100×100×100 mm and 100×100×400 mm. Mathematical models for determining the compressive strength and the flexural strength of the expanded clay concrete depending on the proportion of basalt fiber and the curing period are developed. The finite element analysis was done by using ANSYS software, a model was developed to validate the different results obtained experimentally. The experimental results show that high percent of basalt fiber in the expanded clay concrete gives higher strength. In effect, an influence directly on the failure mode was observed on expanded clay concrete without basalt fiber and then read by the value of strength and ultimate deformation.

1. Introduction

For many years now, it has become very important in construction for rehabilitation and strengthening of reinforced concrete. Reinforced concrete structure as the whole element can withstand tensile flexural loading, however, the concrete cover layer in such structure is not reinforced and cannot withstand such loading, it causes cracking of the structures during their operation which leads to corrosion of steel reinforcement and damage of the structure [1–3]. The reinforcement materials for concrete structures varies based on the properties. With the air pollution related problems increasing globally and rising of the mean temperature around the globe, it became a necessity investigate to investigate new solutions in order to diminish the magnitude of such environmental issues [4]. The author investigated the use of bamboo in concrete reinforcement to serve in high temperate region and solve environmental issues.

The tensile flexural strength of concrete is an important method to determine cracking behavior of concrete and to compute deflection under flexure. Many factors have been shown to influence on the flexural tensile strength, particularly the level of concrete strength, size of member, age of concrete and confinement to flexure member etc [5].

The physical, mechanical and durability properties of basalt fiber (BF) reinforced lightweight pumice concrete including water absorption, bulk density, strength and sulfate attack resistance were investigated [5, 6]. In the study [6], Taguchi method was proposed by the author to optimize compressive strength, flexural strength and sulfate resistance properties.

Recently, basalt fiber reinforced polymer (BFRP) has been developed because of its properties, such as high elastic modulus and elastic strength, better tensile strength than E-glass fibers, better failure strain than carbon fibers [7–10]. In addition, it has good resistance to chemical attack and high temperature, impact load and fire with less poisonous fumes, lower cost as compared with other types of fibers [11–13]. BF can be



considered as a green product as compared with other materials because the natural raw materials are used for their production, any chemical additives or hazardous materials are not used in the melting process, any chemical does not appear during the production process, which is dangerous to health [14–16].

The use of fiber reinforced polymer (FRP) materials in flexural strengthening of reinforced concrete shallow beams has been investigated quite extensively by many researchers [17–20]. The results of these investigations have demonstrated the effectiveness of different forms of FRP systems to achieve the desired effects.

In most part of research works [21–25], the authors pointed that concrete, reinforced with BF, has high flexural strength and tensile strength as compared with concrete without the fiber. However, compressive strength of concrete with BF increases slightly at the early age and even decreases at the late age.

Generally, there is less information documented on the workability of expanded clay as an aggregate in concrete, reinforced with BF [26]. From our point of view, expanded clay concrete (ECC) is a perspective structural material because of its certain advantages, such as lightweight, heat and sound insulating properties [27–33]. However, due to its brittleness and low strength to flexure and compression it cannot be used in load bearing structures. Safe performance of connecting joint applied to different concrete ages is highly important

when joints are placed in composite structures since joint is involved in mutual deformation of precast and monolithic concretes [34].

In research work [35], the authors considered the energy efficiency light-weight wall technology for over story of buildings. Further in the research work was developed a mathematical model of non-stationary heat transfer through the enclosing wall using the lightweight wall technology and evaluated the efficiency of various designs of lightweight wall.

The introduction of silica fume into the cement system lowers the pH of the aqueous extract by 28 days of hardening relative to the composition without silica fume by 3 %, which indicates a decrease in the CaO content in the system and better preservation of basalt fiber. It confirmed by the absence of changes in the pH of aqueous extracts of compositions with fiber and without fiber in compositions containing MK-85 for all periods of hardening of cement stone. Thus, to increase the durability of basalt fiber in cement systems effectively use silica fume (micro silica) addition, which reduces the amount of free lime in the environment of hydrating cement [36]. Series of studies and experiments on the durability of basalt fiber reinforced concrete, the construction environments and methods of constructions are explained in detail [37].

Finite element analysis is a numerical method for analyzing complex structural problems. Like homogeneous materials, composite materials can also be analyzed using pre- and post-processing facilities of ANSYS to study their behavior under different load conditions [38], temperature distribution over the thickness of the experimental wall cover can also be analyzed in ANSYS [39].

The displacements of the concrete structures are small compared to the dimensions of the structure and hence in the present study geometric non-linearity is neglected. Since the concrete is a non-homogeneous material and behaves linearly over a small percentage of its strength, material non-linearity is considered [40].

Nonlinear finite element analysis is a powerful tool in determining the internal stress, strain distribution in concrete structures. Nonlinear analysis gives enhanced data of serviceability and ultimate strength. The finite element analysis is adopted with the different material nonlinearities such as stress-strain behavior of concrete, cracking of concrete [41].

Taking the above into account, the aim of this research work is to study the influence of chopped basalt fiber on physical-mechanical properties of ECC, especially compressive and flexural behavior of the concrete.

The following tasks are determined to reach the above aim:

- Preparation and test of ECC specimens, reinforced with and without dispersed chopped BF, with sizes of 100×100×100 mm and 100×100×400 mm;
- Determination of compressive and flexural strength of ECC specimens with and without BF;
- Finite element analysis of compressive and flexural behaviors of the ECC structures with BF by modeling nonfinite element solutions (data), derived from laboratory experiments in a finite element software (ANSYS) and inputting the boundary conditions for better results.

Due to the properties of ECC reinforced with dispersed BF, this concrete can be used in high temperature regions.

This research paper investigates and analyses the strength of ECC reinforced with dispersed BF. Due to the brittleness of ECC mostly in flexure, this paper is faced with the task to investigate, identify and suggest the material for reinforcement that will cure the brittleness, increase the strength of ECC.

2. Materials and methods of research

According to the plan of study the following materials were used to prepare ECC specimens for determination of compressive strength and flexural strength:

- Lightweight Expanded Clay Aggregate (LECA) with fractions of 5-10 mm = 200 kg/m³ as the coarse aggregate;
- Quartz sand with fineness modulus of 2.7 = 585 kg/m³ as the fine aggregate;
- Quartz flour of 50 µm = 100 kg/m³ as the mineral filler;
- Portland cement CEM I 42.5 N = 500 kg/m³ as the binder;
- Micro silica = 62.5 kg/m³ and fly ash = 62.5 kg/m³ as the organo-mineral additives;
- SikaPlast®Concrete in liquid form = 8 l/m³ as the super plasticizing and water reducing admixture;
- Tap water = 255 l/m³ for mixing.

LECA used in this experimental study was obtained from the Production Plant "Keramzit", Serpukhov District in Moscow Region, Russia. The physical properties and sieve analysis of LECA used in this study is illustrated in Table 1.

Table 1. Physical properties and sieve analysis of LECA.

Physical Property	Value
Specific gravity	0.69
Fineness modulus	5.93
Bulk density (compacted), [kg/m ³]	278
Water absorption (24 h), [%]	26.4
Sieve Analysis, [mm]	Cumulative Percent by weight passing
10.0	90.4
8.0	5.7
5.0	3.9
3.0	0

Before adding LECA to concrete mix, the coarse aggregate was pre-immersed in the water for 24 hours before mixing. The LECA is removed from the water and placed on a sieve for 2 hours to dry off the water in order to reach to almost saturated surface dry condition.

Quartz sand and quartz flour used in the experiment were obtained from the Quarry Plant "Tyutchevo", Naro-Fominsky District in Moscow Region, Russia. The binder Portland cement CEM I 42.5 N, mineral additives micro silica and fly ash were obtained from the Maltsovsky Cement Plant, Fokino District, Bryansk Region, Russia.

The physical properties of quartz sand and the chemical compositions of quartz flour, Portland cement, micro silica and fly ash respectively are presented in Tables 2 and 3.

Table 2. Physical properties of quartz sand.

Physical Property	Value
Grain size, [mm]	0.5–1.0
Bulk density (compacted), [kg/m ³]	1430
Hardness (on the Mohs scale)	7
Crushability	0.3
Humidity, [%]	1.7

Table 3. Chemical compositions of quartz flour, Portland cement, micro silica and fly ash in percentage (%).

Chemical Elements	SiO ₂	Al ₂ O ₃	Fe ₂ O ₃	K ₂ O	CaO	MgO	SO ₃	P ₂ O ₅	TiO	MnO	Na ₂ O
Quartz Flour	99.63	0.23	0.12	-	0.02	-	-	-	-	-	-
Portland Cement	21.90	4.86	3.3	0.56	65.77	1.15	2.1	-	-	-	0.36
Micro silica	98.77	0.23	0.07	0.26	0.31	0.04	0.17	-	-	-	0.15
Fly Ash	66.24	19.81	6.41	1.39	3.13	1.21	-	0.36	0.86	0.05	0.54

SikaPlast® Concrete is the super plasticizing and water reducing admixture used in this experiment and it is a brown color aqueous solution of modified polycarboxylate esters and lignosulfonates.

The chopped BF, used in this study, was obtained from a famous BF Manufacturing Plant known as Russkiy Bazalt, located in Chelyabinsk, Russia. Table 4 below presents the chemical compositions of chopped BF used in this experiment.

Table 4. Chemical compositions of chopped BF.

Chemical Elements	SiO ₂	Al ₂ O ₃	FeO + Fe ₂ O ₃	Na ₂ O + K ₂ O	CaO	MgO	TiO ₂	Others
Percentage (%)	57.3	15.4	11.7	1.9	7.3	4.1	1.6	0.7

Five different mixes of ECC were accepted for this study, containing of the above mixes and the chopped BF with diameter of 15 µm and length of 20 mm in the ratio of 1:0, 1:0.045, 1:0.09, 1:0.012 and 1:0.016 by weight.

Experimental study of ECC was carried out in accordance with the CIS Interstate Standard GOST 10180-2012 [42], considering the requirements of ACI 211.1-91 [43].

Total 10 series of ECC test specimens were produced from the stated compositions with dimensions of 100×100×100 mm in 5 series; 100×100×400 mm in 5 series.

In accordance with the plan of experiment, each series consists of 9 specimens, total 90 specimens. All ECC specimens were cured in air-humid condition in wet sawdust at the room temperature of 19–22 °C.

Experimental study of ECC was carried out at the curing periods of 7, 14 and 28 days on a hydraulic press of up to 1500 kN at the compression test, and up to 150 kN at the flexural test.

The destruction of the surface of the fiber occurs when its interaction with hydrated lime released during the hardening process. In order to increase fiber resistance, silica fume was additionally introduced into the composition of cement concrete. Detailed research on this is seen in the study [36].

Mathematical processing of the experimental data was carried out based on probability theory and mathematical statistics which allowed obtaining the results of experimental study with the reliability of $\alpha \approx 0.95$.

Using of the mentioned materials to produce ECC specimens, and their study by the above method allowed obtaining the statistically significant results of experimental study.

For finite element analysis ANSYS software was chosen. It is a finite element general-purpose modeling package for solving numerical and wide range of mechanical problems. These problems can be solved using static linear structural analysis [41].

In general, a finite element analysis and solution in ANSYS may be broken into three stages. Before these three stages are listed, the project must be specialized. For the project analyzed in this research paper, structural was selected in the preferences. The three main stages are:

1. Preprocessing – defining the problem: it is necessary that every task and problem be defined. The major steps in preprocessing are:

- a. Define key points/lines/areas/volumes;
- b. Define element type and material/geometric properties;
- c. Mesh lines/areas/volumes as required.

2. Solution – assigning loads, constraints, and solving it is necessary to specify the loads (pressure) and constraints then, solve the resulting set of equations.
3. Postprocessing – further processing and viewing of the results are:
 - a. Lists of nodal displacements;
 - b. Element forces and moments;
 - c. deflection plots;
 - d. Stress contour diagrams or temperature maps. But in this research, the displacement at all degrees of freedom was checked [38].

To calculate tasks in ANSYS software, the finite element method is used. The essence of this method is that the continuous medium is replaced by a finite number of structural elements of finite size, connected with each other only at the nodal points.

To analyze the concrete, some important properties and conditions must be considered. These properties are modules of elasticity and Poisson's ration which were derived from the laboratory experiments of the ECC with BF. For comprehensive strength, a load of 22.5 MPa was imposed on the analysis in Fig. 6, 28.5 MPa in Fig. 7 and 36.2 MPa in Fig. 8. The dimensions of ECC with BF specimen are 100×100×100 mm.

For flexural strength, a load of 3.7 MPa was imposed on the analysis of Fig. 9, 4.9 MPa in Fig. 10, 6.5 MPa in Fig. 11 [39]. The dimensions of the ECC specimen are 6000×6000×150 mm. A boundary condition of all degrees of freedom (UX, UY, UZ) = 0 for the support was considered making the support fixed. One of the most important stage in finite element analysis in ANSYS software is the element type and property (Fig. 1). In modeling and analyzing this concrete cube and prisms, brick 8 node 185 element property is used.

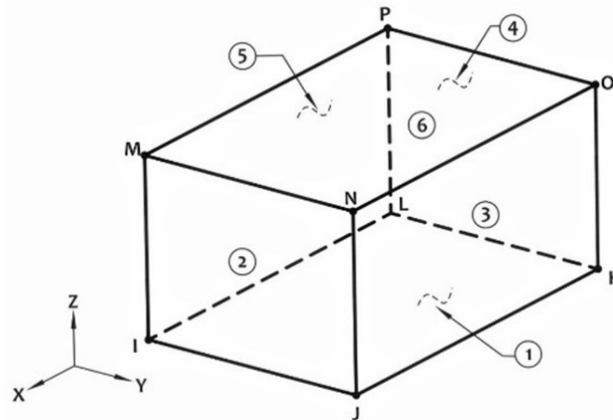


Figure 1. Solid 185 homogeneous structural solid.

Fig. 1 expresses the element type used. Where letters I-P show the nodes and numbers 1-6 show the solid plane (surface) of the concrete solid [40].

Brick 8 node 18 means SOLID 185. It is a 3D element consisting 8 nodes in it. SOLID 185 is used for 3D modeling of solid structures. It is expressed by 8 nodes with 3 degrees of freedom at each node. This element type is assumed to possibly can undergo plasticity, stress stiffness, creep large deflection, and large strain.

3. Result and Discussion

The most important physical and mechanical properties of concrete are the compressive strength and the flexural strength. In the framework of this research the experimental determination of the compressive strength and the flexural strength of ECC produced with chopped BF and without BF were carried out. The experimental results are gotten at structural strength. The properties of basalt fiber like thermal resistance, acidic resistance, water resistance give this concrete a high durability which are fully illustrated by previous authors [36, 37].

Results of the laboratory tests of ECC specimens of 100×100×100 mm on the compressive strength are shown in Table 5.

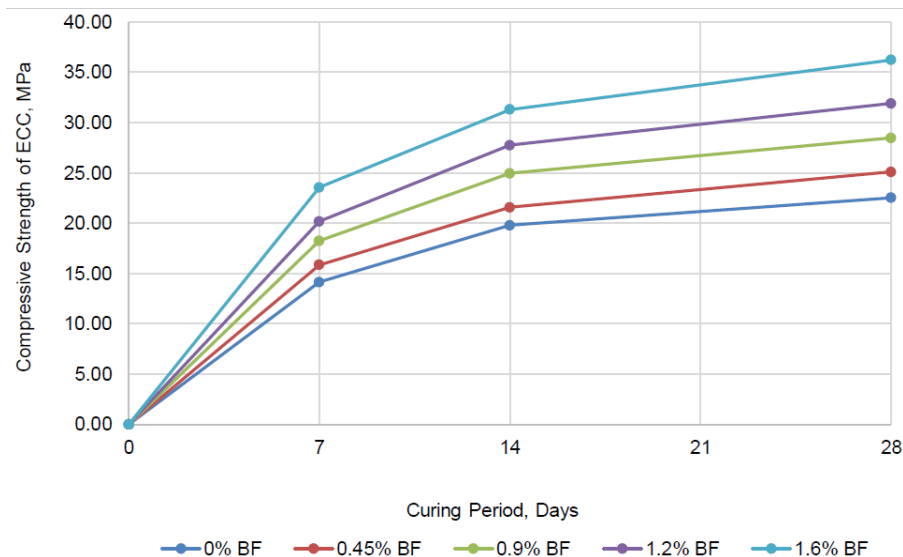
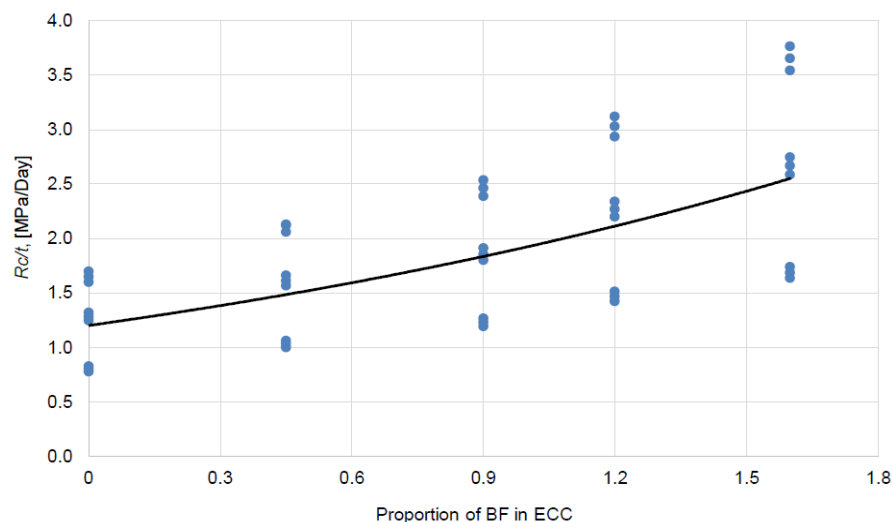
Table 5. Results of the laboratory tests of ECC specimens of 100×100×100 mm on the compressive strength.

Curing period, [days]	Compressive strength, [MPa]				
	0% BF	0.45% BF	0.9% BF	1.2% BF	1.6% BF
7	14.156	15.862	18.247	20.191	23.572
14	19.794	21.597	24.972	27.772	31.328
28	22.535	25.122	28.498	31.927	36.236

Fig. 2 shows the diagrams of changes in compressive strength of ECC depending on the curing period.

Experimental study of ECC specimens (Table 5 and Fig. 2) showed that addition of BF in ECC resulted an increase in the compressive strength which differs from some of the experimental studies done by previous authors where the authors checked the compressive strength of conventional high strength concrete with addition of chopped basalt fiber. Their results showed that addition of chopped basalt fiber in these conventional concrete specimens reduced the compressive strength of the concrete [17, 18, 19]. The results also showed that the compressive strength in 7 days of curing can reach about 60 % of the compressive strength of 28 days curing period regardless of whether ECC is without BF or with BF.

Fig. 3 shows the dependency of the compressive strength of ECC on the proportion of BF and the curing period.

**Figure 2. Compressive strength of ECC depending on the curing period of ECC specimens of 100×100×100 mm.****Figure 3. Dependency of the compressive strength of ECC on the percentage of BF and the curing period.**

Based on analytical data (Fig. 3), using the probability theory and mathematical statistics, a mathematical model of compressive strength of ECC depending on the percentage of cement and curing period was developed:

$$R_C = R_C^t + \frac{1.245 \times t \times e^{45 \times F}}{e^{45 \times F} + \frac{e^{45 \times F}}{t_F}} \quad (1)$$

where R_C is compressive strength of ECC, MPa; R_C^t is compressive strength of ECC (without BF) of the corresponding grade on the day of determination, MPa; 1.245 is coefficient of compressive strength changes of ECC with BF over the period, MPa/day; e is exponential function, $e \approx 2.71828$; F is proportion of BF in ECC, in relative units; t is curing period, day ($t \leq 28$ days); t_F – exposure of BF in ECC, $t_F = t$ without unit.

The proposed mathematical model is advisable to apply for assessment of the compressive strength of ECC with the accuracy of $\pm 4-5\%$ and the determination coefficient of $R^2 = 0.935$. It allows determining the permissible load on the structure that works on compression, such as walls.

Results of the laboratory tests of ECC specimens of 100×100×400 mm on the flexural strength are shown in Table 6.

Table 6. Results of the laboratory tests of ECC specimens of 100×100×400 mm on the flexural strength.

Concrete curing, [days]	Flexural strength, [MPa]				
	0% BF	0.45% BF	0.9% BF	1.2% BF	1.6% BF
7	2.422	2.844	3.219	3.728	4.397
14	3.298	3.836	4.411	5.028	5.855
28	3.658	4.278	4.905	5.668	6.488

Fig. 4 shows the diagrams of changes in flexural strength of ECC depending on the curing period.

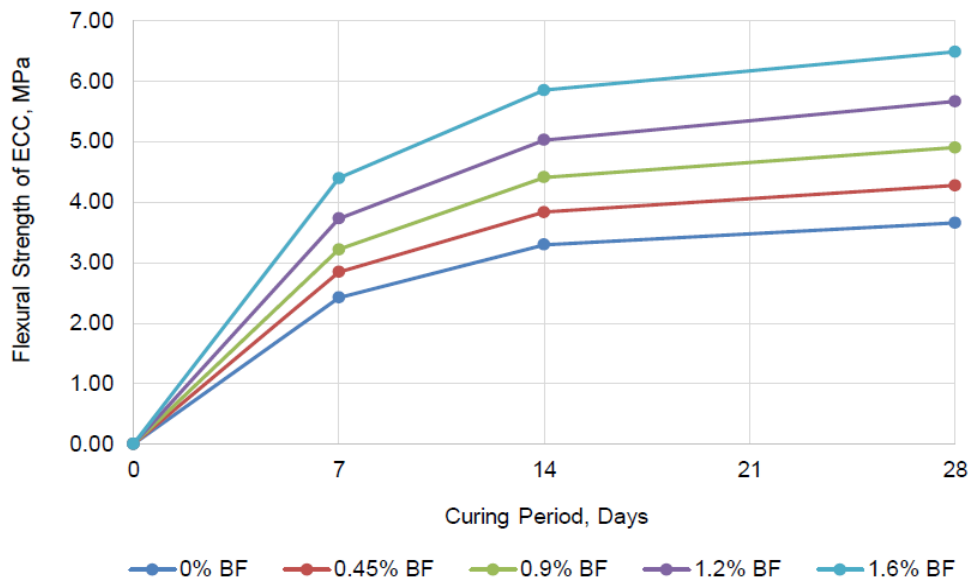


Figure 4. Flexural strength of ECC depending on the curing period of ECC specimens of 100×100×400 mm.

Analysis of the diagrams of the Fig. 2 and 4 shows that the strength growth in ECC specimens is smooth and uniform as in conventional concrete regardless of whether ECC is without BF or with BF. Though the growths in the flexural strength of concrete with addition of chopped basalt fiber were faster and higher in ECC than in conventional concrete, the growth in both types of concrete are significant in comparison with experiments of other researchers [17–20].

Analyzing the diagrams in Fig. 2 and 4, and tables 2 and 3, it can be concluded that ECC with 0.9 wt.% BF increases the compressive strength by more than 20 %, while 1.6 wt.% BF enhances more than 50 %, and the flexural strength by more than 30 %, while 1.6 wt.% BF enhances more than 75 %, i.e. a high percentage of BF in ECC gives a higher strength.

Fig. 5 shows the dependency of the flexural strength of ECC on the proportion of BF and the curing period.

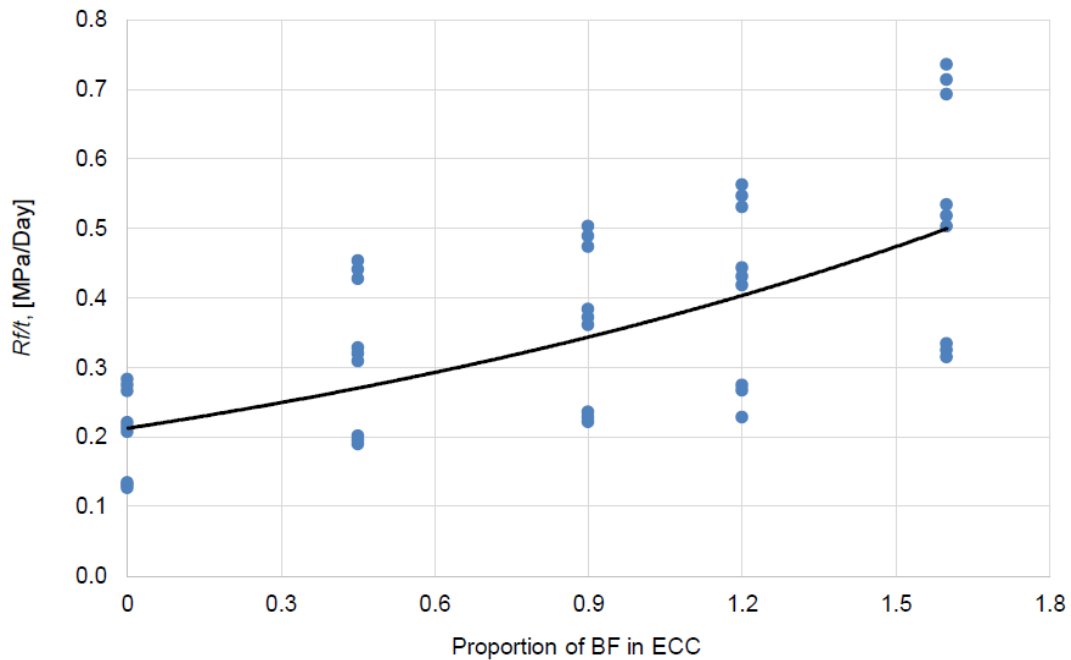


Figure 5. Dependency of the flexural strength of ECC on the proportion of BF and the curing period.

Analysis of diagrams in Fig. 3 and Fig. 5 shows that the nature of changes of compressive strength and flexural strength of ECC on the proportion of BF and the curing period is identical and grows exponentially.

Based on the analytical data (Fig. 5), using the probability theory and mathematical statistics, a mathematical model of flexural strength of ECC depending on the percentage of cement and curing period was developed:

$$R_f = R_f^t + \frac{0.215 \times t \times e^{53 \times F}}{e^{53 \times F} + \frac{e^{53 \times F}}{t_F}} \quad (2)$$

where R_f is flexural strength of ECC, MPa; R_f^t is flexural strength of ECC (without BF) of the corresponding grade on the day of determination, MPa; 0.215 is coefficient of flexural strength changes of ECC with BF over the period, MPa/day; e is exponential function, $e \approx 2.71828$; F is proportion of BF in ECC, in relative units; t is curing period, day ($t \leq 28$ days); t_F is exposure of BF in ECC, $t_F = t$ without unit.

The proposed mathematical model is advisable to apply for forecasting the flexural strength of ECC with the accuracy of $\pm 4-5\%$ and the determination coefficient of $R^2 = 0.927$. It allows determining the permissible load on the structure that works on flexion, such as slabs.

From the non-finite element results derived from laboratory experimental results, the data was inputted in the ANSYS finite element software to derive the deformation effect and influence of the load imposed on the ECC with and without BF. The results derived from finite element analysis is illustrated in Fig. 6–11. In Fig. 6–11, the maximum displacements and maximum stress are denoted as DMX and SMX respectively.

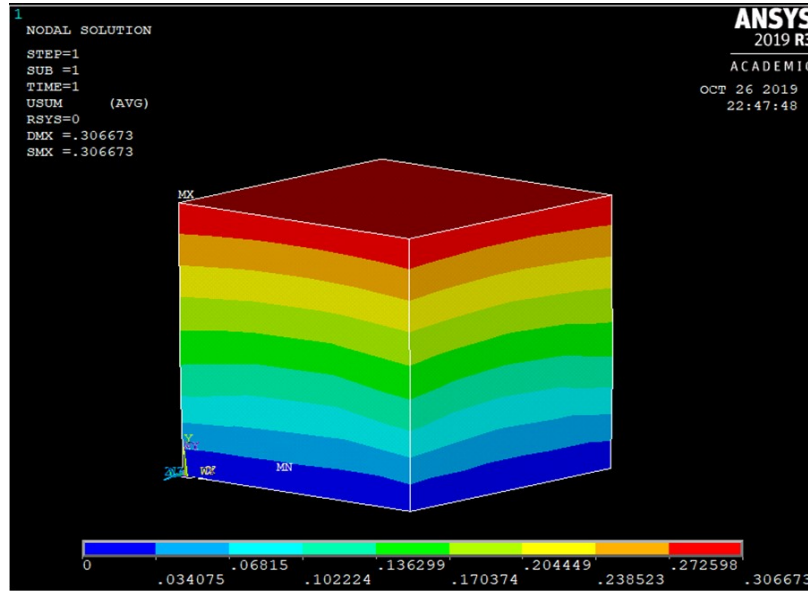


Figure 6. Nodal solution of ECC without BF.

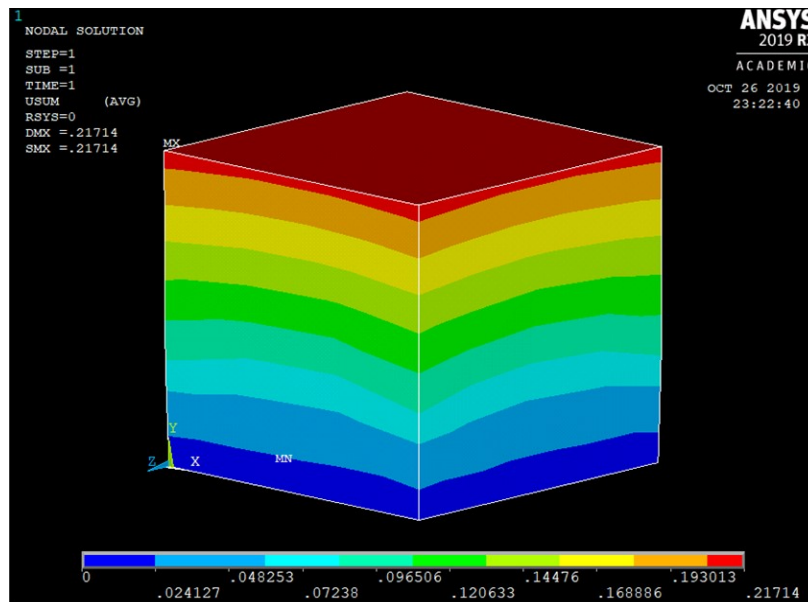


Figure 7. Nodal solution of ECC with 0.9 % BF.

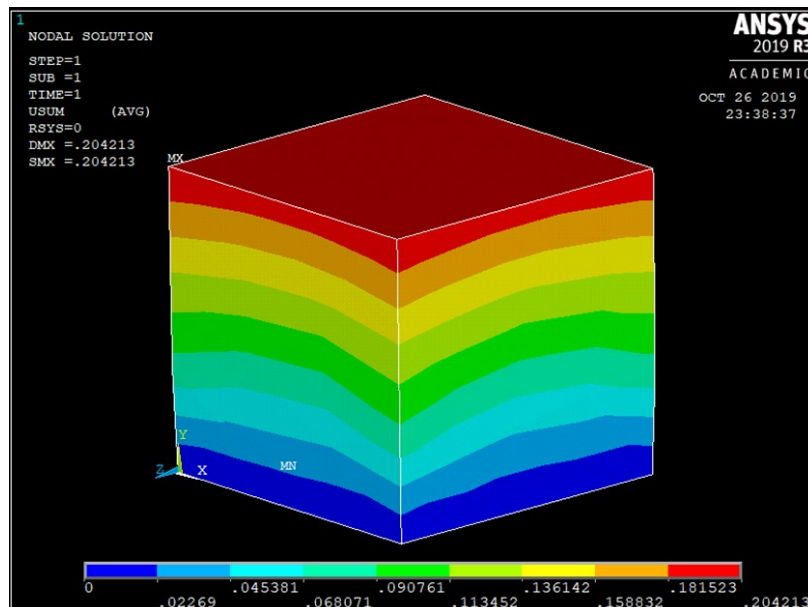


Figure 8. Nodal solution of ECC with 1.6 % BF.

The results derived from the finite element analysis, it is seen that ECC without BF (Fig. 6) shows more displacement when compared to the results of Fig. 7 and 8, while Fig. 6 shows more displacement than the result in Fig. 8.

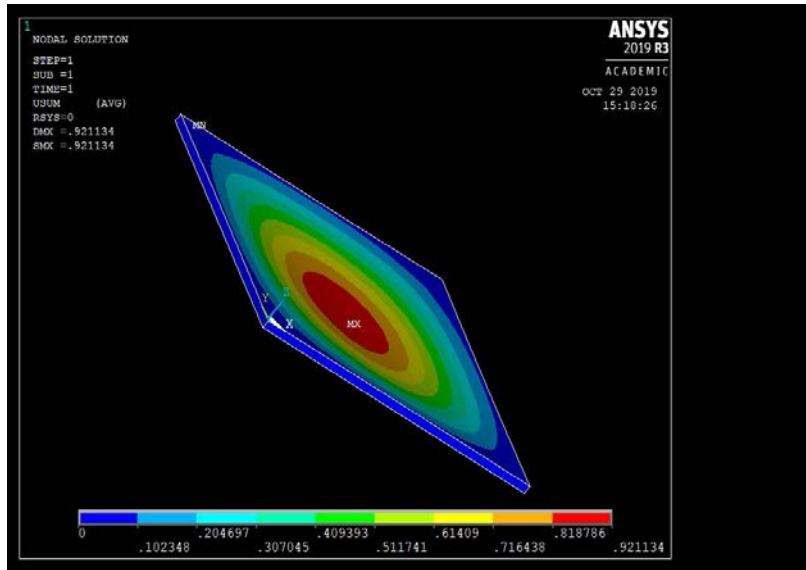


Figure 9. Nodal solution of ECC slab without BF.

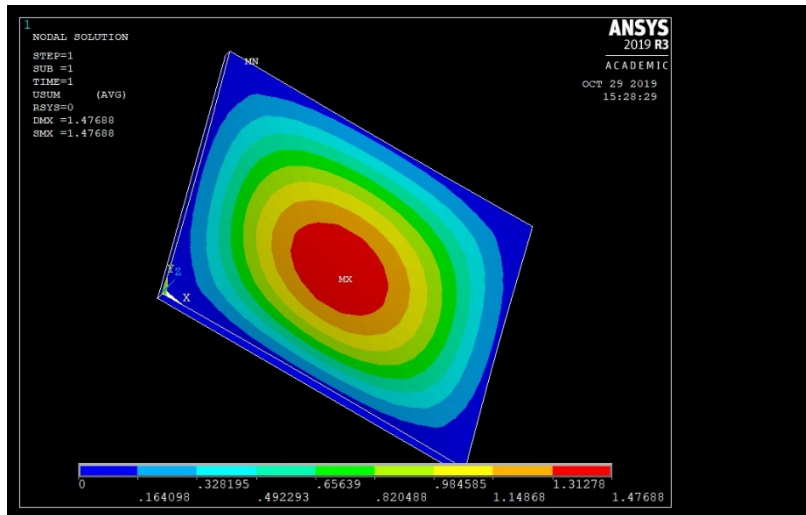


Figure 10. Nodal solution of ECC slab with 0.9 % BF.

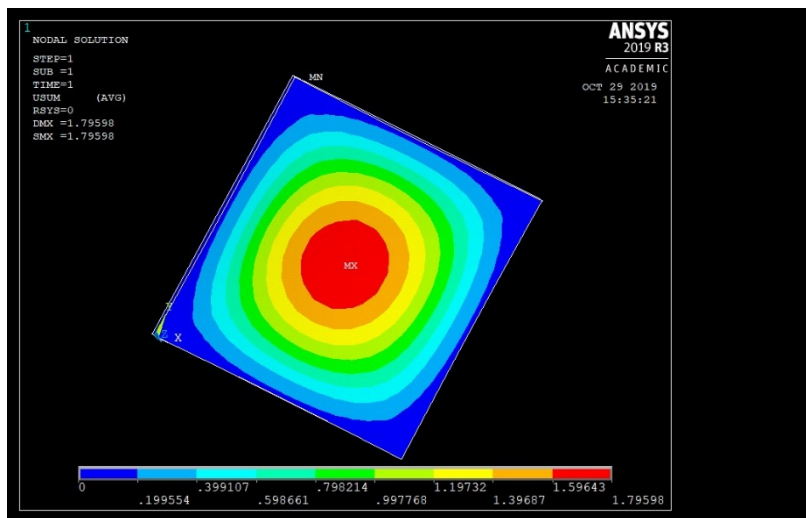


Figure 11. Nodal solution of ECC slab with 1.6 % BF.

The results from the ANSYS finite element analysis Fig. 6–11 show the maximum and minimum displacements at the critical stages. The results derived from the finite element analysis, it is seen that ECC

slab without BF (Fig. 9) shows more less displacement when compared to the results of Fig. 10 and 11, while Fig. 10 shows less displacement than the result in Fig. 11. Reason for this increase in displacement of the slab with increase in the percent of BF is, as a result, of the slab span. The boundary conditions for this analysis is all degrees of freedom where (U_x , U_y and U_z) = 0. The loads applied are the loads from the flexural strength on 28th day of Table 5.

From the experimental results, ECC with 1.6 % BF has highest compressive and flexural strength. To model ECC structures in a finite element software ANSYS, the dimensions and properties of this structure should be inputted in the software.

The finite element analysis using ANSYS software allowed to validate the different results obtained experimentally, such as for the specimens with 100×100×100 mm dimensions shows an increase of strength with increase of BF dosage, while in the specimens with 6000×6000×150 mm dimensions taken as slab shows a reduction in strength with increase in BF dosage that can be justified by supporting beams and columns at shorter distances.

4. Conclusion

Based on the study, the following conclusion can be drawn:

1. BF works well with ECC, and high percentage of BF in ECC gives higher compressive and flexural strength which contradicts the experimental motions that addition of BF in concrete decreases the compressive strength of concrete. This is so because of the compatibility of ECC with BF. And confirms the research work done by previous authors reviewed in this study which showed that the quantity of fiber in concrete affects strength of concrete.

2. The proposed mathematical models allow to determine the permissible loads on the structures during construction works. From the finite element analysis using ANSYS software allows to validate the different results obtained experimentally.

3. Analysing the results of previous authors, BF showed better effects to the concrete if compared to steel fiber and glass fiber. Based on the review analysis, it is seen that there are very little or no information on the workability of ECC and BF, but this research experiment showed better results based on the properties of expanded clay aggregate and BF.

5. Acknowledgements

The publication has been prepared with the support of the "RUDN University Program 5-100".

References

1. Francois, R., Laurens, S., Deby, F. Corrosion and its Consequences for Reinforced Concrete Structures. ISTE Press – Elsevier. London, 2018. 232 p. doi.org/10.1016/C2016-0-01228-7
2. Lushnikova, V.Y., Tamrazyan, A.G. The effect of reinforcement corrosion on the adhesion between reinforcement and concrete. Magazine of Civil Engineering. 2018. No. 80(4). Pp. 128–137. DOI: 10.18720/MCE.80.12
3. Uglyanitsa, A.V., Gilyazidinova, N.V., Zhikharev, A.A., Kargin, A.A. Study of reinforcement corrosion in expanded clay concrete. HBRC Journal. 2015. 11(3). Pp. 307–310. doi.org/10.1016/j.hbrj.2014.08.001
4. Bonivento Bruges, J.C., Vieira, G., Revelo Orellana, D.P., Togo, I. Parameter of thermal resistance of bamboo multilayer wall. Magazine of Civil Engineering. 2018. 83(7). Pp. 92–101. DOI: 10.18720/MCE.83.9
5. Weerheijm, J. Understanding the tensile properties of concrete. A volume in Woodhead Publishing Series in Civil and Structural Engineering. Woodhead Publishing. Cambridge, 2013. 398 p.
6. Yildizel SA, Calis G. Design and optimization of basalt fiber added lightweight pumice concrete using taguchi method. Romanian Journal of Materials 2019. 49 (4). Pp. 544–553.
7. Choi, J., Lee B. Bonding properties of basalt fiber and strength reduction according to fiber orientation. Materials. 2015. 8. Pp. 6719–6727. doi.org/10.3390/ma8105335
8. Girgin, Z.C., Yildirim, M.T. Usability of basalt fibers in fiber reinforced cement composites. Materials and Structures. 2016. 49. Pp. 3309–3319. doi.org/10.1617/s11527-015-0721-4
9. Klyuev, S.V., Klyuev, A.V., Vatin, N.I. Fiber concrete for the construction industry. Magazine of Civil Engineering. 2018. 84(8). Pp. 41–47. DOI: 10.18720/MCE.84.4
10. Rassokhin, A.S., Ponomarev, A.N., Figovsky, O.L. The formation of the seabed surface relief near the gravitational object. Magazine of Civil Engineering. 2018. No. 79(3). Pp. 132–139. DOI: 10.18720/MCE.79.14
11. Ronaldo, E., Nerilli, F., Vairo, G. Basalt-based fiber-reinforced materials and structural applications in civil engineering. Composite Structures. 2019. 214. Pp. 246–263. doi.org/10.1016/j.compstruct.2019.02.002
12. Seydibeyoglu, M.O., Mohanty, A.K., Misra, M. Fiber technology for fiber-reinforced composites. A volume in Woodhead Publishing Series in Composites Science and Engineering. Woodhead Publishing. Cambridge, 2017. 336 p. doi.org/10.1016/C2015-0-05497-1
13. Rybakov, V.A., Ananeva, I.A., Pichugin, E.D., Garifullin, M. Heat protective properties of enclosure structure from thin-wall profiles with foamed concrete. Magazine of Civil Engineering. 2020. 94(2). Pp. 11–20. DOI: 10.18720/MCE.94.2
14. Figueiro, R. Fibrous and composite materials for civil engineering applications. Woodhead Publishing Series in Textiles. Woodhead Publishing. Cambridge, 2011. 420 p.
15. Jian-Jun, L., Ying, M., Yan-Chun, L. The performance of green basalt fiber and its application in the civil engineering field. Applied Mechanics and Materials. 2012. 193–194. Pp. 548–552. doi.org/10.4028/www.scientific.net/AMM.193-194.548

16. Gravit, M.V., Golub, E.V., Antonov, S.P. Fire protective dry plaster composition for structures in hydrocarbon fire. *Magazine of Civil Engineering*. 2018. No. 79(3). Pp. 86–94. DOI: 10.18720/MCE.79.9
17. Abed, F., Alhafiz, A.R. Effect of basalt fibers on the flexural behavior of concrete beams reinforced with BFRP bars. *Composite Structures*. 2019. 215. Pp. 23–34. doi.org/10.1016/j.compstruct.2019.02.050
18. Alnahhal, W., Aljidda, O. Flexural behavior of basalt fiber reinforced concrete beams with recycled concrete coarse aggregates. *Construction and Building Materials*. 2018. 169. Pp. 165–178. doi.org/10.1016/j.conbuildmat.2018.02.135
19. Duic, J., Kenno, S., Das, S. Performance of concrete beams reinforced with basalt fibre composite rebar. *Construction and Building Materials*. 2018. 176. Pp. 470–481. doi.org/10.1016/j.conbuildmat.2018.04.208
20. Jumaa, G.B., Yousif, A.R. Size effect on the shear failure of high-strength concrete beams reinforced with basalt FRP bars and stirrups. *Construction and Building Materials*. 2019. 209. Pp. 77–94. doi.org/10.1016/j.conbuildmat.2019.03.076
21. Jiang, C., Fan, K., Wu, F., Chen, D. Experimental study on the mechanical properties and microstructure of chopped basalt fiber reinforced concrete. *Materials and Design*. 2014. 58. Pp. 187–193. doi.org/10.1016/j.matdes.2014.01.056
22. Lago, B.D., Taylor, S.E., Deegan, P., Ferrara, L., Sonebi, M., Crosset, P., Pattarini, A. Full-scale testing and numerical analysis of a precast fibre reinforced self-compacting concrete slab pre-stressed with basalt fibre reinforced polymer bars. *Composites Part B: Engineering*. 2017. 128. Pp. 120–133. doi.org/10.1016/j.compositesb.2017.07.004
23. Lu, Z.Y., Xian, G.J., Li, H. Effects of exposure to elevated temperatures and subsequent immersion in water or alkaline solution on the mechanical properties of pultruded BFRP plates. *Composites Part B: Engineering*. 2015. 77. Pp. 421–430. doi.org/10.1016/j.compositesb.2015.03.066
24. Zhu, H., Cheng, S., Gao, D., Neaz, S.M., Li C. Flexural behavior of partially fiber-reinforced high-strength concrete beams reinforced with FRP bars. *Construction and Building Materials*. 2018. 161. Pp. 587–597. doi.org/10.1016/j.conbuildmat.2017.12.003
25. Karaburc, S.N., Yildizel, S.A., Calis, G.C. Evaluation of the basalt fiber reinforced pumice lightweight concrete. *Magazine of Civil Engineering*. 2020. 94(2). Pp. 81–92. DOI: 10.18720/MCE.94.7
26. Nepomuceno, M., Pereira-de-Oliveira, L.A., Pereira, S.F. Mix design of structural lightweight self-compacting concrete incorporating coarse lightweight expanded clay aggregates. *Construction and Building Materials*. 2018. 166. Pp. 373–385. doi.org/10.1016/j.conbuildmat.2018.01.161
27. Ahmad, M.R., Chen, B., Shah S.F. Investigate the influence of expanded clay aggregate and silica fume on the properties of lightweight concrete. *Construction and Building Materials*. 2019. 220. Pp. 253–266. doi.org/10.1016/j.conbuildmat.2019.05.171
28. Bodnarova, L., Hela, R., Hubertova, M., Novakova, I. Behaviour of lightweight expanded clay aggregate concrete exposed to high temperatures. *International Scholarly and Scientific Research & Innovation*. 2014. 8(12). Pp. 1210–1213.
29. Bogas, J.A., Gomes, M.G. and Real, S. Bonding of steel reinforcement in structural expanded clay lightweight aggregate concrete: The influence of failure mechanism and concrete composition. *Construction and Building Materials*. 2014. 65. Pp. 350–359. doi.org/10.1016/j.conbuildmat.2014.04.122
30. Hubertova, M. and Hela, R. Durability of lightweight expanded clay aggregate concrete. *Procedia Engineering*. 2013. 65. Pp. 2–6. doi.org/10.1016/j.proeng.2013.09.002
31. Lucas, S.S. Moxham, C., Tziviloglou, E., Jonkers, H. Study of self-healing properties in concrete with bacteria encapsulated in expanded clay. *Science and Technology of Materials*. 2018. 30(1). Pp. 93–98. doi.org/10.1016/j.stmat.2018.11.006
32. Pioro, L.S., Pioro, I.L. Production of expanded-clay aggregate for lightweight concrete from non-selfbloating clays. *Cement & Concrete Composites*. 2004. 26. Pp. 639–643. doi.org/10.1016/S0958-9465(03)00103-3
33. Yang, Y., Chen, B. Potential use of soil in lightweight foamed concrete. *Journal of Civil Engineering*. 2016. 20(6). Pp. 2420–2427. doi.org/10.1007/s12205-016-0140-2
34. Koyankin, A.A., Mitasov, V.M., Tskhay, T.A. Compatibility of precast heavy and monolithic lightweight concretes deforming. *Magazine of Civil Engineering*. 2018. 84(8). Pp. 162–172. DOI: 10.18720/MCE.84.16
35. Sergeev, V.V., Petrichenko, M.R., Nemova, D.V., Kotov, E.V., Tarasova, D.S., Nefedova, A.V., Borodinecs, A.B. The building extension with energy efficiency light-weight building walls. *Magazine of Civil Engineering*. 2018. 84(8). Pp. 67–74. DOI: 10.18720/MCE.84.7
36. Borovskikh, I.V., Morozov, N.M. Increased durability of basalt fiber in cement concrete. *Building materials and products*. *Izvestia KGASU* 2012. 2(20). Pp. 160–165.
37. Singh, S.K., Kirthika, S., Maruthupandian, S. Durability Studies on Basalt Fibre Reinforced Concrete. *Indian Concrete Journal*. 2018. 92(4). Pp. 45–55.
38. Thompson, M.K. and Thompson, J.M. *ANSYS mechanical APDL for finite element analysis*. Butterworth-Heinemann. Oxford, 2017. 466 p.
39. Lam, T.V., Vu, D.T., Dien, V.K., Bulgakov, B.I., Korol, E.A. Properties and thermal insulation performance of lightweight concrete. *Magazine of Civil Engineering*. 2018. 84(8). Pp. 173–191. DOI: 10.18720/MCE.84.17
40. Rao, S.S. *The finite element method in engineering*. Butterworth-Heinemann. Oxford, 2018. 782 p. doi.org/10.1016/C2016-0-01493-6
41. Stolarski, T., Yoshimoto, S., Nakasone, Y. *Engineering analysis with ANSYS software*. Butterworth-Heinemann. Oxford, 2018. 562 p. doi.org/10.1016/C2016-0-01966-6
42. GOST 10180-2012. *Concretes. Methods for strength determination using reference specimens*. Moscow, 2013. 30 p.
43. ACI 211.1-91: *Standard practice for selecting proportions for normal, heavyweight, and mass concrete (Reapproved 2009)*. ACI Committee 211, 2002. 38 p.

Contacts:

Vera Galishnikova, galishnikova-vv@rudn.ru

Makhmud Kharun, miharun@yandex.ru

Dmitry Dmitrievich Koroteev, koroteev-dd@rudn.ru

Paschal Chimerezeze Chiadighikaobi, passyding2@mail.ru



DOI: 10.34910/MCE.101.8

Strength of concrete columns reinforced with Glass fiber reinforced polymer

N.P. Duy^{*a}, V.N. Anh^a, D.V. Hiep^b, N.M.T. Anh^a

^a Mien Trung University of Civil Engineering, Tuy Hoa, Phuyen, Vietnam

^b Hanoi Architectural University, Thanhxuan, Hanoi, Vietnam

* E-mail: nguyenphanduy@muce.edu.vn

Keywords: Finite element, glass fiber reinforced polymer (GFRP), reinforced concrete column, Abaqus, concentric compression

Abstract. Due to low compressive strength and low compressive elastic modulus in comparison with these in tension, GFRP reinforcement is often used for bending elements and is rarely used for compressive structures. In this paper, the authors used finite element (FE) method based on Abaqus software to evaluate the axial load-carrying capacity of GFRP reinforced concrete (RC) columns under varying concrete grades, GFRP reinforcement ratios and tie configurations. The model of the specimens is developed using concrete damage plastic (CDP) model and linear elastic material model for GFRP bar. The consistence of the FE method is verified by the experimental results of a series of columns that tested by current authors. The analytical results show that the selected numerical method can accurately predict the behavior as well as the ultimate capacity of the columns. From simulation results, it is clear that the contribution of GFRP to the load-carrying capacity is considerable in columns with low concrete grades. While using higher concrete grades, the contribution of GFRP decrease, at concrete grade B60, contribution of GFRP is almost unimportant (2.74 %). Influence of tie spacing on load-bearing capacity of columns is also investigated. Accordingly, reducing tie spacing leads to increase load-carrying capacity. Based on study results, the authors recommend to limit tie spacing less than eight times of the GFRP bar diameter.

1. Introduction

Nowadays the low durability problem could be solved by applying the new type of reinforcement in concrete structures i.e. the FRP reinforcement. The FRP reinforcement bar includes several different types as Glass Fiber Reinforced Polymer (GFRP), Carbon Fiber Reinforced Polymer (CFRP), Aramid Fiber Reinforced Polymer (AFRP), Basalt Fiber Reinforced Polymer (BFRP). The most popular is GFRP bar because of low price. In corrosive environments, the GFRP bar is considered a good substitute material for steel reinforcement. Compared to steel bar, GFRP is a material with many advantages such as corrosion resistance, high tensile strength, light weight, low electrical conductivity. Besides the advantages, it also has certain disadvantages, one of those is low compressive strength and compressive modulus of elasticity. Therefore, GFRP is mainly used to resist tensile load in tension zone of reinforced concrete structures [1, 2].

In order to expand the field of using GFRP reinforcement, especially for compressive elements of structures, many researchers have conducted study on GFRP RC columns under concentrically axial load. The goal of previous studies mainly focused on: evaluating the effect of longitudinal GFRP reinforcement on bearing capacity of columns; failure modes; the influence of configuration of GFRP transverse reinforcement on the behavior of columns and developing formulas to determine the load-carrying capacity etc. [3–11]. In these previous researches [3–11], it was showed that, when replacing the longitudinal steel bars with the GFRP bars by the same amount, the axial load-carrying capacity of GFRP concentrically RC columns decreases by 13 %–16 %. In GFRP RC columns, GFRP bars contribute about 3 %–10 % of the total load-carrying capacity. The increase of main GFRP reinforcement ratio boosts the ductility of cross section which has a significant effect on ultimate strain (to 19 %) and ultimate loads (to 22 %) of columns. Study results of Ehab M. Lotfy [5] indicated that, with the main reinforcement ratio up to 1.7 %, load-carrying capacity and

Duy, N.P., Anh, V.N., Hiep, D.V., Anh, N.M.T. Strength of concrete columns reinforced with Glass fiber reinforced polymer. Magazine of Civil Engineering. 2021. 101(1). Article No. 10108. DOI: 10.18720/MCE.101.8



This work is licensed under a CC BY-NC 4.0

reinforcement ratio follows a linear trend. Similarly, the author et al. [16] experimentally proved that, with the main reinforcement ratio up to 3.2 %, load-carrying capacity and reinforcement ratio follows a linear trend.

With the help of powerful commercial FE software, the FE modeling and analysis process is becoming increasingly efficient. Turvey and Zhang [12] conducted experiments and numerical simulations to study failure process after the loss of stability of RC columns reinforced with GFRP bars, using Abaqus software and generalized beam theory. In another study, F. Nunes et al. [13] carried out experiments and simulations of 3 series of I-section column from GFRP under eccentric compression. The results showed an excellent match between the experimental and numerical study results of the load-bearing capacity and the type of failures. Zhong Tao et al. [14] adjusted the FE model to simulate high-strength concrete filled steel tube under axial compression. In this model, the authors have adjusted the parameters in the CDP model for concrete, the modified model is more flexible and gives good convergence with the experimental results. Mohamed Elchalakani et al. [15] used CDP model to simulate GFRP RC columns in Abaqus. It can be seen from the results that the load-displacement response of simulations to experiments is in good agreement, the predicted N - M strength interaction diagrams are consistent with the experimental diagrams.

In general, the experimental data on the behavior of GFRP RC columns under axial load is relatively large. However, there are still some issues that have not been paid attention or just partially studied such as the influence of GFRP reinforcement ratios on the load-carrying capacity of the column; contribution of GFRP to load-carrying capacity of RC columns with different concrete grades and the influence of GFRP tie spacings on the load-bearing capacity of the columns. The current research work has been carried out to further investigate these issues using the nonlinear FE model method in Abaqus software. To achieve research objectives, the authors simulate the behavior of GFRP RC columns with different concrete grades, tie spacings and GFRP reinforcement ratios by using the CDP model and linear stress-strain behavior of GFRP in both tension and compression. From the simulation results, the axial load-concrete strain and axial load-displacement curves of columns under increasing static loading are presented and commented.

2. Methods

2.1. Experimental study program

To verify and adjust the parameters of the numerical model of GFRP RC columns, the authors used the previous experimental results of six short GFRP RC columns under axial load [16]. The size of the short columns was 150×150×600 mm. The average compressive strength of concrete determined by the test results of three 150×150×150 mm cubic specimens at 28th day is given in Table 1. The material properties of GFRP bars are also given in Table 1.

Table 1. Details of short GFRP RC column specimens [16].

Column ID	Long. reinf.			Tie		L_f/d_f	R_m , MPa	R_f , MPa	E_f , MPa	R_{fc} , MPa	E_{fc} , MPa
	Bars	A_f , mm ²	μ_f , %	Bars	Spacing, mm						
C1-4F6-F6S100	4F6	81.6	0.37	F6	100	16.67	29.9				
C2-4F12-F6S50	4F12	360.0	1.62	F6	50	4.17	32.2				
C3-4F12-6S100	4F12	360.0	1.62	F6	100	8.33	32.2				
C4-4F12-6S200	4F12	360.0	1.62	F6	200	16.67	32.2	970	44300	581	27930
C5-4F14-6S100	4F14	510.4	2.29	F6	100	7.14	30.3				
C6-8F12-6S100	8F12	720.0	3.24	F6	100	8.33	33.2				

F (d_f), mm is nominal diameter of GFRP bar; S (L_f), mm is tie spacing; A_f and μ_f are the area and percentage of longitudinal reinforcement respectively. R_m is the average compressive strength (cube 150×150×150 mm) at the age of 28 days. R_f and E_f are respectively, tensile strength and elastic modulus under tension of GFRP bar, R_{fc} and E_{fc} are respectively, compressive strength and elastic modulus under compression of GFRP bar

Tested columns differ in longitudinal reinforcement ratios μ_f and tie spacings S . The geometry, the reinforcement details of all column specimens are shown in Figure 1 and Table 1. In order to prevent crushing at the ends of column, thereby ensure failure at the middle of the column, the two ends of the columns are reinforced with steel nets. The purpose of the experiment is to build the axial strain versus axial load, as well as to determine the load-carrying capacity of the columns. The test setup and instrumentation employed to investigate the compression behavior of the GFRP RC columns are showed on Figure 2.

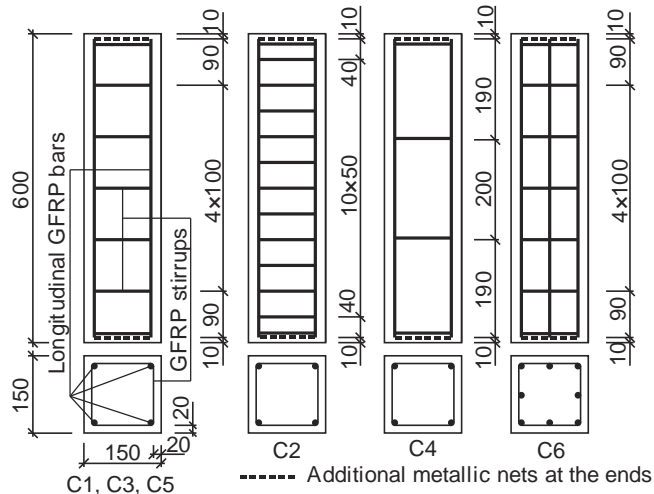
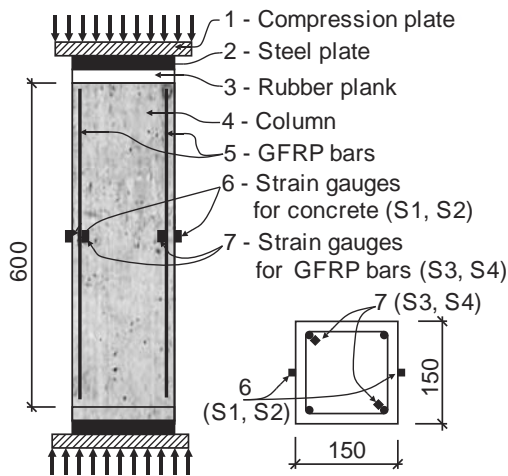


Figure 1. Details and configuration of the tested GFRP RC columns (units: mm).



a) Schematic diagram



b) Actual

Figure 2. Test setup and instrumentation for testing GFRP RC columns.

Loading of the column is applied on a testing machine of 100 tons. The columns were supported at both ends with two pairs of 8 mm thick steel plates. To fill the gaps between the steel plates and the surfaces of specimens, ensure uniform distribution of the applied load across the cross section and avoid eccentricity during loading, the authors used two rubber planks.

2.2. Numerical modeling and verification of numerical models

2.2.1. Numerical modeling

a) Describing structural parts and choosing element types

Abaqus software has a rich FE library, so selecting the appropriate element types for each component is necessary to simulate the column as close as possible to reality. In this paper, the eight-noded solid elements C3D8R with reduced integration is selected for concrete, steel plates and longitudinal GFRP bars, while GFRP stirrups is represented with two-noded linear truss element (T3D2).

b) Material properties

Concrete: full stress-strain diagram of concrete is displayed on Figure 3. It is seen that behavior of concrete is divided into two stages: elastic stage and inelastic stage. Under compression, elastic stage of concrete is built according to Model Code 2010 [17] and this stage is characterized by a secant modulus E_0 corresponding to a stress of $0.4f_{cm}$ and Poisson's ratio $\mu_c = 0.2$. Under tension, elastic stage of concrete is represented with E_0 and concrete tensile stress $f_{tm} = 0.3016f_{ck}^{2/3}$. For the inelastic stage of concrete in both tension and compression, concrete damaged plasticity (CDP) model proposed by J. Lubliner et al. [18], J. Lee, G.L. Fenves [19] with some modifications according to B. Alfarah et al. [20] is employed. In Abaqus, plastic failure stage is declared through the following coefficients: ratio of second stress invariants on tensile and compressive meridians $k_c = 0.7$; the ratio of biaxial compressive yield strength and uniaxial compressive yield strength $f_{b0}/f_{c0} = 1.16$; the dilatancy angle of concrete $\psi = 13^\circ$; the eccentricity of plastic potential surface $\epsilon = 0.1$.

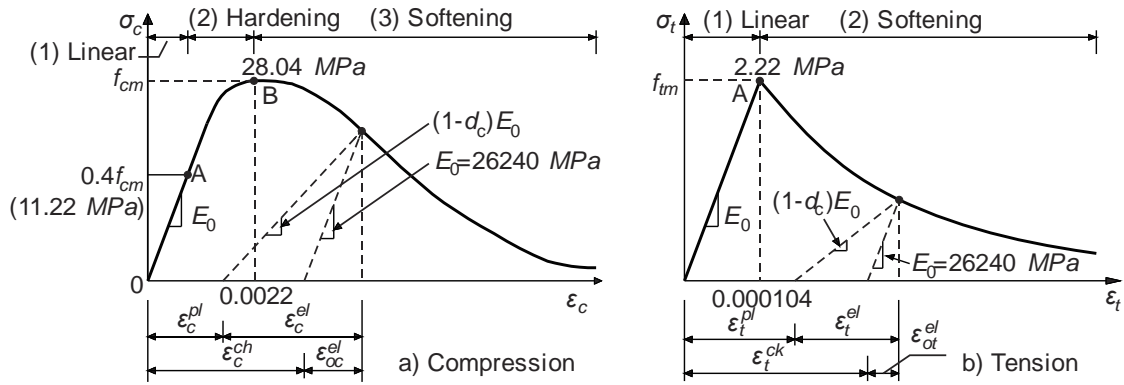


Figure 3. CDP model for concrete with $R_m=32 \text{ MPa}$ [18–20].

GFRP for longitudinal and transverse reinforcement: GFRP bar used in this experiment is provided by FRP VIETNAM., JSC [21]. Under tension, linear elastic model until failure based on the tensile test [22] is used to describe the behavior of GFRP (Figure 4 a). Under compression, the stress-strain diagram is built based on the Qasim S. Khan’s proposal [23] and the results of tensile test mentioned above. Accordingly, the stress-strain diagram also has linear type as shown on Figure 4 b. According to the experimental results of GFRP bars in compression conducted by O.S. Al Ajarmeh et al. [24], slenderness ratio (L_f/d_f) affected significantly the failure behavior of GFRP bars in compression. With the $L_f/d_f \leq 8$, the compressive strength of GFRP is stable, in case $L_f/d_f > 8$, the compressive strength of GFRP reduces linearly. From the experimental research results by these authors, slenderness ratio does not affect significantly on the compressive elastic modulus. Therefore, in this study if $L_f/d_f \leq 8$, the compressive stress-strain relationship is used as shown in Figure 4 b, for the case of $L_f/d_f > 8$ a reduction in compressive stress and axial strain proposed in [24] is employed.

Steel plates (at the ends of columns) are made from CT3 steel and modeled with bi-linear elasto-plastic material properties without hardening stage (Figure 5). Steel plate uses CT3 material according to GOST 380–89. It is noted that the perfect bond between the GFRP bars and concrete is assumed.

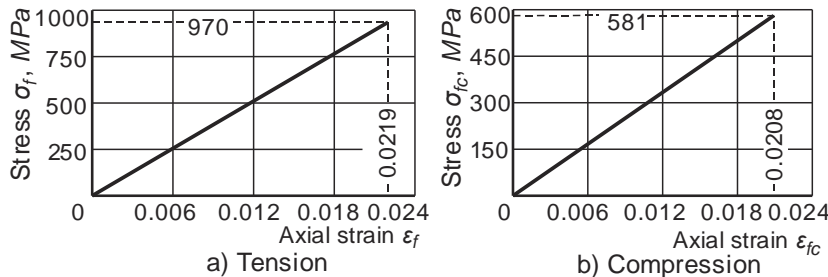


Figure 4. Stress-strain diagram of GFRP bars [22–24].

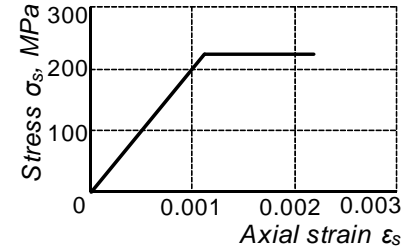


Figure 5. Stress-strain diagram of steel for plates.

c) Assembly of element parts: in Abaqus, each element of columns (concrete; steel plate; longitudinal GFRP bars; stirrups) is built independently in its local coordinate systems. Therefore, it is necessary to use assembly function to assemble discrete components to form a complete model. Figure 6a shows a complete model of column after assembly.

d) Conditions of interaction: in order to ensure the collaboration of all separate parts of the model, it is necessary to connect them together. Abaqus program provides different types of interaction. For GFRP RC columns, the interactions are as follows: tie constraint is used for interaction between reinforcement and concrete; embedded element is selected for stirrups; surface-to-surface contact with friction coefficient 0.4 is used for interaction between concrete and steel load transfer plate.

e) Mesh of elements: Abaqus provides different mesh element types depending on the geometry of the model. Use of appropriate mesh element type will make the simulation close to the experimental result of columns, reducing the error between simulation results and the experimental results. With the dimensions of tested columns, all parts of element are meshed with size 10 mm (Figure 6 b).

f) Boundary conditions: support boundary conditions and load boundary conditions in the model are presented in Figure 6 c.

g) Column loading: The loading on the column is carried out by displacement increment assigned on the load transfer plate.

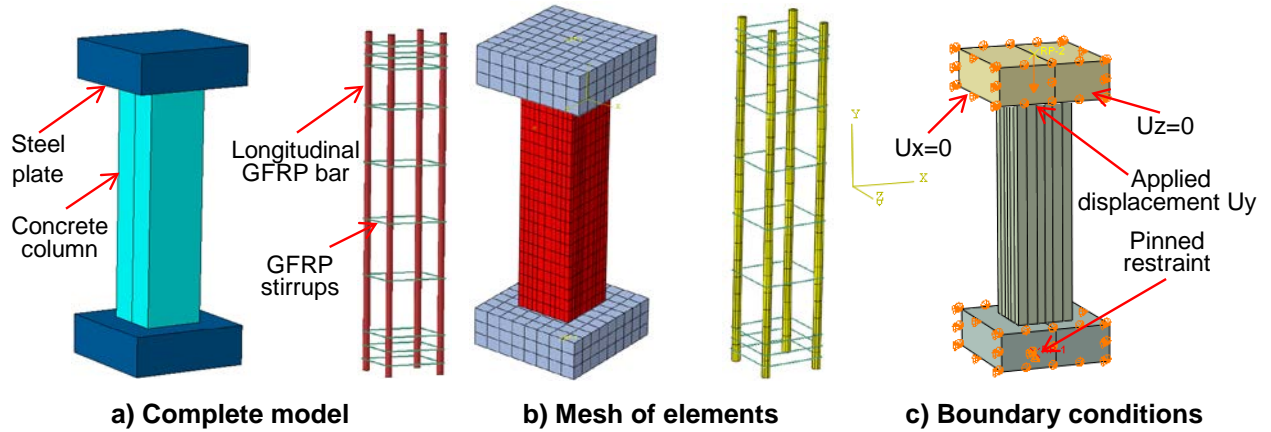


Figure 6. Model of short GFRP RC columns in Abaqus.

2.2.2. Verification of numerical models

From the numerical simulation results of GFRP RC columns by aforementioned models, the axial load-strain relationship in concrete at middle of columns curves are established and then comparing with the results obtained from the experiments, these curves are illustrated on Figure 7. Analysis of comparison results on Figure 7 shows a good match between simulation and experiment in all stages of behavior from beginning loading to failure. Failure mode of GFRP RC columns is illustrated on Figure 8. The GFRP bar is considered to be damaged when the stress reaches R_{cf} . Comparing the load-carrying capacity (maximum deviation of 10.5 %), failure modes and load-axial strain curves in concrete between experiment and simulation shows that the simulation method by Abaqus software ensures reliability.

3. Results and Discussion

By using the proven numerical simulation model above, the parametric study on the influence of longitudinal GFRP reinforcement ratios, compressive strengths of concrete and tie spacings on the load-carrying capacity of short GFRP RC columns can be conducted.

3.1. Investigation of contribution of GFRP reinforcement to the load-bearing capacity of RC columns using different concrete strengths (grades)

Contribution of GFRP reinforcement to the load-bearing capacity of RC columns is investigated on specimen 4F12-F6S100 with concrete grades B30, B35, B40, B45 and B60. For these columns, the GFRP reinforcement ratio μ_f and stirrup spacing S are fixed – $\mu_f = 1.62\%$ and $S = 100$ mm. The load-axial strain and load-displacement of these columns from the numerical simulation are shown in Figure 9. When fixing the stirrup configuration, the load-carrying capacity of the column mainly depends on the compressive strength of concrete and the longitudinal GFRP bars, in which concrete strength plays a decisive role. Therefore, when increasing the strength of using concrete, the load-bearing capacity of the column also increases. Accordingly, the load-bearing capacity of the investigated column made from B60 concrete increases 175 % in comparison to that of the column made from concrete B30. However, as the strength of concrete increases, the ductility of the column decreases, which is displayed on the downward branch of the load-displacement curves (Figure 9 b).

The contribution of GFRP bars is defined as the percentage of total axial force in the GFRP bars to maximum load is P_f/P_u , %. In which, P_f depends on the strains in the GFRP bars ε_f at the maximum load and compressive modulus of elastic is $P_f = \varepsilon_f E_{fc} A_f$. The value of ε_f is equal to strain in concrete at maximum stress – i.e. 0.0022 (Figure 3 a). Figure 10 shows the contribution ratio of GFRP bars to total load-carrying capacity of RC columns fabricated from different concrete grades (from B30 to B60). It is clear that contribution of GFRP bars with amount of reinforcement ratio $\mu_f = 1.62\%$ to overall load-carrying capacity of RC columns reduces significantly when concrete grade increases from B30 to B60. In GFRP RC columns made from concrete B60, contribution of GFRP bars accounts for 2.74 % and can be ignored. It should bear in mind that this value is only true in this study range (column dimension 150×150 mm, tie spacing 100 mm and diameter of longitudinal GFRP bar 12 mm, GFRP reinforcement ratio $\mu_f = 1.62\%$). Previous studies [4–6, 16, 27] reported that contribution of GFRP reinforcement to load-carrying capacity of GFRP RC columns varies from 3 % to 10 %. However, the research results in this paper show that the contribution of GFRP bars is a variable value depending on many factors such as: concrete strength; GFRP reinforcement ratio; tie spacing etc.

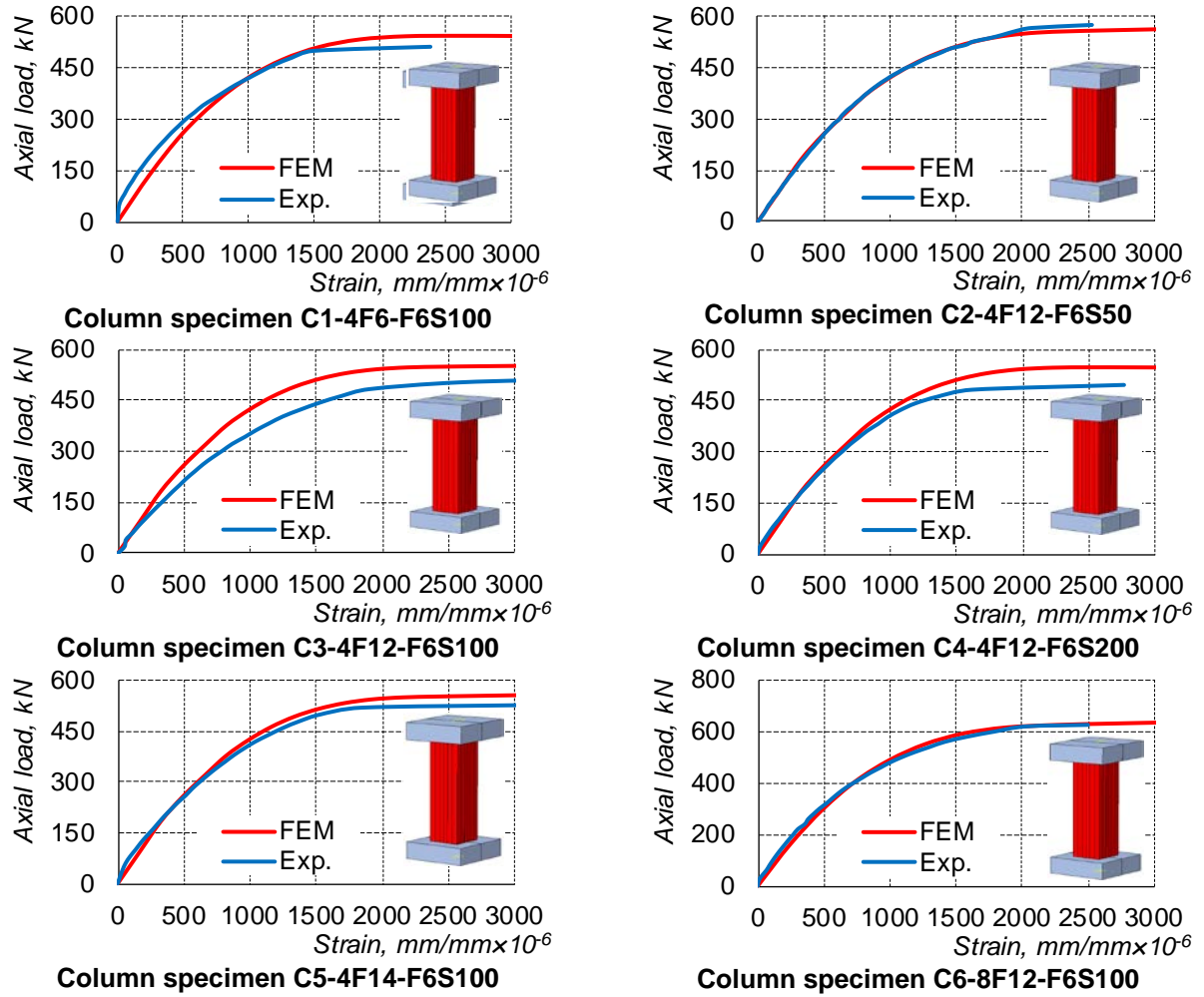
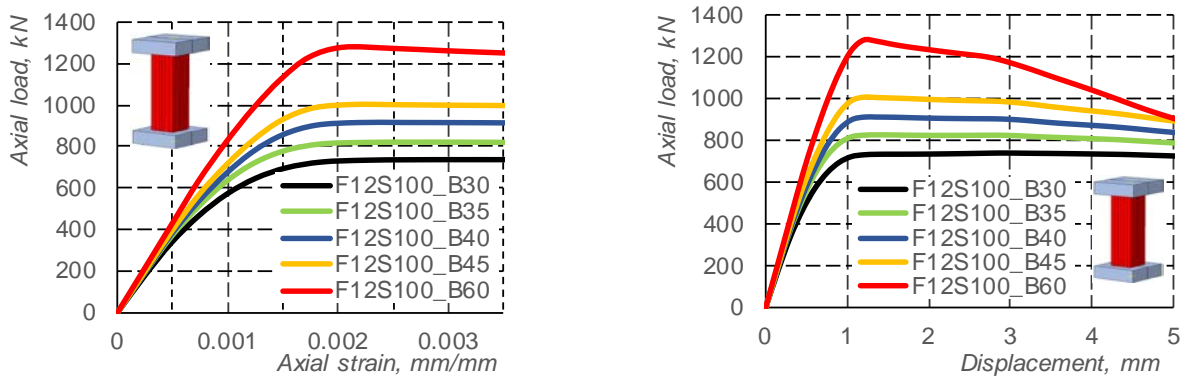


Figure 7. Load versus axial strain in concrete.



Figure 8. Failure mode of GFRP RC column C5-4F14-6S100.



a) Axial load versus axial strain curves

b) Axial load versus displacement curves

Figure 9. Axial load versus axial strain and displacement curves.

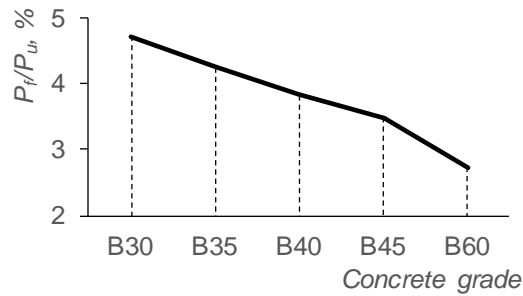


Figure 10. Contribution of GFRP bars to load-carrying capacity of RC columns.

3.2. Influence of tie spacing on load-carrying capacity

Tie spacing significantly influences load-carrying capacity, confinement effect, and failure modes of RC columns. Reducing stirrup spacing can prevent buckling of longitudinal bars, increasing load-carrying capacity. However, smaller stirrup spacing will affect concrete working, causing waste of materials. Design standards always limit the maximum stirrup spacing (S_{max}). According to Vietnamese Design standard 5574:2018 [25] and SP 63.13330.2018 [26], S_{max} should be smaller than $15d$ ($10d$) and 400 mm (300 mm) (values in parentheses apply to columns with total reinforcement ratio greater than 3.0 %).

The simulation was conducted on 3 groups of column specimens with longitudinal GFRP reinforcement $4d10$, $4d12$ and $4d14$, the tie spacing varying from 25 mm to 300 mm. The load-displacement relationship diagrams of investigated columns from numerical simulation are shown in Figure 11, Figure 12 and Figure 13. From these figures, it can be seen that tie spacings mainly affect the inelastic stage of behavior curves of GFRP RC columns. For RC columns with tie spacings greater than 100 mm, in the inelastic stage, the axial load-displacement curve tends to go down. In contrast, for columns with tie spacing of 100 mm or less, after elastic stage, axial load-displacement curve tends to go up and the column still carries loads. Stirrups with small spacing improve flexibility, increase confinement effects of columns and ensure stability of longitudinal GFRP bars, thereby increase the total load-bearing capacity of the columns. Increasing tie spacings leads to decrease in the load-bearing capacity of GFRP RC columns (Figure 14). Particularly, when reducing the tie spacing from 300 mm to 50 mm, the bearing capacity of the columns reinforced with longitudinal bars $4d14$, $4d12$ and $4d10$ increases by 23.3 %, 21.3 % and 12.3 %, respectively. Study results reported by Lotfy [5] indicated that if reducing steel tie spacing from 120 mm to 60 mm, load-carrying capacity of columns reinforced with $4d12$ GFRP increases by 20 %. In this study, the same simulation results in an increase by only 11.2 % (after from Fig. 14). This difference could be explained by the fact that Lotfy [5] used steel tie instead of GFRP tie, with better confinement effect than GFRP tie.

Analyzing the load-carrying capacity of RC columns versus tie spacings relationships on Figure 14 shows that, within the study scope, when tie spacing exceeds $16.7d$, the bearing capacity of the column almost becomes constant and no longer depends on the tie spacing. This means that the load-bearing capacity of such GFRP RC columns becomes close to that of the plain concrete column. Therefore, in order to take advantage of the bearing capacity of the longitudinal GFRP bars, ensure the simultaneous activation of longitudinal GFRP bars with concrete, it is necessary to limit the tie spacing. It is possible to use the limit of tie spacing according to Vietnamese design standard TCVN 5574:2018 [25] or SP 63.13330.2018 [26], Accordingly, the tie spacing is limited to less than $15d$. However, based on the research results of O.S. Al Ajarmeh et al. [24], in order to ensure stability and promote full compressive strength of GFRP bars, it is recommended to limit the tie spacing to less than $8d$.

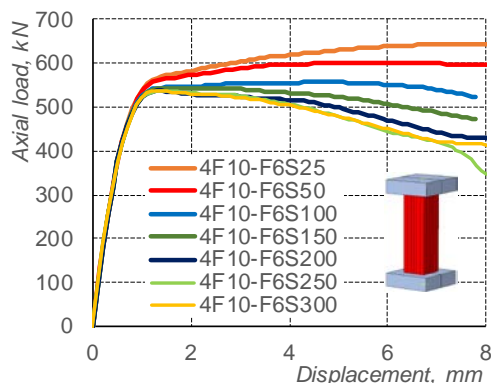


Figure 11. Load versus displacement curves of RC columns 4GFRP10 with different tie spacings.

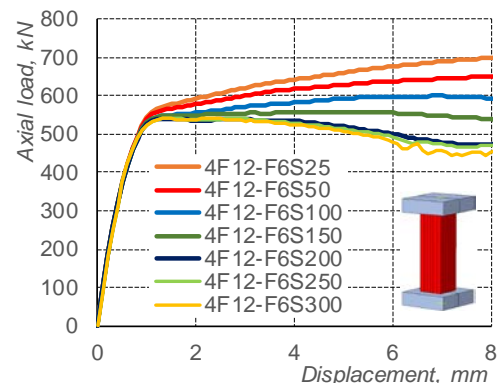


Figure 12. Load versus displacement curves of RC columns 4GFRP12 with different tie spacings.

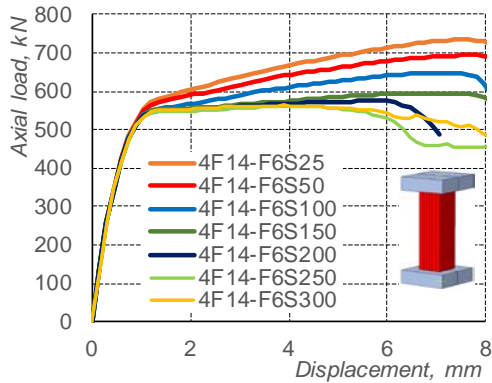


Figure 13. Load versus displacement curves of RC columns 4GFRP14 with different tie spacings.

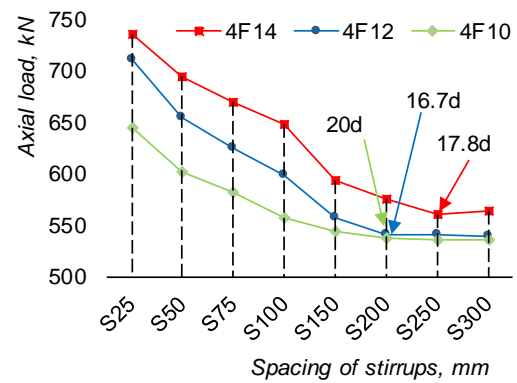


Figure 14. Load-carrying capacity versus tie spacings relationship.

3.3. Influence of GFRP reinforcement ratios on compressive behavior of columns

In order to assess the load-bearing capacity of the GFRP RC columns with a wide range of reinforcement ratios, a numerical study on the behavior of the RC columns with reinforcement ratio varying from $\mu_f=0.37\%$ to 3.4% when fixing the concrete strength $R_m=32$ MPa and stirrup configuration $d6S100$ is conducted. Figure 15 shows axial load–displacement of these columns. As mentioned above, load-carrying capacity of GFRP RC columns mainly depends on concrete strength and longitudinal reinforcement. According to the results of numerical study, the load-bearing capacity of columns increases by 29.7% when the reinforcement ratio increases from $\mu_f=0.37\%$ to $\mu_f=3.24\%$. This result is similar to the experimental study of the author [16] and Lotfy [5]. In addition, GFRP longitudinal reinforcement also promotes the flexibility of concrete columns in the inelastic stage (shown in the ascending branches on Figure 15).

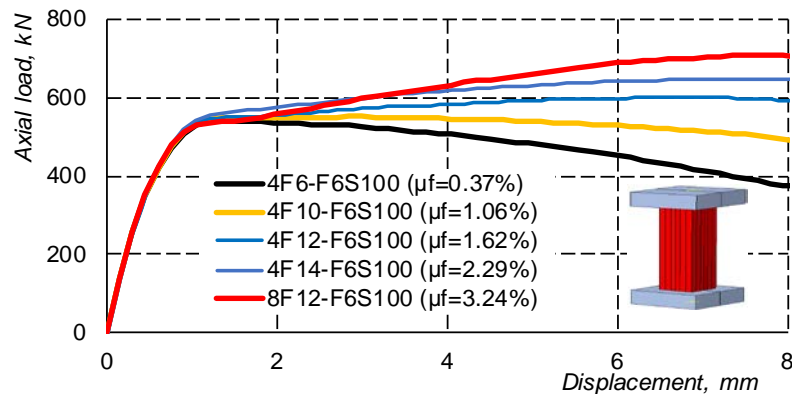


Figure 15. Axial load-displacement curves of GFRP RC columns with different reinforcement ratios.

4. Conclusion

In this study, modeling and verification of behavior of six short concrete columns reinforced with GFRP bars under axial compression load were conducted. By using verified model of GFRP RC columns on Abaqus software, the authors investigated contribution of GFRP bars to load-carrying capacity of RC columns with different concrete grades; the influence of tie spacing on load-bearing capacity and the behavior of GFRP RC columns when increasing GFRP reinforcement ratios. Based on the numerical simulation results presented in this study, the following conclusions can be drawn:

1. Numerical simulation model of GFRP RC columns based on CDP model and the linear stress-strain relationship of GFRP bars gives similar results to the experiment. Therefore, the proposed simulation technique of columns is reliable and can be used for parametric study;
2. Using the compressive strength of GFRP bar equal to about 60% of the tensile strength when $L_f/d_f \leq 8$ and additional reduction coefficient when $L_f/d_f > 8$ for numerical simulation model of GFRP RC columns gives consistent results with experimental values;
3. - Concrete strength significantly influences the load-bearing capacity and the behavior of the GFRP RC columns in both elastic and nonlinear stages. Using high-strength concrete reduces ductility of the column and decreases the contribution of GFRP bars to load-carrying capacity of columns. Changing the class of

concrete from B30 to B60 leads to a decrease in the contribution to load-bearing capacity of columns from 4.73 % to 2.74 %;

4. - Tie spacing greatly affects the bearing capacity and behavior of the column, especially in the nonlinear stage. Reducing the tie spacing increases the flexibility of the column, the confinement effect and the stability of the longitudinal GFRP bars, thereby increases the bearing capacity of the columns. From parametric study results in this paper, it is recommended that the maximum tie spacing in GFRP RC columns should be smaller than $8d$;

5. - Increase of longitudinal GFRP reinforcement ratio improves the bearing capacity and ductility of the columns.

References

1. Uğur, A., Unal, A., Akgöbek, B., Kamanli, M., Cengiz, S. Use of GFRP Bar in Civil Engineering. 4th International Symposium on Innovative Approaches in Engineering and Natural Sciences. 2019. Pp. 95–100. DOI: 10.36287/sets.4.6.029
2. Husain, S.F., Shariq, M., Masood, A. GFRP bars for RC structures – A Review. International Conference on Advances in Construction Materials and Structures (ACMS-2018). 2018. (March).
3. Alsayed, S.H., Al-Salloom, Y.A., Almusallam, T.H., AMJAD, M.A. Concrete Columns Reinforced by GFRP Rod. Fourth International Symposium on Fiber-Reinforced Polymer Reinforcement for Reinforced Concrete Structures. 1999. Pp. 103–112.
4. Luca, A., Matta, F., Nanni, A. Behavior of Full-Scale Glass Fiber-Reinforced Polymer Reinforced Concrete Columns under Axial Load. ACI Structural Journal. 2010. 107. Pp. 589–596.
5. Lotfy, E. Nonlinear analysis of Reinforced Concrete Columns with Fiber Reinforced Polymer Bars. World Journal of Engineering. 2011. 8(4). Pp. 357–368. DOI: 10.1260/1708-5284.8.4.357
6. Tobbi, H., Farghaly, A.S., Benmokrane, B. Concrete columns reinforced longitudinally and transversally with glass fiber-reinforced polymer bars. ACI Structural Journal. 2012. 109(4). Pp. 551–558. DOI:10.14359/51683874.
7. Mohamed, H.M., Afifi, M.Z., Benmokrane, B. Performance evaluation of concrete columns reinforced longitudinally with FRP bars and confined with FRP hoops and spirals under axial load. Journal of Bridge Engineering. 2014. 19(7). Pp. 1–12. DOI: 10.1061/(ASCE)BE.1943-5592.0000590
8. Afifi, M.Z., Mohamed, H.M., Chaallal, O., Benmokrane, B. Confinement model for concrete columns internally confined with carbon FRP spirals and hoops. Journal of Structural Engineering (United States). 2015. 141(9). Pp. 1–11. DOI: 10.1061/(ASCE)ST.1943-541X.0001197
9. Pateriya, R., Akhtar, S., Rajvaidya, P.N. Analysis of Compressive Strength of Columns Reinforced with Steel & FRP Bars. 2015. 4(6). Pp. 4–8.
10. Hadi, M.N.S., Karim, H., Sheikh, M.N. Experimental Investigations on Circular Concrete Columns Reinforced with GFRP Bars and Helices under Different Loading Conditions. Journal of Composites for Construction. 2016. 20(4). Pp. 1–12. DOI: 10.1061/(ASCE)CC.1943-5614.0000670
11. Tu, J., Gao, K., He, L., Li, X. Experimental study on the axial compression performance of GFRP-reinforced concrete square columns. Advances in Structural Engineering. 2019. 22(7). Pp. 1554–1565. DOI: 10.1177/1369433218817988
12. Turvey, G., Zhang, Y. A computational and experimental analysis of the buckling, postbuckling and initial failure of pultruded GRP columns. Computers & Structures – COMPUT STRUCT. 2006. 84. Pp. 1527–1537. DOI: 10.1016/j.compstruc.2006.01.028
13. Nunes, F., Correia, M., Correia, J.R., Silvestre, N., Moreira, A. Experimental and numerical study on the structural behavior of eccentrically loaded GFRP columns. Thin-Walled Structures. 2013. 72. Pp. 175–187. DOI: 10.1016/j.tws.2013.07.002
14. Tao, P.Z., Wang, Z.-B., Yu, Q. Finite element modelling of concrete-filled steel stub columns under axial compression. Journal of Constructional Steel Research. 2013. 89. Pp. 121–131. DOI: 10.1016/j.jcsr.2013.07.001
15. Elchalakani, M., Ma, G., Aslani, F., Duan, W. Design of GFRP-reinforced rectangular concrete columns under eccentric axial loading. Magazine of Concrete Research. 2017. 69(17). Pp. 865–877. DOI: 10.1680/jmacr.16.00437
16. Duy, N.P., Anh, V.N., Minh, N., Anh, T., Eduardovich, P.A. Load-Carrying Capacity of Short Concrete Columns Reinforced with Glass Fiber Reinforced Polymer Bars Under Concentric Axial Load. International Journal of Engineering and Advanced Technology. 2019. 9(2). Pp. 1712–1719. DOI: 10.35940/ijeat.b2372.129219
17. FIB (International Federation for Structural Concrete). Fib Model Code for Concrete Structures 2010. Ernst & Sohn, a Wiley brand, 2013.
18. Lubliner, J., Oliver, J., Oller, S., Oñate, E. A plastic-damage model for concrete. Int. J. Solids and Structures. 1989.
19. Lee, J., Fenves, G.L. Plastic-damage model for cyclic loading of concrete structures. Journal of engineering mechanics. 1998. 124(8). Pp. 892–900.
20. Alfarah, B., López-Almansa, F., Oller, S. New methodology for calculating damage variables evolution in Plastic Damage Model for RC structures. Engineering Structures. 2017. 132. Pp. 70–86.
21. FRP Vietnam JSC. Technical Specifications of GFRP. Viet Nam 2014.
22. Lucier, G. Tension Tests of GFRP Bars (Prepared for: Fiber reinfor plymer Vietnam) 2014.
23. Khan, Q.S., Sheikh, M.N., Hadi, M.N.S. Tension and compression testing of fibre reinforced polymer (FRP) bars. The 12th International Symposium on Fiber Reinforced Polymers for Reinforced Concrete Structures (FRPRCS-12). 2015. Pp. 1–6.
24. AlAjarmeh, O.S., Manalo, A.C., Benmokrane, B., Vijay, P.V., Ferdous, W., Mendis, P. Novel testing and characterization of GFRP bars in compression. Construction and Building Materials. 2019. 225. Pp. 1112–1126. DOI: 10.1016/j.conbuild-mat.2019.07.280.
25. IBST. TCVN 5574:2018 Concrete and reinforced concrete structures - Design standard 2018.
26. NIIZHB imeni A.A. Gvozdeva. SP 63.13330.2018 Concrete and Reinforced Concrete Structures. General provisions 2018.
27. Fillmore, B., Sadeghian, P. Contribution of longitudinal glass fiber-reinforced polymer bars in concrete cylinders under axial compression. Canadian Journal of Civil Engineering. 2018. 45(6). Pp. 458–468. DOI: 10.1139/cjce-2017-0481

Contacts:

Nguyen Phan Duy, nguyenphanduy@muce.edu.vn

Vu Ngoc Anh, vungocanh@muce.edu.vn

Dang Vu Hiep, dangvuhiep2009@yahoo.com

Nguyen Minh Tuan Anh, nguyenminhtuananh@muce.edu.vn

© Duy, N.P., Anh, V.N., Hiep, D.V., Anh, N.M.T., 2021



DOI: 10.34910/MCE.101.9

Stabilization of lateritic soil for masonry applications

A. Jose*, **A. Kasthurba**

National Institute of Technology Calicut, Kozhikode, Kerala, India

**E-mail: alexjose.scaria@gmail.com*

Keywords: durability, compressive strength, water absorption, ordinary Portland cement, scanning electron microscopy

Abstract. Construction using local soil is encouraged globally to minimize environmental impacts and to promote sustainable construction. However, the reluctance in using soil for construction is mainly due to the lack of strength and durability. This study investigates the influence of Ordinary Portland Cement (OPC) as stabilization agent for masonry blocks using lateritic soil, being a predominant soil in South India. Lateritic soil collected from three different locations in Kozhikode district of Kerala, India was used for the study. Engineering properties of stabilized soil blocks made with varying quantities of cement (such as 2.5, 5, 7.5, 10 & 12.5 % by weight of soil) was determined using standard procedures. The results were compared with ordinary laterite blocks and un-stabilized laterite soil blocks. It was observed that the strength of lateritic soil stabilized blocks increases with the quantity of cement content. The dry density, compressive strength and flexural strength increase with cement content, whereas, water absorption decreases with cement content. Weathering resistance was also considerably enhanced with increase in cement content. Based on the performance comparison, the optimum quantity of cement for stabilization of lateritic soil in Kerala was observed as 8 % by weight of soil. Even though laterite blocks in natural form being the popular masonry material in northern Kerala for centuries, its compressive strength was found 30 % lesser than manufactured lateritic soil-cement blocks. This study reveals that the stabilization of lateritic soil using the optimum quantity of cement can replace conventional natural laterite blocks for economic, environmental friendly and sustainable construction initiatives.

1. Introduction

The Conventional masonry construction practices using materials like burnt clay bricks, cement blocks and sand-concrete blocks involve high energy for the raw material extraction and manufacturing, which is environmentally hazardous and uneconomical. The release of carbon dioxide and other pollutants during their life cycle contaminates the nature, flora, fauna, as well as humans [1]. The threat to sustainability due to over-exploitation of resources and the lack of naturally occurring materials encourages the need for sustainable, economical and easily accessible material for construction [2]. Construction using local soil can be a sustainable solution for these issues. Earth construction has been in practice since more than 9000 years [1]. Soil used for construction during the beginning was unstabilized, which over the course of time, became stabilized for more strength and durability. Numerous researches have been conducted on different soils and their stabilization techniques globally. The commonly used nomenclature like compressed earth block, pressed earth block, compressed stabilized earth block, soil cement block, stabilized soil bricks, etc., all refer to the same earth construction either using a stabilization agent or without it [3–6]. However, the major hindrance to the popularization of earth construction is their instability in presence of water, lack of strength and low durability [7, 8]. All stabilization techniques studied so far focused on these shortcomings of earth construction. Previous research studies have established cement and lime as efficient stabilization agents for most of the soils [9–12]. However, cement has been more efficient and popular than lime in terms of strength and durability [13]. The type of soil and the stabilization agent has a great influence on the performance of stabilized earth blocks [14–16].

Apart from moulding of soil and using for construction purposes, natural stones are also significantly used around the globe. One such natural stone that is extensively used in India [17] and African countries [18] is Natural Laterite Blocks (NLB). The properties of NLB are similar to that of lateritic soil [19]. Even though NLB

Jose, A., Kasthurba, A. Stabilization of lateritic soil for masonry applications. Magazine of Civil Engineering. 2021. 101(1). Article No. 10109. DOI: 10.34910/MCE.101.9



This work is licensed under a CC BY-NC 4.0

is being used as popular masonry material for centuries, the supply of natural blocks is unable to meet the demand of the present construction industry. This paves the way for the stabilization and remoulding of lateritic soil as a replacement for natural laterite block, which has not been scientifically explored.

The aim of this study is to analyze the performance of blocks made using lateritic soil stabilized with cement and to compare the results with that of NLB. Lateritic soil collected from three different locations in Kozhikode district of Kerala, India were used for the study. Properties such as dry density, water absorption, compressive strength, flexural strength and weathering resistance of stabilized lateritic soil blocks made using varying proportions of cement were analyzed. The results were substantiated with scanning electron microscope images.

2. Methods

2.1. Materials

Lateritic soils were collected from three distinct locations in Kozhikode district, Kerala, India. The locations are namely Kunnamangalam, Kotooli and Atholi and are represented as lateritic soil 1 (LS1), lateritic soil 2 (LS2) and lateritic soil 3 (LS3) respectively. Three soils were used for the study to assess the variation in performance and to generalize the findings. Characterization of the collected lateritic soil samples were carried out in accordance with SP 36 (Part 1) – 1987 [20] of IS specification and are presented in Table 1. The chemical analysis of soil samples was carried out using X-ray fluorescence method using Bruker model S8 Tiger X-ray spectrometer and results are reported in Table 2. The major compounds identified in all samples include SiO_2 , Al_2O_3 and Fe_2O_3 . X-ray diffraction test was carried out using Rigaku Miniflex 600 diffractometer to identify the mineral presence in the lateritic soil samples. The minerals identified by X-ray diffraction is presented in Table 3. Kaolinite, was present in all the soil samples as the major component. Minerals identified in all three lateritic soil samples were similar and also confirms to previous studies on lateritic soils of Kerala [21]. The fraction of minerals in soil has a strong influence on the strength and durability characteristics of soil-cement blocks. Soils containing non-expansive clay minerals like kaolinite, are generally considered suitable for cement stabilization and soils with predominant expansive clay minerals are not proffered for cement stabilization [22].

The cement used for stabilization was Ordinary Portland Cement (OPC 53 grade) that complies with IS 12269 – 1987 [23]. The chemical and mineral composition of cement used is presented in Table 4. The mineral composition of OPC was calculated using the empirical formula of Bogue [24].

Table 1. Properties of lateritic soil samples.

Properties	Soil location		
	LS1	LS2	LS3
Optimum moisture content (%)	20	16	20.5
Maximum dry density (g/cm^3)	1.59	1.61	1.67
Liquid limit (%)	41.5	36	37.5
Plastic limit (%)	27.2	20.8	22.6
Plasticity index (%)	14.3	15.2	14.9
Particle size distribution			
Gravel + Sand (%)	53.0	58.3	64.5
Silt size (%)	36.1	32.3	21.2
Clay size (%)	10.9	9.4	14.3
Specific gravity	2.338	2.431	2.436
pH value	5.22	5.62	5.31

Table 2. Chemical composition of lateritic soil samples.

Compound	Composition (%)		
	LS1	LS2	LS3
SiO_2	55.68	57.45	53.71
Al_2O_3	23.18	18.26	20.43
Fe_2O_3	6.83	9.54	8.97
CaO	1.21	0.76	0.89
MgO	0.82	1.84	0.63
Na_2O	0.21	0.17	0.42
K_2O	0.65	2.85	2.21
TiO_2	0.96	0.79	1.08

Table 3. Mineral composition of lateritic soil samples.

Soil location	Minerals identified
LS1	Kaolinite, Quartz, Gibbsite, Feldspar, Goethite
LS2	Kaolinite, Quartz, Gibbsite, Feldspar, Mica, Goethite
LS3	Kaolinite, Quartz, Gibbsite, Feldspar, Mica, Goethite

Table 4. Composition of cement.

Chemical composition (%)									Mineral composition (%)			
SiO ₂	Al ₂ O ₃	Fe ₂ O ₃	CaO	MgO	SO ₃	K ₂ O	Na ₂ O	Ignition loss	C ₃ S	C ₂ S	C ₃ A	C ₄ AF
21.43	4.97	3.87	63.86	1.05	1.47	0.51	0.19	1.05	58.13	17.60	6.62	11.78

2.2. Preparation

Stabilization of soil was done using different proportions of cement and soil. Blocks were casted, cured and tested for properties such as dry density, water absorption, compressive strength, flexural strength and weathering resistance. Three blocks of each mix proportion were tested to obtain the average value of the mentioned properties.

The soil collected from all three locations was initially spread out in thin layers for drying and then sieved through 4.75 mm sieve, as larger particles were unsuitable for block preparation [8]. Five different proportions of cement such as 2.5 %, 5 %, 7.5 %, 10 % and 12.5 % by weight of soil were used for the study. For block preparation, the required quantity of soil was weighed and taken from the prepared sieved soil and was mixed with cement at different predetermined proportions. Quantity of water taken for mixing was the sum of optimum moisture content mentioned in Table 1 for each soil and 30 % by weight of cement for its hydration. The measured quantity of water was then sprinkled over the soil-cement mixture and turned well multiple times to obtain a homogenous mixture. Blocks of size 305×143×100 mm were casted using a manual press using the soil-cement mixture and were cured by spraying water for 28 days and then stacked after labeling.

2.3. Testing

Dry density tests for the blocks were determined in accordance with IS 1725 – 2013 [25]. Oven-dried sample (at 105 °C) after attaining constant weight was weighed and all the dimensions were noted. Dry weight divided by the volume is the dry density.

Water absorption of the blocks were determined in accordance with IS 3495 (Part 2) [26]. Oven-dried sample was weighed and immersed in water for 24 hours and saturated weight was measured. The difference of saturated weight and dry weight represented as a percentage of dry weight is the water absorption.

Wet compressive strength of blocks were determined in accordance with IS 3495 (Part 1) [26]. Compressive strength was determined using an Universal Testing Machine of 1000 kN capacity. Saturated specimen was placed in the machine and load was applied at a rate of 14 N/mm²/minute till failure. Peak load divided by the surface area is the compressive strength.

Flexural strength of blocks were determined in accordance with ASTM C293/C293M [27]. Center point loading method was done to obtain the value of modulus of rupture.

Weathering resistance of blocks were determined in accordance with IS 1725 – 2013 [25]. The block was dried in an oven at 65 °C till it achieved constant weight. The block was then immersed in water for 5 hours and subsequently dried in oven at 75 °C for 42 hours. All sides of the block were then scratched twice with wire brush at approximately 14.7 N force. This completes one cycle of test. Twelve cycles of the wire brush scratch procedure were performed on blocks to ascertain the weight loss.

Scanning electron microscope (SEM) images of blocks were taken using Hitachi SU660SEM to analyze the internal structure and effect of cement particles.

3. Results and Discussion

3.1. Dry density

Variation of dry density of blocks with cement content is shown in Fig. 1. It was observed that the density of blocks increases with cement content. The increase in dry density was about 17 % for LS1 for 12.5 % of cement by weight of soil, whereas LS2 and LS3 had an increase of about 4.5 % only. However, the general behavior of dry density with cement content was observed similar for all three soils. Also, similar results were observed in previous studies on soil stabilization with cement [13]. The reason for the increase in dry density may be due to the filling of all voids and pores by cement particles, which in turn increases the total solid mass. Also, the cement hydration products provide much stronger and closer bonding between soil particles. The

dry density of blocks using LS1 was lower than LS2 and LS3. The reason for this may be due to the higher silt content of LS1 compared to the other two soils, as the unit weight of silt is lesser than sand and gravel.

3.2. Water absorption

Variation in water absorption of blocks with cement content is as shown in Fig. 2. It is observed that water absorption reduces with an increase in cement content. An average reduction of 19 %, 11 % and 9.5 % were observed for LS1, LS2 and LS3 respectively for 12.5 % cement content. The hydration products of two anhydrous calcium silicates (C_3S and C_2S) of cement forms two other compounds, calcium hydroxide (hydrated lime) and calcium silicate hydrate (CSH) [28]. The CSH gel occupies higher volume inside the soil-cement matrix than the C_3S and C_2S minerals [29]. Hence, the lesser the volume of voids, lesser will be the water absorption. It may also be noted that the water absorption is maximum for blocks of lowest dry density as the number of voids are relatively higher. In general, it was observed that the water absorption of blocks decreased with increase in dry density. Soil types LS2 and LS3 displayed lower water absorption than LS1 soil. The reason for this may be the presence of mica, for which the water absorption property is negligible and as such, the total absorption mass of LS2 and LS3 is reduced.

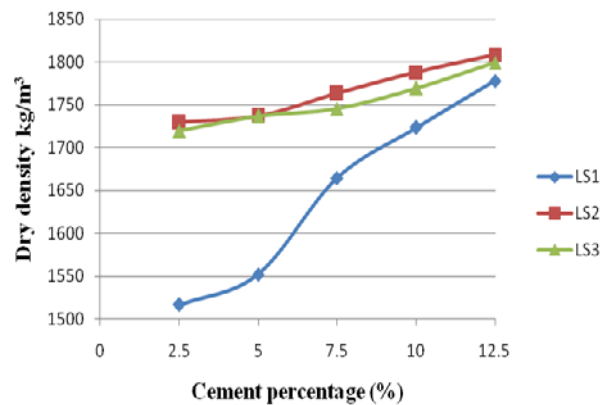


Figure 1. Variation of dry density with cement.

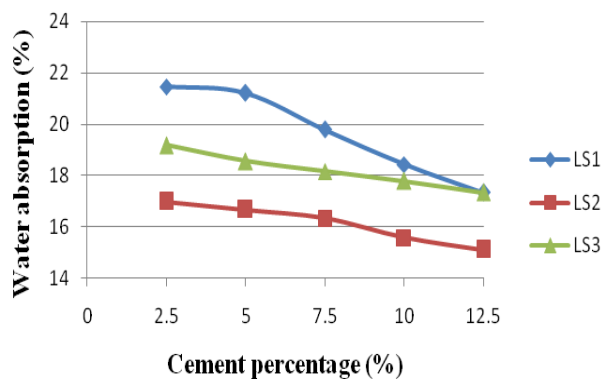


Figure 2. Variation of water absorption with cement.

3.3. Compressive strength

The results of compressive strength test are presented in Fig. 3. It is well evident that the compressive strength of blocks increases with an increase in cement content. It may also be noted that all three soils show almost similar variation with cement. The increase in compressive strength is more than double when cement content is increased from 2.5 to 5 % for all three soils. The strength had increased by more than five folds when the cement content was raised to 12.5 %. However, the minimum compressive strength specified for stabilized soil blocks in IS 1725-2013 is only 3.5 N/mm² which was achieved with around 8 % cement by weight of soil. The reason for the increase in compressive strength may be attributed to the binding action of cement that holds the soil particles together and the strong hydration products of cement (CSH and calcium hydroxide, as mentioned in section 3.2). The CSH and calcium hydroxide compounds are results of self-hydration of cement rather than reaction between cement and soil minerals as cement powder contains in itself everything it needs to hydrate [28]. The binding property of hydration products and the physical links between particles, helps the soil surface to distribute the load to the adjacent particle. Similar results were observed in previous studies on cement stabilized blocks [30], [31]. The compressive strength of blocks is dependent on cement as well as clay content [32]. As clay content increases, sand and gravel decrease and strength decreases. However, in this study, the clay content is similar for all three soils and there is no significant variation in compressive strength with different soil types at a constant cement content.

3.4. Flexural strength

The measure of flexural strength is represented in terms of modulus of rupture and the variation of the same with cement content is shown in Fig. 4. The modulus of rupture curve shows a steady increase with cement content for all three soils. The value increases by almost 50 % each time when the cement content is increased by 2.5 % from the previous cement content until 12.5 %. Maximum modulus of rupture was observed in blocks made using soil type LS1. Addition of cement enhances the flexural load carrying capacity of the blocks by improving the binding property of particles. The modulus of rupture displays a similar trend as compressive strength behavior with cement content.

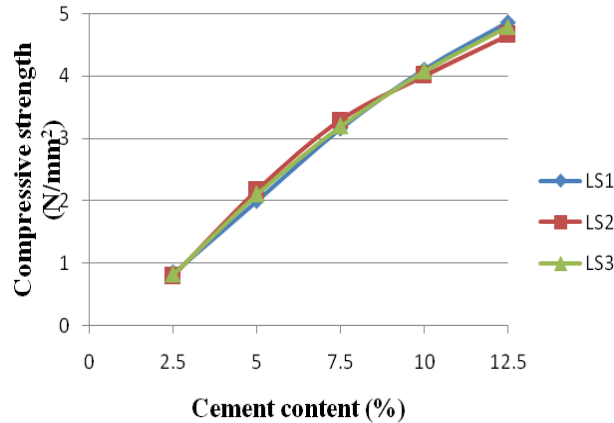


Figure 3. Variation of compressive strength with cement.

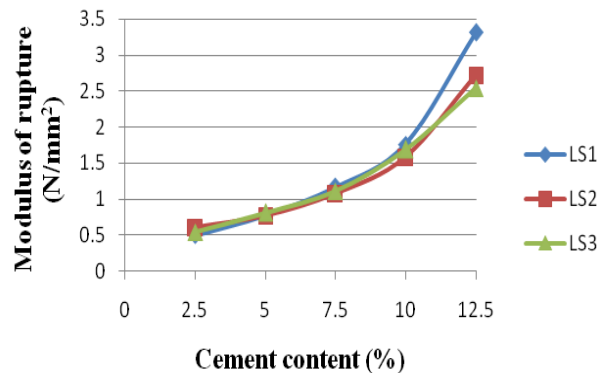


Figure 4. Variation of modulus of rupture with cement.

3.5. Weathering resistance

Weathering test results are displayed in Fig. 5. The results show a sudden drop (more than 60 %) in the weight loss when cement was increased from 2.5 % to 5 % for all soils. Weight loss is considered as the measure of durability. As weight loss decreases, more durable is the block. The reason for the increase in durability may be due to the action of hydration products of cement which holds the soil particles together and resist the wearing action on the surface by any foreign particles. Unstabilized soil particles are detrimental to the durability and hence the quantity of cement used for stabilization is important. Cement content above 5 % displayed a weight loss below 3 % for all soil types. It may also be noted that there is no significant increase in durability with cement content above 10 % as the weight loss is below 1 % for all soils. As in compressive strength property, the clay content of soil also influences the durability of the blocks. As clay content increases, it disrupts the bonding of soil and cement particles and thereby decreases the durability [32].

3.6. Comparison of strength with natural laterite block

The compressive strength result of lateritic soil-cement blocks (LSCB) with 8 % cement was compared with that of remoulded lateritic blocks (RLB) and natural lateritic block (NLB) and is shown in Fig. 6. RLB was prepared using soil obtained by crushing NLB and moulding it again using manual press without using any external stabilizing agents. It can be seen that the compressive strength of RLB is negligible compared to LSCB. This low strength may be attributable to the absence of a stabilizing agent. Without stabilizing agent, the moulded soil is highly unstable and weak in withstanding external stress. NLB, a popular masonry material in Kerala, has a strength of around 2.5 N/mm². However, the strength of NLB is almost 30 % lesser than that of LSCB with 8 % cement.

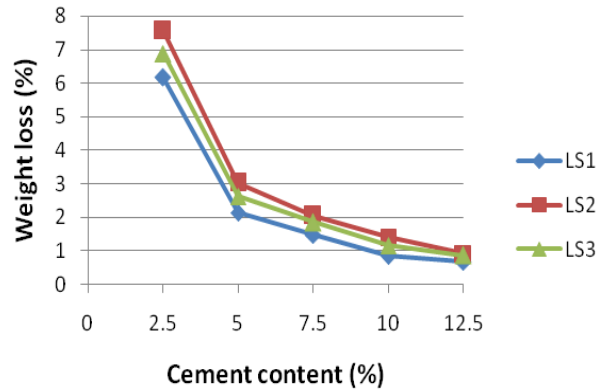


Figure 5. Variation of weight loss with cement.

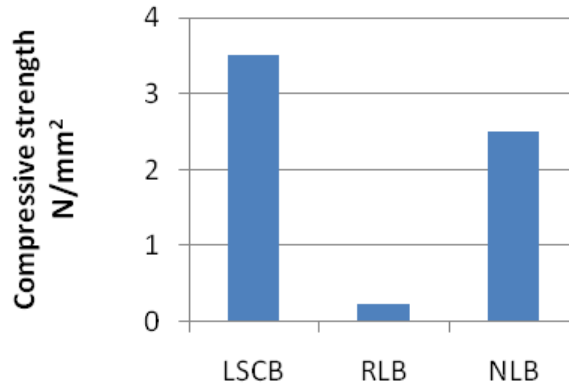


Figure 6. Comparison of compressive strength of LSCB, RLB and NLB.

3.7. Microstructure of blocks

The SEM images of blocks made using LS1 soil and different cement proportions are shown in Fig. 7. The SEM images of all three soil types were similar. It was observed that the number of pores and their sizes decreased with increase in cement content. Cement particles, which are smaller in size than soil, tend to occupy and fill the voids inside the soil matrix. Numerous pores were seen on the block surfaces with a minimum cement content of 2.5 %. However, blocks with 7.5 % and more cement appear to have a uniform surface with minimum number of pores and more binding between particles. The homogeneous structure seen in SEM images at higher cement contents indicates the stability and strength of the block. The images thus substantiate the results discussed in the above sections.

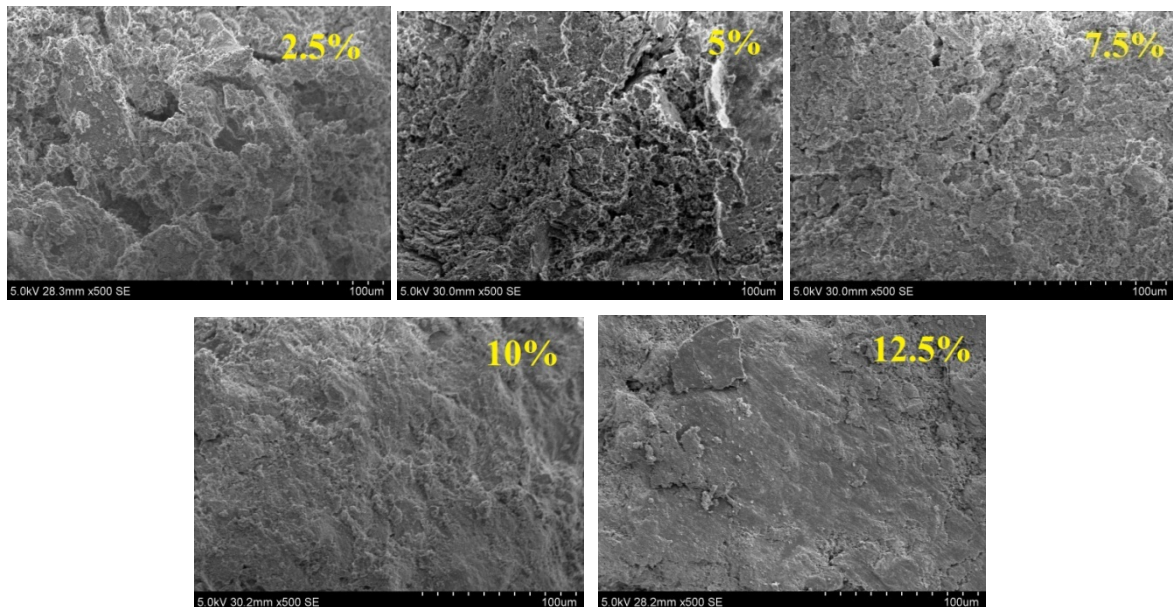


Figure 7. SEM images of lateritic soil-cement blocks with different cement contents.

4. Conclusion

The following conclusions can be drawn from the analysis on stabilization of lateritic soil using cement for masonry applications.

1. The major clay mineral observed in lateritic soil used for the study was kaolinite, which is non-expansive and as such, cement stabilization of lateritic soil was found effective in terms of enhancement in engineering properties of lateritic soil-cement blocks.

2. A significant reduction in water absorption was observed with increase in cement content. The average reduction in water absorption was observed as 11 % for 12.5 % cement content by weight of soil. Water absorption being a critical issue of soil blocks, can be resolved and brought under 18 % (limit specified in IS 1725 – 2013) with an addition of 8 % cement.

3. Mechanical properties such as compressive strength and flexural strength were enhanced manifold times with increase in cement content up to 12.5 %. However, over usage of cement is uneconomic and against sustainability concepts. The minimum compressive strength for soil blocks specified in IS 1725 – 2013 is 3.5 N/mm² which can be achieved with around 8 % cement.

4. The durability characteristics of blocks displayed significant improvement with increase in cement content. The maximum allowable limit of weight loss specified in IS 1725 – 2013 is 3 %. By addition of even 5 % cement, the weight loss was observed to be below 3 % and no significant weight loss was observed beyond 10 % cement.

5. Both strength and durability of stabilized soil blocks are enhanced by cement content and impaired by clay content. As far as lateritic soils used for the study are concerned, the clay content and other mineral contents are almost similar and the performance of stabilized soil depends on the variation in cement content.

6. Considering the critical aspects of soil blocks for masonry purposes, i.e., compressive strength, durability and water absorption, the optimum desirable results were observed with a cement content of 8 % by weight of soil for lateritic soils in Kerala.

It may be noted that the study was conducted exclusively for lateritic soils in Kozhikode district of Kerala. The performance of blocks may vary with the type of soil.

References

1. Cid-Falceto, J., Mazarrón, F.R., Cañas, I. Assessment of compressed earth blocks made in Spain: International durability tests. *Construction and Building Materials*. 2012. 37. Pp. 738–745. DOI: 10.1016/j.conbuildmat.2012.08.019.
2. Danso, H., Martinson, D.B., Ali, M., Williams, J.B. Physical, mechanical and durability properties of soil building blocks reinforced with natural fibres. *Construction and Building Materials*. 2015. 101. Pp. 797–809. DOI: 10.1016/j.conbuildmat.2015.10.069.
3. Sitton, J.D., Zeinali, Y., Heidarian, W.H., Story, B.A. Effect of mix design on compressed earth block strength. *Construction and Building Materials*. 2018. 158. Pp. 124–131. DOI: 10.1016/j.conbuildmat.2017.10.005.
4. Catalina, M., Villamizar, N., Spinosi, V., Alberto, C., Reyes, R., Sandoval, R. Effect of the addition of coal-ash and cassava peels on the engineering properties of compressed earth blocks. *Construction and Building Materials*. 2012. 36. Pp. 276–286. DOI: 10.1016/j.conbuildmat.2012.04.056
5. Taallah, B., Guettala, A., Guettala, S., Kriker, A. Mechanical properties and hygroscopicity behavior of compressed earth block filled by date palm fibers. *Construction and Building Materials*. 2014. 59. Pp. 161–168. DOI: 10.1016/j.conbuildmat.2014.02.058
6. Omar, S., Messan, A., Prud, E., Escadeillas, G., Tsohnang, F. Stabilization of compressed earth blocks (CEBs) by geopolymer binder based on local materials from Burkina Faso. *Construction and Building Materials*. 2018. 165. Pp. 333–345. DOI: 10.1016/j.conbuildmat.2018.01.051.
7. Galán-marín, C., Rivera-gómez, C., Petric, J. Clay-based composite stabilized with natural polymer and fibre. *Construction and Building Materials*. 2010. 24(8). Pp. 1462–1468. DOI: 10.1016/j.conbuildmat.2010.01.008.
8. Zhang, L., Gustavsen, A., Petter, B., Yang, L., Gao, T., Wang, Y. Thermal conductivity of cement stabilized earth blocks. *Construction and Building Materials*. 2017. 151. Pp. 504–511. DOI: 10.1016/j.conbuildmat.2017.06.047.
9. Reddy, B.V.V., Hubli, S.R. Properties of lime stabilised steam-cured blocks for masonry. *Materials and Structures/Materiaux et Constructions*. 2002. 35(June). Pp. 293–300.
10. Reddy, B.V.V., Gupta, A. Characteristics of soil-cement blocks using highly sandy soils. *Materials and Structures/Materiaux et Constructions*. 2005. 38(July). Pp. 651–658. DOI: 10.1617/14265
11. Venkatarama Reddy, B. V., Prasanna Kumar, P. Embodied energy in cement stabilised rammed earth walls. *Energy and Buildings*. 2010. 42(3). Pp. 380–385. DOI: 10.1016/j.enbuild.2009.10.005
12. Nagaraj, H.B., Sravan, M. V., Arun, T.G., Jagadish, K.S. Role of lime with cement in long-term strength of Compressed Stabilized Earth Blocks. *International Journal of Sustainable Built Environment*. 2014. 3(1). Pp. 54–61. DOI: 10.1016/j.ijbsbe.20-14.03.001
13. Sekhar, D.C., Nayak, S. Utilization of granulated blast furnace slag and cement in the manufacture of compressed stabilized earth blocks. *Construction and Building Materials*. 2018. 166. Pp. 531–536. DOI: 10.1016/j.conbuildmat.2018.01.125.
14. Millogo, Y. Microstructure and physical properties of lime-clayey adobe bricks. *Construction and Building Materials*. 2008. 22. Pp. 2386–2392. DOI: 10.1016/j.conbuildmat.2007.09.002
15. Walker, P., Stace, T. Properties of some cement stabilised compressed earth blocks and mortars. *Materials and Structures/Materiaux et Constructions*. 1997. 30(November). Pp. 545–551.
16. Nagaraj, H.B., Rajesh, A., Sravan, M. V. Influence of soil gradation , proportion and combination of admixtures on the properties and durability of CSEBs. *Construction and Building Materials*. 2016. 110. Pp. 135–144. DOI: 10.1016/j.conbuildmat.2016.02.023.

17. Kasthurba, A.K., Santhanam, M., Achyuthan, H. Investigation of laterite stones for building purpose from Malabar region, Kerala, SW India – Chemical analysis and microstructure studies. *Construction and Building Materials*. 2005. 22(12). Pp. 2400–2408. DOI: 10.1016/j.conbuildmat.2006.12.003
18. Abhilash, H.N., Mcgregor, F., Millogo, Y., Fabbri, A., Séré, A.D., Aubert, J.E., Morel, J.C. Physical , mechanical and hygrothermal properties of lateritic building stones (LBS) from Burkina Faso. *Construction and Building Materials*. 2016. 125. Pp. 731–741. DOI: 10.1016/j.conbuildmat.2016.08.082.
19. Kasthurba, A.K., Santhanam, M., Achyuthan, H. Investigation of laterite stones for building purpose from Malabar region, Kerala , SW India – Chemical analysis and microstructure studies. *Construction and Building Materials*. 2008. 22. Pp. 2400–2408. DOI: 10.1016/j.conbuildmat.2006.12.003
20. IS SP 36 (Part 1): 1987 Compendium of Indian Standards on Soil Engineering Part 1 by Bureau of Indian Standards.
21. Chandran, P., Ray, S.K., Bhattacharyya, T., Srivastava, P., Krishnan, P., Pal, D.K. Lateritic soils of Kerala, India: Their mineralogy, genesis, and taxonomy. *Australian Journal of Soil Research*. 2005. 43(7). Pp. 839–852. DOI: 10.1071/SR04128
22. Reddy, B.V.V. Pressed soil-cement block: an alternative building material for masonry. *Sustainable construction*. 1994. 1. Pp. 425–433.
23. IS 12269-1987 Specification for 53 grade Ordinary Portland Cement (Reaffirmed 2004) by Bureau of Indian Standards.
24. Bogue, R.H. The chemistry of portland cement. New York, Reinhold Pub. Corp., 1955.
25. IS 1725 2013 Stabilized Soil Blocks Used In General Building Construction- Specification by Bureau of Indian Standards. Second rev (New Delhi).
26. IS 3495 (Parts 1 to 4) :1992 Methods of Test of Burnt Clay Building Bricks (Reaffirmed 2002) by Bureau of Indian Standards.
27. ASTM C293/C293M – 16 Standard Test Method for Flexural Strength of Concrete (Using Simple Beam With Center-Point Loading).
28. Lemougna, P.N., Melo, U.F.C., Kamseu, E., Tchamba, A.B. Laterite based stabilized products for sustainable building applications in tropical countries: Review and prospects for the case of Cameroon. *Sustainability*. 2011. 3(1). Pp. 293–305. DOI: 10.3390/su3010293
29. Yaragal, S.C., Gowda, S.N.B., Rajasekaran, C. Characterization and performance of processed lateritic fine aggregates in cement mortars and concretes. *Construction and Building Materials*. 2019. 200. Pp. 10–25. DOI: 10.1016/j.conbuildmat.2018.12.072. URL: <https://doi.org/10.1016/j.conbuildmat.2018.12.072>.
30. Reddy, B.V.V., Kumar, P.P. Cement stabilised rammed earth. Part B : compressive strength and stress – strain characteristics. *Materials and Structures/Materiaux et Constructions*. 2011. 44. Pp. 695–707. DOI: 10.1617/s11527-010-9659-8
31. Aguwa, J.I. Study of Compressive Strengths of Laterite-Cement Mixes as a Building Material. *Au J.T.* 2009. 13(2). Pp. 114–120.
32. Walker, P.J. Strength, durability and shrinkage characteristics of cement stabilised soil blocks. *Cement and Concrete Composites*. 1995. 17(4). Pp. 301–310. DOI: 10.1016/0958-9465(95)00019-9

Contacts:

Alex Jose, alexjose.scaria@gmail.com

Ayikkara Kasthurba, kasthurba@nitc.ac.in

© Jose, A.,Kasthurba, A., 2021



DOI: 10.34910/MCE.101.10

Flood events dynamics estimation methodology in a GIS environment

A. Nikonorov*, **V.L. Badenko**

Peter the Great St. Petersburg Polytechnic University, St. Petersburg, Russia

* E-mail: coolhabit@yandex.ru

Keywords: river basins, floods, flood protection, self-regulated dams, GIS environment

Abstract. Hard floods of rare frequency can cause significant damage to the ecosystem of the river basin, as well as to settlements and infrastructure. Therefore, the urgent task is to develop sustainable measures of minimization of the dangerous effects of these phenomena. One of the feasible technical measure is the construction of a self-regulating flood control dams with temporarily filled reservoirs system in the river basin. This article proposes an improved technique for flood events modeling, taking into account the proposed measures. The proposed method is based on the modeling in a GIS environment coupled with hydrologic simulation software. GIS modeling is preceded by the development of the digital elevation model. According to the results of the research, the requirements for the input data were formulated. An algorithm for creating models was given, as well as examples of already created models. The viability of this technique is shown, together with the limitations identified during the simulation.

1. Introduction

Hard floods of a rare occurrence annually take place in Russia. The average annual flood damage is estimated at about 40 billion rubles [1]. Flood damage assessment is a multi-criteria task of calculating the integral risk, which includes technological, economic, environmental and social risks [2].

From the often-recurring nature of flood events, it is obviously necessary to take timely and accurate measures to prevent and minimize damage from these phenomena [3, 4]. Flood protection measures are divided into operational (urgent) and technical (preventive) [5]. Operational measures include timely forecasting of maximum flood levels, timely notification of possible dangerous levels, organization of evacuation of the population and material assets, etc. [2]

Technical measures are precautionary in nature, and their implementation requires the advance construction of special engineering structures with the expenditure of significant material and financial resources. The complex of technical measures distinguishes between active and passive methods of protection (Fig. 1).

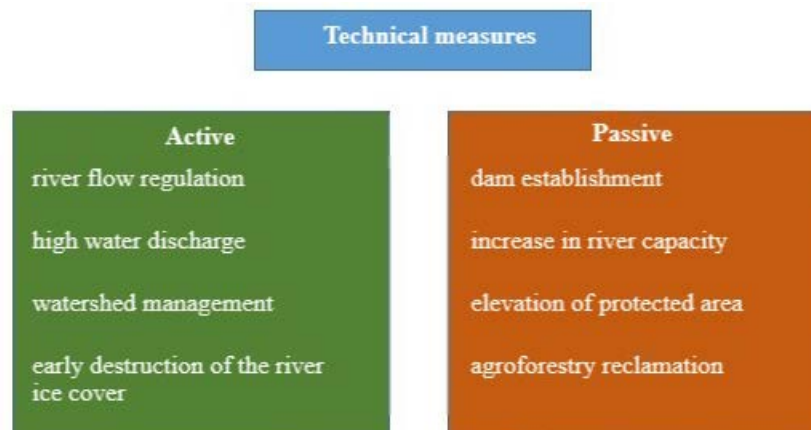


Figure 1. Technical flood protection measures.

Nikonorov, A., Badenko, V.L. Flood events dynamics estimation methodology in a GIS environment. Magazine of Civil Engineering. 2021. 101(1). Article No. 10110. DOI: 10.34910/MCE.101.10



This work is licensed under a CC BY-NC 4.0

The choice of method for protecting flooded areas depends on many factors, such as the hydraulic regime of the watercourse, terrain, engineering-geological and hydrogeological conditions, the presence of engineering structures in the riverbed and floodplain (dams, reservoirs, bridges, roads, water intakes, dams), the presence of an agricultural facilities located in the flooded zone, etc.

Nowadays, research on the prevention and minimization of flood consequences is also being conducted in the direction of flood events modeling on river basin modified by different engineering solutions appliance [6].

Geoinformational modeling (GIS modeling) of river basins is the most demanded area of practical application of digital elevation models (DEM). Recently, not a single hydrological and geomorphological study has been complete without such modeling. The DEM allocation technology for the hydrographic network and river basins was tested on the example of the territory of Switzerland near the city of Waldkirch [7]. As a result of modeling watercourses in the ArcGIS software package and visual stereo decryption in the DSP PHOTOMOD images to the corresponding territory, a map of the hydrographic network was created. A map of catchment areas was built. The main advantage of the modeling procedure compared to visual stereo decryption was the automation of the process and, as a result, the shorter execution time [8, 9].

Another interesting model example in terms of the research is the HiResFlood-UCI. It was developed by coupling the NWS's hydrologic model (HL-RDHM) with the hydraulic model (BreZo) for flash flood modeling at decameter resolutions [10]. The coupled model uses HL-RDHM as a rainfall-runoff generator and replaces the routing scheme of HL-RDHM with the 2D hydraulic model (BreZo) in order to predict localized flood depths and velocities. A semi-automated technique of unstructured mesh generation was developed to cluster an adequate density of computational cells along river channels such that numerical errors are negligible compared with other sources of error, while ensuring that computational costs of the hydraulic model are kept to a bare minimum [11, 12].

In conditions of aggravation of the flood situation in Russia and in the world, information support for managerial decision-making is of particular importance. Therefore, executive authorities are in demand to obtain the results of GIS modeling of floods based on remote sensing data [7, 9].

An interesting modern technical flood protection passive measure for the problem solution is the creation of a distributed network of self-regulated flood dams (SRFD) with temporarily filled reservoirs on river basin to minimize the consequences of flood events [13]. The study [14, 15] considers the issue of finding the parameters of a system that includes a hydroelectric power station (cascade of hydroelectric power stations) for complex purposes (electricity generation, flood control) on the main river with minimal reference mark and capacity for regulating maximum flow. An algorithm was developed and mathematical programs were implemented with the mathematical models of operating modes of a channel hydropower plant and flood control measures on the side tributaries. Authors of this article propose the improvement of the multicriteria selection technique for the distributed network of reservoirs location determination.

The developed method was designed to research the changes in the flood situation in the river basin with different options for the location of SRFD with various parameters. This will justify the location of the SRFD system with certain parameters in the river basin and evaluate the impact of the SRFD on ecosystems in the river basin. Proposed method is based on the GIS modeling with the DEM usage.

The design of self-regulatory flood dams is a multi-criteria task, and the final decision should be determined taking into account technological, economic, environmental and social factors.

Previous studies have shown the feasibility of flood control measures in the form of temporarily filled self-regulated flood dams with temporary filled reservoirs [16, 17]. The aperture of the dam is designed with an unregulated spillway without the use of gates, which increases the reliability of the operation and reduces the cost of maintenance. During the period of accumulation of flood discharge, the bed of such a reservoir is flooded for a short time, and after self-emptying until the next flood, it remains in its natural state without any changing of natural discharge.

The aims and tasks of the current research, presented in the article, were:

1. Confirmation of the relevance of the problem of flash floods and review of the modern state of an its consequences minimization question.
2. Proposal of a modern technical flood protection passive measure for the problem solution – system of SRFD with temporary-filled reservoirs.
3. Theoretical description of the method, definition of the demanded initial data.
4. Practical example of the developed method usage – the creation of a model according to the detailed algorithm.
5. Conclusion based on the results of the modeling, determination of the advantages, disadvantages and limitation of the proposed method.

2. Materials and Methods

2.1. Prerequisites of the modeling

The study of the environmental aspect of managerial decision-making when taking flood control measures is very relevant in our time, as evidenced by numerous publications of works by researchers-hydrologists, limnologists, ecologists, bio-, geochemists, hydrogeologists, etc. [18], engaged in studies of the current environmental situation on water bodies of our country. The strongest pollution of water bodies is observed, which leads not only to unsuitability of water for consumption, but also to the death of aquatic flora and fauna. This also fully applies to small-scale water bodies (small rivers) [13].

Changes in the hydrological regime of water bodies located in protected areas, due to a decrease or complete loss of the regulatory capacity of hydraulic structures, have a negative impact on both aquatic and terrestrial ecosystems [19]. It is also important to pay attention to the environmental aspect when directly implementing flood control measures. If you analyze the territorial planning schemes, you can see the protected areas or others, in which any construction and activities are prohibited in principle. This imposes a certain restriction on the choice of a place for flood control measures. Also, engineering decisions that can be made can affect the environment, for example, when creating hydropower facilities with reservoirs, even temporary ones, it is possible to cause irreparable damage to the natural environment, therefore it is necessary to correctly analyze the proposed places for flood control measures in order to identify restrictions, primarily on the environmental aspect [20].

The main parameter under consideration is the dynamic boundary of the water level (the territory covered by water) – It is for this purpose that the usage of GIS is necessary (Fig. 2) [11].

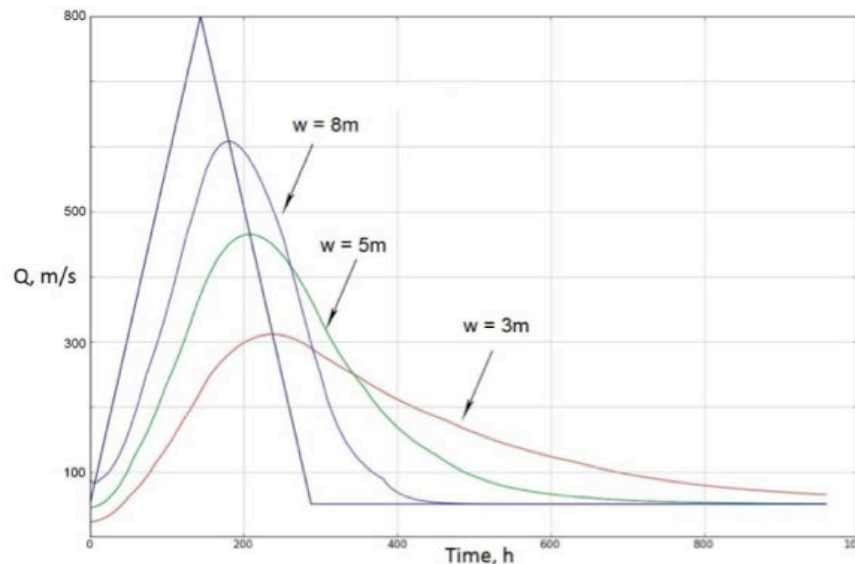


Figure 2. Hydrograph in the downstream of self-regulated flood dam, with different widths of the aperture.

Obtaining data on the dynamic boundary of the water level, it is possible to determine which ecosystems (or their parts) could be flooded as well as the timing of these events. In accordance with these facts, it is possible to choose the location of the proposed network of structures on the watercourse taking into account specific criteria, primarily ecological. The remaining parameters (the width of apertures of dams, as well as the cross-sectional area of watercourse at the selected locations) are set in a simplified form, their values are not calculated in method proposed. The main criterion for choosing (comparing) the location of the SRFD is the level of environmental impact – which territory can be flooded in the temporarily filled reservoir and for how long. More details about the method could be found in the previous works of the authors [10, 11].

2.2. Computational basis of the modeling

There are a large number of hydrological modeling systems based on GIS for water management [21–25]. Based on the results of the comparative analysis [26–29], it was decided to conduct modeling in the HEC-RAS software package, using the HEC-GeoRAS module to work with a digital elevation model in ArcGIS or QGIS [30]. Currently, HEC-RAS is able to perform one-dimensional calculations of the water surface profile for a steady, gradually changing flow in natural or constructed channels (Fig. 3) [31]. Water surface profiles with subcritical, supercritical, and mixed flow patterns can be calculated. The calculation model of the complex is based on the calculation of water surface profiles.

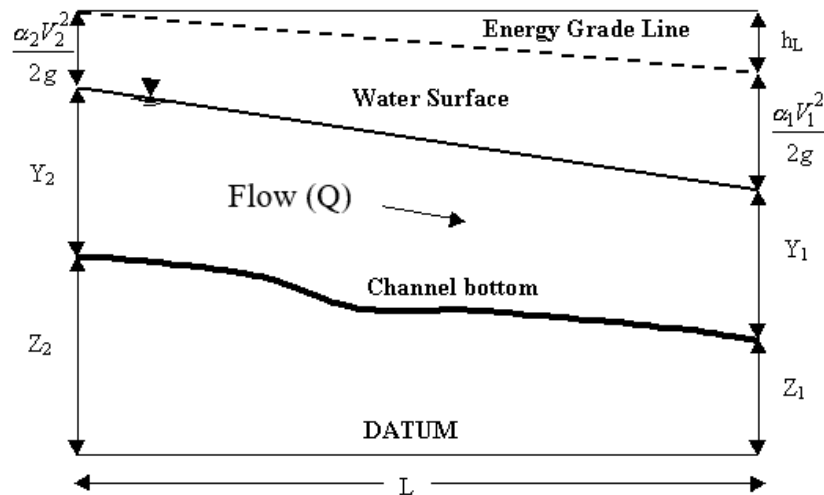


Figure 3. Method diagram.

Water surface profiles are calculated from one section to another by solving the Bernoulli equation with an iterative procedure, the so-called standard step method. The Bernoulli equation is the energy conservation law for two neighboring sections and is written as follows:

$$Z_2 + Y_2 + \frac{\alpha_1 * v_1^2}{2g} + h_e \quad (1)$$

where: Z_1, Z_2 are heights at points of the main channel taken at the center of gravity; Y_1, Y_2 are water depth in cross sections; V_1, V_2 are average velocities; a_1, a_2 are weighting coefficients for velocities; g is gravity accelerations; h_e is head losses.

The equation for head losses used in HEC is as follows:

$$h_e = L \overline{S_f} + C \left| \frac{\alpha_2 * v_2^2}{2g} - \frac{\alpha_1 * v_1^2}{2g} \right| \quad (2)$$

where: L is weighted average element length; $\overline{S_f}$ is characteristic hydraulic slope between two sections; C is compression ratio or expansion loss.

For the velocity of surface runoff under assumption that the Manning equation can be used the following equation is used:

$$v = k_r H^{2/3} \sqrt{I} \quad (3)$$

where k_r is roughness (according land use), I is a slope, H is a depth of water at a soil surface. For a pulse inflow, outflow peaks after a time given by the time lag, and then decays exponentially as follow:

$$Q_0 = (1 - x / (dt / K)) Q_i; x = 1 - e^{(-dt/K)} \quad (4)$$

where Q_0 is outflow, dt is a time step, Q_i is inflow, K is a delay parameter.

The calculation of the flood volume $V_S(t)$ that could be potentially accumulated in a system of reservoirs at a specific time is calculated using balance method:

$$V_S(t) = V_S(t-1) + (Q_i(t) - Q_0(t)) dt \quad (5)$$

where $Q_i(t)$ is inflow to SRFD, $Q_0(t)$ is outflow through the aperture of SRFD, dt is time step.

2.3. Initial data

The construction of a model of a section of the river basin for determining the alignment for the erection of the SRFD in each case begins with the collection of initial data. The most important source of up-to-date environmental information for various layers of GIS database are remote sensing data [32]. The concept of a GIS model for hydrological systems should include the following actions (Fig. 4):

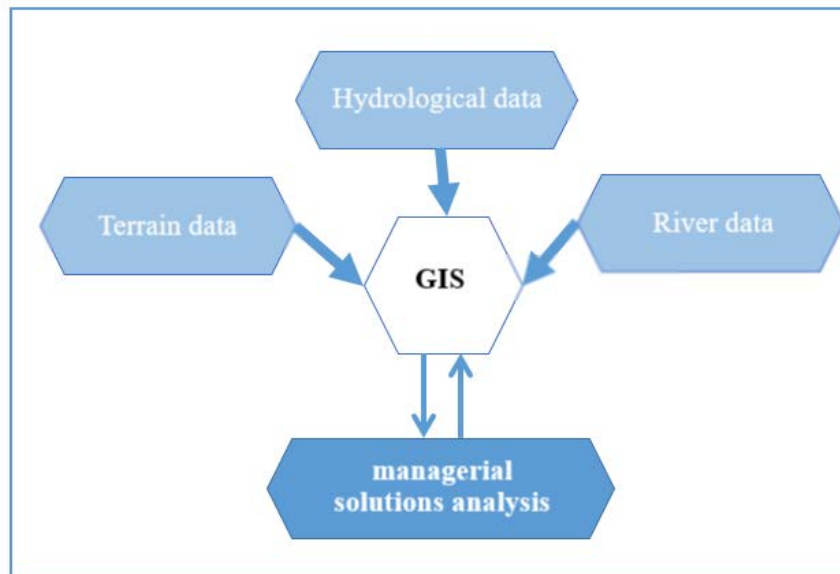


Figure 4. GIS-based model for building a hydrological system.

2.2.1 Terrain data

The terrain data is represented by the digital elevation model (DEM) (Fig. 5). The use of digital photogrammetric stations (DFS) for the creation of DEM by remote sensing is a successfully established method. DFS are a set of software and hardware designed to analyze data from space and aerial photography. It is possible to extract terrain data using special stereo processing tools both in automatic and in manual mode [22]. Based on such compiled DEMs, with the help of GIS software packages, it is possible to obtain important geometric, morphometric, hydrological, and other relief characteristics for simulated river basins [23].

During the processing of a DEM with GIS tools, geoinformation modeling of the hydrographic network, catchment areas and flood areas is implemented, which in turn provides the necessary basis for building more complex databases: floods and their consequences [31].

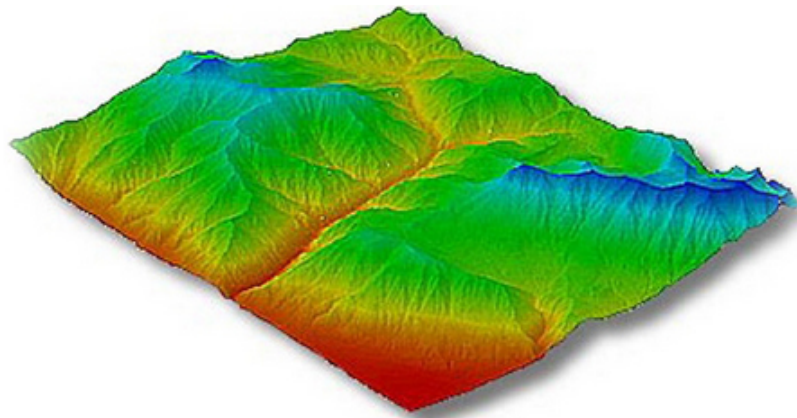


Figure 5. Terrain data example.

2.2.2 Hydrological data

Characteristics of river flow, including maximum flow rates and water levels in representative river basins, periods and duration of high water standoff, and other data can be found in the following sources:

- map materials (Fig. 6);
- Data from hydrological posts (Table 1);

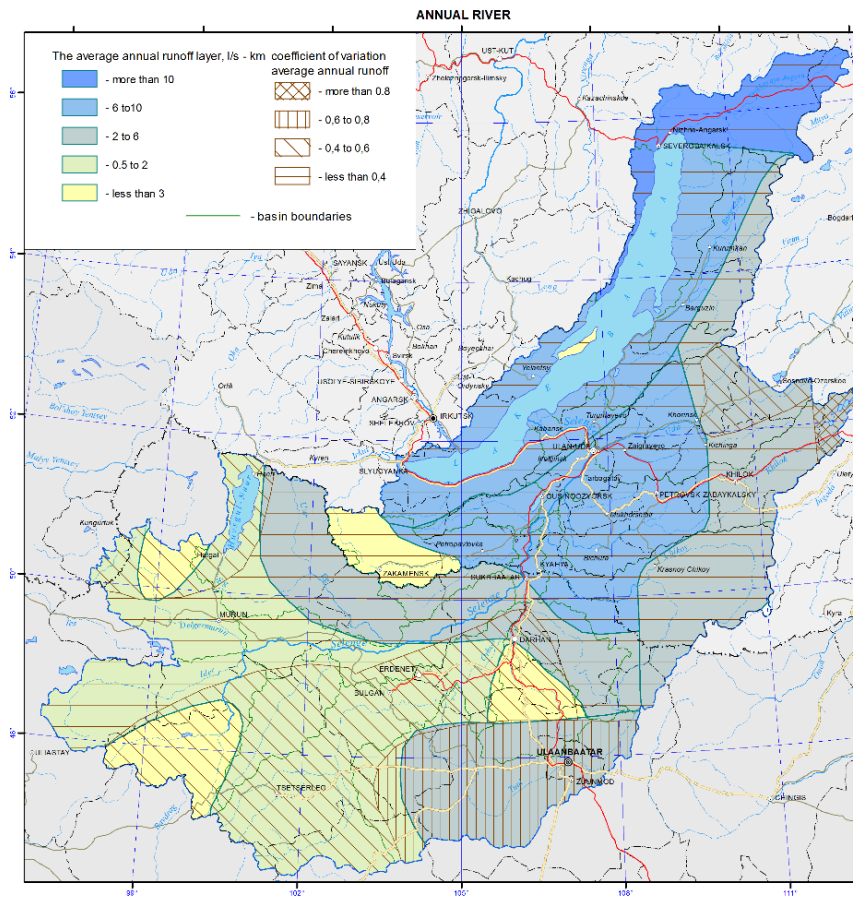


Figure 6. Annual river runoff map example.

Table 1. Hydrological post data example.

Post code	Name	Water object code	Distance from estuary, km	Drainage area, km ²	Zero level, m	Average level
6362	Met.station Selemdzha	118103384	544	1660	0	0
6363	s.Ekimchan	118103384	449	11600	480.29	0
6364	s.Stoyba	118103384	326	19600	339.66	0
6365	s.Selemdzhinsko e	118103384	262	20700	279.52	0
6367	s.Vissynskoe	118103384	197	27900	259.24	0
6369	city Norsk	118103384	134	46500	200.49	0
6370	v.Ulanochka	118103384	108	48800	190.12	0

2.2.3 River data

During the modeling process the time of a water standing at a certain level could be obtained, with a particular hydrograph and the SRFD configuration characteristics. Accordingly, the river data for the certain area of the river basin should be obtained, in order to have an appropriate solution of the problem in terms of environmental criteria. With the use of abovementioned data, so as with the land cover and land use data, the possible affection of SRFD to the environment could be estimated. This could help to understand, is it possible to build a SRFD at this section of the watercourse at all without or with any restrictions to the configuration.

3. Results and Discussions

For the assessment of the proposed method, a hypothetical river basin was considered. The work of creating a model consists of the following steps:

- modeling inside the ArcGIS software package with the HEC-GeoRAS module for working with terrain and creating river networks and cross-sections;
- direct work in the HEC-RAS software package [28], where editing of river sections and objects on them, and determining the hydrological properties of the watercourse itself;
- creation of the required model [27, 29–30], both static and dynamic (by setting hydrographs in a specific site).

Based on the data of remote sensing, a river network, a coastline are laid, and the direction of the river flow could be also indicated. Next, cross sections should be created. When calculating flood zones, HEC uses the constructed cross sections in accordance with the abovementioned and other formulas. They can be set automatically, with a defined interval and width, as well as manually. The software package analyzes data taking into account distances and elevations of the terrain and creates a file for export to HEC-RAS. At the next stage, using the tools of the HEC-RAS software package, the imported data from ArcGIS are processed and the hydrological conditions are set. After creating a separate project within the framework of HEC-RAS, modeling begins with the Geometric Data tab. Here it is possible to edit each cross section, reduce the number of points on which it is built, or smooth the alignment, if it is impossible to work with the original channel due to software limitations. Such restrictions arise due to the possible appearance of the «false channel» effect. If there are large differences in elevation of the relief, the program can identify them as independent channels, and this will cause an error in the calculation.

Also, the Manning coefficient is set in the Geometric Data tab, the characteristics of the river network are changed. In addition, any hydrological structures could be specified at a certain site (an easy adjustment of the cross sections was carried out and a synthetic roughness coefficient was set. The next step should be either SteadyFlow Data or UnsteadyFlow Data, depending on the type of a demanded model. As a result, the analysis of the given data was carried out using the SteadyFlow Analysis module and we obtain a model of the flood zone of a specific section of the river basin. The obtained data can be exported to ArcGIS to create a visual map. Modeling process at its various stages can be seen in Fig. 7–10.

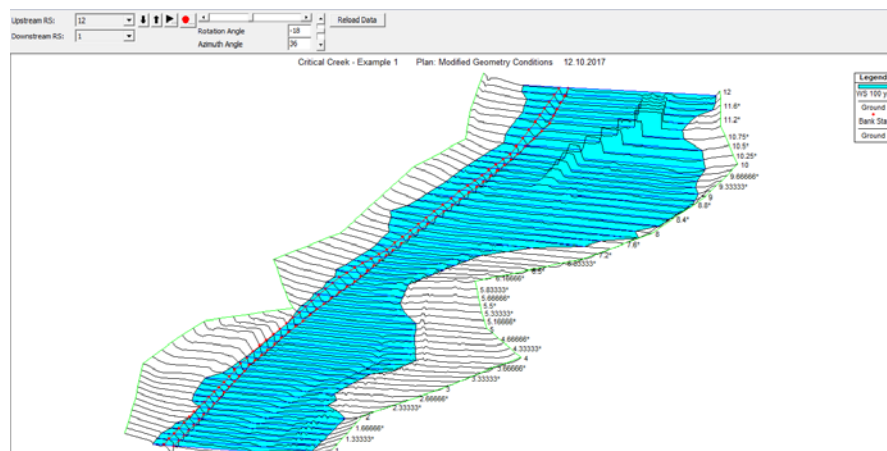


Figure 7. The modeling result without SRFD.

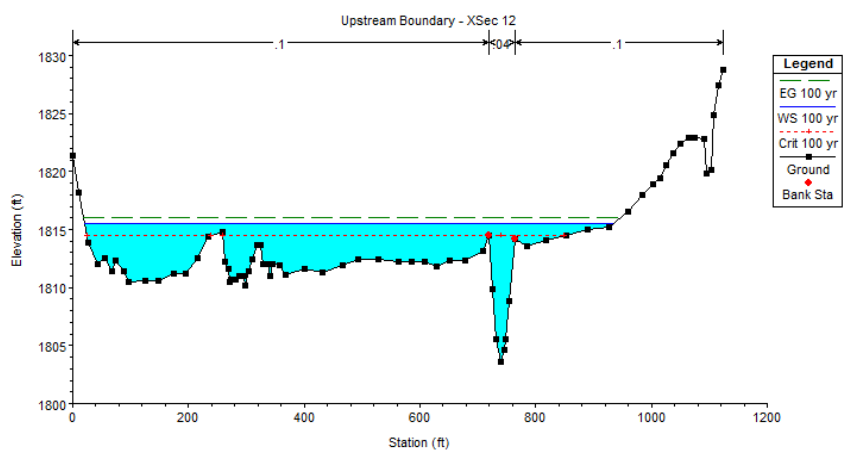


Figure 8. Cross-section without SRFD.

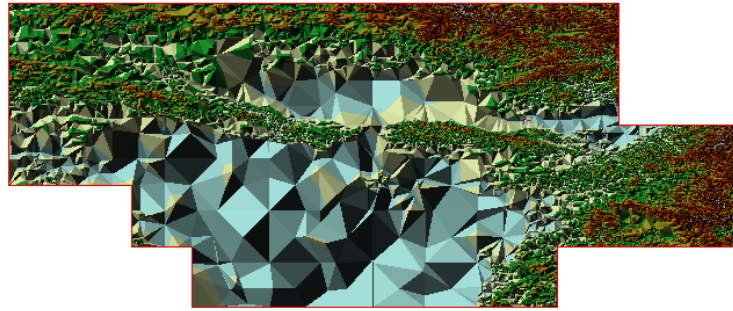


Figure 9. DEM with a specific rendering error.

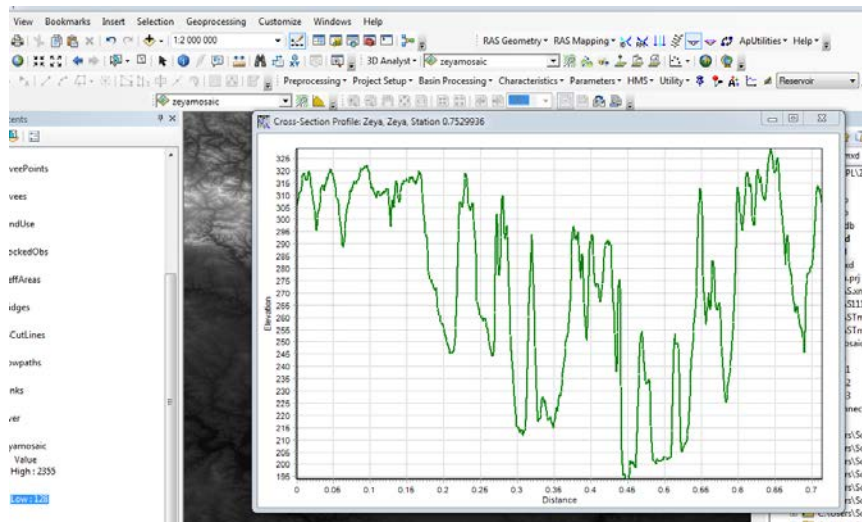


Figure 10. Cross-section with a “false channel” effect.

As we can see, there is a problem of source data related to DEM. Correct modeling is possible only if the terrain model is in the TIN format. When working with a raster image (obtained using SRTM), or with a model generated from a raster, incorrect data may be obtained. This is due to the specifics of the SRTM method [7, 8] (a general map is created from square tiles, each pixel has its own height, but error situations may occur at the junction of the squares), as well as due to incorrect terrain generation from the raster in the GIS environment (the terrain is generated triangular polygons). This problem seems to be a significant limitation, since fairly accurate initial data are required, otherwise there is a need to create synthetic river networks in which there will be no false channels and other deviations, but the modeling accuracy will suffer, the output model will differ significantly from the real one situation [32].

4. Conclusion

1. In the context of an increase in anthropogenic impact on the environment and the global economic crisis, a system of self-regulating flood control facilities with temporarily-filled reservoirs in the river basin is an appropriate measure to reduce the risk of floods. In this case, the regulatory capacity from flooding can be distributed evenly, while it is possible to protect large areas both in the floodplain of the river and in its upper tributaries, and on the side tributaries, from the harmful effects of flood waters.

2. In the course of the research, a flood modeling technique was formulated based on the use of GIS-based software systems, requirements for the initial data and the main algorithm of actions were formulated. The results of the study convincingly show that thanks to the created models of flooding the territories with the use of technical means of protection (in the form of a network of SRFD and temporarily filled reservoirs), it is possible to analyze both flood floods that have already occurred and to simulate possible floods of a given coverage. Based on such models, management decisions regarding flood control measures are possible. The advantage of the proposed methodology is the ability to justify the location of the proposed technical measures (systems of SRFD with certain parameters in the river basin), taking into account the assessment of the impact on ecosystems in the river basin. The disadvantage of this method is the extreme degree of dependence on the source data regarding the DEM, as well as the need for powerful personal computer to create a model for large sections of river basins, since due to the peculiarities of the GIS-systems operation, loading the generated model on weak computers takes considerable time.

3. The following areas of development in this research area can be distinguished:

- Updating cartographic information on modern infrastructure in river basins – the boundaries of settlements in the flood zone, roads, linear structures, as well as on the configuration of river channels.
- Obtaining information about the relief of river basins. For these purposes, DEMs obtained on the basis of highly detailed space and aircraft images are preferred.
- Calibration and verification of hydrodynamic models based on information about the boundaries of flooding from satellite images.

References

1. Danilov-Danilyan, V.I., Gelfan, A.N., Motovilov, Y.G., Kalugin, A.S. Disastrous flood of 2013 in the Amur basin: Genesis, recurrence assessment, simulation results. *Water Resources*. 2014. 41(2). Pp. 115–125. DOI: 10.1134/S0097807814020055
2. Abt, S.R., Wittier, R.J., Taylor, A., Love, D.J. HUMAN STABILITY IN A HIGH FLOOD HAZARD ZONE. *JAWRA Journal of the American Water Resources Association*. 1989. DOI: 10.1111/j.1752-1688.1989.tb05404.x
3. Aronica, G.T., Candela, A., Fabio, P., Santoro, M. Estimation of flood inundation probabilities using global hazard indexes based on hydrodynamic variables. *Physics and Chemistry of the Earth*. 2012. DOI: 10.1016/j.pce.2011.04.001
4. Evans, E., Hall, J., Penning-Rowsell, E., Sayers, P., Thorne, C., Watkinson, A. Future flood risk management in the UK. *Proceedings of the Institution of Civil Engineers: Water Management*. 2006. DOI: 10.1680/wama.2006.159.1.53
5. Apel, H., Thieken, A.H., Merz, B., Blöschl, G. Flood risk assessment and associated uncertainty. *Natural Hazards and Earth System Science*. 2004. DOI: 10.5194/nhess-4-295-2004
6. Habersack, H., Hein, T., Stanica, A., Liska, I., Mair, R., Jäger, E., Hauer, C., Bradley, C. Challenges of river basin management: Current status of, and prospects for, the River Danube from a river engineering perspective. *Science of the Total Environment*. 2016. DOI: 10.1016/j.scitotenv.2015.10.123
7. Aref'ev, N.V., Badenko, V.L., Osipov, G.K. Basin-landscape approach to the organization of environmental monitoring of hydropower complexes on the basis of geographical information technologies. *Power Technology and Engineering*. 1998.
8. Nogueira Vilanova, M.R., Perrella Balestieri, J.A. Energy and hydraulic efficiency in conventional water supply systems. 2014.
9. Merkuryeva, G., Merkuryev, Y., Sokolov, B. V., Potryasaev, S., Zelentsov, V.A., Lektuers, A. Advanced river flood monitoring, modelling and forecasting. *Journal of Computational Science*. 2015. DOI: 10.1016/j.jocs.2014.10.004
10. Rafieeinasab, A., Norouzi, A., Kim, S., Habibi, H., Nazari, B., Seo, D.J., Lee, H., Cosgrove, B., Cui, Z. Toward high-resolution flash flood prediction in large urban areas – Analysis of sensitivity to spatiotemporal resolution of rainfall input and hydrologic modeling. *Journal of Hydrology*. 2015. DOI: 10.1016/j.jhydrol.2015.08.045
11. Mirsaidov, M.M., Toshmatov, E.S. Spatial stress state and dynamic characteristics of earth dams. *Magazine of Civil Engineering*. 2019. DOI: 10.18720/MCE.89.1
12. Kantardgi, I.G., Zheleznyak, M.I., Anshakov, A.S. Numerical modeling of nonlinear hydrodynamics of the coastal areas. *Magazine of Civil Engineering*. 2019. DOI: 10.18720/MCE.87.7
13. Fedorov, M.P., Maslikov, V.I., Badenko, V.L., Chusov, A.N., Molodtsov, D.V. Reducing the Risk of Flooding by Using Hydro Complexes Distributed on the Drainage Basin. *Power Technology and Engineering*. 2017. DOI: 10.1007/s10749-017-0840-x
14. Chusov, A., Maslikov, V., Molodtsov, D., Manukhina, O. Determination of Environmental Impact Factors of Flood Control Hydrosystems with Temporarily Filled Self-regulating Reservoirs. *Advances in Intelligent Systems and Computing*. 2018. DOI: 10.1007/978-3-319-70987-1_113
15. Davydov, R., Antonov, V., Molodtsov, D., Cheremisin, A., Korablev, V. The simulation model for a flood management by flood control facilities. *MATEC Web of Conferences*. 2018. DOI: 10.1051/mateconf/201824515002
16. Nikonorov, A., Badenko, V., Terleev, V., Togo, I., Volkova, Y., Skvortsova, O., Nikonova, O., Pavlov, S., Mirschel, W. Use of GIS-environment under the Analysis of the Managerial Solutions for Flood Events Protection Measures. *Procedia Engineering*. 2016. DOI: 10.1016/j.proeng.2016.11.916
17. Nikonorov, A., Terleev, V., Badenko, V., Mirschel, W., Abakumov, E., Ginevsky, R., Lazarev, V., Togo, I., Volkova, Y., Melnichuk, A., Dunaieva, I., Akimov, L. Modeling the hydrophysical soil properties as a part of self-regulated flood dams projection in gis-environment for sustainable urban development. *IOP Conference Series: Earth and Environmental Science*. 2017. DOI: 10.1088/1755-1315/90/1/012109
18. Ahmad, S., Simonovic, S.P. System dynamics modeling of reservoir operations for flood management. *Journal of Computing in Civil Engineering*. 2000. DOI: 10.1061/(ASCE)0887-3801(2000)14:3(190)
19. Kaspersen, B.S., Jacobsen, T.V., Butts, M.B., Boegh, E., Müller, H.G., Stutter, M., Fredenslund, A.M., Kjaer, T. Integrating climate change mitigation into river basin management planning for the Water Framework Directive – A Danish case. *Environmental Science and Policy*. 2016. DOI: 10.1016/j.envsci.2015.10.002
20. Molina-Navarro, E., Hallack-Alegría, M., Martínez-Pérez, S., Ramírez-Hernández, J., Mungaray-Moctezuma, A., Sastre-Merlín, A. Hydrological modeling and climate change impacts in an agricultural semiarid region. Case study: Guadalupe River basin, Mexico. *Agricultural Water Management*. 2016. DOI: 10.1016/j.agwat.2015.10.029
21. Sanders, B.F. Evaluation of on-line DEMs for flood inundation modeling. *Advances in Water Resources*. 2007. DOI: 10.1016/j.advwatres.2007.02.005
22. Motovilov, Y.G., Danilov-Danilyan, V.I., Dod, E.V., Kalugin, A.S. Assessing the flood control effect of the existing and projected reservoirs in the middle amur basin by physically—based hydrological models. *Water Resources*. 2015. DOI: 10.1134/S0097807815030124.
23. Meert, P., Pereira, F., Willems, P. Computationally efficient modelling of tidal rivers using conceptual reservoir-type models. *Environmental Modelling and Software*. 2016. DOI: 10.1016/j.envsoft.2015.11.010
24. Sainov, M.P., Soroka, V.B. Ultra-high rockfill dam with combination of the reinforced concrete face and clay-cement diaphragm. *Magazine of Civil Engineering*. 2018. DOI: 10.18720/MCE.81.14
25. Bazarov, D.R., Mavlyanova, D.A. Numerical studies of long-wave processes in the reaches of hydrosystems and reservoirs. *Magazine of Civil Engineering*. 2019. DOI: 10.18720/MCE.87.10
26. Prakash, M., Rothauge, K., Cleary, P.W. Modelling the impact of dam failure scenarios on flood inundation using SPH. *Applied Mathematical Modelling*. 2014. DOI: 10.1016/j.apm.2014.03.011

27. Papathanasiou, C., Makropoulos, C., Mimikou, M. Hydrological modelling for flood forecasting: Calibrating the post-fire initial conditions. *Journal of Hydrology*. 2015. DOI: 10.1016/j.jhydrol.2015.07.038
28. Zazo, S., Molina, J.L., Rodríguez-González, P. Analysis of flood modeling through innovative geomatic methods. *Journal of Hydrology*. 2015. DOI: 10.1016/j.jhydrol.2015.03.011
29. Saleh, A.M., Belal, A.B., Mohamed, E.S. Land resources assessment of El-Galaba basin, South Egypt for the potentiality of agriculture expansion using remote sensing and GIS techniques. *Egyptian Journal of Remote Sensing and Space Science*. 2015. DOI: 10.1016/j.ejrs.2015.06.006
30. Halwatura, D., Najim, M.M.M. Application of the HEC-HMS model for runoff simulation in a tropical catchment. *Environmental Modelling and Software*. 2013. DOI: 10.1016/j.envsoft.2013.03.006
31. Mohammadi, S.A., Nazariha, M., Mehrdadi, N. Flood damage estimate (quantity), using HEC-FDA model. Case study: The Neka river. *Procedia Engineering*. 2014. DOI: 10.1016/j.proeng.2014.02.130
32. Arefiev, N., Nikonova, O., Badenko, N., Ivanov, T., Oleshko, V. Development of automated approaches for hydropowerpotential estimations and prospective hydropower plants siting. *Vide. Tehnologija. Resursi – Environment, Technology, Resources*. 2015. DOI: 10.17770/etr2015vol2.260

Contacts:

Aleksandr Nikonorov, coolhabit@yandex.ru

Vladimir Badenko, vbadenko@gmail.com

© Nikonorov, A.,Badenko, V.L., 2021



DOI: 10.34910/MCE.101.11

Stochastic model of the construction process implemented with application of sliding formwork

M.M. Matskina, M.V. Petrochenko, A.E. Radaev*

Peter the Great St. Petersburg Polytechnic University, St. Petersburg, Russia

* E-mail: TW-inc@yandex.ru

Keywords: construction, sliding formwork, concrete layer, concrete maturing, concrete pouring, stochastic model

Abstract. The paper covers issues connected to the determination of most preferred values for the parameters of construction processes implemented with application of sliding formwork and defined by the factors of stochastic nature. On the basis of the review of different literature sources connected to the modeling of mentioned above processes it has been concluded that existing scientific developments provide relatively low adequacy of the results due to the simplified mathematical models that do not take into account stochastic factors. That circumstance has determined the necessity for creation of stochastic model for the construction process implemented with sliding formwork. The initial data for the model include baseline duration of the wall construction process, wall height, concrete layer thickness, characteristics of stochastic values of the concrete layer's pouring and maturing duration (mathematical expectation and mean-square deviation), etc.; parameters to be determined are the sliding formwork's panel height and movement base (average) speed. The created model has been implemented on the practical example – wall construction process as the element of the project "Arctic NLG 2". On the basis of the received results the conclusion has been made about high practical significance of the developed tool.

1. Introduction

Modern conditions of the construction industry's development are defined by the increase of requirements for the time and cost parameters of the technological processes assumed by construction projects, increase of the complexity of works performed and implementation of structurally modified innovative materials. In that conditions the issues connected to the determination of the most preferred values for the parameters of technological processes based on different factors of stochastic nature – especially, wall construction with application of sliding formwork technology – gain particular importance as mentioned factors have significant influence on the duration and cost of the works performed in accordance with construction project. This circumstance has determined the necessity for conduction of the research which object is a construction process implemented with application of sliding formwork; corresponding subject is determined by the parameters of the mentioned processed that are connected to the factors of stochastic nature.

Sliding formwork technology is one of the modern technologies applied for building of reinforced concrete structures. A feature of the technology is connected to the application of specific equipment providing continuous movement of the formwork during its pouring with concrete in layers and, as sequence, continuity of the concreting pouring. As the formwork slowly and continuously rises, reinforcing and concrete pouring goes on the upper level and the fresh surface processing on the level below (see Fig. 1).

Matskina, M.M., Petrochenko, M.V., Radaev, A.E. Stochastic model of the construction process implemented with application of sliding formwork. Magazine of Civil Engineering. 2021. 101(1). Article No. 10111.

DOI: 10.34910/MCE.101.11



This work is licensed under a [CC BY-NC 4.0](https://creativecommons.org/licenses/by-nc/4.0/)

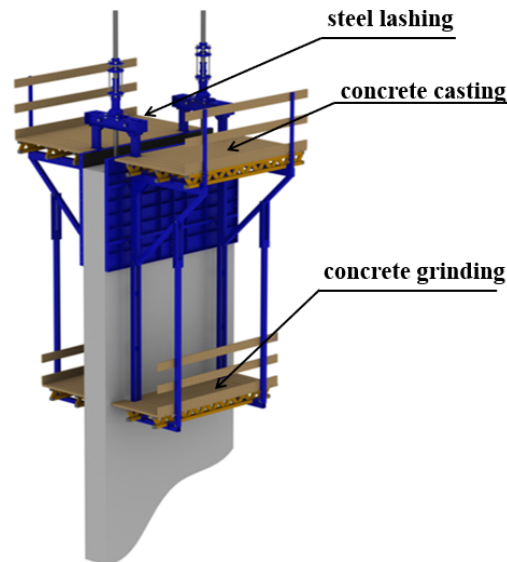


Figure 1. Sliding formwork's general view.

At the initial stage of the research the general analysis of the object under consideration and the review of the scientific developments connected to the modeling of construction processes implemented with application of sliding formwork have been carried out. On the basis of the corresponding results the following conclusions have been made:

1. The literature sources connected to the technology described above can be divided into the following categories:

1.1 Works connected to the comparative analysis of the sliding formwork technology with other technologies of concreting pouring [1–4]. That works contain description of both main advantages of the sliding formwork technology – including relatively high speed of work and the tightness of the finished structure (no joints during continuous concreting) and its disadvantages – increase of operational costs connected to the use of more complex mechanized or automated equipment, a significant impact on the accuracy of formwork positioning on the quality of work performed, etc.

1.2 Works connected to the analysis of the influence of different factors on the aggregate indicators (duration, cost, quality) of the works performed [5–9], including the following studies:

- influence of the formwork occupancy (the level concrete poured in the height of the formwork) on the quality of works performed [5–7]; on the one hand, increase of the formwork volume used for concreting pouring within one continuous operation determines increase of technological process's reliability in terms of possible intervals of technological idle time; on the other hand, ensuring empty volume within the framework provides flexibility of technological process in terms of framework's movement speed regulation in accordance with the dynamics of the concrete hardening or as the adjustment to different events in internal (connected to the technological resources involved) or external environment; researchers have formulated the practical recommendations connected to the formwork occupancy – particularly, the height of the empty volume within the formwork should be equal to the value that 2–3 times higher than concrete pouring level thickness (in case the thickness is 10–15 cm, the mentioned empty volume height is 30–40 cm);

- influence of the thickness of the poured layer on the sliding formwork's movement speed and quality of the concreting pouring [8]; the experimental data showed that with the layer thickness increase the maximum temperature arising during its hardening also increases but with decreasing rate; researchers conclude that in conditions of layer-by-layer casting it is much easier to control thermal cracking in comparison with the block-casting method.

1.3 Works connected to the creation of mathematical models for the construction process implemented with application of sliding formwork [10–21], including the following scientific developments:

- developments connected to the determination of the formwork's technological parameters with application of Building Information Modeling (BIM) for the provision of synchronized scheduling tool [10–14]; those developments are not directly connected to the mathematical modeling as corresponding scientific works include description of different block schemes describing connection between implemented technological process and corresponding BIM models;

- developments connected to the formwork method selection with application of artificial neural networks [15–17], fuzzy logic algorithms [18], multi-criteria decision making [19] and analytical approach [20–22]; the corresponding scientific results – models and algorithms – provide determination of optimal

combination of values for unknown characteristics of formwork technology but don't take into account the stochastic nature of different parameters describing technological process under consideration;

- developments connected to the determination of aggregate indicators of the technological process implemented with application of the formwork on the basis of simulation modeling methods [23, 24] – corresponding models don't take into account features of sliding formwork technology and connected with high laboriousness for provision of relatively high adequacy of the results;

- developments connected to the analysis of the physical processes connected to pouring of a concrete into the formwork with different technical characteristics of pumping equipment [25–27] – corresponding models can be used for optimization of the formwork filling process during the design phase but the corresponding factors taken into account don't have significant influence on the technological process's duration that depends also on the time characteristics of other processes (including formwork movement, reinforcement dressing, etc.).

2. Most of existing scientific developments are based on a deterministic (not stochastic) nature of the parameters of construction process implemented with application of sliding formwork and therefore do not correspond to the real conditions of technological process's implementation and, as a sequence, have relatively small practical significance.

On the basis of all mentioned above the general description of the research has been formulated in terms of the following elements:

- research aim – development of the tool for justification of parameters of the construction process implemented with application of sliding formwork.
- research tasks:
 1. Creation of the stochastic model of the construction process implemented with application of sliding formwork – in terms of main provisions, initial data and calculated characteristics.
 2. Implementation of the stochastic model on a practical example for objective estimation of the practical significance of the created model.

The detailed description of the corresponding structural elements of the research is presented in the following sections of the work.

2. Methods

During the next stage of the research the stochastic model for determination of the most preferred values for parameters of construction process implemented with application of sliding formwork has been created. The main provisions of the created mathematical model are the following:

1. The object under consideration is the technological process of the wall erection performed with application of sliding formwork within a limited time interval (determined by the construction project forecast characteristics).

2. The technological process of the wall erection with sliding formwork includes the following main steps:

- 2.1. Panels installation in its lowest position; sequential laying (pouring) of concrete layers in an amount that takes into account the legal limit concrete level in the formwork height and the height of one layer with simultaneous control of the layer maturing dynamics.

- 2.2. Formwork lifting is performed starting from the latest of the following events: development of sufficient strength of the lower layer; the end of the filling of the last stationary formwork (located in the lowest position).

- 2.3. The movement of the formwork is carried out at a stationary speed within the thickness of one layer of concrete pouring; the movement speed is determined by the standard (most preferred) value, as well as the maximum relative deviation that determines the range of speed values in the case of a relatively low or high speed of next concrete layer maturing.

- 2.4. The processes described in paragraphs 2.2 and 2.3 are repeated until the formwork reaches the upper extreme position while the process of layer-by-layer concrete pouring will continue until the formwork height is filled.

3. It is necessary to determine the structural parameters of the formwork – the height of the panel and the nominal speed of its movement – to ensure minimal operational costs and the duration of the wall erection should not exceeding the maximum allowable values in conditions when the durations of laying and maturing of the next layer of concrete are stochastic values corresponding to the normal distribution.

It is important to note that stochastic nature of the duration parameters for laying and maturing of the concrete layer is caused by the influence of big amount of factors on the characteristics of corresponding

technological processes. In the case of concrete laying, the mentioned factors are connected to the qualifications of the worker manipulating the trunk of a concrete pumping unit, the amount of preparatory work determined by the configuration of the reinforcement, the state of the previous layer, etc. In the case of concrete maturing, the mentioned factors are connected to the physical and mechanical properties of concrete, the impossibility of enduring of the fixed thickness of concrete layer, etc. The spread of the values of the corresponding time parameters is not critical in the case of the use of standard technologies for the construction of reinforced concrete structures, however, in the case of the sliding formwork technology, which is based mainly on ensuring the continuity and synchronization of the operations of concrete laying and maturing, as well as the movement of the formwork, the specified spread gets much larger significance.

Developed model is based in the initial data specified in Table 1 and assumes carrying out of calculations of individual quantitative characteristics presented in Table 2 (the sequence of calculations is determined by the order of characteristics' numbering in the last specified table). The model's connection to the real conditions is determined by the correspondence of the duration of repeated technological operations to the normal probability distribution. The proposed calculation formulas are based on the probability theory elements.

Table 1. Initial data for created mathematical model.

No	Characteristic name	Designation	Meas. unit
1	General initial data		
1.1	Parameters of the alternative solutions set		
1.1.1	Number of sliding formwork's panel height alternative values	units	m
1.1.2	Number of sliding formwork's movement speed alternative base values	units	n
1.2	Time parameters		
1.2.1	Baseline duration of the wall construction process	hours	$T^{\Sigma \max}$
1.2.2	Mathematical expectation of the one layer pouring duration	hours	\bar{T}_m
1.2.3	Mean-square deviation of the one layer pouring duration	hours	σ_m
1.2.4	Mathematical expectation of the one layer maturing duration	hours	\bar{T}_c
1.2.5	Mean-square deviation of the one layer maturing duration	hours	σ_c
1.3	Design parameters		
1.3.1	Wall height	m	H^{Σ}
1.3.2	The height of the top gape area	m	Δh^e
1.3.3	Thickness of the concrete layer	m	h
1.3.4	Maximal deviation from the sliding formwork's movement base speed	-	Δ_v
1.4	Probabilistic parameters		
1.4.1	The minimal probability that the layer maturing duration will not exceed the total layers pouring duration within the valid formwork occupancy height	-	P_{cm}^{\min}
1.4.2	The minimal probability that the layer maturing duration will not exceed the duration of the minimum speed formwork movement to the valid formwork occupancy height	-	P_{h-}^{\min}
1.4.3	The minimal probability that the layer pouring duration will exceed the duration of the minimum speed formwork movement to the one layer height	-	P_{t-}^{\min}
1.4.4	The minimal probability that the layer pouring duration will not exceed the duration of the maximum speed formwork movement to the one layer height	-	P_{t+}^{\min}
1.5	Cost parameters		
1.5.1	Unit costs per sliding formwork's panel height unit	CU/m	c^H
1.5.2	Unit costs per sliding formwork's movement base speed unit	CU / (m/hour)	c^v
2	Indexes		
2.1	Index of the sliding formwork's panel height alternative value	-	$i = 1, 2, \dots, m$
2.2	Index of the sliding formwork's movement speed alternative base value	-	$j = 1, 2, \dots, n$

No	Characteristic name	Designation	Meas. unit
3	Parameters for each alternative value i ($i = 1, 2, \dots, m$) of sliding formwork's panel height		
3.1	Sliding formwork's panel height alternative value	m	H_i
4	Parameters for each alternative base value j ($j = 1, 2, \dots, n$) of sliding formwork's movement speed		
4.1	Sliding formwork's panel height alternative base value	m/hour	v_j

Table 2. Calculated characteristics for created mathematical model.

No	Characteristic name	Meas. unit	Formula
1	Characteristics calculated for each alternative value i ($i = 1, 2, \dots, m$) of sliding formwork's panel height		
1.1	Number of layers inside the formwork	units	$z_i^H = \frac{H_i - \Delta h^e}{h}$
1.2	Number of formwork movements	hours	$z_i^{H\Sigma} = \frac{H^\Sigma}{z_i^H \cdot h}$
1.3	Mathematical expectation of the layers pouring duration within the formwork's panel height (without technological time between the layers) ⁽¹⁾	hours	$M_{Hi} = \bar{T}_m \cdot z_i^H$
1.4	Mean-square deviation of the layers pouring duration within the formwork's panel height (without technological time between the layers) ⁽²⁾	hours	$\sigma_{Hi} = \sigma_m \cdot \sqrt{z_i^H}$
1.5	Actual probability that the layer maturing duration will not exceed the total layers pouring duration within the valid formwork occupancy height ⁽³⁾⁽⁴⁾	-	$P_{cmi} = \Phi' \left(\frac{M_{Hi} - \bar{T}_c}{\sqrt{\sigma_{Hi}^2 + \sigma_c^2}} \right)$
1.6	Total costs per formwork height	CU	$C_i^H = c^H \cdot H_i$
2	Characteristics performed for each alternative base value j ($j = 1, 2, \dots, n$) of sliding formwork's movement speed		
2.1	Duration of the formwork movement via the layer thickness at minimum speed	hour	$t_{hj}^{\min} = \frac{h}{v_j \cdot (1 - \Delta_v)}$
2.2	Duration of the formwork movement via the layer thickness at base (average) speed	hour	$t_{hj}^{\text{aver}} = \frac{h}{v_j}$
2.3	Duration of the formwork movement via the layer thickness at maximum speed	hour	$t_{hj}^{\max} = \frac{h}{v_j \cdot (1 - \Delta_v)}$
2.4	Actual probability that the layer pouring duration will exceed the duration of the minimum speed formwork movement to the one layer height ⁽³⁾⁽⁵⁾	-	$P_{t-j} = 1 - \Phi' \left(\frac{t_{hj}^{\min} - \bar{T}_m}{\sigma_m} \right)$
2.5	Actual probability that the layer pouring duration will not exceed the duration of the maximum speed formwork movement to the one layer height ⁽³⁾⁽⁵⁾	-	$P_{t+j} = \Phi' \left(\frac{t_{hj}^{\max} - \bar{T}_m}{\sigma_m} \right)$
2.6	Total costs determined by formwork base speed	CU	$C_j^v = c^v \cdot v_j$
3	Characteristics calculated for each alternative value i ($i = 1, 2, \dots, m$) of sliding formwork's panel height and for each alternative base value j ($j = 1, 2, \dots, n$) of sliding formwork's movement speed		
3.1	Duration of the minimum speed formwork movement via the valid formwork occupancy height	hour	$t_{Hij} = \frac{H_i - \Delta h^e}{v_j \cdot (1 - \Delta_v)}$
3.2	Actual probability that the layer maturing duration will not exceed the duration of the minimum speed formwork movement to the valid formwork occupancy height ⁽³⁾⁽⁵⁾	hour	$P_{h-ij} = \Phi' \left(\frac{t_{Hij} - \bar{T}_c}{\sigma_c} \right)$

No	Characteristic name	Meas. unit	Formula
3.3	Expected estimated duration of wall construction process	days	$T_{ij}^{\Sigma} = \left(P_{cmi} \cdot P_{h-ij} \times \right. \\ \left. \times \left(P_{t-j} \cdot P_{t+j} \cdot z_i^H \cdot t_{hj}^{aver} + \right. \right. \\ \left. \left. + \left(1 - P_{t-j} \right) \cdot P_{t+j} \cdot z_i^H \cdot t_{hj}^{min} \right) + \right. \\ \left. + P_{cmi} \cdot \left(P_{h-ij} \cdot \left(1 - P_{t+j} \right) + \right. \right. \\ \left. \left. + \left(1 - P_{h-ij} \right) \right) \cdot z_i^H \cdot \bar{T}_m + \right. \\ \left. + \left(1 - P_{cmi} \right) \cdot \bar{T}_c \right) \cdot z_i^{H\Sigma}$
3.4	Total costs	CU	$C_{ij}^{\Sigma} = C_i^H + C_j^v$
3.5	The indicated value of the total costs with taking into account of acceptable solutions area	CU	$C_{ij}^{\prime\Sigma} = \begin{cases} C_{ij}^{\Sigma}, & \text{if } T_{ij}^{\Sigma} \leq T^{\Sigma \max}, \\ & P_{cmi} \geq P_{cm}^{\min}, \\ & P_{h-ij} \geq P_{h-}^{\min}, \\ & P_{t-j} \geq P_{t-}^{\min}, \\ & P_{t+j} \geq P_{t+}^{\min}; \\ \text{null} & \text{otherwise} \end{cases}$
3.6	Indicator of the option feasibility for various formwork moving forms	-	$y_{ij} = \begin{cases} 1, & \text{if } i, j: \\ C_{ij}^{\prime\Sigma} = \min \left\{ \min_j \{ C_{ij'}^{\Sigma} \} \right\} \\ 0 & \text{otherwise} \end{cases}$
4	Aggregate calculated characteristics		
4.1	Design characteristics		
4.1.1	Sliding formwork's panel height actual value	m	$H = \sum_{i=1}^m \left(H_i \cdot \sum_{j=1}^n y_{ij} \right)$
4.1.2	Sliding formwork's movement speed actual base value	m/hour	$v = \sum_{j=1}^n \left(v_j \cdot \sum_{i=1}^m y_{ij} \right)$
4.2	Probabilistic characteristics		
4.2.1	The actual value of probability that the another layer maturing time will not exceed the duration of the formwork's movement within thickness of one layer with base speed	-	$P_{cm} = \sum_{i=1}^m \left(P_{cmi} \cdot \sum_{j=1}^n y_{ij} \right)$
4.2.2	The actual value of probability that the another layer maturing time will not exceed the duration of the formwork's movement within thickness of one layer with minimal speed	-	$P_{h-} = \sum_{i=1}^m \sum_{j=1}^n P_{h-ij} \cdot y_{ij}$
4.2.3	The actual value of probability that the layers maturing time inside the formwork will not exceed the maximal reserve of technological time	-	$P_{t-} = \sum_{j=1}^n \left(P_{t-j} \cdot \sum_{i=1}^m y_{ij} \right)$
4.2.4	The actual value of probability that the actual duration of the wall construction will not exceed the planned value	-	$P_{t+} = \sum_{j=1}^n \left(P_{t+j} \cdot \sum_{i=1}^m y_{ij} \right)$
4.3	Time characteristics		
4.3.1	The actual value of the expected estimated duration of wall construction	hours	$T^{\Sigma} = \sum_{i=1}^m \sum_{j=1}^n T_{ij}^{\Sigma} \cdot y_{ij}$
4.4	Cost characteristics		
4.4.1	The actual costs for pouring into layers of a certain thickness	CU	$C^H = c^H \cdot \sum_{i=1}^m \left(H_i \cdot \sum_{j=1}^n y_{ij} \right)$
4.4.2	The actual costs due to formwork movement speed changes	CU	$C^v = c^v \cdot \sum_{j=1}^n \left(v_j \cdot \sum_{i=1}^m y_{ij} \right)$

No	Characteristic name	Meas. unit	Formula
4.4.3	The actual total costs	CU	$C^\Sigma = C^H + C^v$

Note:

- (1) characteristic is calculated with the correspondence the summation rule for the stochastic values' mathematical expectations;
- (2) characteristic is calculated with the correspondence the summation rule for the stochastic values' mean-square deviations;
- (3) designation Φ' (in the calculated expression) defines the inverse Laplace function, which provides a probability determination based on the initially known normalized deviation (argument);
- (4) characteristic is calculated on the basis of the formulas for estimation of the probabilistic parameters for the comparison of random variables corresponding to the normal distribution;
- (5) characteristic is calculated on the basis of the dependence between probabilistic parameters and values of a random variable for a function of standard normal distribution.

3. Results and Discussions

At the last stage of the research created mathematical model has been implemented on a practical example – technological process connected to the wall construction in accordance with the project “Arctic NLG 2” (construction of production unit for liquefied natural gas located on the Gydan Peninsula in the Yamal-Nenets Autonomous Area) – with application of Microsoft Excel software. The general view of the corresponding worksheet (including initial data and calculation results) is presented in Fig. 2–4. The principles of the worksheet's fulfillment with the data connected to the task are presented in Table 3. The most preferred values for the initially unknown parameters of the technological process under consideration are the following: sliding formwork's panel height – 1.5 meters, corresponding movement base (average) speed – 1.2 meters per day.

	A	B	C	D	E	F	G	H	I	J	K	L	
1	Table 1. Initial data												
2	No.	Characteristic name						Designation	Meas. unit	Value			
3	4	1 Time parameters											
4	1.1	Baseline duration of the wall construction process						$T^{\Sigma, \max}$	hours	480			
5	1.2	Mathematical expectation of the one layer pouring duration						T_{-m}^-	hours	2			
6	1.3	Mean-square deviation of the one layer pouring duration						σ_m	hours	0.3			
7	1.4	Mathematical expectation of the one layer maturing duration						T_{-c}^-	hours	25			
8	1.5	Mean-square deviation of the one layer maturing duration						σ_c	hours	5			
9	2	Design parameters											
10	2.1	Wall height						H^{Σ}	m	10			
11	2.2	The height of the top gap area						Δh^{Σ}	m	0.2			
12	2.3	Thickness of the concrete layer						h	m	0.1			
13	2.4	Maximal deviation from the sliding formwork's movement base speed						Δv	-	0.1			
14	3	Probabilistic parameters											
15	3.1	The minimal probability that the layer maturing duration will not exceed the total layers pouring duration within the valid formwork occupancy height						P_{-im}^{\min}	-	0.5			
16	3.2	The minimal probability that the layer maturing duration will not exceed the duration of the minimum speed formwork movement to the valid formwork occupancy height						P_{-b}^{\min}	-	0.5			
17	3.3	The minimal probability that the layer pouring duration will exceed the duration of the minimum speed formwork movement to the one layer height						P_{-p}^{\min}	-	0.2			
18	3.4	The minimal probability that the layer pouring duration will not exceed the duration of the maximum speed formwork movement to the one layer height						P_{-t}^{\min}	-	0.2			
19	4	Cost parameters											
20	4.1	Unit costs per sliding formwork's panel height unit						c^H	CU/m	2.25			
21	4.2	Unit costs per sliding formwork's movement base speed unit						$c^{v'}$	CU/(m/hour)	2.5			
22													
23													
24													
25													
26													
27													
28													
29													
30													
31													
32													
33													
34													
35	Table 3. Aggregate calculated characteristics												
36	No.	Characteristic name						Designation	Meas. unit	Value			
37	1	Design characteristics											
38	1.1	Sliding formwork's panel height actual value						H	hour	1.5			
39	1.2	Sliding formwork's movement speed actual base value						v	m/hour	0.049679			
40	2	Probabilistic characteristics											
41	2.1	The actual value of probability that the another layer maturing time will not exceed the duration of the formwork's movement within thickness of one layer with base speed						P_{-on}	-	0.577491			
42	2.2	The actual value of probability that the another layer maturing time will not exceed the duration of the formwork's movement within thickness of one layer with minimal speed						P_{-m}	-	0.792479			
43	2.3	The actual value of probability that the layers maturing time inside the formwork will not exceed the maximal reserve of technological time						P_{-t}	-	0.215193			
44	2.4	The actual value of probability that the actual duration of the wall construction will not exceed the planned value						P_{-c}	-	0.285371			
45	3	Time characteristics											
46	3.1	The actual value of the expected estimated duration of wall construction						T^{Σ}	hours	199.2108			
47	4	Cost characteristics											
48	4.1	The actual costs for pouring into layers of a certain thickness						C^{II}	CU	3.375			
49	4.2	The actual costs due to formwork movement speed changes						$C^{v'}$	CU	2.980769			
50	4.3	The actual total costs						C^{Σ}	CU	6.355769			

Figure 2. General view of the Microsoft Excel worksheet created during the implementation of elaborated model on a practical example (beginning).

	M	N	O	P	Q	R	S	T	U	V	W	X	Y	Z	AA	AB	AC	AD	AE	AF	AG	AH	AI	AJ	AK	AL	AM	AN	AO	AP	AQ	AR	AS				
1	Table 2. Calculated characteristics for alternative variants																																				
2															The indicator of the feasibility of selection of the alternative variant (j)														Total value	Layers pouring duration within the formwork's panel height (without technological time between the layers)		Actual probability that the layer maturing duration will not exceed the total layers pouring duration within the valid formwork occupancy height	Total costs per formwork height				
3	Variant number	Sliding formwork panel height	Amount of layers inside the formwork	Number of formwork movements	Variant number	f_{vj}																															
4							Alternative base value of formwork speed	v_j																													
5																																					
6																																					
7																																					
8	l	H_j	Z_j^H	$Z_j^{H\Sigma}$	-	-	-	$Y_{j,1}$	$Y_{j,2}$	$Y_{j,3}$	$Y_{j,4}$	$Y_{j,5}$	$Y_{j,6}$	$Y_{j,7}$	$Y_{j,8}$	$Y_{j,9}$	$Y_{j,10}$	$Y_{j,11}$	$Y_{j,12}$	$Y_{j,13}$	$Y_{j,14}$	$\Sigma_j Y_{j,i}$	M_{Hj}	σ_{Hj}	P_{emj}		C_j^H										
9	-	m	units	hours	-	-	-	-	-	-	-	-	-	-	-	-	-	-	-	-	-	-	-	hours	hours	-		d.c.									
10	1	1.2	10	10	-	-	-	0	0	0	0	0	0	0	0	0	0	0	0	0	0	0	0	20	0.948683	0.162934		2.7									
11	2	1.3	11	9.090909	-	-	-	0	0	0	0	0	0	0	0	0	0	0	0	0	0	0	22	0.994987	0.278111		2.925										
12	3	1.4	12	8.333333	-	-	-	0	0	0	0	0	0	0	0	0	0	0	0	0	0	0	24	1.03923	0.422377		3.15										
13	4	1.5	13	7.692308	-	-	-	0	0	0	0	0	0	0	0	0	0	0	0	0	0	0	26	1.081665	0.577491		3.375										
14	5	1.6	14	7.142857	-	-	-	0	0	0	0	0	0	0	0	0	0	0	0	0	0	0	28	1.122497	0.72087		3.6										
15	6	1.7	15	6.666667	-	-	-	0	0	0	0	0	0	0	0	0	0	0	0	0	0	0	30	1.161895	0.834983		3.825										
16	7	1.8	16	6.25	-	-	-	0	0	0	0	0	0	0	0	0	0	0	0	0	0	0	32	1.2	0.913297		4.05										
17	8	1.9	17	5.882353	-	-	-	0	0	0	0	0	0	0	0	0	0	0	0	0	0	0	34	1.236932	0.95971		4.275										
18	9	2	18	5.555556	-	-	-	0	0	0	0	0	0	0	0	0	0	0	0	0	0	0	36	1.272792	0.983497		4.5										
19	10	2.1	19	5.263158	-	-	-	0	0	0	0	0	0	0	0	0	0	0	0	0	0	0	38	1.30767	0.994055		4.725										
20	11	2.2	20	5	-	-	-	0	0	0	0	0	0	0	0	0	0	0	0	0	0	0	40	1.341641	0.998119		4.95										
21	12	2.3	21	4.761905	-	-	-	0	0	0	0	0	0	0	0	0	0	0	0	0	0	0	42	1.374773	0.999478		5.175										
22	13	2.4	22	4.545455	-	-	-	0	0	0	0	0	0	0	0	0	0	0	0	0	0	0	44	1.407125	0.999873		5.4										
23	14	2.5	23	4.347826	-	-	-	0	0	0	0	0	0	0	0	0	0	0	0	0	0	0	46	1.438749	0.999973		5.625										
24	Total value							$\Sigma_j Y_{j,i}$	-	0	0	0	0	0	0	0	0	0	0	0	0	0	0	0	0	0	0	0	0	0	0	0	0				
25	Duration of the formwork movement via the layer thickness				at minimum speed		$t_{h,i}^{\min}$	hour	5.333	4.333	3.649	3.152	2.773	2.476	2.237	2.039	1.874	1.733	1.612	1.507	1.415	1.333															
26					at base (average) speed		$t_{h,i}^{\text{aver}}$	hour	4.8	3.9	3.284	2.836	2.496	2.229	2.013	1.835	1.686	1.56	1.451	1.357	1.273	1.2															
27					at maximum speed		$t_{h,i}^{\max}$	hour	4.364	3.545	2.986	2.579	2.269	2.026	1.83	1.668	1.533	1.418	1.319	1.233	1.158	1.091															
28	Duration of the minimum speed formwork movement via the valid formwork occupancy height for the sliding formwork's panel height alternative value (i)				1	$t_{H,i-1,j}$	hour	53.33	43.33	36.49	31.52	27.73	24.76	22.37	20.39	18.74	17.33	16.12	15.07	14.15	13.33																
29					2	$t_{H,i-2,j}$	hour	58.67	47.67	40.14	34.67	30.51	27.24	24.6	22.43	20.61	19.07	17.74	16.58	15.56	14.67																
30					3	$t_{H,i-3,j}$	hour	64	52	43.79	37.82	33.28	29.71	26.84	24.47	22.49	20.8	19.35	18.09	16.98	16																
31					4	$t_{H,i-4,j}$	hour	69.33	56.33	47.44	40.97	36.05	32.19	29.08	26.51	24.36	22.53	20.96	19.59	18.39	17.33																
32					5	$t_{H,i-5,j}$	hour	74.67	60.67	51.09	44.12	38.83	34.67	31.31	28.55	26.23	24.27	22.57	21.1	19.81	18.67																
33					6	$t_{H,i-6,j}$	hour	80	65	54.74	47.27	41.6	37.14	33.55	30.59	28.11	26	24.19	22.61	21.22	20																
34					7	$t_{H,i-7,j}$	hour	85.33	69.33	58.39	50.42	44.37	39.62	35.78	32.63	29.98	27.73	25.8	24.12	22.64	21.33																
35					8	$t_{H,i-8,j}$	hour	90.67	73.67	62.04	53.58	47.15	42.1	38.02	34.67	31.86	29.47	27.41	25.62	24.05	22.67																
36					9	$t_{H,i-9,j}$	hour	96	78	65.68	56.73	49.92	44.57	40.26	36.71	33.73	31.2	29.02	27.13	25.47	24																
37					10	$t_{H,i-10,j}$	hour	101.3	82.33	69.33	59.88	52.69	47.05	42.49	38.75	35.6	32.93	30.64	28.64	26.88	25.33																
38					11	$t_{H,i-11,j}$	hour	106.7	86.67	72.98	63.03	55.47	49.52	44.73	40.78	37.48	34.67	32.25	30.14	28.3	26.67																
39					12	$t_{H,i-12,j}$	hour	112	91	76.63	66.18	58.24	52	46.97	42.82	39.35	36.4	33.86	31.65	29.71	28																
40					13	$t_{H,i-13,j}$	hour	117.3	95.33	80.28	69.33	61.01	54.48	49.2	44.86	41.23	38.13	35.47	33.16	31.13	29.33																
41					14	$t_{H,i-14,j}$	hour	122.7	99.67	83.93	72.48	63.79	56.95	51.44	46.9	43.1	39.87	37.09	34.67	32.54	30.67																
42	Actual probability that the layer maturing duration will not exceed the duration of the minimum speed formwork movement to the valid formwork occupancy height for the sliding formwork's panel height alternative value (i)				1	$P_{h,i-1,j}$	hour	1	1	0.989	0.904	0.708	0.481	0.299	0.178	0.105	0.063	0.038	0.024	0.015	0.01																
43					2	$P_{h,i-2,j}$	hour	1	1	0.999	0.973	0.865	0.673	0.468	0.304	0.19	0.118	0.073	0.046	0.03	0.019																
44					3	$P_{h,i-3,j}$	hour	1	1	0.995	0.951	0.827	0.643	0.458	0.308	0.2	0.129	0.083	0.054	0.036																	
45					4	$P_{h,i-4,j}$	hour	1	1	0.999	0.986	0.925	0.792	0.619	0.449	0.311	0.21	0.14	0.093	0.063																	
46					5	$P_{h,i-5,j}$	hour	1	1	1	0.997	0.973	0.897	0.761	0.597	0.442	0.314	0.218	0.15	0.103																	
47					6	$P_{h,i-6,j}$	hour	1	1	1	0.992	0.956	0.868	0.733	0.579	0.435	0.316	0.225	0.159																		
48					7	$P_{h,i-7,j}$	hour	1	1	1	0.998	0.984	0.936	0.84	0.708	0.563	0.43	0.318	0.232																		
49					8	$P_{h,i-8,j}$	hour	1	1	1	1	0.995	0.973	0.915	0.814	0.685	0.55	0.425	0.32																		
50					9	$P_{h,i-9,j}$	hour	1	1	1	1	0.999	0.99	0.96	0.893	0.789	0.665	0.537	0.421																		
51					10	$P_{h,i-10,j}$	hour	1	1	1	1	1	0.997	0.983	0.944	0.87	0.767	0.647	0.527																		
52					11	$P_{h,i-11,j}$	hour	1</																													

	M	N	O	P	Q	R	S	T	U	V	W	X	Y	Z	AA	AB	AC	AD	AE	AF	AG	AH	AI	AJ	AK	AL	AM	AN	AO	AP	AQ	AR	AS								
59	Actual probability that the layer pouring duration will not exceed the duration of the maximum speed formwork movement to the one						$P_{t,j}$	-	1	1	0.999	0.973	0.815	0.534	0.285	0.135	0.06	0.026	0.012	0.005	0.002	0.001																			
60	layer height																																								
62	Expected estimated duration of wall construction process for the sliding formwork's panel height alternative value (i)						1	$T_{i=1,j}^{\Sigma}$	days	296.2	279.9	268.4	258.4	249.1	243.8	242.1	241.8	241.8	241.8	241.8	241.9	241.9	241.9																		
63							2	$T_{i=2,j}^{\Sigma}$	days	312.4	284.6	265.5	250	234.8	224.3	220.4	219.6	219.6	219.7	219.7	219.7	219.7	219.7	219.7	219.7	219.7	219.7														
64							3	$T_{i=3,j}^{\Sigma}$	days	345.6	303.4	274.4	251.9	230.1	213.4	206.3	204.7	204.6	204.7	204.8	204.8	204.8	204.8	204.8	204.8	204.8	204.8	204.8													
65							4	$T_{i=4,j}^{\Sigma}$	days	389.2	331.5	291.9	261.4	232.6	209.9	199.2	196.5	196.4	196.6	196.7	196.7	196.7	196.7	196.7	196.7	196.7	196.7	196.7													
66							5	$T_{i=5,j}^{\Sigma}$	days	434.3	362.2	312.8	274.8	239.3	211.4	197.5	193.6	193.4	193.7	193.9	194	194	194	194	194	194	194	194													
67							6	$T_{i=6,j}^{\Sigma}$	days	472.8	389.3	332.1	288.1	247	215	198.8	194	193.6	194	194.3	194.4	194.5	194.5	194.5	194.5	194.5	194.5	194.5													
68							7	$T_{i=7,j}^{\Sigma}$	days	500.6	409.3	346.7	298.5	253.7	218.7	201	195.6	195.1	195.5	195.9	196.1	196.2	196.2	196.2	196.2	196.2	196.2	196.2													
69							8	$T_{i=8,j}^{\Sigma}$	days	517.8	421.8	356.1	305.4	258.3	221.6	203	197.2	196.6	197	197.5	197.7	197.8	197.8	197.8	197.8	197.8	197.8	197.8													
70							9	$T_{i=9,j}^{\Sigma}$	days	526.8	428.5	361.1	309.2	260.9	223.3	204.3	198.3	197.6	198.1	198.5	198.8	198.9	199	199	199	199	199	199													
71							10	$T_{i=10,j}^{\Sigma}$	days	530.9	431.5	363.4	311	262.1	224.2	204.9	198.9	198.1	198.6	199.1	199.3	199.5	199.5	199.5	199.5	199.5	199.5	199.5													
72							11	$T_{i=11,j}^{\Sigma}$	days	532.6	432.8	364.4	311.7	262.7	224.5	205.2	199.2	198.4	198.8	199.3	199.6	199.7	199.8	199.8	199.8	199.8	199.8	199.8													
73							12	$T_{i=12,j}^{\Sigma}$	days	533.1	433.2	364.7	312	262.8	224.7	205.3	199.3	198.5	198.9	199.4	199.7	199.8	199.9	199.9	199.9	199.9	199.9	199.9													
74							13	$T_{i=13,j}^{\Sigma}$	days	533.3	433.3	364.8	312	262.9	224.7	205.4	199.3	198.5	198.9	199.4	199.7	199.8	199.9	199.9	199.9	199.9	199.9	199.9													
75							14	$T_{i=14,j}^{\Sigma}$	days	533.3	433.3	364.8	312	262.9	224.7	205.4	199.3	198.5	198.9	199.4	199.7	199.8	199.9	199.9	199.9	199.9	199.9	199.9													
76	Total costs determined by formwork base speed						$C_{i,j}^U$	CU	1.25	1.538	1.827	2.115	2.404	2.692	2.981	3.269	3.558	3.846	4.135	4.423	4.712	5																			
77	Total costs for the sliding formwork's panel height alternative value (i)						1	$C_{i=1,j}^{\Sigma}$	CU	3.95	4.238	4.527	4.815	5.104	5.392	5.681	5.969	6.258	6.546	6.835	7.123	7.412	7.7																		
78							2	$C_{i=2,j}^{\Sigma}$	CU	4.175	4.463	4.752	5.04	5.329	5.617	5.906	6.194	6.483	6.771	7.06	7.348	7.637	7.925																		
79							3	$C_{i=3,j}^{\Sigma}$	CU	4.4	4.688	4.977	5.265	5.554	5.842	6.131	6.419	6.708	6.996	7.285	7.573	7.862	8.15																		
80							4	$C_{i=4,j}^{\Sigma}$	CU	4.625	4.913	5.202	5.49	5.779	6.067	6.356	6.644	6.933	7.221	7.51	7.798	8.087	8.375																		
81							5	$C_{i=5,j}^{\Sigma}$	CU	4.85	5.138	5.427	5.715	6.004	6.292	6.581	6.869	7.158	7.446	7.735	8.023	8.312	8.6																		
82							6	$C_{i=6,j}^{\Sigma}$	CU	5.075	5.363	5.652	5.94	6.229	6.517	6.806	7.094	7.383	7.671	7.96	8.248	8.537	8.825																		
83							7	$C_{i=7,j}^{\Sigma}$	CU	5.3	5.588	5.877	6.165	6.454	6.742	7.031	7.319	7.608	7.896	8.185	8.473	8.762	9.05																		
84							8	$C_{i=8,j}^{\Sigma}$	CU	5.525	5.813	6.102	6.39	6.679	6.967	7.256	7.544	7.833	8.121	8.41	8.698	8.987	9.275																		
85							9	$C_{i=9,j}^{\Sigma}$	CU	5.75	6.038	6.327	6.615	6.904	7.192	7.481	7.769	8.058	8.346	8.635	8.923	9.212	9.5																		
86							10	$C_{i=10,j}^{\Sigma}$	CU	5.975	6.263	6.552	6.84	7.129	7.417	7.706	7.994	8.283	8.571	8.86	9.148	9.437	9.725																		
87							11	$C_{i=11,j}^{\Sigma}$	CU	6.2	6.488	6.777	7.065	7.354	7.642	7.931	8.219	8.508	8.796	9.085	9.373	9.662	9.95																		
88							12	$C_{i=12,j}^{\Sigma}$	CU	6.425	6.713	7.002	7.29	7.579	7.867	8.156	8.444	8.733	9.021	9.31	9.598	9.887	10.18																		
89							13	$C_{i=13,j}^{\Sigma}$	CU	6.65	6.938	7.227	7.515	7.804	8.092	8.381	8.669	8.958	9.246	9.535	9.823	10.11	10.4																		
90							14	$C_{i=14,j}^{\Sigma}$	CU	6.875	7.163	7.452	7.74	8.029	8.317	8.606	8.894	9.183	9.471	9.76	10.05	10.34	10.63																		
91	The indicated value of the total costs with taking into account of acceptable solutions area for the sliding formwork's panel height alternative value (i)						1	$C_{i=1,j}^{\Sigma}$	CU	-	-	-	-	-	-	-	-	-	-	-	-	-	-																		
92							2	$C_{i=2,j}^{\Sigma}$	CU	-	-	-	-	-	-	-	-	-	-	-	-	-	-	-	-	-	-														
93							3	$C_{i=3,j}^{\Sigma}$	CU	-	-	-	-	-	-	-	-	-	-	-	-	-	-	-	-	-	-														
94							4	$C_{i=4,j}^{\Sigma}$	CU	-	-	-	-	-	-	-	-	-	6.356	-	-	-	-	-	-	-	-														
95							5	$C_{i=5,j}^{\Sigma}$	CU	-	-	-	-	-	-	-	-	-	6.581	-	-	-	-	-	-	-	-														
96							6	$C_{i=6,j}^{\Sigma}$	CU	-	-	-	-	-	-	-	-	-	6.806	-	-	-	-	-	-	-	-														
97							7	$C_{i=7,j}^{\Sigma}$	CU	-	-	-	-	-	-	-	-	-	7.031	-	-	-	-	-	-	-	-														
98							8	$C_{i=8,j}^{\Sigma}$	CU	-	-	-	-	-	-	-	-	-	7.256	-	-	-	-	-	-	-	-														
99							9	$C_{i=9,j}^{\Sigma}$	CU	-	-	-	-	-	-	-	-	-	7.481	-	-	-	-	-	-	-	-														
100							10	$C_{i=10,j}^{\Sigma}$	CU	-	-	-	-	-	-	-	-	-	7.706	-	-	-	-	-	-	-	-														
101							11	$C_{i=11,j}^{\Sigma}$	CU	-	-	-	-	-	-	-	-	-	7.931	-	-	-	-	-	-	-	-														
102							12	$C_{i=12,j}^{\Sigma}$	CU	-	-	-	-	-	-	-	-	-	8.156	-	-	-	-	-	-	-	-														
103							13	$C_{i=13,j}^{\Sigma}$	CU	-	-	-	-	-	-	-	-	-	8.381	-	-	-	-	-	-	-	-														
104							14	$C_{i=14,j}^{\Sigma}$	CU	-	-	-	-	-																											

Table 4. The contents of the cells within Microsoft Excel worksheet prepared during the implementation of the developed procedure on a practical example.

Worksheet cell addresses*	Content / formula	Structural element of mathematical model
Table 1		
K5:K9	initial data elements	Table 1, lines 1.2.1–1.2.5
K11:K14	initial data elements	Table 1, lines 1.3.1–1.3.4
K16; K19; K22; K25	initial data elements	Table 1, lines 1.4.1–1.4.4
K29; K31	initial data elements	Table 1, lines 1.5.1, 1.5.2
Table 2		
N10:N23	initial data elements	Table 1, line 3.1
O10(:O23)	= $(N10 - \$K\$12) / \$K\13	Table 2, line 1.1
P10(:P23)	= $\$K\$11 / (O10 * \$K\$13)$	Table 2, line 1.2
U5:AH5	initial data elements	Table 1, line 4.1
U6(:AH6)	=U5/24	-
U10(:AH23)	=IF(AND(NOT(ISERROR(MATCH(MIN(\$U\$91:\$AH\$104),U\$91:U\$104,0))),NOT(ISERROR(MATCH(MIN(\$U\$91:\$AH\$104),U\$91:\$AH91,0)))),1,0)	Table 2, line 3.6
AI10(:AI23)	=SUM(U10:AH10)	-
AK10(:AK23)	=O10*\$K\$6	Table 2, line 1.3
AM10(:AM23)	= $\$K\$7 * \text{SQRT}(O10)$	Table 2, line 1.4
AP10(:AP23)	=NORM.S.DIST((AK10-\$K\$8)/SQRT(\$K\$9^2+AM10^2),1)	Table 2, line 1.5
AS10(:AS23)	= $\$K\$29 * N10$	Table 2, line 1.6
U24(:AI24)	=SUM(U10:U23)	-
U25(:AH25)	= $\$K\$13 / (U\$6 * (1 - \$K\$14))$	Table 2, line 2.1
U26(:AH26)	= $\$K\$13 / U6$	Table 2, line 2.2
U27(:AH27)	= $\$K\$13 / (U\$6 * (1 + \$K\$14))$	Table 2, line 2.3
U28(:AH41)	= $(\$N10 - \$K\$12) / (U\$6 * (1 - \$K\$14))$	Table 2, line 3.1
U42(:AH55)	=NORM.S.DIST((U28-\$K\$8)/\$K\$9,1)	Table 2, line 3.2
U56(:AH56)	=1-NORM.S.DIST((U25-\$K\$6)/\$K\$7,1)	Table 2, line 2.4
U59(:AH59)	=NORM.S.DIST((U27-\$K\$6)/\$K\$7,1)	Table 2, line 2.5
U62(:AH75)	=(\$AP10*U42*(U\$56*U\$59*\$O10*U\$26+(1-U\$56)*U\$59*\$O10*U\$25)+\$AP10*(U42*(1-U\$59)+(1-U42))*\$O10*\$K\$6+(1-\$AP10)*\$K\$8)*\$P10	Table 2, line 3.3
U76(:AH76)	=U\$5*\$K\$31	Table 2, line 2.6
U77(:AH90)	=\$AS10+U\$76	Table 2, line 3.4
U91(:AH104)	=IF(AND(U62<=\$K\$5,\$AP10>=\$K\$16,U42>=\$K\$19,U\$56>=\$K\$22,U\$59>=\$K\$25),U77,"-")	Table 2, line 3.5
Table 3		
K39	=SUMPRODUCT(N10:N23,AI10:AI23)	Table 2, line 4.1.1
K40	=SUMPRODUCT(U6:AH6,U24:AH24)	Table 2, line 4.1.2
K42	=SUMPRODUCT(AP10:AP23,AI10:AI23)	Table 2, line 4.2.1
K45	=SUMPRODUCT(U10:AH23,U42:AH55)	Table 2, line 4.2.2
K48	=SUMPRODUCT(U24:AH24,U56:AH56)	Table 2, line 4.2.3
K51	=SUMPRODUCT(U24:AH24,U59:AH59)	Table 2, line 4.2.4
K55	=SUMPRODUCT(U62:AH75,U10:AH23)	Table 2, line 4.3.1
K57	=K29*SUMPRODUCT(N10:N23,AI10:AI23)	Table 2, line 4.4.1
K58	=K31*SUMPRODUCT(U24:AH24,U5:AH5)	Table 2, line 4.4.2
K59	=K57+K58	Table 2, line 4.4.3

Note:

* the abstract designation A1(:B10) means that in the cell A1 you need to enter the formula indicated in the corresponding column of the table, after which "stretch" (copy) the result to cell B10.

For the objective estimation of the practical significance of the created tool the analysis of dependences of different indicators connected to the technological process under consideration on mentioned above parameters has been carried out. The corresponding results are presented in Fig. 5 and 6. On the basis of mentioned results, the following particular conclusions have been made:

- the duration of the movement of the formwork is directly proportional to the height of the formwork and decreases hyperbolically with formwork's movement base speed increase (Fig. 5,a), while the range of the duration of the movement of the formwork depending on the formwork's movement base speed rises as the formwork's panel height increases;
- for large values of the height of the shield, the nominal speed of movement practically does not affect the duration of the erection of the wall structure (Fig. 5,b). The main reason is that with an increase in the preferred speed of formwork movement, the probability that the maturing time of the layer does not exceed the preferred speed of movement of the formwork asymptotically approaches zero, thereby determining the maturing speed of the concrete layer as a key parameter that affects the duration of the erection of the wall structure;
- the graph shows that the total costs increase monotonously and in direct proportion to the determined parameters – the formwork's panel height and movement base speed – in accordance with the originally specified relationships (Fig. 5,c); it is also important to note that in general case an arbitrary dependence can be specified, including a nonlinear one;
- the actual value of probability that the layer maturing duration will not exceed the total layers pouring increases nonlinearly and monotonically with increasing formwork height and has an inflection point corresponding to the probability value $P_{cmi} = 0.5$ and a speed value of approximately $H_i \approx 1.45$ m (Fig. 6,a);
- the actual value of probability that the layer pouring duration will exceed the duration of the minimum speed formwork movement to the one-layer height increases nonlinearly and monotonically with an increase of the formwork's movement base speed and has an inflection point corresponding to the probability value $P_{t-j} = 0.5$ and the velocity value of approximately $v_j \approx 1.33$ m/day (Fig. 6,b);
- the actual value of probability that the layer pouring duration will not exceed the duration of the maximum speed formwork movement to the one-layer height decreases non-linearly and monotonically with increasing of the formwork's movement base speed and has an inflection point corresponding to the value of probability $P_{t+j} = 0.5$ and the value of speed of approximately $v_j \approx 1.08$ m/day (Fig. 6,c);
- the influence (determined by the difference in duration values for the current j and previous $j-1$ alternative values of the duration) of the deviation from the base (average) value of the formwork's movement speed is significant only at relatively low base value of the speed ($v_j \leq 1.3$ m/day) and ranges from 3.7% to 18.75% of the largest duration value; in case of relatively large base value of the formwork's movement speed ($v_j > 1.3$ m/day), the mentioned above effect can be considered insignificant.

4. Conclusions

On the basis of conducted research described above the following results have been received:

1. Review of the literature sources connected to the modeling of construction processes. On the basis of the results for corresponding procedure it has been concluded that existing scientific developments don't take into account the factors of stochastic nature and therefore can not ensure the high adequacy of the calculated results.
2. Stochastic model of the construction process implemented with application of sliding formwork has been created. The model ensures determination of the most preferred values for technological parameters describing sliding formwork's panel height and base (average) movement speed on the basis of wall height, baseline duration of the wall construction process and characteristics of the stochastic values of concrete layer's pouring and maturing duration.
3. Created stochastic model has been implemented on a practical example for the wall construction process assumed by the construction project "Arctic LNG 2". Results of the calculation satisfied the conditions of construction processes' implementation and became the basis for the conclusion about high practical significance of the developed tool.

It is necessary to note that due to the absence of the scientific developments connected directly the application of stochastic modeling tools to the construction process implemented with using of sliding formwork it is impossible to compare received results of the research with the data obtained by other researchers. Therefore the practical significance of the developed model described in the work has been estimated on the

basis of the degree of correspondence of calculation results to the real conditions for implementation of the construction process under consideration.

It is also should be emphasized that the created model can be used not only for the wall construction with application of sliding formwork, but for any technological process connected to the erection of buildings and structures (including installation of ceiling and wall structures, separation partitions, etc.) in the area of civil, industrial and road construction that has following features:

- unknown parameters are independent from each other (the number of the parameters can be not only two, but three and more) and have influence on economic indicator (for example, operational costs) to be minimized or maximized;

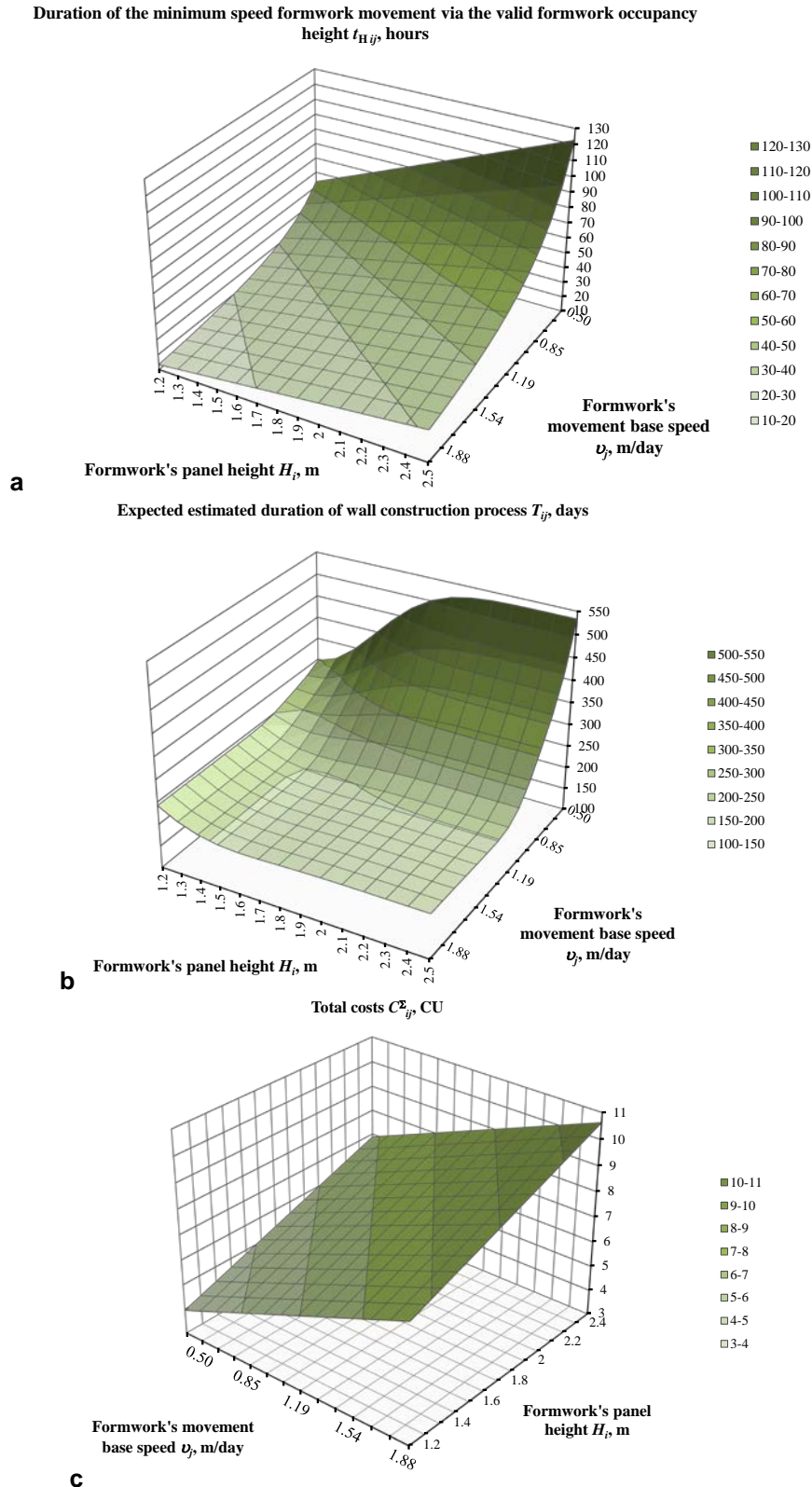


Figure 5. Dependences of different indicators connected to the technological process under consideration on technological parameters (beginning).

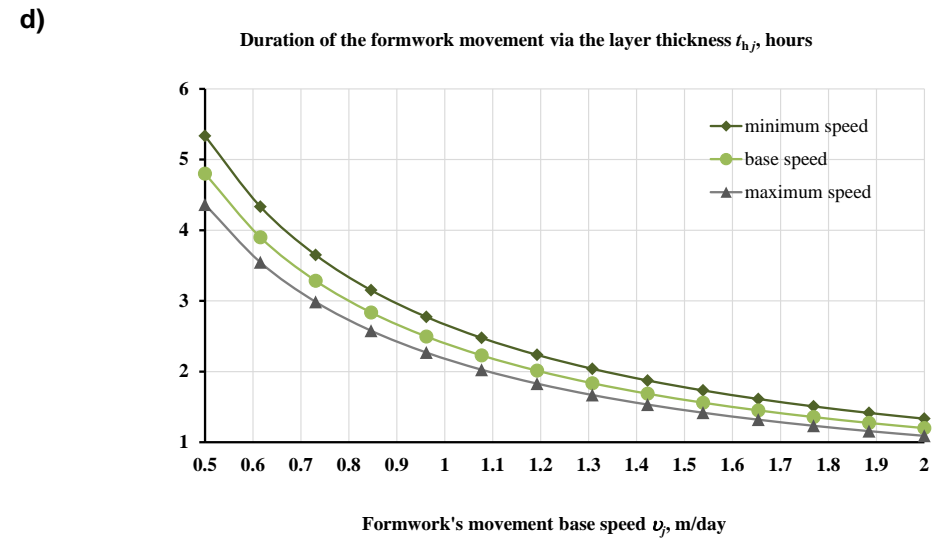
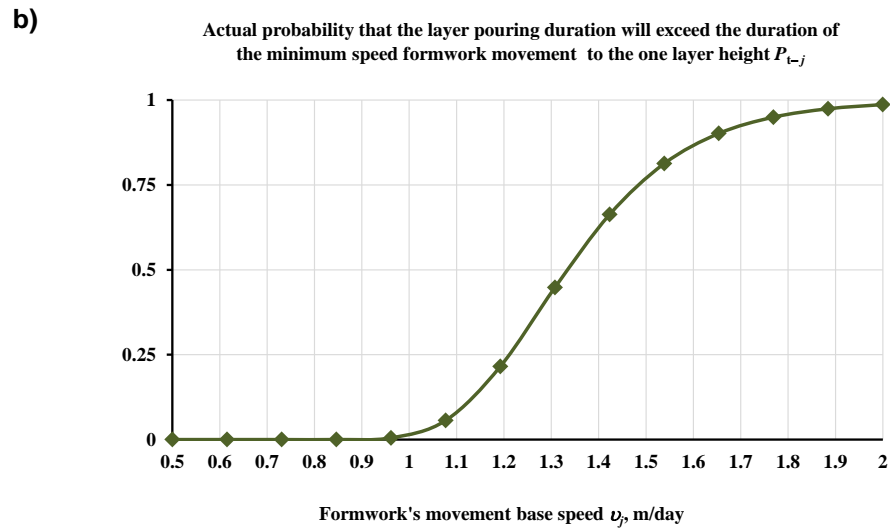
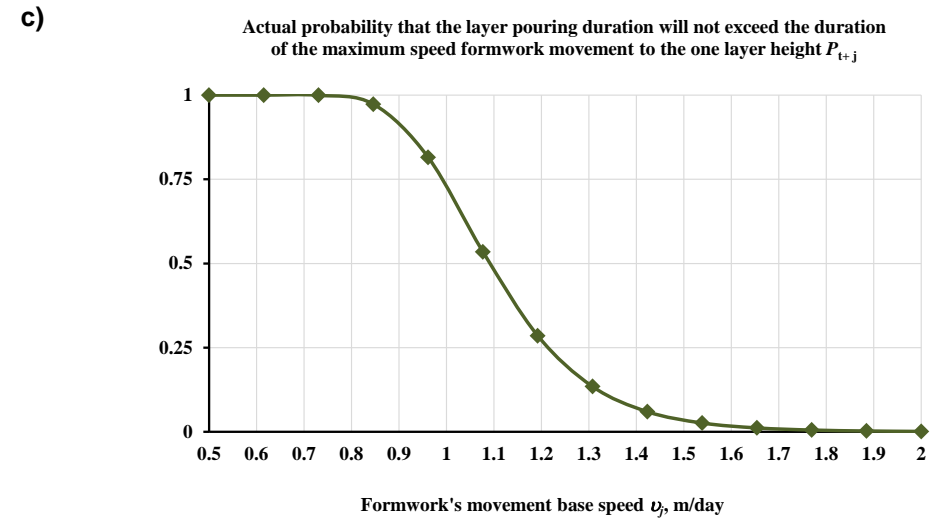
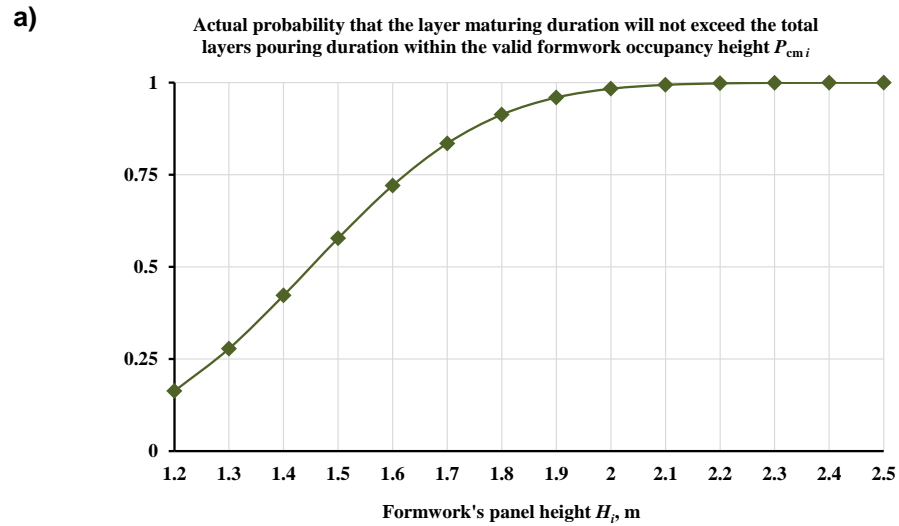


Figure 6. Dependences of different indicators connected to the technological process under consideration on technological parameters (ending).

– structure of technological process can be described as the sequence of elemental processes (implemented one after another) each of which is described by a stochastic time parameter corresponding to normal distribution.

– baseline duration of the whole technological process is known.

The analysis of possibilities for application of the created model for the different categories of technological processes in the area of construction will be carried out at the further stages of the research activity.

References

1. Daukšys, M. Productivity analysis of concrete slab construction by using different types of formwork. *Journal of Sustainable Architecture and Civil Engineering*. 2016. 2. Pp. 38–46. DOI: 10.5755/j01.sace.15.2.15789.
2. Golafshani, E. M., Talatahari, S. Predicting the climbing rate of slip formwork systems using linear biogeography-based programming. *Applied Soft Computing Journal*. 2018. 70. Pp. 263–278. DOI: 10.1016/j.asoc.2018.05.036.
3. Bulgakov A., Kruglova T., Sayfeddine D. Simulation Mathematical Model of Mechatronic Sliding Formwork for Monolithic Tower with Variable Cross Section. *Advanced Construction and Building Technology for Society*. 2016. Pp. 8-14.
4. Heiza, K., Abo El enen, N., Mahdi, I. Value methodology of vertical slip form construction system in high rise buildings. *The International Conference on Civil and Architecture Engineering*. 2016. Pp. 19–21. DOI: 10.21608/iccae.2016.43437.
5. Zayed, T., Sharifi, M.R., Baciu, S., Amer, M. Slip-form application to concrete structures. *Journal of Construction Engineering and Management*, 2008. 134(3). Pp. 134–142. DOI: 10.1061/(ASCE)0733-9364(2008)134:3(157).
6. Tregger, N., Voigt, T., Shah, S.P. Improving the slipform process via material manipulation. *Advances in Construction Materials*, 2007. Pp. 539–546. DOI: 10.1007/978-3-540-72448-3_55.
7. Reichverger, Z., Jaegermann, C. Optimal regime in slip form concreting. *Matériaux et Constructions*. 1980. 13. Pp. 109–113. DOI: 10.1007/BF02473807.
8. Choktaweekarn, P., Tangtomsirikul, S. Effect of aggregate type, casting, thickness and curing condition on restrained strain of mass concrete. *Songklanakarin Journal of Science and Technology*. 2010. 32(4). Pp. 391–402.
9. Gamayunova, O., Spitsov, D. Technical features of the construction of highrise buildings E3S Web of Conferences. 2020. 164. 08008.
10. Mansuri, D., Chakraborty, D., Elzarka, H., Deshpande, A., Gronseth, T. Building Information Modeling enabled Cascading Formwork Management Tool. *Automation in Construction*. 2017. 83. Pp. 259–272. DOI: 10.1016/j.autcon.2017.08.016.
11. Lee, J., Park, Y. J., Choi, C. H., Han, C. H. BIM-assisted labor productivity measurement method for structural formwork. *Automation in Construction*. 2017. 84. Pp. 121–132. DOI: 10.1016/j.autcon.2017.08.009.
12. Lu, N., Korman, T. Implementation of Building Information Modeling (BIM) in Modular Construction: Benefits and challenges. *Construction Research Congress 2010: Innovation for Reshaping Construction Practice – Proceedings of the 2010 Construction Research Congress*. 2010. Pp. 1136–1145. DOI: 10.1061/41109(373)114.
13. Meadati, P., Irizarry, J., Aknoukh, A. BIM and Concrete Formwork Repository. *47th ASC Annual International Conference Proceedings*. 2011.
14. Romanovskiy, R., Sanabria Mejia, L., Rezazadeh Azar, E. BIM-based decision support system for concrete formwork design. *Proceedings of the 36th International Symposium on Automation and Robotics in Construction, ISARC*. 2019. Pp. 1129–1135. DOI: 10.22260/isarc2019/0150.
15. Shin, Y., Kim, T., Cho, H., Kang, K.I. A formwork method selection model based on boosted decision trees in tall building construction. *Automation in Construction*. 2012. 23. Pp. 47–54. DOI: 10.1016/j.autcon.2011.12.007.
16. Kamarthi, S.V., Sanvido, V.E., & Kumara, S.R.T. Neuroform—neural network system for vertical formwork selection. *Journal of Computing in Civil Engineering*. 1992. 6(2). Pp. 178–199. DOI: 10.1061/(ASCE)0887-3801(1992)6:2(178).
17. Roe, B. P., Yang, H. J., Zhu, J., Liu, Y., Stancu, I., McGregor, G. Boosted decision trees as an alternative to artificial neural networks for particle identification. *Nuclear Instruments and Methods in Physics Research, Section A: Accelerators, Spectrometers, Detectors and Associated Equipment*. 2005. 543. Pp. 577–584. DOI: 10.1016/j.nima.2004.12.018.
18. Elbeltagi, E., Hosny, O.A., Elhakeem, A., Abd-Elrazek, M.E., Abdullah, A. Selection of slab formwork system using fuzzy logic. *Construction Management and Economics*. 2011. 29(7). Pp. 659–670. DOI: 10.1080/01446193.2011.590144.
19. Struková, Z., Kozlovská, M., Kováčová, B. Determination of optimal supporting system of deep foundation pit based on multi-criteria decision analysis. *12th International Multidisciplinary Scientific GeoConference and EXPO – Modern Management of Mine Producing, Geology and Environmental Protection, SGEM*. 2012. 2. Pp. 47–54.
20. Baskova, R., Krajnak, M. An analytical approach to optimization of the costs for construction formwork. *International Multidisciplinary Scientific GeoConference Surveying Geology and Mining Ecology Management, SGEM*. 2013. 2. Pp. 35–40. DOI: 10.5593/SGEM2013/BE5.V2/S21.005.
21. Bolotin, S., Dadar, A., Ptuhina, I. Construction work tasks duration: Pessimistic scenarios based on PERT method. *Advanced Materials Research*. 2014. 945–949. Pp. 3026–3031. DOI: 10.4028/www.scientific.net/AMR.945-949.3026.
22. Mishakova, A., Vakhrushkina, A., Murgul, V., Sazonova, T. Project Control Based on a Mutual Application of Pert and Earned Value Management Methods. *Procedia Engineering*. 2016. 165. Pp. 1812–1817. DOI: 10.1016/j.proeng.2016.11.927.
23. Gurmu, A.T., Ongkowitzo, C.S. Stochastic-Based Model for Setting Formwork-Productivity Baseline. *Journal of Construction Engineering and Management*. 2020. 146(9). 04020099.
24. Lim, H., Kim, T., Cho, H., Kang, K.I. Simulation-based planning model for table formwork operation in tall building construction. *Journal of Asian Architecture and Building Engineering*. 2017. 16(1). Pp. 115–122. DOI: 10.3130/jaabe.16.115.
25. Tichko, S., Van De Maele, J., Vanmassenhove, N., De Schutter, G., Vierendeels, J., Verhoeven, R., Troch, P. Numerical simulation of formwork pressure while pumping self-compacting concrete bottom-up. *Engineering Structures*. 2014. 70. Pp. 218–333. DOI: 10.1016/j.engstruct.2014.04.008.
26. Le, H.D., De Schutter, G., Kadri, E.H., Aggoun, S., Vierendeels, J., Troch, P. Velocity profile of self compacting concrete and traditional concrete flowing in a half open pipe. *Concrete Repair, Rehabilitation and Retrofitting III – Proceedings of the 3rd International Conference on Concrete Repair, Rehabilitation and Retrofitting (ICRRR)*. 2012. P. 1382–7.
27. Puente, I., Santilli, A., Lopez, A. Lateral pressure over formwork on large dimension concrete blocks. *Engineering Structures*. 2010. 32(1). Pp. 195–206. DOI: 10.1016/j.engstruct.2009.09.006.

Contacts:

Margarita Matskina, rmatskina@gmail.com

Marina Petrochenko, mpetroch@mail.ru

Anton Radaev, TW-inc@yandex.ru

© Matskina, M.M., Petrochenko, M.V., Radaev, A.E., 2021



DOI: 10.34910/MCE.101.12

Silica concrete compressive behavior under alternating magnetic field

A. Safari Tarbozagh, O. Rezaifar*, M. Gholhaki

Department of Civil Engineering, Semnan University, Semnan, Iran

* E-mail: orezayfar@semnan.ac.ir

Keywords: Alternating Magnetic Field (AMF), concrete, silica sand, compressive strength, magnetic circuit

Abstract. Due to the importance of inventing new techniques capable of enhancing concrete structural properties while reducing environmental issues associated with CO₂ emissions in concrete industry, which preoccupies environmental scientists, a novel investigation was performed on feasibility of benefitting from Alternating Magnetic Field (AMF) and silica particles to attain this goal. Hence, some experiments were conducted on cylindrical concrete specimens comprising different silica sand contents of up to 10 %, wherein the influence of exposing fresh and hardened concrete to AMF of frequency 50 Hz and density 0.5 Tesla (T) on compressive strength of 7 and 28-day specimens was evaluated. For this, a specialized test setup was assembled such that the specimen could be subjected to compressive force and AMF, simultaneously. It was found that AMF can improve concrete compressive strength, where this technique is more efficient as to exposing hardened concrete. What was significant about the results was the fact that adding silica sand not only improved concrete mechanical strength but also considerably enhanced the effectiveness of AMF in increasing concrete compressive strength, when applied to hardened concrete. For instance, replacing 10 % of cement content with silica sand increased compressive strength of 28-day specimens by 8.4, but adding 10 % silica sand along with exposing specimens to AMF yielded an increase of nearly 21 % in real-time. Thus, developing this method can result in a new generation of smart constructions. Moreover, by adding 10 % silica sand, the emission of carbon dioxide, a greenhouse gas, reduces by 10 percent while significantly enhancing compressive strength.

1. Introduction

Nowadays, the need for improving concrete properties, such as workability and compressive, tensile and flexural strength has resulted in the invention of numerous ways, which are generally divided into two categories; the first is associated with using additives, such as nano- or micro-particles in concrete. The second is equipping concrete by non-cementitious phenomena, saying magnetic fields and electricity.

As to methods that use additives in concrete, the primary aim is to enhance concrete strength by replacing a proportion of cement constituent with other particles. This not only improves concrete structural properties but also reduces adverse environmental effects of using high cement content in concrete, which preoccupies environmental engineers. One of such cementitious admixtures, which has widely been studied according to technical literature, are silica particles. Recently, the use of nano- and/or micro-silica has been widely expanded because of their capability in enhancing mechanical properties and microstructure of concrete due to pozzolanic reaction between micro-silica and Ca(OH)₂ [1, 2]. Some of these improvements are increase in compressive, tensile and flexural strength, reduction of concrete setting time and permeability, immunity against chemical and corrosive reactions [3–6].

Wang et al. investigated the effect of nano-silica on hydration and microstructure of alkali-activated slag. They concluded that adding nano-silica improves concrete compressive strength, microscopic morphology and hydration [7]. Assaedi et al. studied the influence of methods for mixing nano-silica on microstructural evolution and performance of Geopolymer paste prepared with fly ash. They found that concrete strength improvement and optimization in microstructure depends on hydrated calcium silicate and hydrated calcium aluminosilicate gel [8]. Regarding silica sand, Mithaq investigated compressive strength improvement using

Safari Tarbozagh, A., Rezaifar, O, Gholhaki, M. Silica concrete compressive behavior under alternating magnetic field. Magazine of Civil Engineering. 2021. 101(1). Article No. 10112. DOI: 10.18720/MCE.101.12



This work is licensed under a CC BY-NC 4.0

silica sand [9]. Sayed et al. found that substituting silica sand for a proportion of cement enhances compressive and flexural strength by 55.7 % and 46.9 %, respectively, while reducing workability [10].

With regard to using phenomena other than additives in concrete, one of the well-known methods is enhancing concrete elements performance through magnetic fields and/or electricity, where studies in this field are divided into two major categories; a) enhancing concrete mechanical properties through applying magnetic field to concrete constituents in fresh state and b) benefiting from magnetism and electricity in real time controlling of smart structures behavior.

Recently, improving concrete properties through magnetizing its constituents has drawn the attention of many structural engineers. One method is preparing magnetic concrete via magnetic treatment of water, where water is exposed to a high power magnetic field. This method was first suggested by Lorenz in 1902 for the first time. When water is exposed to magnetic field, the size of its molecules increases [11]. Hence, its properties, such as surface tension, temperature, PH, permeability, solubility and specific weight are influenced [12, 13].

Most research studies on concrete reported that using magnetic water increases workability and compressive strength by 10 to 25 % [14–18]. Bharath et al. [19] concluded that mixing concrete with magnetized water improves workability of concrete comprising copper slag by 5 %. According to a work done by Gholhaki et al. [20], magnetic treatment of water improves flowability and viscosity of self-compacting concrete. According to the work of Ghorbani et al. [21] magnetic water considerably improves concrete microstructure and makes concrete more consistent compared with ordinary concrete. Another study done by Su et al. [16] revealed that magnetized water increases compressive strength of mortar comprising blast-furnace slag. But, the extent of such effect depends on magnetic field strength. This method was also found to have a positive influence on concrete with Egyptian nano-alumina [14].

Not only magnetizing water but also exposing other concrete constituents has recently been investigated. Nair et al. exposed fresh concrete containing carbonyl iron powder to magnetic field. They said this technique affects concrete paste shear resistance but does not influence compressive strength [22]. In another study, different cement paste specimens of ages up to 7 days were subjected to static magnetic fields of up to 25.37 Gauss (1 Gauss= 10^{-4} T). It was concluded that magnetic field enhances Calcium Silicate Hydrate (CSH) gel constituent and improves its morphology [23].

Moreover, magnetic field and electricity have found their way into real time controlling of concrete elements behavior. In this regard, electromagnetism has been commonly used for performance monitoring in concrete elements [24], [25], where the apparatus mainly consists of sensors and actuators. Such systems are mainly based on smart materials, such as shape memory alloys [26–28], piezoelectric [29–31], fiber optics [32–35], and magneto-rheological materials[36]. Apart from applying electromagnetism in sensors and actuators systems, exposing concrete itself to magnetic field has recently been found to influence concrete performance in real time, which can be considered as a base for a new smart construction system [37–41]. Abavisani et al. [37] studied the influence of exposing fresh and hardened concrete to Alternating Magnetic Field (AMF) on its properties. They observed that AMF has a positive effect on concrete compressive strength as long as AMF is applied to hardened concrete. They also subjected some small-scale RC beams to AMF and/or alternating current (AC) electricity[38]. They found that this technique affects flexural properties of the beams, such as load-bearing capacity, flexural stiffness, ductility and deflection. For instance, exposing fresh concrete to AMF, when placing, enhanced ductility of RC beams by 15.4 % and subjecting hardened RC beams to AMF enhanced their ductility index by 135.8 %. In another study, Rezaifar et al. [39] Prepared some small-scale RC columns and subjected them to AMF and/or AC. It was found that load bearing capacity of the RC columns increased during AMF exposure but they became more brittle, on the other hand AC made them more ductile.

However, studies on the influence of AMF on concrete are still scarce and almost limited to plain concrete without admixtures. Hence, it is necessary to investigate further on this issue and evaluate the effect of AMF on other concrete additives. This study aims to take this area further and evaluate the effectiveness of AMF in improving compressive strength of concrete containing other additives, which has not been studied before.

In this study, the influence of AMF on cylindrical concrete specimens containing silica sand as admixture in the ages of 7 and 28 days is evaluated. The study is divided into two; the effect of applying AMF to fresh concrete and the influence of exposing hardened concrete to AMF on compressive strength. Section 2 is devoted to explaining research method and practical issues about using AMF. Then in section 3, the experimental data will be presented and the effect of both silica and AMF on concrete compressive strength will be discussed. This is followed by discussing the advantages of this technique in terms of environmental benefits as well as designing issues. Since RC beams have an important role in structural ductility, which withstand transverse loading through interactions between compressive and tensile stresses in concrete and reinforcing bars, part of design advantages will be discussed as to RC beams. Finally, conclusions are presented in section 4.

2. Methods

2.1. Test program

In this investigation, the effect of AMF on compressive strength of concrete cylinders containing different proportions of silica sand was the target. Hence, 54 concrete samples, in total, were tested. The variables are as follows:

- The occasion when concrete is exposed to AMF. In this regard, specimens are categorized as:
 - Non-Magnetized (NM): where AMF is not applied to concrete
 - Pre-Magnetized (PrM): where AMF is applied to ready mixed concrete casted into mold
 - Post-Magnetized (PoM): where AMF is applied to hardened concrete as it is subjected to compressive force during the test.
- Silica sand content; the specimens are categorized into three groups containing silica sand contents of 0 %, 5 % and 10 % of the cement weight.
- Concrete age; concrete samples are divided into 7-day and 28-day specimens.

Specimens are labeled according to these variables. Each label is composed of three parts separated by full stops; the first one is related to variable I, which is NM, PrM or PoM. The second is a number connoting the percentage of silica concrete, which takes one of the amounts of 0,5,10. The last section identifies the age of concrete, which is either 7 or 28. All labels are presented in Table 1.

Table 1. Specimen labels.

AMF	Silica sand content (%)	Label	
		7-day specimen	28 days specimen
NM	0	NM.0.7	NM.0.28
	5	NM.5.7	NM.5.28
	10	NM.10.7	NM.10.28
PrM	0	PrM.0.7	PrM.0.28
	5	PrM.5.7	PrM.5.28
	10	PrM.10.7	PrM.10.28
PoM	0	PoM.0.7	PoM.0.28
	5	PoM.5.7	PoM.5.28
	10	PoM.10.7	PoM.10.28

2.2. Material Properties

In all specimens Portland cement type ii with a trade name of Shahroud Cement was used. The cement properties are listed in Tables 2 and 3. The water used was tap water. For aggregate with a diameter of less than 4.75 mm, sand was graded as per ASTM-C33 [42]. The grading diagram for sand constituent is shown in Fig. 1. Water absorption test was performed on sand and gravel and its results are listed in Table 4. In this study, silica sand of diameter less than 75 μm was utilized as a partial substituent for cement. The technical properties and proportions of the silica sand are presented in Table 5. To improve workability, a carboxylate superplasticizer under a trade name of PX-MIX was employed, where its properties are listed in Table 6.

For magnetization, an AMF equipment run by main electricity, generating a magnetic field of strength 0.5 Tesla (T) with a frequency of 50 Hz was employed. Due to the fact that steel molds have a high level of magnetic permeability, there would have been a huge magnetic leakage if fresh concrete had been magnetized in such molds. As a consequence, the amount of magnetic flux passing through ready mixed concrete would have been drastically reduced. Therefore plastic cylindrical molds of 20x10 cm with a thickness of 3 mm were used.

Table 2. Material Chemical proportions of the Cement (as a proportion of cement weight %).

SiO ₂	Al ₂ O ₃	Fe ₂ O ₃	CaO	MgO	SO ₃	Na ₂ O	K ₂ O	TiO ₂	P ₂ O ₅	Mn ₂ O ₃	Loss on ignition
21.11	4.42	3.96	63.36	1.51	2.61	0.38	0.51	0.28	0.19	0.07	1.6

Table 3. Mineral proportions of the Cement (as a proportion of cement weight %).

C ₃ S	C ₂ S	C ₃ A	C ₄ AF	Loss on ignition
54.7	19.3	5	12.5	8.5

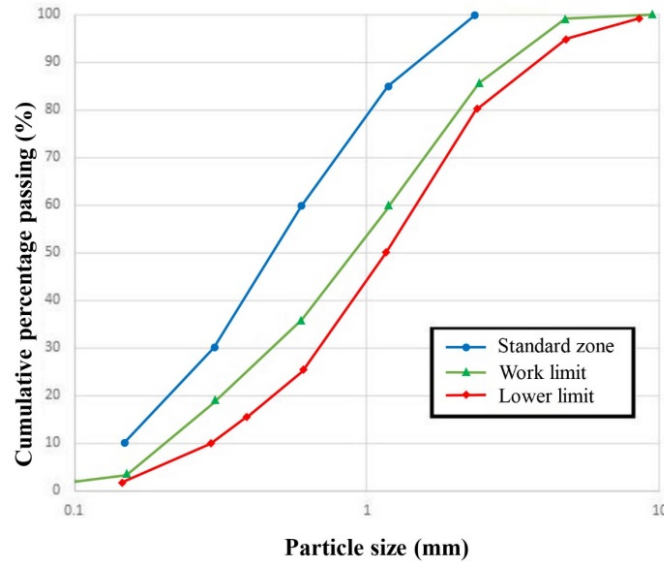


Figure 1. The aggregate grading diagram.

Table 4. The results of water absorption of aggregate.

	Weight of saturated aggregate with a dry surface (g)	Weight of aggregate after 24 h heated in oven (g)	Water absorption
gravel	504.1	498.5	1.1%
Sand	534.6	485.8	10%

Table 5. The silica sand properties.

Constituent	SiO ₂	Al ₂ O ₃	Fe ₂ O ₃	CaO	MgO	Na ₂ O	K ₂ O
Proportions (%)	98.27	0.48	0.12	0.18	0.08	0.63	0.24

Table 6. The superplasticizer properties.

Physical phase	Liquid
Color	Light yellow
Standard	ISIRI2930 & ASTM-C494
Specific weight	1.4 gr/cm ³

2.3. Magnetic circuit

For magnetizing concrete in this study a simple magnetic circuit was adopted, where the schematic formation of this circuit is illustrated in Fig. 2. This gapped circuit consists of a coil, a core of iron and an air gap where concrete specimens are placed and magnetized.

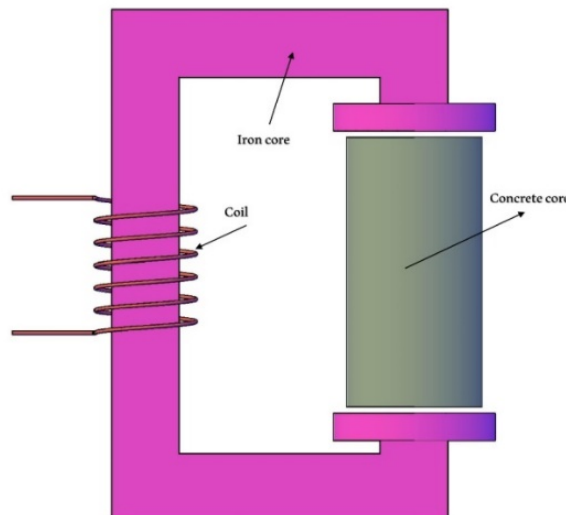


Figure 2. The gapped magnetic circuit designed for magnetizing the specimens.

When an element is subjected to a magnetic field, magnetic flux passes through it. The density of such flux is calculated as:

$$B = \frac{\phi}{A}, \quad (1)$$

where B is magnetic flux density measured (in T);

ϕ is magnetic flux measured in Weber (Wb);

A is cross-sectional area of the element (measured in m^2).

Magneto Motive Force (MMF) which represents the amount of magnetic forces along a circuit is follows:

$$F = NI, \quad (2)$$

where F , N , and I denote, MMF (measured in ampere-turn (At)), the number of the turns of the coil, and the current intensity running through the coil (in amperes (A)), respectively. Since in this study fixed amounts of I and N are adopted, MMF remains constant.

The reluctance of an element to allow magnetic flux through itself, which is called magnetic reluctance of the element, is calculated as:

$$R = \frac{l}{\mu A}, \quad (3)$$

where l represents the length of that element measured in (m);

A connotes the cross-sectional area of the element measured in (m^2);

μ is magnetic permeability of the material which the element is made of, measured in henries per meter ($H.m^{-1}$).

The magnetic flux running through the circuit (ϕ) is as:

$$\phi = \frac{F}{R_I + R_C}, \quad (4)$$

where R_I and R_C denote magnetic reluctances of iron and concrete elements, respectively.

Eqs. (3) and (4) are based on static magnetic field which is created by Direct Current (DC) electricity. As to AMF, these equations are modified as Eqs. (5) and (6).

$$Z_\mu = \frac{l}{\dot{\mu}S}, \quad (5)$$

$$\dot{\phi} = \frac{\dot{N}}{Z\mu_I + Z\mu_C}, \quad (6)$$

where Z_μ represents complex magnetic reluctance;

l denotes the length of the element measured in (m);

$\dot{\mu}$ is the complex magnetic permeability, which relates to the material quality;

S represents the cross-sectional area of the element;

$\dot{\phi}$ denotes the amplitude of magnetic flux;

\dot{N} is the amplitude of magneto motive force (MMF);

$Z\mu_I$ and $Z\mu_C$ stand for Z_μ of iron and concrete elements, respectively. The amounts of μ and $\dot{\mu}$ for iron are by far larger than those for concrete core. Therefore, R_C and $Z\mu_C$ are markedly larger than R_I and $Z\mu_I$, respectively. Considering Eqs. (4) and (6), since F and \dot{N} are fixed amounts, there is a sharp

decrease in magnetic flux only because of the concrete gap (R_C and/or $Z\mu_C$ are large numbers). Since the aim of the experiments in this study is to run as much magnetic flux across concrete specimens as possible, the smallest length for concrete cylinders (20 cm) was adopted as a way to keep magnetic reluctance of concrete as low as possible (according to Eqs. (3) and/or (5)). The simplified structure of the AMF generating equipment employed for magnetizing the specimens is shown in Fig. 3.

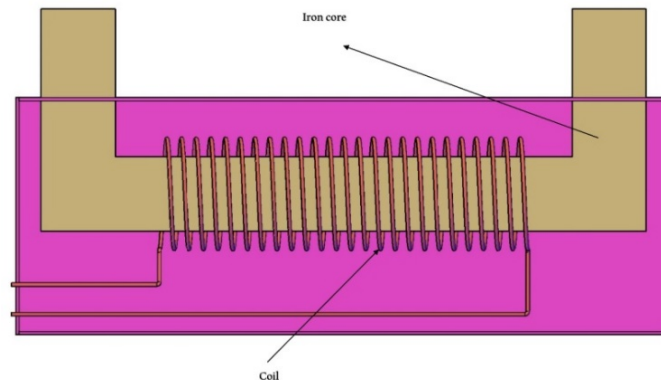


Figure 3. The AMF generator used for magnetization of the concrete samples.

2.4. Specimen preparation

After searching some articles working on silica concrete in literature and experimenting with different concrete proportions through trial and error, the best mix proportions as presented Table 7 were used. First, gravel and sand were combined with each other in a mixer. Then, a portion of the mix water, enough to render aggregates in a saturated-surface-dry (SSD) condition, was poured into the mixer and the mixture was stirred for about 1 min. Subsequently, cement (along with silica sand in case of 5 % and 10 % silica sand specimens) was added to the saturated aggregates. Meanwhile aggregates and cementitious constituents were mixed together, the rest of water content mixed with superplasticizer was poured, gradually, into the mixer. Totally, the mix procedure took around 3 to 4 min. Then, the concrete slump was performed on the freshly mixed concrete according to ASTM-C143 [43] to ensure a desirable slump (Fig. 4). Due to high specific surface area of silica, it has a water absorption capability, reducing slump of concrete. In this study, slump for all mix proportions was targeted to remain within the range of 5 to 10 cm.

After that, ready mixed concrete was placed into molds and compacted by a shaker table. For each type of specimens three samples were fabricated. Finally, PrM specimens were subjected to the AMF as shown in Fig. 5. As is seen in the figure, to ensure the coverage of magnetic flux across the entire of specimens, two rectangular prisms were put along two opposite sides of the mold. Fig. 6 shows the direction of AMF applied to the PrM specimens.

Concrete cylinders were demolded after 24 h. In order to prevent $\text{Ca}(\text{OH})_2$ from coming out of concrete the specimens were cured into saturated limewater until their compressive testing date.

Table 7. Mix proportions of specimens.

Specimen	Gravel (kg/m^3)	Sand (kg/m^3)	Cement (kg/m^3)	Silica sand (%)	Water (kg/m^3)	w/c	Superplasticizer (kg/m^3)	Slump (cm)
NM.0.7	516	1204	400	0	180	0.45	0.8	9.4
NM.0.28								
PrM.0.7								
PrM.0.28								
PoM.0.7								
PoM.0.28								
NM.5.7	516	1204	380	5	180	0.45	0.87	8.6
NM.5.28								
PrM.5.7								
PrM.5.28								
PoM.5.7								
PoM.5.28								
NM.10.7	516	1204	360	10	180	0.45	0.98	5
NM.10.28								
PrM.10.7								
PrM.10.28								
PoM.10.7								
PoM.10.28								

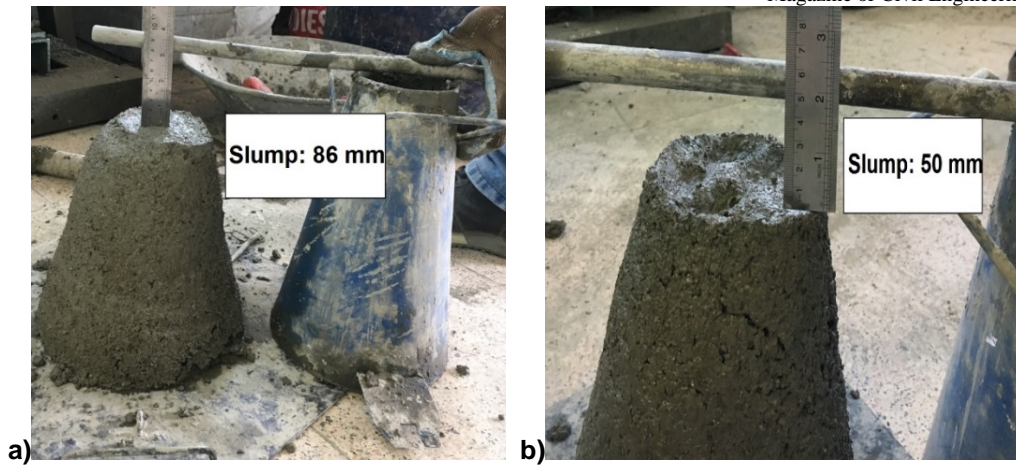


Figure 4. The slump test for: a) A specimen comprising 5 % silica sand
b) A specimen comprising 10 % silica sand.

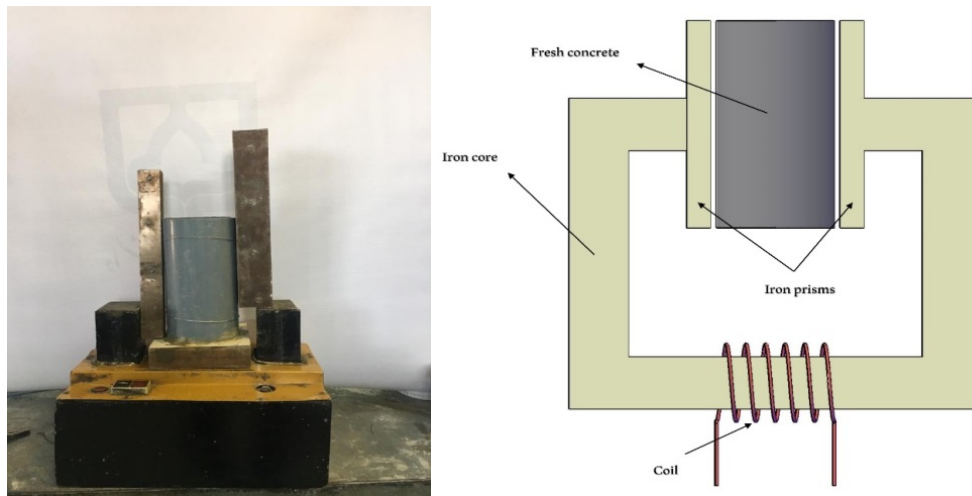


Figure 5. A PrM specimen subjected to AMF.



Figure 6. The direction of magnetization of PrM specimens.

2.5. Test procedure

The concrete cylinders were tested as per ASTM-C39 [44]. For testing the PoM specimens, a test setup was devised in a way that concrete could be subjected to both pressure and AMF, simultaneously, as shown in Fig. 7. As can be seen, the two terminals of the AMF generator were in touch with the upper and lower platens of the compression measuring apparatus. These specimens were exposed to AMF throughout the experiment. In fact this setup was used for testing all the three magnetic categories (NM, PrM, PoM) but only for PoM specimens was the AMF generator in work.

In order to make sure AMF did not affect digital sensors of measuring machine during testing of the PoM specimens, which renders test results unreliable, a non-digital compression equipment with the trade name Wykehaln Farrance was employed.

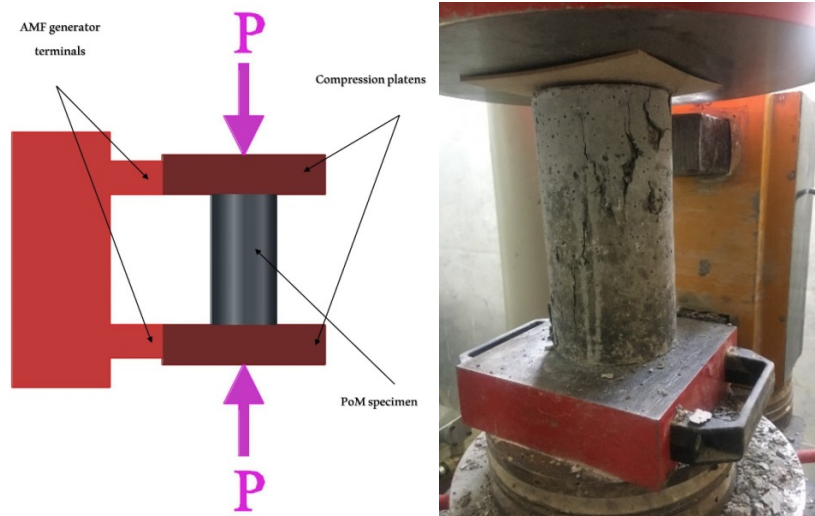


Figure 7. The test apparatus for specimens.

3. Results and Discussion

The compressive test results for 7-day and 28-day specimens are presented in Tables 8 and 9. In these tables compressive strength of NM.0.7 and NM.0.28 are regarded as a benchmark in order to better discuss the results.

Table 8. The compressive results of 7-day specimens.

AMF	Silica (%)	Specimen	Compressive strength			Enhancement relative to NM.0.7 (%)
			exact data	average	Standard deviation (σ)	
	0	NM.0.7	28.4,28.6,29.1	28.7	0.36	0
NM	5	NM.5.7	30.5,31,31.3	30.9	0.4	7.7
	10	NM.10.7	31.9,32.1,32.3	32.1	0.2	11.8
PrM	0	PrM.0.7	29.6,30,30.1	29.9	0.26	4.2
	5	PrM.5.7	31.9,32.4,32.6	32.3	0.36	12.5
	10	PrM.10.7	33.3,33.7,34.2	33.7	0.45	17.4
PoM	0	PoM.0.7	30,30.7,30.8	30.5	0.44	6.3
	5	PoM.5.7	33.3,33.8,34	33.7	0.36	17.4
	10	Pom.10.7	36,36.3,36.9	36.4	0.46	26.8

Table 9. The compressive results of 28-day specimens.

AMF	Silica (%)	Label	Compressive strength			Enhancement relative to NM.0.28 (%)
			exact data	average	Standard deviation (σ)	
	0	NM.0.28	38.7,39,39.6	39.1	0.46	0
NM	5	NM.5.28	39.7,39.9,40.4	40	0.36	2.3
	10	NM.10.28	41.9,42.6,42.7	42.4	0.44	8.4
PrM	0	PrM.0.28	40.2,40.4,40.9	40.5	0.36	3.6
	5	PrM.5.28	41,41.6,41.9	41.5	0.46	6.1
	10	PrM.10.28	43.7,44,44.6	44.1	0.46	12.8
PoM	0	PoM.0.28	41,41.1,41.8	41.3	0.44	5.6
	5	PoM.5.28	42.8,43,43.5	43.1	0.36	10.2
	10	PoM.10.28	47,47.1,47.5	47.2	0.26	20.7

2.6. The effect of adding silica sand

Since non-magnetized (NM) specimens were not exposed to AMF, these samples were adopted to discuss the influence of only silica sand content on compressive strength. The empirical data and approximate curves fitted to them for compressive strength enhancement of NM specimens comprising 0, 5 and 10 % silica sand, due to silica particles content, relative to the benchmark data are illustrated in Fig. 8. As is evident, with increase in silica sand constituent in concrete, the compressive strength of concrete increased, where maximum increases for 7-day and 28-day specimens were 11.8 % and 8.4 %, respectively, adding 10 % silica sand.

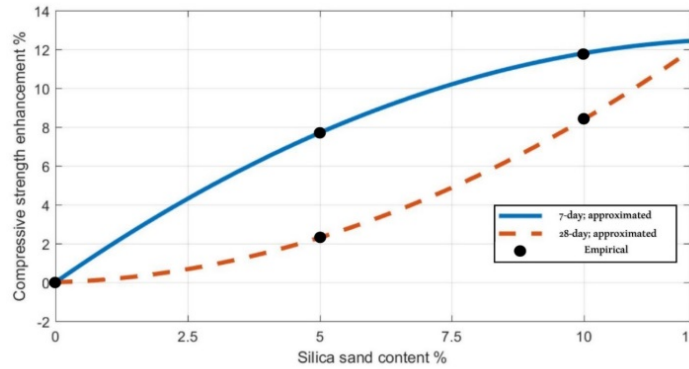


Figure 8. Compressive strength improvement for NM specimens due to adding silica sand: the experimental data and the cures fitted to them.

For better formulation of the effect of silica on compressive strength improvement, the enhanced extent of 7-day and 28-day NM specimens can be estimated through Eqs. (7) and (8), respectively, as a function of silica sand content. Note that R-square for both equations are 1.

$$E = -0.072S^2 + 1.9S + 1.83 \times 10^{-15} \quad \text{For the age of 7 days} \quad (7)$$

$$E = 0.076S^2 + 0.08S - 2.144 \times 10^{-15} \quad \text{For the age of 28 days} \quad (8)$$

Where E and S are compressive strength enhancement percentage and silica sand content (%), respectively.

As is seen, although the rate of compressive strength enhancement due to adding silica sand at percentages of this study is more significant as to 7-day concrete cylinders compared to the 28-day aged ones, which may be attributed to the fact that most of C_3SH in concrete is formed in the first days after concrete preparation [45], This rate for 7-day specimens is decreasing as silica sand content increases whereas the trend for 28-day concrete is reversed; at a silica content more that 10 % the enhancement of compressive strength in 28-day concrete would be more significant than 7-day one.

2.7. The effect of AMF

To discuss the effect of pre-magnetization and post magnetization on compressive strength, the enhancement data of NM specimens in Tables 8 and 9 are subtracted from the corresponding data of PrM and PoM specimens, respectively. The resultant data are visually presented in Fig. 9.

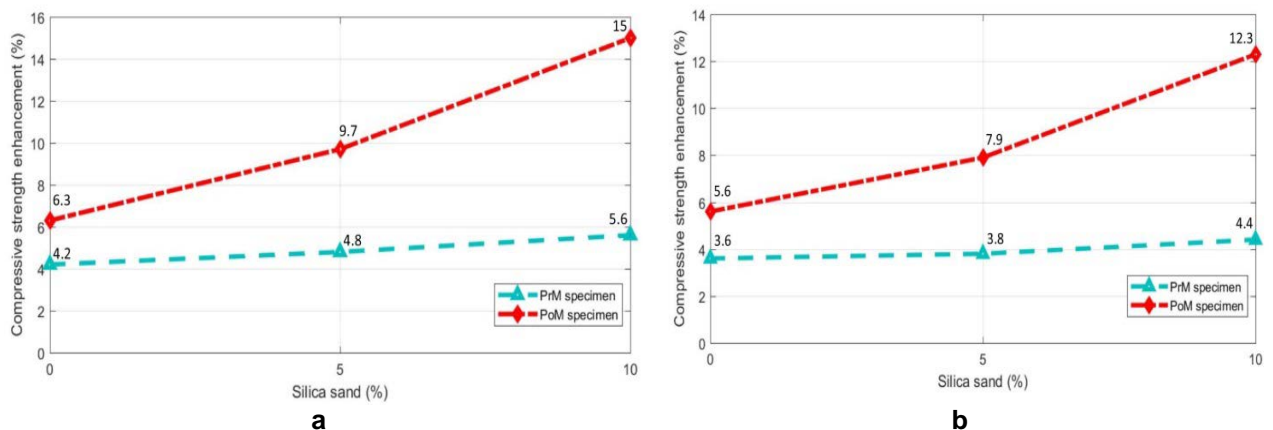


Figure 9. Enhancement of compressive strength for PrM and PoM specimens under the effect of only AMF: a) 7-day specimens, b) 28-day specimens.

In order for better realization of the issue, experimental data of compressive strength improvement along with the approximated curves fitted to them for PrM and PoM specimens of age 7 and 28 days are illustrated in Fig. 10.

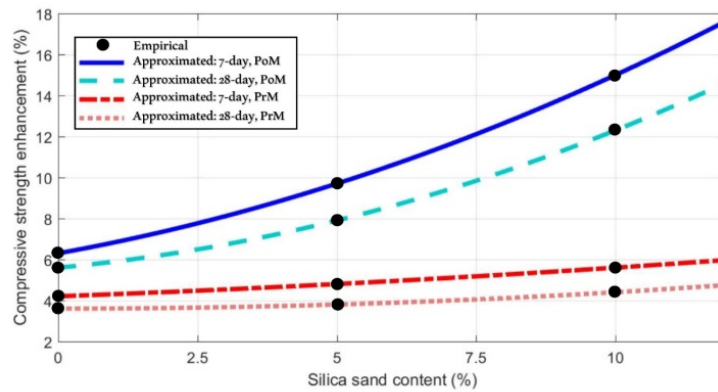


Figure 10. Compressive strength improvement for PoM and PrM specimens due to only AMF: the experimental data and the cures fitted to them.

All the approximated curves are cube functions as listed below, where the amount of R-square for all of them is 1.

$$E = 0.038S^2 + 0.49S + 6.3 \quad \text{7-day, PoM} \quad (9)$$

$$E = 0.042S^2 + 0.25S + 5.6 \quad \text{28-day, PoM} \quad (10)$$

$$E = 0.004S^2 + 0.1S + 4.2 \quad \text{7-day, PrM} \quad (11)$$

$$E = 0.008S^2 - 3.979 \times 10^{-16} S + 3.6 \quad \text{28-day, PrM} \quad (12)$$

A comparison of the approximate curves reveals that the effectiveness of AMF for 7-day specimens is more significant than 28-day ones. Moreover, with increase in silica sand proportions, AMF is more effective in enhancing concrete compressive strength, where the greatest increase for 7-day and 28-day samples (15 and 12.3 %, respectively, according to Fig. 9). Resulted from adding 10 % silica sand.

The most obvious fact is that post-magnetization has been by far more effective in improving concrete compressive strength compared with pre-magnetization. This may be rooted in the fact that silica is a diamagnetic substance. Such materials contain charged microparticles that can be influenced by an external magnetic field but as soon as it disappears the material reverts to its regular condition. When diamagnetic particles are subjected to a magnetic field they are repelled back because a magnetic field is induced in them in the opposite direction (Fig. 11) [46]. Compressive testing of PrM samples was carried out in a situation that AMF was not present and most of charged particles had reverted to their original position but testing of PoM specimens were conducted in the presence of AMF. That is, most of charged particles were influenced by magnetic field and this may be reason why PoM specimens showed a greater improvement compared to PrM ones.

According to Fig. 9, post magnetization enhanced compressive strength of 7-day concrete with 10 % silica sand by 15 % while pre-magnetization increased its strength up to only 5.6 %. Likewise, the figures for 28-day samples are 12.3 and 4.4, respectively.

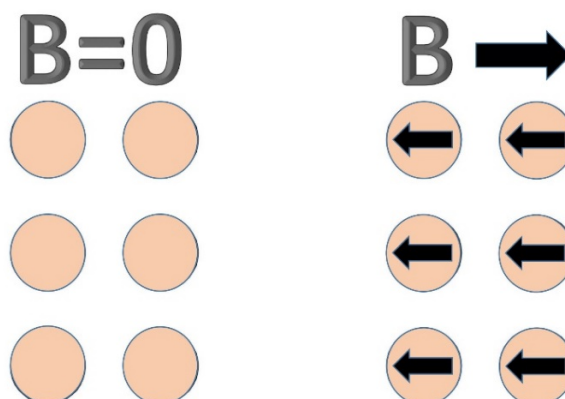


Figure 11. The orientation of diamagnetic particles in the presence and absence of magnetic field.

2.8. Advantages of this techniques

2.1.1. Environmental advantages

The advantages of adding silica sand as a partial replacement for cement in this study can be discussed environmentally. To explain, the cement industry, is one of the two major CO₂ producers, accounting for up to 8 % of man-made emissions of this gas throughout the world. The amount of CO₂ emitted due to concrete fabrication depends, directly, on cement content in concrete mixture. For preparation of one ton of cement, 900 kg of CO₂ are released, which amounts to 88 % of the emissions for the average concrete mix [47, 48]. Therefore, replacing a portion of cement with other additives is justifiable and a wide variety of such admixtures as silica particles has been established in concrete industry. According to Table 9, replacing 10 % percent of cement content with silica sand and then post-magnetizing it not only enhanced compressive strength of concrete by more than 20 %, but also resulted in a reduction of 10 % in CO₂ emissions.

2.1.2. Advantages of post-magnetization: theoretical discussion

As stated earlier exposing hardened concrete can improve concrete compressive strength as long as magnetic field is present. This implies that this technique could be a base for developing a new model for smart concrete structures where their behavior in the presence of powerful dynamic forces, saying earthquake, can be controlled by AMF. Therefore, in this section some advantages of this technique are theoretically discussed according to ACI [49].

- *Controlling structural behavior of concrete element*

A wide variety of patterns for relationship between stress and strain of concrete have been proposed. One of the most well-known models is the one suggested by Hognestad [50] in which at any stage of loading before reaching maximum load bearing capacity of concrete, f'_c , stress in concrete is calculated as a function of strain as follows:

$$f_c = f'_c \left[2 \frac{\varepsilon_c}{\varepsilon'_c} - \left(\frac{\varepsilon_c}{\varepsilon'_c} \right)^2 \right] \quad (13)$$

where f_c is stress in concrete.

ε_c is strain in concrete.

ε'_c is the strain corresponding to f'_c .

After hitting the peak point (f'_c) stress is calculated by a linear function as:

$$f_c = f'_c \left[1 - 0.15 \left(\frac{\varepsilon_c - \varepsilon'_c}{\varepsilon_{cu} - \varepsilon'_c} \right) \right] \quad (14)$$

where ε_{cu} represents the ultimate strain in concrete.

According to the test results, magnetizing hardened 28-day 10 % silica sand concrete (PoM.10.28) enhanced its compressive strength by 12.3 % ($f'_c \Rightarrow 1.123f'_c$). According to ACI [49] formulas ε'_c is proportional to $\sqrt{f'_c}$. As a result, ε'_c turns into $\sqrt{1.123}\varepsilon'_c$. Modifying Eq. (13), the stress-strength relation for a PoM.10.28 specimen is as:

$$f_c = 1.06f'_c \left[2 \frac{\varepsilon_c}{\varepsilon'_c} - \frac{1}{1.06} \left(\frac{\varepsilon_c}{\varepsilon'_c} \right)^2 \right] \quad (15)$$

Hognestad diagrams for PoM.10.28 and NM.10.28, where AMF is 0.5T and 0T, respectively, are illustrated in Fig. 12(a) (Note that since NM.10.28 specimens were not exposed to AMF, the enhancement of compressive strength due to AMF for them is 0. Therefore the diagram associated with AMF= 0T is drawn according to Eq. (13), where ε'_c is assumed to be 0.002).

If a concrete element in a smart structure is designed in a way that when strain (ε_c) reaches a point close to ε'_c (P_1 in Fig. 12(b)), an AMF generating actuator turns on. In this case, a transition from P_1 to P_2 is

expected, theoretically. But due to appearance of micro-cracks, it is likely to see a transition from P_1 to a point, saying P_3 , where the element can withstand a stress equal to or even more than f'_c of the diagram for $AMF=0T$, without reaching ε'_c . This means that there is an increase in modulus of elasticity and stiffness by moving from P_1 to P_3 . After that, the diagram continues towards P_4 and then collapses at P_5 .

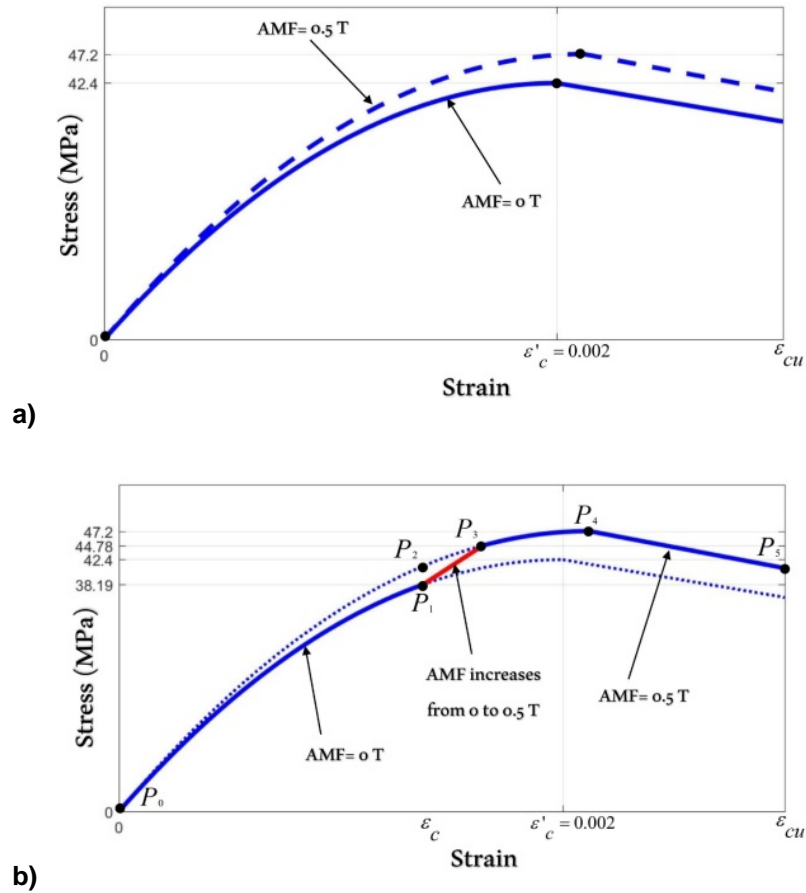


Figure 12. a) Hognestad curves for a smart concrete in the presence and absence of AMF, b) The change in structural behavior of this element due to applying AMF.

- *Moment strength of reinforced concrete beams*

For RC beams the nominal moment strength (M_n) is obtained as:

$$M_n = \rho f_y b d^2 \left(1 - 0.59 \rho \frac{f_y}{f_c} \right), \quad (16)$$

where ρ , b and d stand for, respectively, tension bar ratio, the width of the beam and the effective depth of it. Regarding the increase in compressive strength of 15 and 12.3 % for 7-day and 28-day aged concrete, respectively, containing 10 % silica sand, due to AMF exposure, the nominal moment strength for them is increased and calculated as:

$$M_n = \rho f_y b d^2 \left(1 - 0.51 \rho \frac{f_y}{f_c} \right): \quad \text{For the age of 7 days} \quad (17)$$

$$M_n = \rho f_y b d^2 \left(1 - 0.52 \rho \frac{f_y}{f_c} \right): \quad \text{For the age of 28 days} \quad (18)$$

- *Minimum reinforcement ratio*

The minimum reinforcement ratio for RC beams is obtained as:

$$\rho_{\min} = \frac{\sqrt{f_c}}{4 f_y} \geq \frac{1.4}{f_y} \quad (19)$$

where f'_c and f_y represent concrete compressive strength and reinforcing bars' yield strength, respectively, in MPa. In case f'_c exceeds 31 Mpa, ρ_{\min} is obtained as $\frac{\sqrt{f'_c}}{4f_y}$ where minimum reinforcement is proportional to $\sqrt{f'_c}$. According to Fig. 9(b), post-magnetizing enhanced compressive strength of 28-day specimens containing 10 % silica sand by 12.3 %. As a result ρ_{\min} can be reduced by 6 % if the concrete beam is subjected to AMF in the presence of strong dynamic forces.

- *Ductility of concrete beams*

It is well known that the higher the compressive strength, the more ductile RC beams are [51, 52]. As a result, exposing reinforced concrete elements in some critical areas of smart constructions to AMF, when strong cyclic loads occur, can increase their ductility, making it possible to control ductility and displacement of concrete structures in real time.

4. Conclusion

According to this investigation the following conclusions are drawn.

1. With increase in silica sand, concrete compressive strength increases, where the maximum increase for 7-day and 28-day concrete was 11.8 % and 8.4 %, respectively, as to the highest silica sand content used in the present study, 10 %.
2. The rate of increase in concrete compressive strength due to adding silica sand is more significant during the first 7 days after fabrication. However, it seems, as to high silica contents this rate would be larger for 28-day silica sand concrete.
3. The effectiveness of AMF in enhancing compressive strength of 7-day concrete is more significant compared to 28-day one
4. Exposing hardened silica sand concrete to AMF is far more effective in enhancing compressive strength than magnetizing fresh concrete.
5. Adding 10 % silica sand and post-magnetizing concrete reduces CO₂ emissions, which is a greenhouse gas, while enhancing compressive strength by about 21 %.
6. With increase in silica content in concrete, AMF can better improve concrete compressive strength, where maximum increases for 7-day and 28-day silica sand concrete were 15 and 12.3 %, respectively, which resulted from adding 10 % silica sand.
7. Applying AMF to 10 % silica sand concrete has benefits according to ACI [49], namely:
 - Reducing minimum tensile reinforcement ratio in RC beams down to 6 %.
 - Improving RC beam ductility
 - Enhancing moment strength of RC beams

Post-magnetization makes it possible to take control of stress-strain relationship in silica sand concrete elements, opening a new window towards establishing a new generation of smart structures.

5. Acknowledgements

The authors are thankful to Mr I. Abavisani, post graduate from Semnan University for practical guidance in carrying out this study. They also like to appreciate cooperation from Mr A. Firuzbakht, the laboratory technician at civil engineering department of Semnan University, and Mr H. Ghalenoei, the president of Danesh Pajooohan Paya institution and the head of the Electric Machines laboratory of Hakim Sabzevari University.

Funding: This research did not receive any specific grant from funding agencies in the public, commercial, or not-for-profit sectors.

References

1. Alexander, M., Magee, B. Durability performance of concrete containing condensed silica fume. *Cement and Concrete Research*. 1999. 29(6). Pp. 917–922. DOI: 10.1016/S0008-8846(99)00064-2
2. Detwiler, R.J., Mehta, P.K. Chemical and physical effects of silica fume on the mechanical behavior of concrete. *ACI Structural Journal*. 1989. 86(6). Pp. 609–614.
3. Björnström, J., Martinelli, A., Matic, A., Börjesson, L., Panas, I. Accelerating effects of colloidal nano-silica for beneficial calcium-silicate-hydrate formation in cement. *Chemical Physics Letters*. 2004. 392(1–3). Pp. 242–248. DOI: 10.1016/j.cplett.2004.05.071
4. Li, H., Xiao, H., Yuan, J., Ou, J. Microstructure of cement mortar with nano-particles. *Composites Part B: Engineering*. 2004. 35(2). Pp. 185–189. DOI: 10.1016/S1359-8368(03)00052-0.

5. Lee, S.-J. Synthesis and hydration study of Portland cement components prepared by organic steric entrapment method. *Materials and Structures*. 2004. 38(275). Pp. 87–92. DOI: 10.1617/14018.
6. Lin, D.F., Lin, K.L., Chang, W.C., Luo, H.L., Cai, M.Q. Improvements of nano-SiO₂ on sludge/fly ash mortar. *Waste Management*. 2008. 28(6). Pp. 1081–1087. DOI: 10.1016/j.wasman.2007.03.023.
7. Wang, J., Du, P., Zhou, Z., Xu, D., Xie, N., Cheng, X. Effect of nano-silica on hydration, microstructure of alkali-activated slag. *Construction and Building Materials*. 2019. 220. Pp. 110–118. DOI: 10.1016/j.conbuildmat.2019.05.158.
8. Assaedi, H., Shaikh, F.U.A., Low, I.M. Influence of mixing methods of nano silica on the microstructural and mechanical properties of flax fabric reinforced geopolymer composites. *Construction and Building Materials*. 2016. 123. Pp. 541–552. DOI: 10.1016/j.conbuildmat.2016.07.049.
9. Louis, M.A. Strength of reactive silica sand powder concrete made of local powders. *Journal for Engg. Science*. 2010. 3.
10. Abd El-Baky, S., Yehia, S., Khalil, I.S. Influence of Nano Silica Addition on Properties of fresh & hardened Cement Mortar. *Housing & Building National Research Center, Cairo*. 2013.
11. Reddy, B.S.K., Ghorpade, V.G., Rao, H.S. Effect of magnetic field exposure time on workability and compressive strength of magnetic water concrete. *Int. J. Adv. Eng. Technol.* 2013. 4(3). Pp. 120–122.
12. Cai, R., Yang, H., He, J., Zhu, W. The effects of magnetic fields on water molecular hydrogen bonds. *Journal of Molecular Structure*. 2009. 938(1–3). Pp. 15–19. DOI: 10.1016/j.molstruc.2009.08.037.
13. Soltani-Todoshki, A.R., Raeisi-Vanani, H., Shayannejad, M., Ostad-Ali-Askari, K. Effects of magnetized municipal effluent on some chemical properties of soil in furrow irrigation. *Int. J. Agric. Crop Sci.* 2015. 8(3). Pp. 482–489.
14. Ahmed, H.I. Behavior of magnetic concrete incorporated with Egyptian nano alumina. *Construction and Building Materials*. 2017. 150. Pp. 404–408. DOI: 10.1016/j.conbuildmat.2017.06.022.
15. Khorshidi, N., Ansari, M., Bayat, M. An investigation of water magnetization and its influence on some concrete specificities like fluidity and compressive strength. *Computers and Concrete*. 2014. 13(5). Pp. 649–657. DOI: 10.12989/cac.2014.13.5.649.
16. Su, N., Wu, Y.-H., & Mar, C.-Y. Effect of magnetic water on the engineering properties of concrete containing granulated blast-furnace slag. *Cement and Concrete Research*. 2000. 30. Pp. 599–605.
17. Gholizadeh, M., Arabshahi, H. The Effect of Magnetic Water on Strength Parameters of Concrete. *Research Journal of Applied Sciences*. 2011. 6(1). Pp. 66–69. DOI: 10.3923/rjasci.2011.66.69.
18. Su, N., Wu, C.-F. Effect of magnetic field treated water on mortar and concrete containing fly ash. *Cement and Concrete Composites*. 2003. 25(7). Pp. 681–688. DOI: 10.1016/S0958-9465(02)00098-7.
19. Bharath, S., Subraja, S., & Kumar, P.A. Influence of magnetized water on concrete by replacing cement partially with copper slag. *Journal of Chemical and Pharmaceutical Sciences*. 2016. 9(4).
20. Gholhaki, M., Kheyroddin, A., Hajforoush, M., Kazemi, M. An investigation on the fresh and hardened properties of self-compacting concrete incorporating magnetic water with various pozzolanic materials. *Construction and Building Materials*. 2018. 158. Pp. 173–180. DOI: 10.1016/j.conbuildmat.2017.09.135.
21. Ghorbani, S., Gholizadeh, M., de Brito, J. Effect of Magnetized Water on the Mechanical and Durability Properties of Concrete Block Pavers. *Materials*. 2018. 11(9). Pp. 1647. DOI: 10.3390/ma11091647.
22. Nair S.D., F.R.D. Set-on-demand concrete. *Cement and Concrete Research*. 2014. 57. Pp. 13–27. DOI: 10.1016/j.cemconres.2013.12.001
23. Soto-Bernal, J.J., Gonzalez-Mota, R., Rosales-Candelas, I., Ortiz-Lozano, J.A. Effects of Static Magnetic Fields on the Physical, Mechanical, and Microstructural Properties of Cement Pastes. *Advances in Materials Science and Engineering*. 2015. 2015. Pp. 1–9. DOI: 10.1155/2015/934195.
24. Ko, J.M., Ni, Y.Q. Technology developments in structural health monitoring of large-scale bridges. *Engineering Structures*. 2005. 27(12). Pp. 1715–1725. DOI: 10.1016/j.engstruct.2005.02.021.
25. Chang, P.C., Flatau, A., Liu, S.C. Review Paper: Health Monitoring of Civil Infrastructure. *Structural Health Monitoring: An International Journal*. 2003. 2(3). Pp. 257–267. DOI: 10.1177/1475921703036169.
26. Abdulridha, A., Palermo, D., Foo, S., Vecchio, F.J. Behavior and modeling of superelastic shape memory alloy reinforced concrete beams. *Engineering Structures*. 2013. 49. Pp. 893–904. DOI: 10.1016/j.engstruct.2012.12.041.
27. Shin, M., Andrawes, B. Experimental investigation of actively confined concrete using shape memory alloys. *Engineering Structures*. 2010. 32(3). Pp. 656–664. DOI: 10.1016/j.engstruct.2009.11.012.
28. Deng, Z., Li, Q., Sun, H. Behavior of concrete beam with embedded shape memory alloy wires. *Engineering Structures*. 2006. 28(12). Pp. 1691–1697. DOI: 10.1016/j.engstruct.2006.03.002.
29. Wen, S., Chung, D.D.L. Piezoelectric cement-based materials with large coupling and voltage coefficients. *Cement and Concrete Research*. 2002. 32(3). Pp. 335–339. DOI: 10.1016/S0008-8846(01)00682-2.
30. Tawie, R., Lee, H.K. Piezoelectric-based non-destructive monitoring of hydration of reinforced concrete as an indicator of bond development at the steel-concrete interface. *Cement and Concrete Research*. 2010. 40(12). Pp. 1697–1703. DOI: 10.1016/j.cemconres.2010.08.011.
31. Voutetaki, M.E., Papadopoulos, N.A., Angeli, G.M., Providakis, C.P. Investigation of a new experimental method for damage assessment of RC beams failing in shear using piezoelectric transducers. *Engineering Structures*. 2016. 114. Pp. 226–240. DOI: 10.1016/j.engstruct.2016.02.014.
32. Leung, C.K.Y., Wan, K.T., Inaudi, D., Bao, X., Habel, W., Zhou, Z., Ou, J., Ghandehari, M., Wu, H.C., Imai, M. Review: optical fiber sensors for civil engineering applications. *Materials and Structures*. 2015. 48(4). Pp. 871–906. DOI: 10.1617/s11527-013-0201-7
33. Perry, M., Yan, Z., Sun, Z., Zhang, L., Niewczas, P., Johnston, M. High stress monitoring of prestressing tendons in nuclear concrete vessels using fibre-optic sensors. *Nuclear Engineering and Design*. 2014. 268. Pp. 35–40. DOI: 10.1016/j.nucengdes.2013.12.038
34. Uva, G., Porco, F., Fiore, A., Porco, G. Structural monitoring using fiber optic sensors of a pre-stressed concrete viaduct during construction phases. *Case Studies in Nondestructive Testing and Evaluation*. 2014. 2. Pp. 27–37. DOI: 10.1016/j.csndt.2014.06.002
35. Li, H.-N., Li, D.-S., Song, G.-B. Recent applications of fiber optic sensors to health monitoring in civil engineering. *Engineering Structures*. 2004. 26(11). Pp. 1647–1657. DOI: 10.1016/j.engstruct.2004.05.018.
36. Zhang, X.W., Tao, Z., Qian, Z.Y. Experimental study on the energy absorption of porous materials filled with magneto-rheological fluid. *International Journal of Impact Engineering*. 2019. 133. Pp. 103347. DOI: 10.1016/j.ijimpeng.2019.103347.
37. Abavisani, I., Rezaifar, O., Kheyroddin, A. Alternating Magnetic Field Effect on Fine-aggregate Concrete Compressive Strength. *Construction and Building Materials*. 2017. 134. Pp. 83–90. DOI: 10.1016/j.conbuildmat.2016.12.109.

38. Abavisani, I., Rezaifar, O., Kheyroddin, A. Magneto-Electric Control of Scaled-Down Reinforced Concrete Beams. *ACI Structural Journal*. 2017. 114(1). DOI: 10.14359/51689452.
39. Rezaifar, O., Abavisani, I., Kheyroddin, A. Magneto-Electric Active Control of Scaled-Down Reinforced Concrete Columns. *ACI Structural Journal*. 2017. 114(5). DOI: 10.14359/51700790.
40. Abavisani, I., Rezaifar, O., Kheyroddin, A. Alternating Magnetic Field Effect on Fine-Aggregate Steel Chip–Reinforced Concrete Properties. *Journal of Materials in Civil Engineering*. 2018. 30(6). Pp. 04018087. DOI: 10.1061/(ASCE)MT.1943-5533.0002267.
41. Rezaifar, O., Kheyroddin, A., Abavisani, I. Prospect of Magneto-Electric Active Control for Smart Concrete Structures. *Smart Nanoconcretes and Cement-Based Materials*. 1st Editio . Elsevier, 2019. Pp. 1–25.
42. ASTM C33 / C33M-18, Standard Specification for Concrete Aggregates, ASTM International, West Conshohocken, PA, 2018, www.astm.org. DOI:10.1520/C0033_C0033M-18.
43. ASTM C143 / C143M-15a, Standard Test Method for Slump of Hydraulic-Cement Concrete, ASTM International, West Conshohocken, PA, 2015, www.astm.org.
44. ASTM C39 / C39M-18, Standard Test Method for Compressive Strength of Cylindrical Concrete Specimens, ASTM International, West Conshohocken, PA, 2018, www.astm.org.
45. Firoozmakan, S., Ramezani-pour, A., Ebadi, T., Bahrami, H. Effects of Nano-Silica on Mechanical Properties and Durability of Concrete. *Journal of Civil and Environmental Engineering*. 2012. 42.1(66). Pp. 35–45.
46. Iacovacci, V., Lucarini, G., Ricotti, L., Menciassi, A. Magnetic Field-Based Technologies for Lab-on-a-Chip Applications. *Lab-on-a-Chip Fabrication and Application*. InTech, 2016.
47. Mahasenan, N., Smith, S., Humphreys, K. The Cement Industry and Global Climate Change Current and Potential Future Cement Industry CO₂ Emissions. *Greenhouse Gas Control Technologies – 6th International Conference*. Elsevier, 2003. Pp. 995–1000.
48. Nisbet, M., Vangeem, M.G., Gajda, J., Marceau, M. Environmental life cycle inventory of portland cement concrete. *Portland Cement Association*, 2002.
49. ACI318-14, Building Code Requirements for Structural Concrete and Commentary (ACI 318R-14), American Concrete Institute, Farmington Hills, MI, USA, 2014.
50. Hognestad, E., Hanson, N.W., McHenry, D. Concrete stress distribution in ultimate strength design. *ACI Structural Journal*. 1995. 52(6). Pp. 455–479.
51. Ganesan, N., Indira, P.V., Sabeena, M.V. Behaviour of hybrid fibre reinforced concrete beam–column joints under reverse cyclic loads. *Materials & Design (1980-2015)*. 2014. 54. Pp. 686–693. DOI: 10.1016/j.matdes.2013.08.076.
52. Pendyala, R., Mendis, P., Patnaikuni, I. Full-range behavior of high-strength concrete flexural members: comparison of ductility parameters of high and normal-strength concrete members. *ACI Structural Journal*. 1996. 93(1). Pp. 30–35.

Contacts:

Alireza Safari Tarbozagh, asafari@semnan.ac.ir

Omid Rezaifar, orezayfar@semnan.ac.ir

Majid Gholhaki, mgholhaki@semnan.ac.ir

© Safari Tarbozagh, A., Rezaifar, O., Gholhaki, M., 2021



DOI: 10.34910/MCE.101.13

Strength of ultra-high rockfill dam concrete face

M.P. Sainov

Moscow State University of Civil Engineering (National Research University), Moscow, Russia

E-mail: mp_sainov@mail.ru

Keywords: concrete faced rockfill dam (CFRD), strength, stress-strain state, bending moment, longitudinal force, concrete deformation modulus, longitudinal bending

Abstract. The problem of providing safety to ultra-high rockfill dams with concrete faces is urgent and unresolved. It is proved by the facts of face structural failure of several ultra-high dams. As a rule, these facts are attributed to the face non-uniform bending deformations or are explained by high compressive stresses in the face central part. With the aid of numerical modeling the author investigated the conditions of forming stress-strain state (SSS) of ultra-high rockfill dams with concrete faces. Analysis was made of internal forces appearing in a concrete face: longitudinal forces and bending moments. It was established that high tensile stresses are most dangerous for concrete face strength in ultra-high rockfill dams. They create a threat by formation of horizontal and inclined cracks oriented along the contact with the foundation. These tensile stresses are the result of not only concrete face transverse bending deformations but also the presence of longitudinal tensile forces and longitudinal bending deformations in it. It is possible to minimize the impact of these adverse effects by decreasing friction at the contact of the face with the dam, however, this does not provide favorable SSS of the concrete face. It is necessary to take special measures on concrete face SSS regulation. Namely, it was established that rockfill deformation modulus should make up at least 300–400 MPa. Absence of precedent cases of crack formation in the faces of the existing ultra-high rockfill dams may be explained by relaxation of stresses due to creep of concrete.

1. Introduction

One of the urgent problems in modern hydraulic engineering is development of a theory and scientific validation of concrete faced rockfill dams (CFRD) structural designs.

The urgent character of this problem is related to a great number of existing dams of this type and hopeful prospects for their future use. By this time several dozens of high and ultra-high CFRDs have been built in the world [1]. There considered alternatives of constructing ultra-high CFRDs on the rivers of Central Asia and Siberia. In China there discussed the plans of constructing CFRDs about 300 m high [2-4].

In spite of the fact that CFRDs have been used for already more than a century, the necessity in scientific validation of their structural designs is still urgent. Till present CFRD structures are being designed and built in compliance with the rules obtained experimentally. The principles of selecting CFRD structural solutions are given in Proceedings of International Commission on Large Dams (ICOLD)¹.

The durable experience permitted considerable refinement of CFRD structural designs and construction sequence, however, technical and technological solutions applied by present do not guarantee their safety. The scientific literature describes several dozens of cases of CFRD seepage-control element integrity failure [3, 5–11]. These failures were demonstrated by formation of large through cracks in concrete faces (CF). Their locations were not similar, which evidences that there is not only one but several causes of crack formation. In CF of some dams the vertical cracks were formed [6, 7], in others there were horizontal cracks [8] or inclined cracks [9].

¹ ICOLD. Concrete Faced Rockfill dam: Concepts for design and construction, International Commission on Large Dams. 2010. Bulletin 141



The magnitude of CF failures evidences that they were caused by unfavorable stress-strain state (SSS). Therefore, a great number of scientific publications of different authors are devoted to analysis and investigations of CFRD SSS. The examples may be demonstrated by papers [1,12–23]. However, they do not create an integrated theory of CFRD operation, and sometimes they contradict each other.

There still existing a concept that CFRD seepage-control element works mainly in bending appearing at rockfill deformations under the action of hydrostatic pressure. At the same time, there are statements in literature that at that, the face is subject to compression in both directions, then crack formation in it cannot be explained. Formation of vertical cracks in CF is attributed to cleavage of the face surface layer in the compressed zone.

To solve the scientific problem in scientific validation of ultra-high CFRD structural designs the author with the aid of numerical modeling fulfilled a number of investigations of their SSS. They permitted determining the conditions of CF SSS formation, reveal the main peculiarities and assess its strength.

2. Methods

SSS studies were conducted by the author with the aid of the finite element method. Analyses were carried out on the example of a 200 m high abstract dam (Fig. 1). The face thickness was assumed to be constant and was equal to 2 m. The structure of the dam body was assumed to be uniform by deformation properties. At analyses the sequence of SSS formation was taken into account: several stages of the dam construction and the reservoir impoundment were considered.

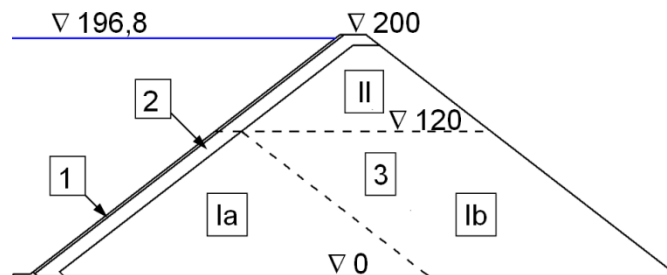


Figure 1. Structural diagram of an ultra-high rockfill dam with a concrete face
1 – concrete face – the first stage in scheme 3; II – the second stage in scheme 2; Ib, II – the dam second stage in scheme 3.

The specific feature of the research methodology for modeling of a CF thin-walled structure was use of solid finite elements with a cubic degree of approximation of high-order displacements. Thanks to use of high-order elements, calculations allowed us to obtain a continuous function of the stress distribution in a rigid thin-walled structure in all directions.

Due to use of solid finite elements, rather than plate or shell finite elements, all components of the stress tensor in CF were determined. This provides the ability to perform a more complete analysis of its stress state. Using the components of the tensor, the internal forces in the sections of the CF structure were calculated: longitudinal forces and bending moments.

When developing the finite element models of the structure, it was possible to exhibit non-linear effects at the contacts between structures, the rigidity of whose materials varies greatly. This is a possibility of tearing off and slipping. When modeling the slippage effect, the Coulomb model was used. For this, contact finite elements (Goodman elements) were used. These elements were provided between the face and rockfill, between rockfill and the rock foundation, and also simulated the behavior of the perimeter joint.

The analyses were carried out for various alternatives of rockfill deformability, using the model of linear deformation of soil. To assign the values characterizing rockfill deformability the data of field measurements of CFRD deformations was processed. It showed that depending on the quality of rockfill compaction the value of rockfill linear deformation modulus E varies within a wide range: from 30 MPa to 500 MPa [24]. SSS calculations were carried out for four values of E : 60, 120, 240 and 480 MPa. The Poisson's ratio of rockfill was taken equal to 0.2.

3. Results and Discussion

Analysis of the results of numerical modeling revealed the main characteristic features of the CF SSS of rockfill dams. It turned out to be more complicated than in approximate, speculative representations. This is due to the complicated nature of the dam body deformations and the interaction between the CF and the dam body.

It was revealed that not only cross bending but also other forms of deformation are characteristic of the face SSS. They appear even in the simplest loading scheme (scheme 1), when the reservoir is impounded only after the completion of the dam construction.

The cross bending of the face is not the prevailing form of its deformations; taking into account other forms of the face deformations leads to a considerable change of stresses in it.

Cross bending of the face is caused by the non-uniform height-wise distribution of deflections of the face (movements in the direction across the slope). As a rule, the bend of the face towards the downstream side prevails, but it may also occur in the opposite direction. This is illustrated in Fig.2.

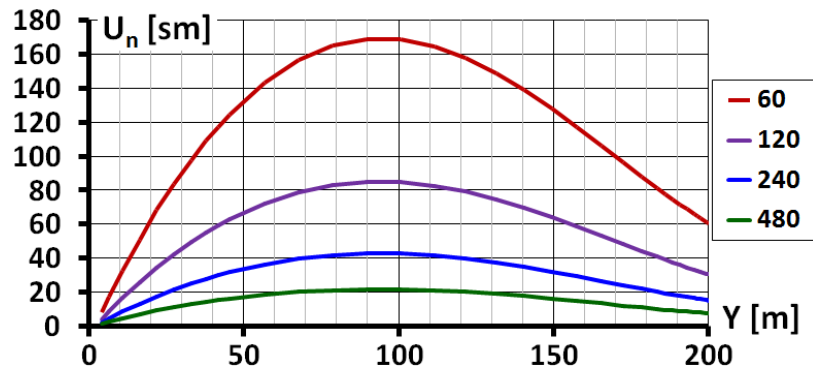


Figure 2. Distribution of deflections (movements in the direction across the slope) of the concrete face height-wise Y. Figures designate values of rockfill linear deformation modulus E.

With a simple construction sequence (scheme 1), the bending of the face towards the downstream side is characteristic of its part which is below the water level. The greatest intensity of bending deformations is observed at the very bottom of the face (Fig. 3). In the zone of water level, the face bends towards the upstream side. As the reservoir is impounded the shape of the deflection curve changes, and the upward bend zone toward the upstream side moves upward as a “wave” (Fig. 3).

Presence of the face bend in the upstream direction is confirmed by field measurements at the existing dams. The outward bend of the face is accompanied by formation of thin horizontal cracks in it. Mori1 indicates that such cracks have openings of about a few tenths of a millimeter, but they close after rising water levels in the reservoir.

At complicated construction sequence, the nature of cross bending deformations is significantly more complicated. The characteristic effect is the presence of the face upward bend in the upstream direction observed on the crest of each stage of the dam (Fig. 4). The presence of this effect was found at SSS numerical modeling of the Tianshengqiao-I dam in China, as well as during field measurements [14]. Separation of the face from the dam body is also possible. The presence of this separation is a typical feature indicating the danger of cracking in the face.

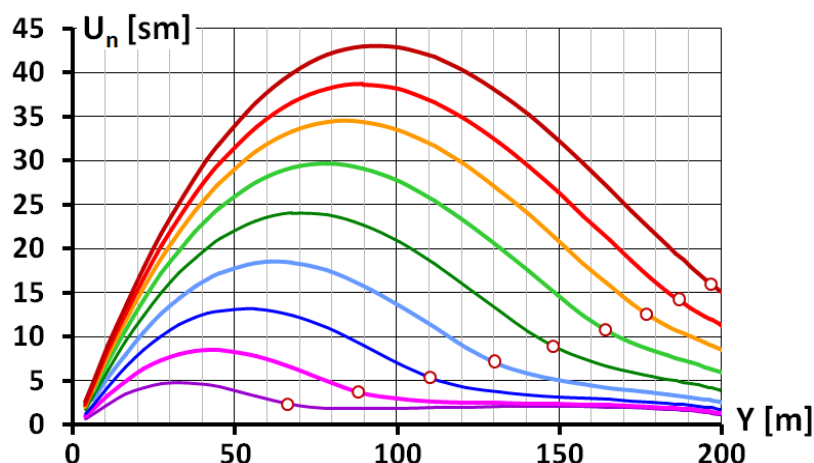


Figure 3. Variation of concrete face deflections with growth of the upstream water level (at E=120 MPa). Circles designate the upstream level corresponding to the curve of deflections.

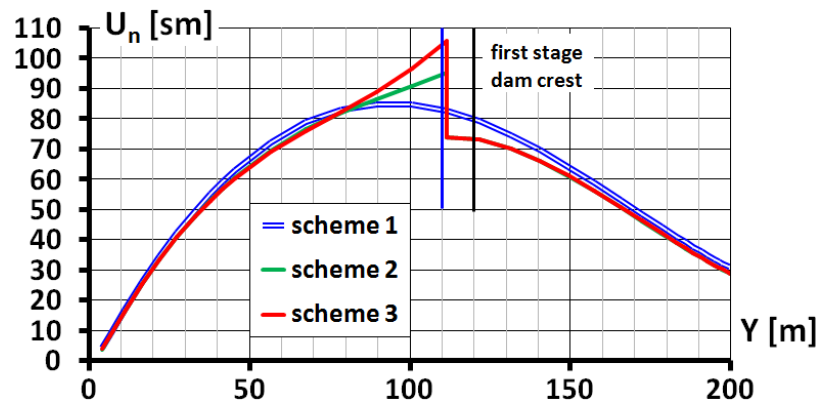


Figure 4. Variation of distribution pattern height-wise the face deflections depending on the sequence of the dam construction and the reservoir impoundment at $E=120$ MPa). Scheme 1 – reservoir impoundment after full completion of the dam construction; schemes 2, 3 – 2nd stage dam construction and the reservoir impoundment.

Fig.4 shows the example of variation of the 200 m high dam face deflections. Three schemes of sequence of dam construction and reservoir impoundment were considered. In Scheme 1, the reservoir is filled only after full completion of the dam construction. In schemes 2 and 3, the construction of the dam and the reservoir impoundment are carried out in two stages. The height of the first stage is 120 m, and the level of the upstream level is 110 m. In scheme 2, the profile of the first stage of the dam has a very wide crest, and in scheme 3 – 10 m (Fig. 1).

From Fig. 4 it is seen that construction of the 2nd stage dam reduces deflection of the face in the lower part of the 1st stage dam and in the 2nd stage dam. However, on the crest of the 1st stage dam the deflections sharply increase. In this zone, the face bends towards the upstream side, and these deformations are very significant in magnitude. Formation of tensile stresses in the face may be expected. It is confirmed by formation of cracks in the upper part of the face of the first stages at dams Tianshengqiao-I [14], Shuibuya and Buxi [8].

It should be noted that when the dam is erected by stages, the danger of cracking is characteristic not only of the 1st stage face, but also of the 2nd stage face. In Fig. 4, an increase in deformations of the 2nd stage face cross bending in the zone adjacent to the dam of the first stage is noticeable.

To minimize additional bending deformations, it is necessary that the crest of the first stage dam should be very wide: in scheme 3 the bend is less than in scheme 2 (Fig. 4). This confirms the statement of Marques and Pinto that the asymmetric profile of the first stage contributes to formation of tensile stresses in the face [25]. However, even when using the symmetric profile of the first stage (Scheme 3), the danger of cracking in the CF remains.

However, not only cross bending deformations pose a danger to the integrity of the face. The author's studies showed that in addition to cross bending deformations, the face experiences longitudinal deformations, i.e. linear deformations in the direction along the slope. They arise due to the presence of tangential stresses τ on the contact between the face and the dam.

The assumption of the significant role of shear stresses in the formation of the face SSS was made by Marques and Pinto even in 2005 [25]. They expressed the opinion that during deformations of the dam body, tangential stresses may occur at the contact of the face and the dam, causing deformation of the longitudinal extension of the face. Marques and Pinto proposed a method for determining frictional forces at the contact of the dam face. They pointed out that the tensile strength of concrete may be provided if the stresses did not exceed 3 MPa, and made a supposition that with conventional reinforcement the formation of rupture cracks in the CFRD face was inevitable.

However, the method of determining friction forces proposed by Marques and Pinto, involves reaching by them their limit values, which in real conditions usually does not occur. The exact values of the friction forces may only be determined by numerical modeling. Using numerical modeling, the effect of formation of tensile longitudinal forces in CF was confirmed by the author in 2006 [13] and Arici in 2011 [12].

Let us Consider the conditions for formation of friction forces at the CF contact with the dam body using the simplest dam construction scheme as an example (Scheme 1). Before impoundment of the reservoir the tangential stresses τ are caused only by forces from the dead weight of the face. They are directed from top to bottom and increase evenly from the crest to the foot. In this case, the contact perceives only part of the face dead weight, and the rest is transmitted through the perimeter joint to the foundation.

After filling the reservoir the tangential stresses τ at the contact change. This change is associated with high horizontal displacements of the dam under the effect of hydrostatic pressure on the upstream face. As a rule, the deformation properties of rockfill are such that the displacements and settlement of the dam are

comparable in magnitude. Due to large displacements, the face separates from the foundation: the perimeter joint opens, separating them from each other. The joint opening is confirmed by the data of field measurements at most of CFRDs given in the proceedings of ICOLD. It also indicates the presence of the face movements in the direction along the slope and appearance of linear longitudinal deformations in the face.

Separation of the face from the foundation leads to the fact that the dead weight of the face is entirely perceived by the tangential stresses τ at the contact between the face and the under-face supporting zone and τ grows. But when filling the reservoir, not only growth occurs, but also the redistribution of tangential stresses lengthwise the contact. This redistribution is caused by the uneven deformations of the dam body. As the rigidity of the CF and rockfill varies greatly, the CF cannot be deformed jointly with the dam body; at the contact between them the face and the dam move relative to each other. The consequence of this movement is additional friction forces at the contact, due to which the tangential stresses τ are redistributed lengthwise the contact.

Designs of CFRD provide for arrangement of a special under-face zone to smooth out the unevenness of the face deformations. However, as our studies have shown, this zone does not play a significant role due to its small thickness.

A more important role is played by friction characteristics (shear parameters) at the contact between the CF and the under-face supporting zone. In modern dams (since 1999), the surface of the upstream slope is formed in the form of curb blocks made of low-cement concrete [26]. Moreover, to reduce friction, the contact between the CF and the curb blocks is covered with a bitumen emulsion.

SSS analysis was conducted for two alternatives of CFRD structure. In alternative 1 it was assumed that the under-face zone is made of crushed stone and the curb blocks are not arranged. The tangential stiffness of the contact was taken equal to 200 MPa / m. In alternative 2, the presence of both curbs and an antifriction layer was taken into account. The modulus of deformation of the material of the curb blocks was taken equal to 5 GPa. The tangential stiffness of a contact coated with a bitumen emulsion was approximately assumed to be 20 MPa/m.

Calculations show that the taken measures cannot completely eliminate friction on the contact. Regardless of the tangential stiffness of the contact, the distribution pattern of the tangential stresses τ on the contact does not change basically.

Figure 5 shows the distribution of τ obtained by calculation for alternative 2. It may be seen that in the lowest part of the contact the tangential stresses get the opposite direction (from the crest to the foot), and on the rest of the contact they increase in magnitude (Fig. 5). The indicated effect is not fundamentally new. It also manifests itself at the contact of the foundation of structures with a deformable soil foundation.

This effect of "negative friction" is important in formation of CF SSS; it causes longitudinal extension in the face which affects the strength of the face.

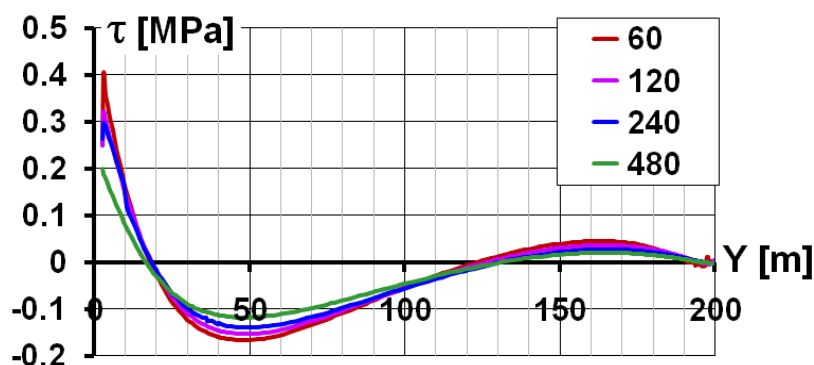


Figure 5. Tangential stresses on the contact of the face with the under-face zone (if bitumen emulsion layer is provided). Figures designate values of rockfill linear deformation modulus.

Figure 6 shows the obtained by calculations pattern of distribution of the longitudinal forces N in the CF for a simple construction scheme (Scheme 1). In the lower quarter of the height the face is subject to tensile force (extension deformations), and in the upper quarter it compresses (contraction deformations). It should be noted that the values of tensile and compressive longitudinal forces are quite significant.

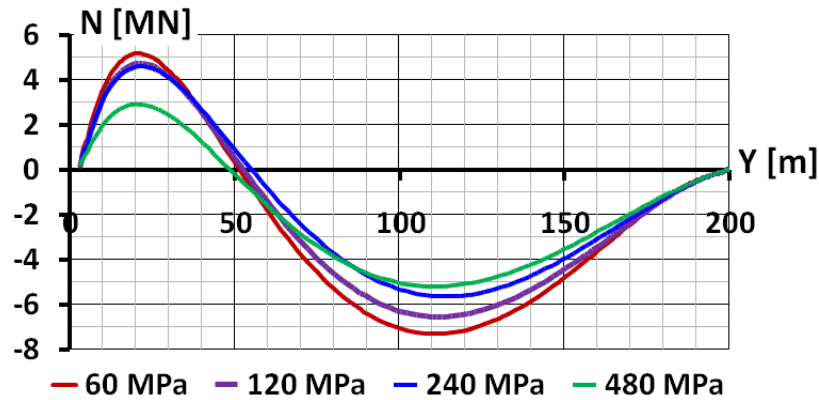


Figure 6. Longitudinal forces in CF (if bitumen emulsion layer is provided). Figures designate values of rockfill linear deformation modulus.

Thus, the author found that the CF SSS is characterized by the presence of not only bending moments M , but also longitudinal forces N . This has an extremely adverse effect on the strength of the CF. The combined action of bending moments and tensile longitudinal forces leads to the appearance of high tensile stresses in the faces of ultra-high CFRDs.

This is illustrated in Figs. 7 and 8, which show the distribution of the longitudinal stresses along the CF height, i.e. stresses acting in the direction along the upstream slope. They clearly show that the lower CF part of an ultra-high dam will experience very high tensile stresses, many times greater than the tensile strength of concrete.

The value of tensile stresses depends on many factors, among which the main impact is exerted by rockfill deformability (E), the shear characteristics of the contact, and also the deformation modulus of concrete E_b .

Fig. 7 corresponds to alternative 1, when the friction reduction at the contact is not performed, and $E_b = 29$ GPa. In this case, even with the most thorough compaction of rockfill tensile stresses are many times higher than the tensile strength of concrete (1.8 MPa). This is due to the fact that tensile stresses only from longitudinal forces (excluding bending) exceed 2 MPa. This indicates an extremely low level of safety of ultra-high CFRDs, as well as the need for measures to reduce friction at the contact between the CF and the dam body.

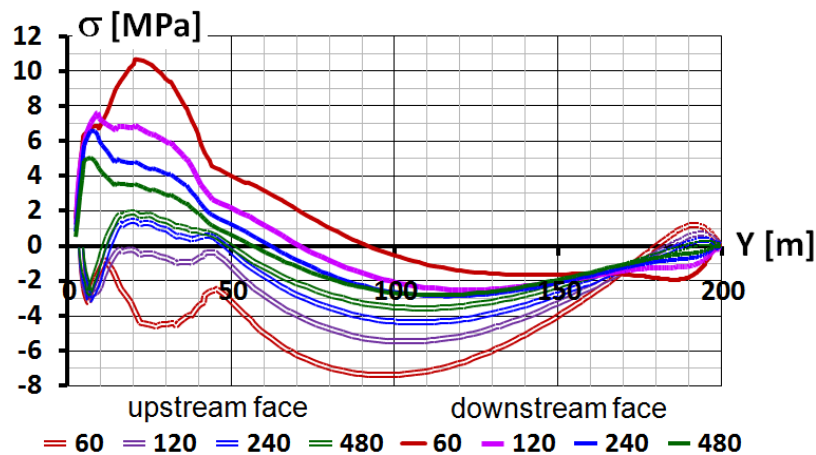


Figure 7. Distribution of longitudinal stresses on the upstream and downstream faces of the dam face (at the face contact with the under-face zone made of soil; simple scheme of dam construction and loading).

Figure 8 shows the calculation results for alternative 2 and $E_b = 29$ GPa. However, even in this case, in all options, the standard tensile strength of the CF is not provided.

Comparison of the results of SSS calculations in two alternatives (Figs. 7 and 8) permits revealing the role of friction in formation of the CF SSS. For analysis by the values of longitudinal stresses in the face, bending moments M were determined. Curves of the distribution of bending moments are shown in Figs. 9 and 10.

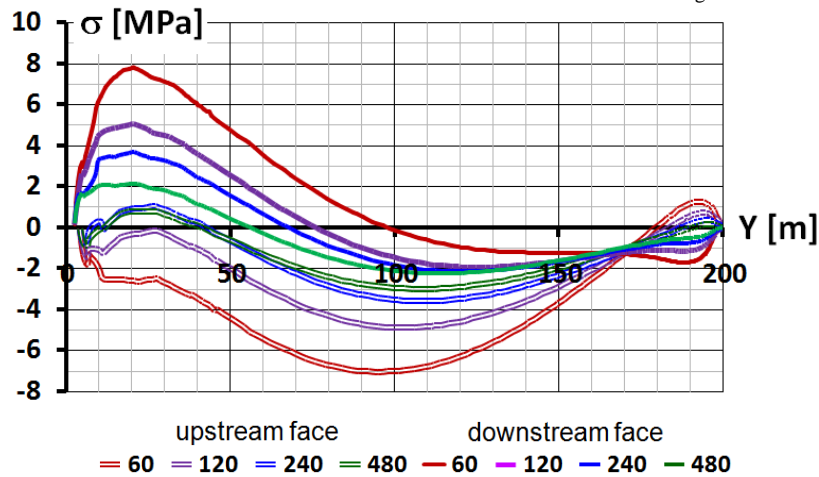


Figure 8. Distribution of longitudinal stresses on the upstream and downstream faces of the dam face (at decrease of friction at the contact of the face with concrete under-face zone; simple scheme of dam construction and loading).

Comparison of the bending moments in alternatives 1 and 2 allowed the author to identify another effect characteristic of CF SSS. This is the effect of the face longitudinal bending. It consists in the appearance of an additional bending moment in the face. In Fig. 9 (alternative 1), a sharp jump in bending moments in the lowest part of the CF is clearly visible, while alternative 2 does not have it (Fig. 10).

The effect of longitudinal bending is characteristic only of the edge sections of the face. It arises due to the peculiarity of their stress state, which consists in the deviation of the lines of action of the main stresses from the longitudinal direction (direction along the slope). Therefore, in the horizontal section of the face, the longitudinal force does not coincide in magnitude with the friction force. This inequality causes an additional moment from the longitudinal bend.

Longitudinal bending has a significant and adverse effect on the SSS of the face in alternative 1; it increases the bending moment directed towards the downstream side. Accordingly, it contributes to formation of transverse cracks in the face. Reduction of tangential stresses on the contact permits avoiding longitudinal bending.

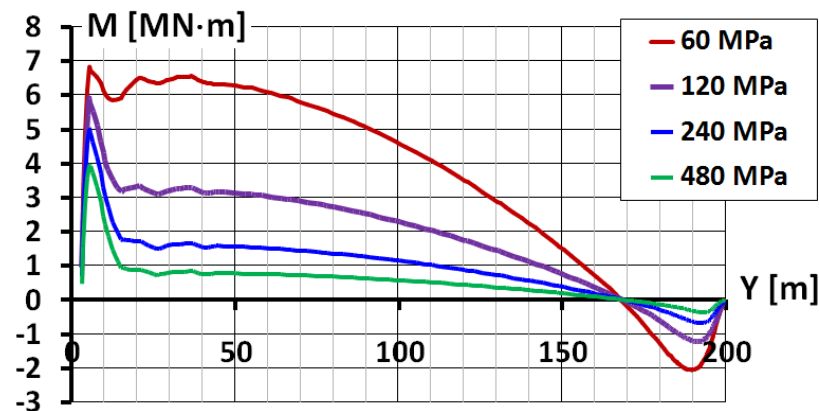


Figure 9. Distribution of bending moments height-wise the face (at the face contact with the under-face zone made of soil; simple scheme of dam construction and loading).

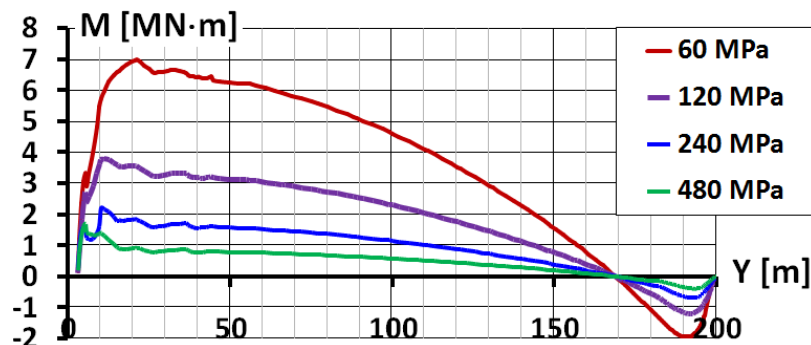


Figure 10. Distribution of bending moments height-wise the face (at decreasing friction at the face contact with concrete under-face zone; simple scheme of dam construction and loading).

Thus, decrease of friction at the CF contact with the dam has a favorable effect on the CF SSS: it reduces the longitudinal tensile force and the moment of longitudinal bending. In ultra-high dams this is a necessary measure.

However, it does not permit providing the necessary level of the CF safety. Even in alternative 2, at $E < 350$ MPa, tensile stresses exceed 3 MPa and formation of transverse cracks in the face may be expected. Calculations of the SSS in the 3D formulation [21] show that the orientation of these cracks will repeat the position of the foundation outline. On the channel sections the cracks will be located horizontally, and on the side sections they will be inclined.

High (almost one hundred percent) probability of formation contradicts the practice of construction and operation of ultra-high dams. Not all ultra-high CFRDs showed cracking. Several explanations can be given for this.

First of all, it is the influence of spatial conditions. Ultra-high dams are erected, as a rule, in narrow rock gorges. The impact of the rock sides leads to decrease of both displacements and settlements of the dam. In this case decrease of horizontal displacements occurs more intensively than that of settlements. This has a favorable effect on CF SSS. Compared to flat conditions, both compressive and tensile forces acting in the CF in the direction along the slope are reduced.

However, studies of the spatial CFRD SSS [21] show that the effect of spatial conditions is not critical in terms of providing the tensile strength of concrete.

Therefore, the more credible assumption is that not one, but several factors act, creating a difference between the calculated conditions for CFRD SSS formation from the real ones.

Firstly, the improvement in the CF SSS may be related to time dependent relaxation of stresses in the face concrete. According to Russian standards, due to creep the deformation modulus of concrete E_b may be reduced by 20 ÷ 60%.

Analyses of CFRD SSS with a value of $E_b = 12$ GPa made it possible to evaluate the effect of this phenomenon on the CF strength. Figure 11 shows the longitudinal stress distribution for alternative 2.

Analyses showed that a 60% decrease in E_b reduces stresses in the CF by about 30 %. Due to this, in alternative 2, at $E > 400$ MPa, the standard value of concrete tensile strength (1.8 MPa) is provided (Fig. 12).

This result allows us to recommend the construction of ultra-high CFRDs to be long and gradual, so that concrete can adapt to rockfill deformations and stresses in it are reduced due to relaxation processes. This recommendation is confirmed by the operating experience of the Mohale dam [7], in which loss of the CF integrity occurred during repeated, but very fast impoundment of the reservoir.

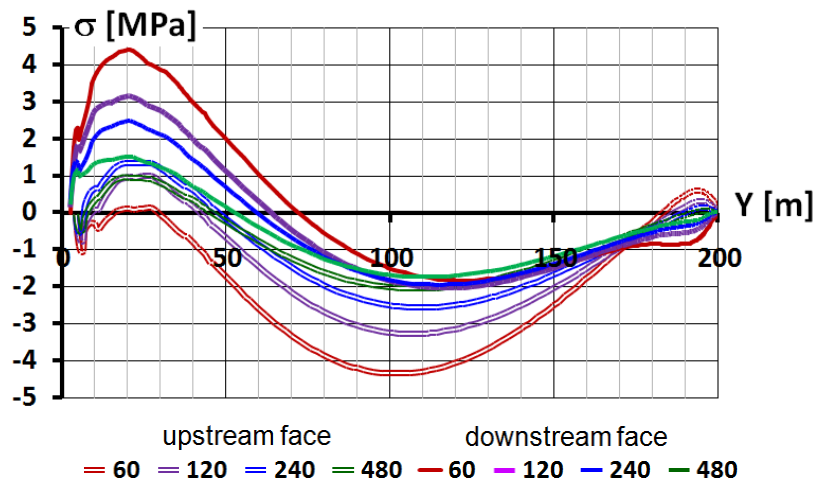


Figure 11. Distribution of longitudinal stresses on the upstream and downstream faces of the dam face (at decreasing friction of the face contact with concrete under-face zone).

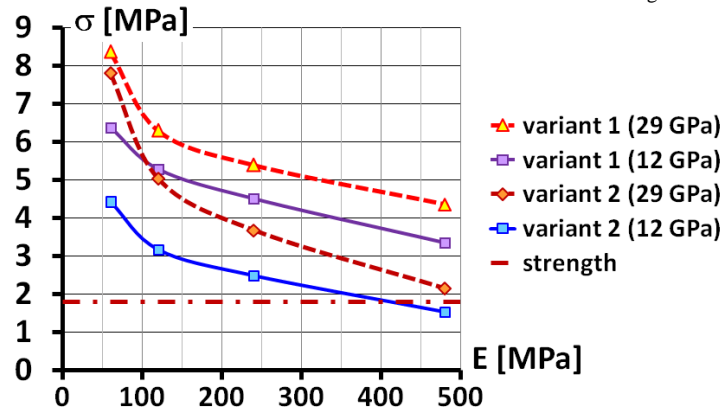


Figure 12. Relationship between maximum values of tensile stresses in the face and rockfill linear deformation modulus E , linear deformation modulus of concrete and friction at the contact. Variants 1, 2 are variants of the contact shear characteristics. Figures in brackets designate the value of concrete linear deformation modulus.

Secondly, it can be expected that in regions with a warm climate, the tangential stiffness of the bitumen emulsion layer will be lower than 20 MPa / m, which reduces friction and longitudinal forces.

Taking into account the influence of other factors (spatial conditions, face reinforcement, staged construction), it is recommended to compact rockfill in ultra-high dams until the values of rockfill deformation modulus $E > 300$ MPa are reached.

Another characteristic feature of the CF SSS of ultra-high dams, which determines their strength, is known from the scientific and technical literature. It consists in the presence of high compressive stresses in the face in the direction along the dam section (from one side to the other side). It is confirmed by the facts of formation vertical cracks in the CF at a number of ultra-high dams [6, 7]; and also it is revealed as a result of numerical studies of the CF spatial SSS by different authors [1, 15, 20].

The reason for formation of high compressive stresses in the CF is not attributed to bending deformations, but the presence of longitudinal compressive force in the direction from one side to the other side. This force arises from the uneven distribution of dam settlements along the alignment. The river channel section of the dam with the highest dam height settles more than the side sections of the dam, which leads to horizontal displacements of the dam in the direction from the sides to the channel. It is due to them that compressive longitudinal forces appear in the face.

The author's calculations [21] showed that the higher is the dam and the narrower is the site, the more intensive are the horizontal compressive forces in it. In ultra-high dams located in narrow sites, compressive stresses can be comparable with the compressive strength of concrete (about 15 MPa). This explains the observed cases of formation of vertical joints at the existing dams.

The non-uniform distribution of dam settlements and displacements along the alignment is associated with one more feature of the CFRD SSS. It can be described as a bend of the face in its plane. The river channel sections of the face receive longitudinal displacements larger in size than the side ones. The plane bending of the face is expressed rather weakly and is almost completely compensated by vertical intersectional joints. It does not pose a serious danger to the strength of CF.

4. Conclusion

The research results revealed the most vulnerable places in the CF structure and possible causes of their integrity failure associated with its unfavorable SSS. Briefly relevant conclusions can be formulated as follows:

1. Failures of the CF integrity should be associated not only with loss of concrete compressive strength, but also with loss of tensile strength;
2. The reason for appearing vertical cracks in the face of an ultra-high dam is high compressive longitudinal forces in the direction from one side to the other side. The formation of such cracks is possible only in the central part of the face;
3. When the dam is constructed by stages, it is very likely that failure of the CF tensile strength may be related to the local effect of an increase in bending deformations in the stage boundary zone;
4. The most dangerous from the point of view of crack formation is the interface zone of the face with rock foundation. In this zone, the face experiences not only the bending moment of the cross bending, but

also the tensile longitudinal force (in the direction along the slope) and the bending moment of the longitudinal bending. This leads to appearance of tensile stresses on the face, which threaten with formation of horizontal and inclined cracks.

According to the results of calculations, the formation of high tensile stresses in the face is almost inevitable and it is very difficult to provide tensile strength of concrete in the face of an ultra-high dam.

Therefore, the urgent task of research is selection and justification of measures to provide tensile and compressive strength of the concrete face. The main of these measures is to reduce rockfill deformability due to the high degree of its compaction. Based on the calculation results, it may be recommended to achieve rockfill linear deformation modulus E of at least 300 MPa.

Bearing this in mind when choosing measures, it should be taken into consideration that, with rockfill low deformability, the main danger to CF strength is posed not by bending deformations, but by longitudinal extension deformations. This is illustrated by the curves in Fig. 13, which show change in the maximum values of bending moments M and tensile longitudinal forces N depending on various factors. On them it is seen that an increase in rockfill modulus E decreases M_{max} to a greater extent (Fig. 13b) than N_{max} (Fig. 13a).

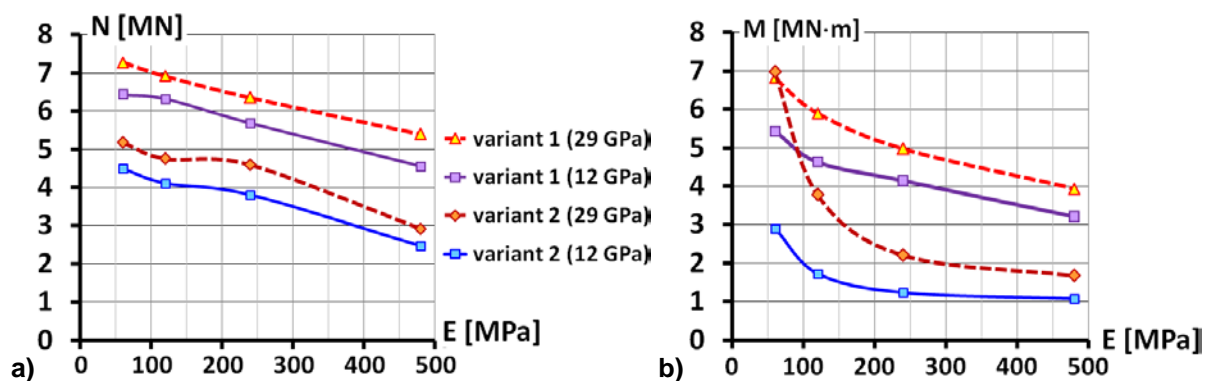


Figure 13. Relationship between maximum values of longitudinal forces (a) and bending moment (b) and rockfill linear deformation modulus E , concrete linear deformation modulus and friction on the contact.

Therefore, measures to provide the CF strength should first of all be aimed at reducing the longitudinal forces in the face and at reducing the part of the stresses caused by these longitudinal forces. One of such measures is reduction of friction at the contact between the face and the dam body. It allows not only reducing the value of tensile and compressive longitudinal forces in the face, but also protection of the face against deformations of longitudinal bending.

Both of the above measures are necessary, but not sufficient to provide strength of concrete in the face of an ultra-high dam. A full complex of measures is required.

References

1. Wen, L., Chai, J., Xu, Z., Qin, Y., Li, Y., Junrui, C. A statistical review of the behaviour of concrete face rockfill dams based on case histories. *Géotechnique*. 2018. 68. No. 9. Pp. 749–771. DOI: 10.1680/jgeot.17.p.095.
2. Li, N.-H., Sun, D.-W., Li, D.-H., Deng, Y.-G., Yang, J. Deformation behavior of 300 m high-concrete face rockfill dams. *Yantu Gongcheng Xuebao/Chinese Journal of Geotechnical Engineering*. 2009. No. 31(2). Pp.155–160.
3. Ma, H., Chi, F. Technical progress on researches for the safety of high concrete-faced rockfill dams. *Engineering*. 2016. 2. Pp. 332–339
4. Ma, H.Q., Cao, K.M. Key technical problems of extra-high concrete faced rock-fill dam. *Science in China. Series E: Technological Sciences*. 2007. Vol. 50(1). Pp.20–33. DOI: 10.1007/s11431-007-6007-5.
5. Marques Filho, P., De Pinto, N.L.S. CFRD dam characteristics learned from experience. *The International Journal on Hydropower & Dams*. 2005. No. 12(1). Pp. 72–76.
6. Freitas, M.S.Jr. Concepts on CFRDs Leakage Control - Cases and Current Experiences. *ISSMGE Bulletin*. 2009. Vol. 3. No. 4. Pp. 11–18.
7. Johannesson, P., Tohlang, S.L. Lessons learned from Mohale. *The International Water Power & Dam Construction*. 2007. Vol. 59. No. 8. Pp. 16–18+20–22+24–25
8. Hu, K., Chen, J., Wang, D. Shear Stress Analysis and Crack Prevention Measures for a Concrete-Face Rockfill Dam, Advanced Construction of a First-Stage Face Slab, and a First-Stage Face Slab in Advanced Reservoir Water Storage. *Advances in Civil Engineering*. 2018. 2951962. <https://doi.org/10.1155/2018/2951962>
9. Xavier, L.V., Albertoni, S.C., Pereira R.F., Antunes J. Campos Novos dam during second impounding. *The International Journal on Hydropower & Dams*. 2008. No. 15. Pp. 53–58.
10. Song, W.J., Sun, Y., Li, L., Wang, Y. Cause analysis and treatment of 1st phase slab cracking of Shuibuya CFRD. *Journal of Hydroelectric Engineering*. 2008. Vol. 27. No. 3. Pp. 33–37.
11. Scuero, A.M., Vaschetti, G.L. Underwater repair of a 113 m high CFRD with a PVC geomembrane: Turimiquire Managing Dams: Challenges in a Time of Change. *Proceedings of the 16th Conference of the British Dam Society*. 2010. Pp. 474–486.

12. Arici, Y. Investigation of the cracking of CFRD face plates. *Computers and Geotechnics*. 2011. No. 38. Pp. 905–916. DOI:10.1016/j.compgeo.2011.06.004.
13. Sainov, M.P. Osobennosti raschetov napriazhenno-deformirovannogo sostoianiia kamennykh plotin s zhelezobetonnymi ekranami [Features of the calculations of the stress-strain state of rockfill dams with reinforced concrete faces]. *Vestnik MGSU [Proceedings of Moscow State University of Civil Engineering]*. 2006. No. 2. Pp. 78–86
14. Zhang, B., Wang, J.G., and Shi, R. Time-dependent deformation in high concrete-faced rockfill dam and separation between concrete face slab and cushion layer. *Computers and Geotechnics*. 2004. No. 31. Pp. 559–573. DOI: 10.1016/j.compgeo.2004.07.004
15. Escobar, C.M., Posada, A.M. Recent Experience on Design, Construction and Performance of CFRD Dam. *International Conference on Case Histories in Geotechnical Engineering*. 2008. 9. <http://scholarsmine.mst.edu/icchge/6icchge/session11b/9>
16. Sun, D., Zhang, G., Wang, K., Yao, H. 3D finite element analysis on a 270m rockfill dam based on Duncan-Chang E-B model. *Advanced Materials Research*. 2011. Pp. 287–290, 1213–1216.
17. Arici, Y. Behaviour of the reinforced concrete face slabs of concrete faced rockfill dams during impounding. *Structural Infrastruct. Engineering*. 2013. No. 9. Pp. 877–890. DOI: 10.1080/15732479.2011.631111
18. Silva da, A.F., Assis de, A.P., Farias de, M.M., Neto, M.P.C. Three-Dimensional Analyses of Concrete Face Rockfill Dams: Barra Grande Case Study. *Electronic Journal of Geotechnical Engineering*. 2015. Vol. 20. Bund 14. Pp. 6407–6426
19. Zhu, Y., Lu, L. Nonlinear Static Analysis of Shuibuya Dam in China – World's Highest CFRD. *Electronic Journal of Geotechnical Engineering*. 2016. Vol. 21. Bund 04. Pp. 1527–1537
20. Zhou, M.-Z., Zhang B., Jie Y. Numerical simulation of soft longitudinal joints in concrete-faced rockfill dam. *Soils and Foundations*. 2016. No. 56(3). Pp. 379–390. DOI: 10.1016/j.sandf.2016.04.005.
21. Sainov, M.P. Impact of dam site configuration on 3D stress-strain state of concrete faced rockfill dam. *Magazine of Civil Engineering*. 2016. No. 3. Pp. 16–39. doi: 10.5862/MCE.63.2
22. Ren, Q., Li, G., Wei, K. Numerical simulation and operation characteristics analysis of folded line concrete face rockfill dam: case study of Yimeng Pumped storage power station. *IOP Conf. Series: Earth and Environmental Science* 304 (2019) 042042. doi:10.1088/1755-1315/304/4/042042
23. Liu, S.-H., Sun, Y., Shen, C.-M., Yin, Z.-Y. Practical nonlinear constitutive model for rockfill materials with application to rockfill dam. *Computers and Geotechnics*. 2020. 119. 103383. DOI: 10.1016/j.compgeo.2019.103383.
24. Soroka, V.B., Sainov, M.P., Korolev, D.V. Concrete-faced rockfill dams: experience in study of stress-strain state. *Vestnik MGSU [Proceedings of Moscow State University of Civil Engineering]*. 2019. 14:2:207-224. DOI:10.22227/1997-0935.2019.2.207-224 (rus.)
25. Marques Filho, P., De Pinto, N.L.S. CFRD dam characteristics learned from experience. *International Journal on Hydropower and Dams*. 2005. No. 12(1). Pp. 72–76.
26. Peng, C., Guo D., Wang Q., Lu, Y. Application of extrusion-sidewall technology to the project of rock fill dam with face slab. *Rock and Soil Mechanics*. 2008. Vol. 29. Pp. 201–203.

Contacts:

Mikhail Sainov, mp_sainov@mail.ru

© Sainov, M.P., 2020



DOI: 10.34910/MCE.101.14

Integration of digital twin and BIM technologies within factories of the future

V.L. Badenko^a, N.S. Bolshakov^{*a}, E.B. Tishchenko^b, A.A. Fedotov^a, A.C. Celani^c, V.K. Yadykin^a

^a Peter the Great St. Petersburg Polytechnic University, St. Petersburg, Russia

^b Faculty of Economics of Moscow State University, Moscow, Russia Federation

^c Architecture Built Environment and Construction Engineering dept Politecnico di Milano, Milano, Italia

* E-mail: nikolaybolshakov7@gmail.com

Keywords: building information modelling, BIM, operation and maintenance, digital twin, digital asset, Industry 4.0, facility management.

Abstract. With the development of information technologies for industrial plants, more and more tools for digital design, creation and operation of industrial facilities are emerged. In particular, significant success in development of Building Information Modeling (BIM) and Digital Twin technologies (DT) should be noted, which act as tools for digital transformation and representation for construction and production technologies respectively. In this regard, in this article, the principles and methods of integrating BIM and DT technologies within the framework of the so-called “Factories of the Future” (FoF) are formulated. Wherein the physical twin of FoF includes both production technologies and production infrastructure with buildings, structures and systems included in it, while particular attention is given to Operation and Maintenances (O&M) stage of object lifecycle which is less developed in comparison with design and creation stages. In addition, this paper also considers the role of systems information modeling (SIM) in such objects. Moreover, the concept of “digital asset”, closely related to the FoF, is examined and semantically analyzed, especially from information ownership point of view. The features of convergence of BIM and DT technologies are analyzed, and the levels of development of these technologies are compared. Finally, the directions of further research in this interdisciplinary branch of researches and development are formulated.

1. Introduction

The Industrial Revolution, Industry 4.0, is determined by the comprehensive implementation of digital technologies and is associated with the urgent need to find an adequate answer to current challenges, which are caused by the need to ensure short timelines for the development of new products, individual product settings for the consumer (customization), and production flexibility, decentralization of management and effective cooperation, as well as resource savings [1–4]. The development of technology in Industry 4.0 has led to the emergence of the concept of a digital Factory of the Future (FoF) as a system of integrated technological solutions that provide the shortest time to design and manufacture globally competitive next-generation products. This system supports the entire production lifecycle from the research and planning stage, when the basic principles of the product are formulated, and ending with the creation of a Digital Mock-Up (DMU) [5], a Smart Digital Twin (SDT) [6], manufacture of a prototype or small series (“paperless production”, “everything digital”) and its further development – the concept of smart and virtual factories [7].

The concept of the FoF usually includes three elements with relevant information technologies: production infrastructure, technological equipment and the product, and the technology of digital twins (Digital Twin – DT) is thus decisive for indicating inclusion in Industry 4.0 [8, 9]. While DT technology refers to the product and technological equipment, Building Information Modelling (BIM) technology provides digitalization of the manufacturing infrastructure of high-tech industry, including buildings and facilities [10–13]. So, for example, in order to optimize the trajectories of the equipment and staff, during the planning and modeling of the FoF, it is necessary to use a navigation environment created on the basis of the actual (as-is) BIM model, which determines the parameters and restrictions of movement for people, as well as autonomous robots [14,

Badenko, V.L., Bolshakov, N.S., Tishchenko, E.B., Fedotov, A.A., Celani, A.C., Yadykin, V.K. Integration of Digital Twin and BIM Technologies within Factories of the Future. Magazine of Civil Engineering. 2020. 101(1). Article No. 10114 DOI: 10.34910/MCE.101.14



15]. Consequently, BIM and DT technologies become key aspects in FoF especially in O&M stage of object lifecycle and LCC (lifecycle cost).

The necessity to establish a close relationship between the key information technologies of the FoF, first of all DT and BIM, is determined primarily by the fact that BIM models contain detailed information about three-dimensional geometry of the FoF facilities and the appropriate rich semantics of structure elements and all engineering networks in buildings where FoF are located, as well as detailed information on the functioning of the infrastructure supporting the production process, which is based on DT [13]. Therefore, the issue regarding the role and place of the concept of FoF, including DT and BIM technologies, in the formation of production assets, including digital assets, is actively discussed by the scientific community and business, but which, in our opinion, has not yet been sufficiently developed [16].

Digital technologies in industries, such as construction [17–19] and mechanical engineering [20–22], despite their close connection, developed in parallel and often without interconnection [23]. At present, in our opinion, the lack of an adequate concept of integration of DT technology with BIM technologies significantly slows down progress in research and development for digital, smart and virtual factories, production, etc. within Industry 4.0. Nevertheless, the scientific community predicts that the integration of BIM and DT technologies that are intended for digital representation of different objects, but which are related to parts of the same physical asset (and, as a result, digital asset) that make up the FoF, is inevitable [2, 4, 8, 10, 21, 22, 24]. Therefore, it is necessary to develop the basic principles of BIM and DT technologies integration, the absence of which impedes the development of digital technologies related to the FoF and does not provide effective coordination and unification of the relevant technical and economic aspects. Thus, we can formulate the thesis that the successful implementation of the concepts of Industry 4.0 as part of the development of advanced production technologies requires research and development in the field of integration of BIM and DT technologies based on the principles to be developed.

The practical implementation of DT technology is restrained by existence of a number of problems throughout the entire lifecycle of the corresponding production activity. Primarily these problems include lack of clear methodological foundations for determining the resulting technological and economic benefits of transformation based on DT, the difficulties in the technical implementation of DT technologies in different industries and various levels of reliability of the results obtained from different case studies of DT implementation [8, 6, 22–24]. At the same time, while there is a certain number of publications presenting research results on possible ways to solve the problems mentioned above [19–28], there are no publications which discuss problems related to the ownership of data and information in DT technologies, as well as integration between virtual objects described by DT technologies. These two problems are only mentioned but not analyzed in publications. Accordingly, the question of integrating DT with information technologies outside it, like BIM, remains unsolved and is also not considered in publications. Therefore, the study of the principles and methods of integrating DT and BIM technologies within the framework of the FoF concept, as well as assessing the economic and technological benefits of convergence of these technologies in the framework of introducing new production technologies, is an urgent task, which is considered in this article. One of the key provisions of digital twin technology is to provide bi-directional connection between a real physical object and a virtual object - its digital twin [9]. Therefore, when developing the principles of BIM and DT integration within the framework of the FoF, two-way information links between the production facility, technological equipment, engineering infrastructure and their virtual digital prototypes, including DT and BIM models, are investigated.

It should also be noted that when introducing BIM-technologies in industry, many problems are associated with the “digitalization” of existing objects, but not new ones, for which suit BIM models can theoretically be created, that initially take into account the future connection with the DTs of the manufactured product, technological equipment and production facility generally on exploitation stage of life cycle [29, 30]. The main technological difficulties in the “digitalization” of existing buildings and facilities are related to the need to reduce the complexity of obtaining initial reliable information for element recognition and filling the as-is BIM database, including the integration of attribute information in BIM, as well as post-processing often hidden and distorted structural and complex semantic information about the object [31]. Studies related to digitalization of asset management also show insufficient integration of BIM technologies and building management systems, including updating asset information and setting up bidirectional data exchange between a physical and virtual object [16, 32–34].

Thus, the objective of this article is to study the ways of integrating DT and BIM technologies, as well as developing appropriate principles and methods, assessing the effectiveness of the interpenetration of these technologies in the framework of FoF forming and solving the problems of introducing advanced production technologies. We emphasize once again that the interaction of DT and BIM technologies is further considered in the context of FoF, since they are objects that contain both production technology (DT) and appropriate production infrastructure (BIM). At the same time, the introduction of the integration of DT and BIM technologies at advanced production facilities will be the driver of FoF development.

2. Methods

2.1. Bridging gaps regarding effective integration of BIM and DT technologies

As already stated, the concept of the FoF is considered as systems of complex technological solutions that provide the shortest possible time for the design and production of globally competitive products of a new generation and implies the presence of three stages (technologies): digital factories, smart factories, virtual factories (Fig. 1) [35, 36]. Moreover, the success of the introduction of these technologies in the high-tech industry, in particular in the engineering industry, is associated primarily with the systematic use of DT technology in the framework of FoF [37–39].

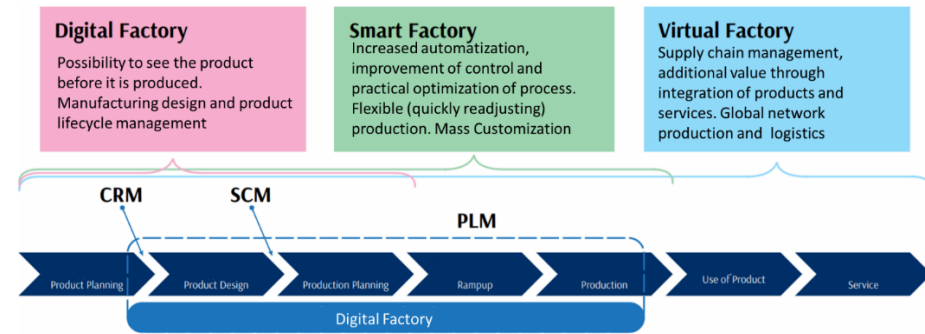


Figure 1. FoF: CRM – Customer Relationship Management; SCM – Supply Chain Management; PLM – Product Lifecycle Management [35].

It should be noted that in industrial and scientific sources, the definitions of DT differ in a certain variety [40–42]. In the framework of this work, we will use the following definition: DT is a digital representation of the behavior in various operating conditions of real physical objects – materials, products, systems, machines, structures, equipment, cyberphysical systems, including technological and production processes, etc., which can only be described by a family of complex multidisciplinary mathematical models, including 3D non-stationary nonlinear partial differential equations with a high level of adequacy to real materials, objects, and physical and mechanical processes [37, 43]. Moreover, when we talk about products, we will use the concept of a “first level digital twin” (DT1), while in case of technological processes we will use definition “second level digital twin” (DT2). Integration of DT1 and DT2 in general refers to Smart Digital Twin (SDT) [37].

The definition of BIM technology, which is presented in the US standards, has a formulation similar to DT: building information modeling (BIM) is a digital representation of the physical and functional characteristics of an object; BIM is a common knowledge resource for obtaining information about an object, which serves as a reliable basis for decision-making throughout the entire lifecycle of an object, which is defined as existing from the earliest concept to demolition [44]. There are a fairly large number of publications that analyze the relationship between the two concepts – DT and BIM [45–49]. Like DT, BIM is a digital representation technology for real physical objects. In both definitions, a high adequacy of reality is noted, in the case of BIM this is incorporated in the reference to “a reliable basis for decision-making”. Both definitions focus not on the static representation of the object, but on its dynamic change over time in the context of the lifecycle. However, in the case of the DT, we are talking about a deeper study of the digitalization of the corresponding products and processes than in BIM.

Definition of the concept of the FoF [35] (Fig. 1) primarily focuses on the product and the technological processes of its production, without taking into account the fact that respective real factory is located within the framework of some production infrastructure that ensures its functioning [50, 51]. Moreover, in the framework of FoF on the part of the product a technology such as DT has already been developed to a large extent. Such approach is based on the definition and decomposition of the parameters and characteristics of the object being developed by DT technology, using the formation of the matrix of targets and resource constraints, including cost constraints, reaches tens of thousands of units [52]. A similar technology used in construction (BIM) is somewhat behind [16, 22, 53]. In our opinion, there are two reasons that further determine how to overcome the difficulties of integrating BIM and DT. Firstly, the dimensions of the construction object, buildings and structures are usually more significant than the objects in mechanical engineering, and the construction of each object is normally unique, only partially implying any kind of mass production. Secondly, until now, BIM technology has been intended to solve its own problems of construction and operation of a production facility – a building and engineering infrastructure, and did not pay due attention to interaction with technological equipment and, moreover, the product manufactured on it, which are “external” in relation to the BIM environment. Consequently, on the way to the development and creation of FoF, there is a necessity to integrate information modeling of buildings and structures (production infrastructure) into the digitalization technology of the entire production process, that is, first of all means to determine the ways and methods of integrating BIM and DT technologies. Thus, it can be stated that DT and BIM technologies can be integrated, as they are both digital and describe different elements of the same object – FoF.

2.2. Integration of BIM and DT

The requirements for the development of the FoF set the trend for new production technologies, and the adaptability of the factories to such new requirements using the integrated DT and BIM technologies will be their competitive advantage. The design, construction and operation of FoF should take into account the necessity in flexible and quick restructuring of production technologies, based on changes in consumer requirements. At the same time, as shown in Fig. 2, BIM and DT technologies are the basic elements of the FoF, while having both areas of contact (corresponding to the physical intersection of production and infrastructure, for example, at the level of supply of water or electricity), and their own elements, not affecting the other technology (for example, premises not used in production in BIM models or modeling of physical processes inside a DT of technological equipment that do not directly affect the external construction environment). We propose to consider DT and BIM technologies in conjunction, without perceiving the BIM technology as a service technology that lags behind the DT technology in terms of development [33], due to the fact that until now they have developed in parallel and solved problems from different spheres: construction and mechanical engineering.

An integral element of the FoF is also a management system, indicated in the Fig. 1 as SIM (System Information Modeling) technology. By SIM technology, we understand the support of the process of digital modeling of a complex connected system, which represents the general information resource, forming a reliable knowledge base [54]. It is important to note that in this situation we use the concept of SIM but not concept of PLM systems (Product Lifecycle Management - product lifecycle management systems) which is close to it, since we assume that SIM includes transformation management systems for both products, technologies, and production infrastructure that are all the objects of management. We can say that SIM takes into account the transformation of PLM depending on changes in technology, adapting to these changes. The issue of including information management systems in the concept of FoF is beyond the scope of this article and requires a separate careful consideration, since, as mentioned above, the problem of ownership and management of information during the lifecycle of a DT object is one of the main obstacles to the development of digital twins. Within the FoF, we distinguish these three technologies that should work in close integration, not excluding the subsequent inclusion of others technology (Fig. 2).

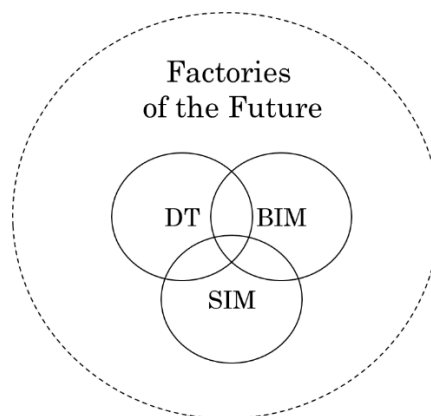


Figure 2. BIM, DT, and SIM technologies in FoF.

The methods for integrating BIM and DT technologies in the framework of FoF should be based on the following points presented below.

Currently, DT technologies are more developed in the sense of digitalization and creation of virtual prototypes of real objects, due to the fact that the objects that are represented by DT are products, which are more clearly defined and specific, for example, engineering products (engine parts, machine tools, etc.) or related technological processes (welding, casting, etc.).

Technological equipment should always be provided with engineering infrastructure, which is responsible for the operation of equipment during its entire lifecycle, including repair, maintenance and other types of work. At the same time, the management system for technological equipment and engineering infrastructure should be interconnected, and should be part of common management system of the FoF. The operation of such management systems should provide optimal operating conditions for both technological equipment and engineering infrastructure, in compliance with all safety requirements. To meet this requirement, it is necessary to model the joint work of all elements of the FoF: engineering infrastructure, technological equipment, products manufactured by the factory, and management system of the FoF.

Integration method of BIM and DT technologies in the framework of FoF should use one of the key and integral elements of existing DT technology which is a multi-level matrix of the targets and resource constraints (time, financial, technological, manufacturing, etc.) for the product as a whole, as well as for all components

and details in separate [9, 55]. Such matrices usually are containing tens of thousands elements. Fig. 3 shows the process of forming such a matrix, which is formed for the FoF.

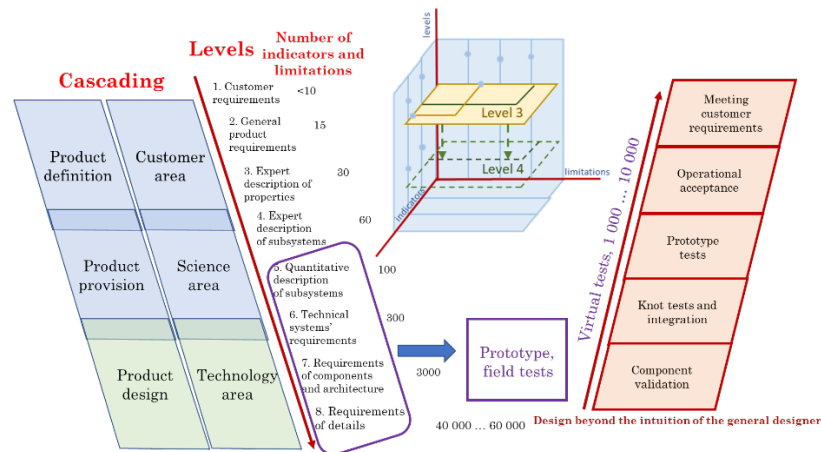


Figure 3. Formation of a matrix of target indicators and resource constraints [9].

The requirements of the upper level of the multi-level matrix of targets and resource constraints for the FoF (Fig. 2) are determined by the customer. These are restrictions on product quality, cost, safety, resource, finance, service, economic costs, and so on. Based on the requirements of the upper level, the next blocks are formed according to the type of tasks being solved. Based on all the data obtained for each block, an appropriate set of models of real objects and physical processes is created. At the same time, the validation of models based on field tests (with real objects) as well as the performance of tens of thousands of virtual tests for each component and the entire system as a whole are also an integral element in creating a highly adequate digital models. Due to its high adequacy, such a digital models allows to significantly approach the condition of real object to satisfy the requirements formed earlier in the constraint matrix (Fig. 3) – it provides a difference between the results of virtual tests and full-scale field tests within $\pm 5\%$.

The same approach, although in more limited amounts, is used in BIM technology. Virtual tests are carried out at all levels of the object: material-element-construction-product [55–60]. Validation can be carried out both on the basis of cataloged data, and on the basis of tests of building materials and individual elements of buildings and structures and building parts – columns, lintels, etc. during the construction process. The transition to full-scale testing of the entire construction object, as it is discussed with most products developed using the DT technology (for example, cars and aircraft), is possible only with the start of operation of the construction object, and therefore the validation of the BIM model of the building or structure is postponed for the period of Operation and Maintenance (O&M). If we consider this situation, according to the theory of DT, based on the accumulated experience of the DT technology, it can be assumed that the driver of the development of BIM technologies for construction projects can be the accumulation of a field test database during construction and operation, the use of smart sensors and the intellectual processing and accumulation of this data, followed by the usage of their Digital Shadows (DS) and Big Data and for taking into account these refinements in the design, construction and operation of subsequent facilities.

It is important to note that, aimed at the digital representation of a real physical object, similar to DT technology, BIM technology focuses more on the work of users than on the object itself [61]. This remark is clearly demonstrated by the example of the analysis of information flows from the virtual world to the real world (virtual-to-physical) and from physical to real (physical-to-virtual), which are considered in detail by the founder of the concept of DT Greaves [62–64]. At the same time, if such a data flow is not organized than information model can be referred only as the Digital Model (DM), if the physical-to-virtual flow is automated than DM becomes a Digital Shadow (DS). If both flows are automated, then we can start talking about a Digital Twin with the full on-line bi-directional connection between virtual and physical objects. It means that DT is updated based on the readings of the sensors, to exactly match the real physical state of the object. It is sometimes noted that virtual-to-physical communications at the DT level are not given enough attention, although this is an important component on the basis of which a digital object can also act as a control element of a physical object, in other words, a change in the state of a physical object directly leads to a change in the state of the digital (virtual) object and vice versa [28]. For BIM, such flows of information are also relevant, given that this virtual-to-physical flow is also controlled by the Facility Manager (FM), which reveals the essence of BIM user orientation to a greater extent than usually in DT technology (Fig. 4).

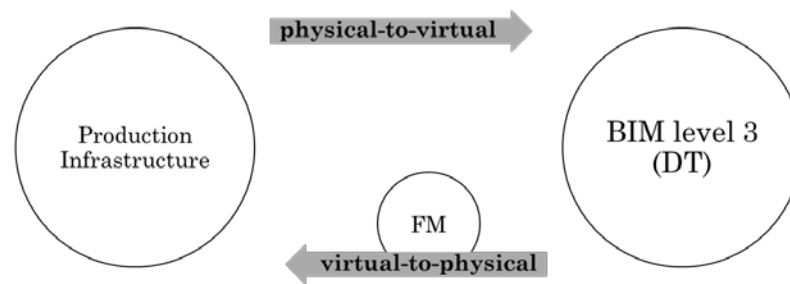


Figure 4. Bidirectionality of information flows between the real and virtual worlds using the example of production infrastructure.

The BIM level indicated in Fig. 4 corresponds to the most complete degree of development of the BIM model in accordance with the building information modeling manual [65]. The previous levels of BIM-0, BIM-1, BIM-2 are considered, respectively, as a two-dimensional non-parameterized model, three-dimensional non-parameterized model, three-dimensional parameterized model without feedback. Accordingly, the third level of BIM differs from the second by adding feedback from the virtual model to the physical (similar to the step from DS to DT). Determining the relationships in the BIM and DT classifications is one of the tools for their integration. In [61], a parallel is drawn identically between the first second and third levels of BIM and, accordingly, the digital model, digital shadow and digital twin [28], which in our opinion is very important for the development of technologies for the FoF. This proposed approach suggests that despite the different development paths of BIM and DT technologies, there are points of contact in the classification and formulation of development levels, since ultimately both technologies are aimed at forming a digital (virtual) analogue of a physical object from the real world and establishing links between real and physical object (Table 1). Here real and virtual objects are indicated by the letters R and V. It is important to note that only a few authors [61] delve into the interconnection of levels, not limited to only superficial interconnections between the technologies.

Table 1. The equivalents of the levels of development of BIM and DT technologies.

Level	Digital Twin (DT) technology	Building Information Modelling (BIM) technology
2D CAD drawings		BIM-level 0
3D	Digital Model	BIM-level 1
3D+R→V	Digital Shadow	BIM-level 2
3D+R↔V	Digital Twin	BIM-level 3

Fig. 5 schematically shows the transformation on the path from digital to virtual factories, taking into account the development of System Information Modeling (SIM) and Enterprise Resource Planning (ERP). Here we assume that at the digital factory level we are talking about creating a DT of only the first level (DT1), while omitting DT of technological processes (DT2 – DT of second level). At the smart factory level, not only the introduction of a digital twin of technological processes (DT2) is assumed, which together with DT1 forms a smart digital twin of the 1st level (SDT1), but also the establishment of feedback from a physical twin to digital twin (DS formation). At the same time, information modeling of the production infrastructure of the FoF (BIM) is gaining specific relevance. At the virtual factory level, in the first place, a system information modeling (SIM) is introduced and the degree of development of DT and BIM is increasing also. In this case, the terminology and concepts of DT1, DT2, SDT, DS are used according to the approach of the competence center of the NTI SPbPU “New Production Technologies” [9].

Obviously, with the growing demand for customized products, it is becoming more important to quickly readjust not only machines and elements of production, but also buildings and their engineering infrastructures. Therefore, when moving to the virtual factory stage, enterprise management information systems become especially important, which are impossible to realize without integration of information models of production elements (DT) and construction objects (BIM). It is important to note that while BIM regulations has already been introduced in some countries, for example in the UK [66], in terms of DT technology and the relationship between BIM and DT, there are currently no such regulatory documents.

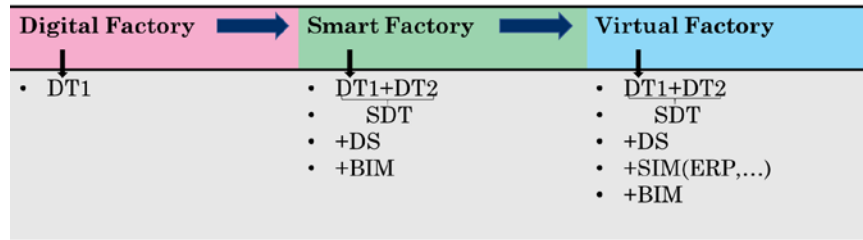


Figure 5. BIM technologies and FoF. Based on [35] with the addition of information modeling of production infrastructure – BIM.

A key factor in managing an asset such as a FoF is time. The construction object, if it is designed taking into account the possibility of subsequent reprofiling of production, change of layouts, etc., is more adaptive and flexible due to the reduction of the time of reconfiguration, which will be one of the key competitive advantages of the FoF, focused on quickly changing consumer needs. The importance of such approaches (adaptability and flexibility) is currently noted not only in the field of mechanical engineering [26–28, 67–69], but also in architecture, namely in the so-called “adaptive architecture” [70].

Due to the fact that up to the present moment BIM and DT technologies have been developing in parallel, at the moment there is no definite conceptual approach to their relationship. The relevance of this problem is growing proportionally to the digitalization of industry and the need for FoF, because, firstly, construction and production facilities are often physically inextricably linked, and secondly, the development of as-built BIM (corresponding the object in initial point in time of exploitation), as-designed BIM (corresponding planned object) and as-is BIM (corresponding actual state of the object during O&M stage) technologies is possible due to the transfer of successful experience from the field of engineering to BIM technology, in other words benchmarking from DT to BIM.

In case of the locating of the production (and, respective digital twins) within a certain production infrastructure (BIM-models respectively), there is the so-called “information silo”, which the founder of the concept of DT Greaves generally defines as the main barrier to the implementation of digital twin technology [62–64]. This means that in real situations one information system is isolated from another, although in reality their physical twins are inextricably linked. Moreover, in accordance with the theory of digital twins, in addition to the already mentioned terms DT and DS, the concept of a digital representation of some real physical component (Digital Instance – DI), created on the basis of a Digital Prototype (DP), is used. Also a set of DI, included in the digital representation of an object is called Digital Aggregate (DA) [62]. The listed technologies are located within the framework of some Digital Environment (DE) [61], which is a digital representation of the real physical environment within which the Physical Twin (PT) is operated. The BIM model for an existing facility, built on the basis of the buildings and structures corresponding to it with engineering systems included in their composition, should be considered as a tool for describing the physical environment based on data entering the virtual BIM environment, including those obtained through sensor systems. However, some of the principles of DT can be transferred to BIM modeling, nevertheless, the production infrastructure and its BIM model should be considered separately in the form of physical and digital objects, also existing within the physical and digital environments, and capable of describing the physical environment according to the principle of digital shadow and affect the physical environment according to the principle of a DT. Both in the DT and in the information model of the building, attention should be paid to all stages of the lifecycle, including the last stage - demolition [71].

3. Results and Discussion

3.1. A method to integrate BIM and DT technologies for FoF

It is obvious that in the modern world the use of 2D CAD technologies (zero-level BIM) is insufficient for organizing the process of managing construction objects [72]. BIM technologies of the second and third levels (with a unidirectional or bidirectional flow of information between the physical and virtual objects) are gradually beginning to be introduced into Facility Management (FM) practice. In the previous section, we considered the BIM classification proposed in the manual on information modeling [65]. Another common classification in the literature of BIM [15, 16, 44, 48, 59] is the division into as-designed BIM, as-built BIM (reflecting a really built object during operation) and as-is BIM (updated during the operation of the facility).

Fig. 6 shows the relationship between BIM and DT, characterizing the method that they are integrated throughout the lifecycle of FoF. The integration method involves the formation of a matrix of target indicators and resource constraints (Fig. 3) of the entire FoF as a whole, including production infrastructure, technological equipment, product and information management system. At the design and construction stage, 2D drawings and non-parameterized 3D models can be used, presented in Fig. 7 under the numbers 1 and 2. Moreover, if the designed digital BIM model is updated according to the actual construction data, then we are talking about state 3, meaning digital shadow. If, based on the results of the data obtained, adjustments are introduced into

the information model that affect the real processes of building a physical asset, we can talk about DT state which is numbered 4. The real and virtual objects are denoted by the letters R and V, respectively. At the time “0” of the start of operation, we are talking about a static as-built BIM model (state 5). The concept of as-built includes the correspondence of the model to the real world (according to the results of sensors, measurements, etc.).

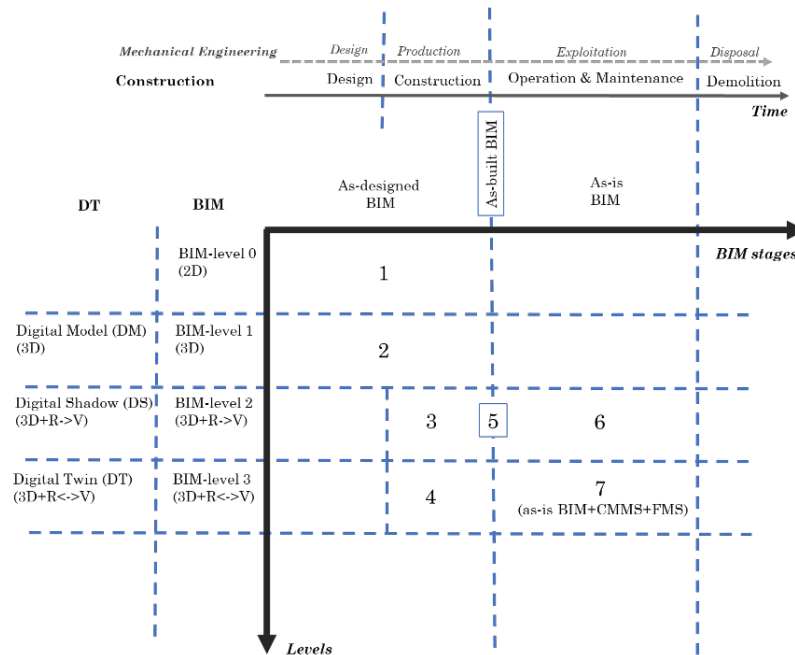


Figure 6. The method to integrate BIM and DT within the FoF: the relationship of BIM and DT levels throughout the lifecycle. (CMMS – Computerized Maintenance Management System, FMS – Facility Management System).

Since the start of operation, provided that the digital model of asset by which we understand the integrated set of information models of asset parts is updated based on the readings of the sensors, we can talk about the digital shadow of a physical construction object (state 6 in Fig.6). If, in this case, not only the conversion of objects and processes into digital form takes place, but decisions are also generated and made about the impact on the physical object based on virtual data, then we can talk about a digital asset model – a DT of asset (state 7 in Fig. 6).

The requirements for the technology of virtual factories are formed on the basis of the manufactured product, which has a minimum lifecycle in the product-production-production infrastructure chain. Therefore, as it has already been mentioned just as production must be flexible and adaptive to changes in the manufactured product, so production infrastructure must be flexible and adaptive to changing and readjusting production. But on the other hand, the production infrastructure, being the most long-lived component of the FoF, having its own lifecycle of tens of years, should be adaptive not only to transformations within the current degree of production development, but also to subsequent new technologies that will inevitably arise on the path of production infrastructure lifecycle.

It is important to note that in the current degree of development of the Architecture, Engineering & Construction (AEC) industry in case of using BIM technology at the design stage, usually, BIM technology is not implemented in the subsequent stages of the lifecycle [31]. According to this fact, the two abscissas indicated in Fig. 6 are not necessarily identically mapped onto each other. If at some stage of the lifecycle, whether it be construction or operation, the use of the updated BIM-model disappears, from that moment it becomes incorrect to refer to digital twins. Then at this moment, the owner's assets pass into a material state only, the dualism of real and virtual also dissolves, which leads to the loss of a digital asset, and therefore a loss of tool to reduce costs (time, material, etc.). At the moment, in the absence of ubiquitous digitalization and the application of conservative methods of cost management, the need for information modeling over the lifecycle of an object is not so tangible in terms of competition, but in the future, with the emergence of modern digital cost management mechanisms, the introduction of technologies such as BIM and DT will be one of the key competitive advantages [73]. Nevertheless, at the moment, an as-designed BIM model that does not meet the requirements of a digital twin should be used in some real estate management tasks at the operational stage, such as for example space planning, provided that these tasks do not need an adequate display of physical objects and processes in numbers [74, 75]. The need to use information modeling over the lifecycle of an object so far is not so tangible from the point of view of competition, but in the future, with the advent of modern digital cost management mechanisms, the introduction of technologies such as BIM and DT will be one of the key competitive advantages [73]. Nevertheless, at the moment, an as-designed BIM model that

does not meet the requirements of a digital twin can be used in some real estate management tasks at the operational stage, such as for example space planning, in case these tasks do not need an adequate display of physical objects and processes in digital way [74, 75].

In accordance with the theory of digital twins, on the basis of SDT it is possible to create digital prototype [62–64]. This is not yet a DT, as it does not have its own real physical twin (PT). We can draw an analogy that in construction, the as-designed BIM model of the building acts as DP. DI (digital instance) at the time “0” of operation in the construction industry is presented as an as-built BIM model. Subsequently, during O&M stage, the DI corresponds to as-is BIM.

According to the British BIM standard [76], all operating processes can be included in the Computerized Maintenance Management System (CMMS) and Facility Management System (FMS). Together with the BIM model of the object, they form the digital asset management information model Asset Information Management model (AIM), as shown in Fig. 7.

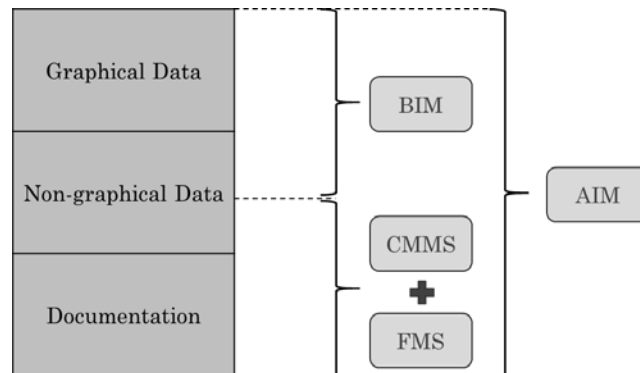


Figure 7. Digital asset management model (SDT of the first level for construction project).

As can be seen from Fig. 7, the object’s lifecycle management concepts are developed, but at the same time they are considered by experts in asset management and, accordingly, solve asset management tasks. If in civil engineering projects or in commercial facilities this approach is sufficient to solve their own problems, then in case of industrial facilities there is a need to expand these concepts and link them with digital twins in the context of FoF.

If we return from the theoretical idea that the BIM model is capable of being updated at any moment during the lifecycle, including consideration and digitalization of changes in site work execution plans, operation, repair, to reality, then we can say that the continuity of the Digital Thread (this definition is borrowed from DT theory), linking all the stages of development of information model, have not been realized in construction sector yet. The Digital Thread of the construction object will not be continuous until the process of “digital certification” is established. The gap occurs at the place of formation of the as-built BIM model of the building, since in the digital field it is not the result of digital processes, but is obtained upon the from measurements and digitalization of actually built models. Nevertheless, in this situation, based on the results of SDT (following the achievements of mechanical engineering), in construction, it becomes possible to determine the necessary places for installing sensors for measuring indicators and the formation of Smart Big Data about the object. Changing a Smart Digital Shadow (SDS) that is optimized and highly adequate [77], reflected in as-is BIM model is actually a virtual tests of the construction site as a whole, which was impossible at the design stage. The most effective solution in this case is to create a public library of data taken from sensors in order to increase the level of adequacy and intelligence of the SDTn digital building twins during the design period, which means creating more intelligent DP as-designed models.

In other words, SDT, on the basis of which more and more intelligent DPs are created, on the basis of which DIs will be built, which will be combined into DAs, will be improved not only by the results of field tests of subsystems individually and virtual tests of systems and subsystems, but also due to DI changes during operation (using DS). If all such DI and DS are integrated into a common library of real-world scenarios, this will speed up the process of “clevering” SDTn of construction objects. As a result, the “learning by doing” approach will be implemented.

3.2. Digital Assets and Integration of BIM and DT Technologies

Minimization of time and errors during the readjustment of production are the main factors which represent major advantages of proposed approach and therefore must be taken into account when developing and operating the FoF. In our opinion management of these factors must be ensured by the integration of BIM and DT technologies, synchronized by data transmission formats and by time. It is the ability of quick operational interaction between BIM and DT, organized in digital environment, that allows to reduce time costs and minimize errors, which is an important competitive advantage.

Integration of BIM and DT technologies into a framework of single information model of the FoF allows to combine all the knowledge and competencies that are formed at key stages of the entire lifecycle: design, construction and operation. Thus, the information model of the FoF becomes a "digital asset", combining the knowledge base about the object. A digital asset, on one hand, must have integrity, which means to be an adequate representation of a unified physical object – the FoF, and on the other hand, have divisibility, which means that it must satisfy the requirement of sharing rights on information between participants of the object lifecycle. Integration of BIM and DT is a necessary condition for the integrity of the digital asset of the FoF in the form of an information model as a knowledge base accumulated by designers, builders and technologists. The integrity of such a digital asset implies a constant synchronization of information about the actual parameters of the FoF entities with their digital representations, as a result of which both the training of digital models and the prediction of the technical and technological parameters of the FoF throughout of their lifecycle take place.

Without a doubt the value of the digital asset can be generated through the introduction of BIM and DT technologies separately [6, 8, 11, 31, 44]. In addition to this fact their integration has multiplicativeness, which means that holistic integration of these technologies also forms the additional value for the FoF, since it is the degree of their consistency that determines how quickly and with which accuracy errors in the organization, readjustment and exploitation processes will be eliminated.

The issues of the right to own information, and in particular the issue of transferring ownership of information, the distribution of these rights among parties involved in changing and managing an object throughout its entire lifecycle, are the key issues in the theory of digital twins [61], and consequently in the theory of digital assets. If information model of production or production infrastructure is considered as an intangible resource of a company that can bring tangible benefits, for example, by reducing operating and time costs, we can consider this information model of the FoF actually as a virtual asset that has some material value [73].

Conceptually, the presence of material value in the information model was formulated by the founder of the theory of digital twins, Greaves [63], Fig. 8. In the figure, the green zone represents all the costs that are not dependent on the presence or absence of the information model, and the red and blue are additional costs in the case of absence or availability of an information model respectively. Accordingly, the introduction of information modeling technologies becomes justified at the moment when the cost of information becomes less than the totality of costs that must be incurred in the absence of this information. This issue should be considered from the point of view of added costs which a generated due to loss of information [78].

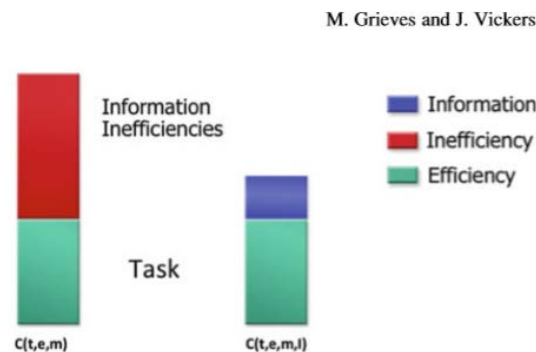


Figure 8. Information as an alternative to time, energy and material costs [63].

It is important to note that the "value of a digital asset" can be considered in two ways. On the one hand, this is the totality of all the costs spent on creating and transforming the information model over time, we denote it as C_1 , the blue zone in Fig. 8. Moreover, this value cannot be identified with the "value" of a digital asset, since on the other hand it is a tool for reducing costs (we denote their total cost as C_2 , the red zone in Fig. 8), the cost of which, to some extent, the information model goes over the barrier of the cost of all costs that were avoided due to the availability of info model and avoiding conservative methods of designing, creating and operating objects using for example CAD systems.

In addition to the conditions formulated by Greaves, under which the introduction of DT becomes profitable, we want to note that the "Information Inefficiencies" also includes the cost of errors and the absence of a quick solution to them that arise in the absence of DT, BIM and their proper integration. The ability to eliminate such errors along with time management is the key factor affecting the "value" of a digital asset.

An important further direction of research, therefore, is determining the impact of the availability and level of BIM and DT models on the value of an asset, as well as qualitative and quantitative assessment of the contribution of various participants in the creation and "operation" of this asset to determine the rights on a digital asset. In addition, it is important to consider the concept of "divisibility" of an asset and whether digital

and physical assets can have different owners. In this case, the digital asset acts as an integrator, accumulating the knowledge of the designers, manufacturers and operators of the facility. To solve the described issues, first of all, a legislatively regulated method for assessing the “value” of a digital asset is needed, which should be considered as value added in the knowledge economy.

3.3. *Current Implementations in the Market*

The principles and methods for integration of BIM and DT proposed in previous sections are reflected in some, as yet few, projects. Some of them are presented below. It should also be noted that in our opinion these projects would be more successful if they were based on the principles and methods presented here. Some aspects of integration of information technologies into O&M stage are present in the market, but most of the time they consider only partial tasks and do not reveal connection of information models and their different layers.

Actual reports of the representatives of industry on the Going Digital 2019 conference of Bentley company state that application of BIM in the reconstruction stage of several Lipetsk iron and steel factory components has shown significant monetary savings in 3D modelling case and up to 76 days reduction of reconstruction time for the components. Therefore, even initial attempts of implementing BIM in maintenance, which is not yet the digital twin has proved its efficiency.

Practical applications of BIM in facility management [79] reveal significant maintenance efficiency improvements and cost savings. One of the indicators in above mentioned study is search for information which was reduced by 30 %. Another indicator is the time spent locating specific defective components, researching data related to those components, and formulating a maintenance plan has been reduced by an estimated 50 %. Another case study on university campuses [80] has proved that integrating BIM in facility management increases the savings on electricity consumption. The topics of energy saving also have proved to be efficiently considered using lifecycle approach [81].

Spanish company ACCIONA announced the completion of a digital twin of one of the largest desalination plants in the Middle East (the city has not been disclosed) [82]. In the process of creating a digital twin, SIMIT software (Siemens) was used. This case includes:

- remote enterprise management;
- analysis and optimization of productivity, operational capabilities in real time;
- troubleshooting and analysis of possible failures before the launch of production systems;
- comparison of data in a digital system and data in a control system facilitates validation of operations and analysis of operational capabilities;
- integration with various technologies, such as virtual reality, augmented reality, the Internet of things, machine learning

ACCIONA digital twin consists of 2 elements: an engineering design system and a control system that allows you to solve production problems in real time. This system should be connected to BIM according to the report. Creating digital counterparts meets current challenges in the field of water management, where high productivity, process efficiency and speed of installation are of great importance - said Alejandro Bevide, Director of Digital Transformation and Management Systems. He also highlights the fact that the most complicated thing about DT is to create. Probably this is one of the major barriers in digitization of industry.

Currently Saint Petersburg Polytechnic University is also working on integrating DT solutions into ERP system according to actual requests from industry.

Another challenge in this case is that costs associated with training building information modeling personnel apart from the initial investment cost, sufficient time and human resources must be allocated for training building professionals to use BIM [83]

According to current state-of-the-art of the issues there are several gaps that remain unsolved due to the absence of complex concept approach which is discussed in this article. We consider approach which includes involvement of BIM & DT integration to be the tool to bridge existing gaps on the way to digitization of industrial assets.

4. *Conclusions*

This article is devoted to the study and development of principles and methods for integrating digital twin technologies and building information modeling in the context of the FoF. Convergence efficiency of BIM and DT is considered. The barriers to the integration of BIM and DT technologies are investigated and ways to overcome them are presented, based on the form of BIM and DT relation shown in Fig. 6.

Both BIM and DT technologies are informational, focusing on creating information models of physical objects and processes that are highly relevant to the real world, but at the same time they have been

developing in parallel in the fields of construction and mechanical engineering. In the context of future factories, BIM and DT refer to the same physical entity. The key difference between BIM and DT technologies is the degree of detail of information models, in particular, DT technology implies full digitalization of technological processes, as well as the presence of a bi-directional information flow between a real and a virtual object, and BIM technology in this sense is less developed. However, BIM technology in a number of countries, such as the United Kingdom, has gradually been consolidated in regulatory documents over the past ten years, which cannot be said about DT technologies. Thus, the following basic principles are proposed, on the basis of which the integration of BIM and DT technologies within the framework of the FoF should occur.

The first principle: the integration of BIM and DT technologies should ensure the design, construction and operation of FoF, taking into account the needs of production in the flexible restructuring of production technologies based on changes in consumer needs. In this case, specific implementations of the integration of BIM and DT technologies are formed on the basis of the manufactured product, which has a minimum lifecycle in the product-production-production infrastructure chain. Therefore, just as production must be flexible and adaptive to changes in the manufactured product, so production infrastructure must be flexible and adaptive to changing and rebuilding production. But on the other hand, production infrastructure, being the most long-lived component of the FoF, having a lifecycle of tens of years, it should be adaptable not only to transformations within the framework of new production needs arising from the release of a new product with a different DT, but also to possible other new technologies that will inevitably arise along the path of the production infrastructure lifecycle.

The second principle: the integration of BIM and DT technologies should ensure the validation of “smart” models for the formation of a highly adequate digital model of the FoF based on both virtual and full-scale tests. This principle is based on the positive experience of digital twin technology, which is characterized by the performance of tens of thousands of virtual tests for each component (assembly, part, mechanism, interface, etc.), materials and the whole system. In the case of BIM technologies, there is experience in virtual tests to validate the model, but full-scale field tests are possible only at the level of a part or a separate system, while testing of the entire building or structure only possible during operation. In this regard, integration of BIM and DT technologies requires the accumulation of experience in the construction and operation of complex technical objects and the filling of a field test database using sensors and digital shadow principles (information flow from a real object to a virtual one), as well as maintaining the relevance of the information model throughout the lifecycle and maintaining the continuity of the Digital thread.

The third principle: in the aggregate, BIM, DT, SIM, and other technologies are designed to form a digital asset – a digital resource of the owner of a physical asset that brings (or can bring, when used correctly) economic benefits throughout the lifecycle of an object in the form of reduced transaction costs, time and material.

Based on the stated principles, the method for integrating DT and BIM technologies in the context of FoF has been formed. The integration method involves the formation of a matrix of target indicators and resource constraints (Fig. 3) of the whole FoF as a whole, including production infrastructure, technological equipment, product and information management system. A highly adequate to real world, tested and validated information model of the FoF should be created to reduce material and time operational costs. The model must support the flexibility and adaptability of the factory, reflecting the properties of objects and technological processes and be capable of influencing physical changes in the objects and processes of the factory throughout lifecycle. To create such model, it is necessary to follow the sequence of synchronous transition from level to level for the coordinated simplification/complication of virtual models created on the basis of BIM and DT technologies, shown in Fig. 7. Thus, since this study primarily addresses the issue of integrating BIM and DT technologies in the concept of FoF, an appropriate method should be based on the interaction points indicated in Fig. 7.

Analysis of the literature showed that the main barriers to the development of DT technology are related to the ownership of data and information in DT technologies and the integration between virtual objects described by DT. These are just some of the problems identified during the study, but other gaps in the development of digital twins are assumed; this article focuses primarily on researching and developing ways to integrate technologies. Therefore, the urgent direction of further research, based on the identified problem of data ownership, is the development of information management systems (SIM) for FoF. It is noteworthy that in the field of BIM-technologies, this particular issue (information ownership) is the key subject of discussion of currently emerging regulatory documents, such as ISO-19650, Part 3, associated with the operational phase of the BIM project and existing ones, such as ISO-19650, Part 1,2, associated with the design and construction stages.

Existing barrier related to the integration between virtual objects described by DT was partially considered in this article. In this case, the BIM model and the DT are considered as virtual objects, between which the so-called “information silo” arises. The actual direction of further research will be the study of technical ways of implementing the developed approaches. At the moment, in some cases, software is developing faster than the real industry representatives need such software. It is necessary to establish a

connection between the developed approaches and the real ways of introducing BIM and DT technologies in complex technical objects.

Transformation of a digital asset is a separate issue that requires careful consideration. In this article, only a preliminary definition and structure of a digital asset is given, but it is necessary to understand that a digital asset is a complex time-transforming resource that does not belong entirely to one person, but is distributed among all participants in the design, production, construction, operation and destruction or demolition of physical objects.

An important area of further research is the issue of ownership and distribution of rights in relation to a digital asset, its integrity and divisibility. The integration of information modeling into Future Factories reduces time and minimizes the errors associated with quick readjustment of production. Based on this, BIM and DT models, as well as their consistency, add "value" to the FoF, which means that it is necessary to consider a digital asset as an integrator of knowledge accumulated by all participants in the lifecycle of an object.

5. Acknowledgements

The research is partially funded by the Ministry of Science and Higher Education of the Russian Federation as part of World-class Research Center program: Advanced Digital Technologies (contract No. 075-15-2020-934 dated 17.11.2020).

References

- Lasi, H., Fettke, P., Kemper, H.G., Feld, T., Hoffmann, M. Industry 4.0. Business & information systems engineering. 2014. 64. Pp. 239–242. DOI: 10.1007/s12599-014-0334-4
- Frank, A.G., Dalenogare, L.S., Ayala, N.F. Industry 4.0 technologies: Implementation patterns in manufacturing companies. International Journal of Production Economics. 2019. 210. Pp. 15–26. DOI: 10.1016/j.ijpe.2019.01.004
- Xu, L.D., Duan, L. Big data for cyber physical systems in industry 4.0: a survey. Enterprise Information Systems. 2019. 132. Pp. 148–169. DOI: 10.1080/17517575.2018.1442934
- Borovkov, A.I., Shcherbina, L.A., Maruseva, V.M., Ryabov, Yu.A. Mirovaya tekhnologicheskaya povestka i globalnyye tendentsii razvitiya promyshlennosti v usloviyakh tsifrovoy ekonomiki [World technology agenda and global industrial development trends in the digital economy]. INNOVATsII. 2018. No. 12(242). Pp. 34–42. (rus)
- Zhang, H.Y., Li, J. Modeling method and application in digital mockup system towards mechanical product. Advanced Materials Research. 2013. Vol. 605. Pp. 604–608. DOI: 10.4028/www.scientific.net/AMR.605-607.604
- Lu, Y., Liu, C., Kevin, I., Wang, K., Huang, H., Xu, X. Digital Twin-driven smart manufacturing: Connotation, reference model, applications and research issues. Robotics and Computer-Integrated Manufacturing. 2020. 61. 101837. DOI: 10.1016/j.rcim.2019.101837
- Borovkov, A.I., Klyavin, O.I., Maruseva, V.M., Ryabov, Yu.A., Shcherbina, L.A. Tsifrovaya fabrika Digital Factory Instituta peredovykh proizvodstvennykh tekhnologiy SPbPU [Digital Factory Digital Factory of Institute of Advanced Manufacturing Technologies SPbPU]. Tramplyn k uspekhu. 2016. No. 7. Pp. 11–13. (rus)
- Tao, F., Qi, Q., Wang, L., Nee, A. Y. C. Digital twins and cyber-physical systems toward smart manufacturing and Industry 4.0: correlation and comparison. Engineering. 2019. 54. Pp. 653–661. DOI: 10.1016/j.eng.2019.01.014
- Borovkov, A.I., Ryabov, Yu.A. Opredeleniye, razrabotka i primeneniye tsifrovoykh dvoynikov: podkhod Tsentra kompetentsiy NTI SPbPU «Novyye proizvodstvennyye tekhnologii» [Definition, development and application of digital twins: the approach of the Competence Center of NTI SPbPU "New production technologies"]. Tsifrovaya podstantsiya. 2019. No. 12. Pp. 20–25. (rus)
- Heaton, J., Parlikad, A.K., Schooling, J. A Building Information Modelling approach to the alignment of organisational objectives to Asset Information Requirements. Automation in Construction. 2019. 104. Pp. 14–26.
- Boje, C., Guerriero, A., Kubicki, S., Rezgui, Y. Towards a semantic Construction Digital Twin: Directions for future research. Automation in Construction. 2020. 114. 103179. DOI: 10.1016/j.autcon.2020.103179
- Knoth, L., Mittlböck, M., Vockner, B. Smart 3D building infrastructures: linking GIS with other domains. ISPRS Annals of the Photogrammetry, Remote Sensing and Spatial Information Sciences. 2016. 4. 187–194. DOI: 10.5194/isprs-annals-IV-2-W1-187-2016
- Badenko, V.L., Yadykin, V.K. Tsifrovaya transformatsiya promyshlennosti i predpriyatiy: rol i mesto BIM tekhnologiy [Digital transformation of industry and enterprises: the role and place of BIM- technologies]. Tsifrovaya transformatsiya ekonomiki i promyshlennosti. Sbornik trudov nauchno-prakticheskoy konferentsii s zarubezhnym uchastiyem. 2019. Pp. 506–516. (rus)
- Delbrügger, T., Lenz, L. T., Losch, D., Roßmann, J. A navigation framework for digital twins of factories based on building information modeling. In 2017 22nd IEEE International Conference on Emerging Technologies and Factory Automation ETFA. 2017. Pp. 1–4. IEEE. DOI: 10.1109/ETFA.2017.8247712
- Hamledari, H., Rezazadeh Azar, E., McCabe, B. IFC-based development of as-built and as-is BIMs using construction and facility inspection data: Site-to-BIM data transfer automation. Journal of Computing in Civil Engineering, 2018. 322. 04017075. DOI: 10.1061/ASCECP.1943-5487.0000727
- Lu, Q., Xie, X., Heaton, J., Parlikad, A.K., Schooling, J. From BIM Towards Digital Twin: Strategy and Future Development for Smart Asset Management. Studies in Computational Intelligence. 2019. 853. Pp. 392–404. DOI: 10.1007/978-3-030-27477-1_30
- Petri, I., Kubicki, S., Rezgui, Y., Guerriero, A., Li, H. Optimizing energy efficiency in operating built environment assets through building information modeling: a case study. Energies. 2017. 108. 1167. DOI: 10.3390/en10081167
- Li, J., Greenwood, D., Kassem, M. Blockchain in the built environment and construction industry: A systematic review, conceptual models and practical use cases. Automation in Construction. 2019. 102. Pp. 288–307. DOI: 10.1016/j.autcon.2019.02.005
- Morgan, B. Organizing for digitalization through mutual constitution: the case of a design firm. Construction Management and Economics, 2019. 377. Pp. 400–417. DOI: 10.1080/01446193.2018.1538560

20. Fernández-Miranda, S.S., Marcos, M., Peralta, M.E., Aguayo, F. The challenge of integrating Industry 4.0 in the degree of Mechanical Engineering. *Procedia manufacturing*. 2017. 13. Pp. 1229–1236. DOI: 10.1016/j.promfg.2017.09.039
21. Liao, Y., Deschamps, F., Loures, E.D.F.R., Ramos, L.F.P. Past, present and future of Industry 4.0—a systematic literature review and research agenda proposal. *International journal of production research*. 2017. 5512. 3609–3629. DOI: 10.1080/00207543.2017.1308576
22. Love, P.E., Matthews, J. The 'how' of benefits management for digital technology: From engineering to asset management. *Automation in Construction*. 2019. 107. 102930. DOI: 10.1016/j.autcon.2019.102930
23. Hicks, B., Culley, S., Gopsill, J., Snider, C. Managing complex engineering projects: What can we learn from the evolving digital footprint? *International Journal of Information Management*. 2020. 51. 102016. DOI: 10.1016/j.ijinfomgt.2019.10.001
24. Castelo-Branco, I., Cruz-Jesus, F., Oliveira, T. Assessing Industry 4.0 readiness in manufacturing: Evidence for the European Union. *Computers in Industry*. 2019. 107. Pp. 22–32. DOI: 10.1016/j.compind.2019.01.007
25. Cohen, Y., Naseraldin, H., Chaudhuri, A., Pilati, F. Assembly systems in Industry 4.0 era: a road map to understand Assembly 4.0. *The International Journal of Advanced Manufacturing Technology*. 2019. 1059. Pp. 4037–4054. DOI: 10.1007/s00170-019-04203-1
26. Wang, J., Ye, L., Gao, R. X., Li, C., Zhang, L. Digital Twin for rotating machinery fault diagnosis in smart manufacturing. *International Journal of Production Research*. 2019. 5712. Pp. 3920–3934. DOI: 10.1080/00207543.2018.1552032
27. Abramovici, M., Göbel, J. C., Savarino, P. Reconfiguration of smart products during their use phase based on virtual product twins. *CIRP Annals*. 2017. 661. Pp. 165–168. DOI: 10.1016/j.cirp.2017.04.042
28. Kritzinger, W., Karner, M., Traar, G., Henjes, J., Sihn, W. Digital Twin in manufacturing: A categorical literature review and classification. *IFAC-PapersOnLine*. 2018. 5111. Pp. 1016–1022. DOI: 10.1016/j.ifacol.2018.08.474
29. Badenko, V., Fedotov, A., Zotov, D., Lytkin, S., Volgin, D., Garg, R. D., Min, L. Scan-to-BIM methodology adapted for different application. *International Archives of the Photogrammetry, Remote Sensing and Spatial Information Sciences*, 2019. 425/W2. Pp. 1–7. DOI:10.5194/isprs-archives-XLII-5-W2-1-2019
30. Badenko, V., Volgin, D., Lytkin, S. Deformation monitoring using laser scanned point clouds and BIM. *MATEC Web of Conferences*. 2018. 245. 01002. DOI: 10.1051/mateconf/201824501002
31. Volk, R., Stengel, J., Schultmann, F. Building Information Modeling BIM for existing buildings—Literature review and future needs. *Automation in construction*. 2014. 38. Pp. 109–127. DOI: 10.1016/j.autcon.2013.10.023
32. Lydon, G.P., Caranovic, S., Hischier, I., Schlueter, A. Coupled simulation of thermally active building systems to support a digital twin. *Energy and Buildings*. 2019. 202. 109298. DOI: 10.1016/j.enbuild.2019.07.015
33. Lu, Q., Xie, X., Parlikad, A.K., Schooling, J.M., Konstantinou, E. Moving from building information models to digital twins for operation and maintenance. *Proceedings of the Institution of Civil Engineers-Smart Infrastructure and Construction*. 2020. Pp. 1–11. DOI: 10.1680/jsmic.19.00011
34. Khajavi, S.H., Mottagh, N.H., Jaribion, A., Werner, L.C., Holmström, J. Digital Twin: Vision, Benefits, Boundaries, and Creation for Buildings. *IEEE Access*. 2019. 7. Pp. 147406–147419. DOI: 10.1109/ACCESS.2019.2946515
35. Barykin, S., Borovkov, A., Rozhdestvenskiy, O., Tarshin, A., Yadykin, V. Staff Competence and Training for Digital Industry. *IOP Conference Series: Materials Science and Engineering*. IOP Publishing. 2020. Vol. 940. No. 1. P. 012106).
36. Oztemel, E., Gursev, S. Literature review of Industry 4.0 and related technologies. *Journal of Intelligent Manufacturing*, 2020. 311. Pp. 127–182. DOI: 10.1007/s10845-018-1433-8
37. Borovkov, A.I., Rozhdestvenskiy, O.I., Kukushkin, K.V., Pavlova, Ye.I., Tarshin, A.Yu. Dorozhnaya karta po razvitiyu skvoznoy tsifrovoy tekhnologii «Novyye proizvodstvennyye tekhnologii». Rezultaty i perspektivy [Roadmap for the development of end-to-end digital technology "New production technologies". Results and prospects]. *Zhurnal «Innovatsii»*. 2019. No. 11(253). Pp. 89–104. (rus)
38. Alcácer, V., Cruz-Machado, V. Scanning the industry 4.0: A literature review on technologies for manufacturing systems. *Engineering Science and Technology, an International Journal*. 2019. 223. Pp. 899–919. DOI: 10.1016/j.jestch.2019.01.006
39. Guo, J., Zhao, N., Sun, L., Zhang, S. Modular based flexible digital twin for factory design. *Journal of Ambient Intelligence and Humanized Computing*. 2019. 103. Pp. 1189–1200. DOI: 10.1007/s12652-018-0953-6
40. Qi, Q., Tao, F. Digital twin and big data towards smart manufacturing and industry 4.0: 360 degree comparison. *Ieee Access*. 2018. 6. Pp. 3585–3593. DOI: 10.1109/ACCESS.2018.2793265
41. Schluse, M., Priggemeyer, M., Atorf, L., Rossmann, J. Experimentable digital twins—Streamlining simulation-based systems engineering for industry 4.0. *IEEE Transactions on industrial informatics*. 2018. 144. Pp. 1722–1731. DOI: 10.1109/TII.2018.2804917
42. Uhlemann, T.H.J., Lehmann, C., Steinhilper, R. The digital twin: Realizing the cyber-physical production system for industry 4.0. *Procedia Cirp*. 2017. 61. Pp. 335–340. DOI: 10.1016/j.procir.2016.11.152
43. Borovkov A.I., Ryabov Yu.A. Tsifrovyye dvoyniki: opredeleniye, podkhody i metody razrabotki [Digital twins: definition, approaches and development methods]. *Tsifrovaya transformatsiya ekonomiki i promyshlennosti*. 2019. Pp. 234–245.
44. Sadeghi, M., Elliott, J.W., Porro, N., Strong, K. Developing building information models BIM for building handover, operation and maintenance. *Journal of Facilities Management*. 2019. 173. Pp. 301–316. DOI: 10.1108/JFM-04-2018-0029
45. Tchana, Y., Ducellier, G., Remy, S. Designing a unique Digital Twin for linear infrastructures lifecycle management. *Procedia CIRP*. 2019. 84. Pp. 545–549. DOI: 10.1016/j.procir.2019.04.176
46. Stojanovic, V., Trapp, M., Richter, R., Hagedorn, B., Döllner, J. Towards The Generation of Digital Twins for Facility Management Based on 3D Point Clouds. In *Proceeding of the 34th Annual ARCOM Conference 2018*. Pp. 270–279.
47. Longo, F., Nicoletti, L., Padovano, A. Ubiquitous knowledge empowers the Smart Factory: The impacts of a Service-oriented Digital Twin on enterprises' performance. *Annual Reviews in Control*. 2019. 47. Pp. 221–236. DOI: 10.1016/j.arcontrol.2019.01.001
48. Lu, Q., Xie, X., Heaton, J., Parlikad, A. K., Schooling, J. From BIM Towards Digital Twin: Strategy and Future Development for Smart Asset Management. In *International Workshop on Service Orientation in Holonic and Multi-Agent Manufacturing* pp. 2019. Pp. 392–404. Springer, Cham. DOI: 10.1007/978-3-030-27477-1_30
49. Lu, Q., Chen, L., Li, S., Pitt, M. Semi-automatic geometric digital twinning for existing buildings based on images and CAD drawings. *Automation in Construction*. 2020. 115. 103183. DOI: 10.1016/j.autcon.2020.103183
50. Shou, W., Wang, J., Wang, X., Chong, H.Y. A comparative review of building information modelling implementation in building and infrastructure industries. *Archives of computational methods in engineering*. 2015. 222. Pp. 291–308. DOI 10.1007/s11831-014-9125-9
51. Yang, H. L., Chang, T. W., Choi, Y. Exploring the research trend of smart factory with topic modeling. *Sustainability*. 2018. 108. 2779. DOI: 10.3390/su10082779

52. Borovkov, A.I., Gamzikova, A.A., Kukushkin, K.V., Ryabov, Yu.A. Tsifrovyye dvoyniki v vysokotekhnologichnoy promyshlennosti. kratkiy doklad sentyabr 2019 g. [Digital twins in the high-tech industry. short report September 2019]. SPb.: Politekh-Press, 2019. 62 p.
53. Rasheed, A., San, O., Kvamsdal, T. 2020. Digital twin: Values, challenges and enablers from a modeling perspective. IEEE Access. 8. Pp. 21980–22012. DOI: 10.1109/ACCESS.2020.2970143
54. Fedorov, A., Shkodyrev, V., Zobnin, S. Knowledge based planning framework for intelligent distributed manufacturing systems. Lecture Notes in Computer Science including subseries Lecture Notes in Artificial Intelligence and Lecture Notes in Bioinformatics. 2015. Vol. 9141. Pp. 300–307 DOI: 10.1007/978-3-319-20472-7_32
55. Borovkov, A.I., Ryabov, Yu.A., Ageev, A.B. Razrabotka i primeneniye tsifrovyykh dvoynikov v sudostroenii i korablestroenii [Development and application of digital twins in shipbuilding and naval architecture]. Materialy 20-y Mezhdunarodnoy nauchno-prakticheskoy konferentsii MORINTEKH-PRAKTIK "Informatsionnyye tekhnologii v sudostroyenii-2019" [Proceedings of the 20th International Scientific and Practical Conference MORINTEKH-PRAKTIK "Information Technologies in Shipbuilding^ 19"]. Saint-Petersburg, 2019. Pp. 9–14.
56. Rossmann, J., Schluse, M., Hoppen, M., Losch, D., Hempe, N., Schlette, C. December. Virtual BIM Testbeds: The eRobotics Approach to BIM and Its Integration into Simulation, Rendering, Virtual Reality and More. International Conference on Developments of E-Systems Engineering DeSE. 2015. Pp. 250–255. IEEE. DOI: 10.1109/DeSE.2015.67
57. Correa, F.R. Cyber-physical systems for construction industry. In 2018 IEEE Industrial Cyber-Physical Systems ICPS. 2018. Pp. 392–397.
58. Franz, B., Messner, J. Evaluating the impact of building information modeling on project performance. Journal of Computing in Civil Engineering. 2019. 333. 04019015. DOI: 10.1061/ASCECP.1943-5487.0000832
59. Andersen, M.T., Findsen, A.L. Exploring the benefits of structured information with the use of virtual design and construction principles in a BIM life-cycle approach. Architectural Engineering and Design Management, 2019. 152. Pp. 83–100. DOI: 10.1080/17452007.2018.1546165
60. Dinis, F.M., Sanhudo, L., Martins, J.P., Ramos, N.M. Improving project communication in the architecture, engineering and construction industry: Coupling virtual reality and laser scanning. Journal of Building Engineering. 2020. 30. 101287. DOI: 10.1016/j.jobe.2020.101287
61. Jones, D., Snider, C., Nassehi, A., Yon, J., Hicks, B. Characterising the Digital Twin: A systematic literature review. CIRP Journal of Manufacturing Science and Technology In Press. 2020. Available online 9 March 2020. DOI: 10.1016/j.cirpj.2020.02.002
62. Grieves, M., Vickers, J. Digital twin: Mitigating unpredictable, undesirable emergent behavior in complex systems. In Transdisciplinary perspectives on complex systems. 2017. Pp. 85–113. Springer, Cham. DOI: 10.1007/978-3-319-38756-7_4
63. Grieves M. Digital twin: Manufacturing excellence through virtual factory replication. White paper, 2014; Available: <http://www.aprison.com>.
64. Grieves, M.W. Virtually Indistinguishable. In IFIP International Conference on Product Lifecycle Management 2012. Pp. 226–242. Springer, Berlin, Heidelberg. DOI: 10.1007/978-3-642-35758-9_20
65. Eastman, C., Teicholz, P., Sacks, R., Liston, K., 2011, BIM handbook: a guide to building information modeling for owners, managers, designers, engineers and contractors. John Wiley Sons.
66. BS EN ISO 19650-1: 2018.
67. Rauch, E., Dallasega, P., Matt, D.T. Distributed manufacturing network models of smart and agile mini-factories. International Journal of Agile Systems and Management. 2017. 103-4, Pp. 185–205.
68. Ding, K., Chan, F.T., Zhang, X., Zhou, G., Zhang, F. Defining a digital twin-based cyber-physical production system for autonomous manufacturing in smart shop floors. International Journal of Production Research, 2019. 5720. Pp. 6315–6334. DOI: 10.1080/00207543.2019.1566661
69. Leng, J., Liu, Q., Ye, S., Jing, J., Wang, Y., Zhang, C. Chen, X. Digital twin-driven rapid reconfiguration of the automated manufacturing system via an open architecture model. Robotics and Computer-Integrated Manufacturing. 2020. 63. 101895. DOI: 10.1016/j.rcim.2019.101895
70. Zimmermann, A., Schmidt, R., Jugel, D., Möhring, M. Adaptive enterprise architecture for digital transformation. Communications in Computer and Information Science. 2016. 567. Pp. 308–319. DOI: 10.1007/978-3-319-33313-7_24
71. Heaton J., Parlikad A.K., Schooling J. Design and development of BIM models to support operations and maintenance. Computers in industry. 2019. 111. Pp. 172–186.
72. Chen W., et al. BIM-based framework for automatic scheduling of facility maintenance work orders. Automation in Construction. 2018. 91. Pp. 15–30.
73. Badenko, V.L., Bolshakov, N.S., Fedotov, A.A., Yadykin, V.Y. Digital twins of complex technical objects in industry 4.0: basic approaches. St. Petersburg State Polytechnical University Journal. Economics. 2020. 13(1). Pp. 20–30. DOI: 10.18721/JE.13102
74. Choi B., et al. Framework for work-space planning using four-dimensional BIM in construction projects. Journal of Construction Engineering and Management. 2014. 140. No. 9. 04014041.
75. Weber J., et al. Ontology for Logistics Requirements on a 4D BIM for Semi-Automatic Storage Space Planning. ISARC. Proceedings of the International Symposium on Automation and Robotics in Construction. IAARC Publications, 2019. 36. Pp. 560–567.
76. British Standards Institute, PAS 1192-2 Specification for Information Management for the capital/delivery Phase of Construction Projects Using Building Information Modelling. 2013. <https://bim-level2.org/en/standards/>.
77. Borovkov A.I., i dr. Tsifrovyye dvoyniki i tsifrovaya transformatsiya predpriyatiy OPK [Digital twins and digital transformation of enterprises of the military-industrial complex]. Vestnik Vostochno-Sibirskoy otkrytoy akademii. 2019. No. 32. Pp. 2–2. (rus)
78. Cecconi, F.R., Maltese, S., Dejacco, M.C. Leveraging BIM for digital built environment asset management. Innovative Infrastructure Solutions. 2017. 2. No. 1, 14.
79. CCC Highways Consultants use open BIM for the maintenance of a bridge across the Yangtze 2019 Building SMART International award submission 2018. Available online at <https://www.buildingsmart.org/wp-content/uploads/2019/10/CCC-Nanjing-Bridge-Case-Study-Final.pdf>
80. UNITEC's integrated information system. Building performance. Available online at <https://www.building.govt.nz/assets/Uploads/projects-and-consents/building-information-modelling/nz-bim-case-study-5-unitec.pdf>
81. Gorshkov, A., Vatin, N., Nemova, D., Shabaldin, A., Melnikova, L., Kirill, P. Using life-cycle analysis to assess energy savings delivered by building insulation. Procedia Engineering. 2015. 117. Pp. 1080–1089.

82. The digital twin, another step forward in ACCIONA's commitment to technology. Available online at <https://www.accionagua.com/pressroom/news/2020/may/the-digital-twin-another-step-forward-in-accionas-commitment-to-technology/>
83. Dixit, M.K. et al. Integration of facility management and building information modeling BIM.Facilities. – 2019.

Contacts:

Vladimir Badenko, vbadenko@gmail.com

Nikolai Bolshakov, nikolaybolshakov7@gmail.com

Elana Tishchenko, elenasemenova@bk.ru

Alexander Fedotov, alexandrefedotov@gmail.com

Alberto Celani, alberto.celani@polimi.it

Vladimir Yadykin, v.yadikin@gmail.com

© Badenko, V.L., Bolshakov, N.S., Tishchenko, E.B., Fedotov, A.A., Celani, A.C., Yadykin, V.K., 2021



ПОЛИТЕХ
Санкт-Петербургский
политехнический университет
Петра Великого

Инженерно-строительный институт
Центр дополнительных профессиональных программ

195251, г. Санкт-Петербург, Политехническая ул., 29,
тел/факс: 552-94-60, www.stroikursi.spbstu.ru,
stroikursi@mail.ru

Приглашает специалистов проектных и строительных организаций,
не имеющих базового профильного высшего образования
на курсы профессиональной переподготовки (от 500 часов)
по направлению «Строительство» по программам:

П-01 «Промышленное и гражданское строительство»

Программа включает учебные разделы:

- Основы строительного дела
- Инженерное оборудование зданий и сооружений
- Технология и контроль качества строительства
- Основы проектирования зданий и сооружений
- Автоматизация проектных работ с использованием AutoCAD
- Автоматизация сметного дела в строительстве
- Управление строительной организацией
- Управление инвестиционно-строительными проектами. Выполнение функций технического заказчика

П-02 «Экономика и управление в строительстве»

Программа включает учебные разделы:

- Основы строительного дела
- Инженерное оборудование зданий и сооружений
- Технология и контроль качества строительства
- Управление инвестиционно-строительными проектами. Выполнение функций технического заказчика и генерального подрядчика
- Управление строительной организацией
- Экономика и ценообразование в строительстве
- Управление строительной организацией
- Организация, управление и планирование в строительстве
- Автоматизация сметного дела в строительстве

П-03 «Инженерные системы зданий и сооружений»

Программа включает учебные разделы:

- Основы механики жидкости и газа
- Инженерное оборудование зданий и сооружений
- Проектирование, монтаж и эксплуатация систем вентиляции и кондиционирования
- Проектирование, монтаж и эксплуатация систем отопления и теплоснабжения
- Проектирование, монтаж и эксплуатация систем водоснабжения и водоотведения
- Автоматизация проектных работ с использованием AutoCAD
- Электроснабжение и электрооборудование объектов

П-04 «Проектирование и конструирование зданий и сооружений»

Программа включает учебные разделы:

- Основы сопротивления материалов и механики стержневых систем
- Проектирование и расчет оснований и фундаментов зданий и сооружений
- Проектирование и расчет железобетонных конструкций
- Проектирование и расчет металлических конструкций
- Проектирование зданий и сооружений с использованием AutoCAD
- Расчет строительных конструкций с использованием SCAD Office

П-05 «Контроль качества строительства»

Программа включает учебные разделы:

- Основы строительного дела
- Инженерное оборудование зданий и сооружений
- Технология и контроль качества строительства
- Проектирование и расчет железобетонных конструкций
- Проектирование и расчет металлических конструкций
- Обследование строительных конструкций зданий и сооружений
- Выполнение функций технического заказчика и генерального подрядчика

По окончании курса слушателю выдается диплом о профессиональной переподготовке
установленного образца, дающий право на ведение профессиональной деятельности

